CALCIUM PHOSPHATE SILICATE CEMENT FOR RISEDRONATE DRUG DELIVERY

by

TIANXING GONG

B.Eng., Nanyang Technological University, 2009
M.M., The University of British Columbia, 2010

A THESIS SUBMITTED IN PARTIAL FULFILLMENT OF THE REQUIREMENTS FOR THE DEGREE OF

DOCTOR OF PHILOSOPHY

in

THE FACULTY OF GRADUATE AND POSTDOCTORAL STUDIES

(Materials Engineering)

THE UNIVERSITY OF BRITISH COLUMBIA

(Vancouver)

December 2014

© Tianxing Gong, 2014

Abstract

The effectiveness of bone cements in treating bone fracture is impaired by osteoporosis, which not only delays the osseointegration but also compromises the stability of implants. As a result, further fractures are not unusual after bone cement implantation in osteoporotic patients. This dissertation reports the investigation of the novel calcium phosphate silicate cement (CPSC) as a possible drug delivery system (DDS) for risedronate (RA) to treat osteoporosis and to restore bone fracture. Risedronate belongs to the family of bisphosphonate and, as the 3rd generation of bisphosphonate, can effectively suppress osteoclast activities and treat osteoporosis. In this work, the CPSC material properties were characterized as a function of RA content. High performance liquid chromatography was used to detect RA release profiles from cements and the Higuchi's Law was employed to explain its release mechanisms. *In vitro* biocompatibility of RA-added CPSC (CPSC-R) was evaluated by MTT assays, flow cytometry, and real-time polymerase chain reaction. In the tibia implantation model from osteoporotic rabbits, biomarkers, X-rays, computed tomography, histology and PCR arrays were used to evaluate CPSC-R *in vivo* performance.

It has been found that RA greatly affected CPSC setting time and compressive strength in a concentration-dependent manner. It was also found that RA disrupted CPSC hydration and delayed calcium silicate hydrate gel formation. RA was progressively adsorbed onto the unreacted calcium silicate and formed calcium-RA complexes. RA release kinetics from cement was controlled by the implant degradation and was in a good agreement with the theoretical calculations. CPSC-R was biocompatible and improved osteoblast proliferation and differentiation. Biomarker studies showed that CPSC-R significantly reduced osteoclast activities as compared to the sham control ($p < 0.05$). The radiographic and histological examination demonstrated that CPSC-R improved osseointegration and bone formation, as compared to RA-free CPSC control group. Gene array

studies indicated that CPSC-R implants could significantly up-regulate osteogenesis-related gene expressions as compared to the control groups.

In conclusion, this study indicates that CPSC is potentially a good Drug Delivery System of RA. The anti-osteoporotic effectiveness of this system could be beneficial in bone fracture treatments for patients who are suffering from osteoporosis.

Preface

Chapter 5, 6 and 7 were written based upon three manuscripts that have been published or submitted for publication. Some results in these chapters were also used for conference presentations and abstracts.

Chapter 5 is the edited version of the journal article, "Preparation, Characterization, Release Kinetics, and *in vitro* Cytotoxicity of Calcium Silicate Cement as A Risedronate Delivery System" which was published in the Journal of Biomedical Materials Research Part A 2014 102A (7) 2295-2304. Some results from this article were also presented at the Society for Biomaterials 2014 Annual Meeting and Exposition in Denver. I performed all experiments, discussed the results and wrote the manuscript myself as the first author. The primary supervisor, Tom Troczynski, was responsible for supervising experimental designs and results discussion in the sections of materials preparation and characterization, and the co-supervisor and corresponding author Urs Häfeli was responsible for supervising experimental designs and result discussions in the drug delivery and *in vitro* cytotoxicity sections. The industrial supervisor, Quanzu Yang, provided crucial raw materials for this study. The co-authors Zhiqin Wang, Yubiao Zhang, and Changshan Sun helped in executing drug delivery and *in vitro* experiments.

Chapter 6 is the edited version of a submitted manuscript, which is currently under review. As the first author, I was responsible for experimental design, results discussion and manuscript writing. As the primary and secondary supervisors, Tom Troczynski and Urs Häfeli, were responsible for supervising experimental designs and results discussion in the sections of material characterization, *in vitro* and *in vivo* evaluation. Prof. Urs Häfeli was also assigned as the primary corresponding author of this article. The industrial supervisor, Quanzu Yang, also provided raw materials for this study. Zhiqin Wang and Mingxiao Hou, coordinated the *in vitro*

and *in vivo* experiments. Other authors in the article provided assistance in *in vitro* and *in vivo* experiments. Some results from this article were also presented at the Vancouver Nanomedicine Day 2014, the presentation titled "Formulation of Microporous Calcium Silicate Cement for Bisphosphonate Risedronate Delivery".

An edited version of another submitted manuscript appears in this dissertation as the Chapter 7. Tom Troczynski and Urs Häfeli were responsible for supervising experimental designs and results discussion in the sections of material characterization, *in vitro* and *in vivo* evaluations. Prof. Urs Häfeli is also the corresponding author of this article. As the first author, my contribution involved designing and conducting experiments, discussing the results and writing the manuscript. Other authors provided assistance in the *in vitro* and *in vivo* experiments. All animal studies were conducted at the Safety Evaluation Centre of Shenyang Research Institute of Chemical Industry (permit No. K002). Since no animal experiments were involved in the University of British Columbia, no permit was required in my doctoral research from the animal care committee at the University of British Columbia.

Table of Contents

Abstract ..... **ii**

Preface ..... **iv**

Table of Contents ..... **vi**

List of Tables ..... **xi**

List of Figures ..... **xii**

List of Abbreviations ..... **xxii**

Acknowledgements ..... **xxvi**

Dedication ..... **xxvii**

Chapter 1: INTRODUCTION **1**

Chapter 2: LITERATURE REVIEW **4**

2.1 Calcium phosphate cement (CPC) 4

2.2 Calcium silicate cement (CSC) 4

2.2.1 Composition and structure of CSC 5

2.2.2 Formation of CSH 7

2.2.3 Surface area and porosity 9

2.3 Calcium phosphate silicate cements (CPSC) 11

2.4 Bisphosphonates 12

2.4.1 Overview of bisphosphonates 12

2.4.2 Risedronate 15

2.5 Controlled drug release 20

2.6 Osteoporosis and osteoporotic fracture 24

2.7 *In vitro* evaluation of biocompatibility of biomaterials 27

2.7.1 Cytotoxicity of biomaterials 27
2.7.2 Real time polymerase chain reaction (PCR) 28
2.7.3 Flow cytometry (FCM) 31
2.8 *In vivo* evaluation of biomaterials 34
2.9 Biochemical markers related to bone resorption 36
Chapter 3: SCOPE AND OBJECTIVES 38
Chapter 4: MATERIALS AND METHODS 44
4.1 Cement preparation 44
4.1.1 RA-added CSC preparation 44
4.1.2 CPSC preparation 44
4.1.3 RA-added CPSC preparation 45
4.2 Cement characterization 45
4.2.1 Setting time and compressive strength determination 45
4.2.2 Structural analysis of CSC 46
4.3 RA release analysis from CSC 47
4.3.1 Risedronate release detection 47
4.3.2 Adsorption/desorption analysis and kinetics of RA onto/from CSC pellets 48
4.3.3 Analysis of RA distribution in the CSC pellet 49
4.4 *In vitro* biocompatibility analysis 49
4.4.1 Cell culture of osteoblast cells 49
4.4.2 MTT assay of RA-added CSC on osteoblast cells 50
4.4.3 MTT assay of CPSC on osteoblast cells 51
4.4.4 MTT assay of RA-added CPSC on osteoblast cells 51

4.4.5 Gene expression analysis on RT-PCR 52
4.4.6 Cell cycles analysis on flow cytometer 53
4.4.7 Statistical analysis 53
4.5 *In vivo* study 53
4.5.1 CPSC *in vivo* animal model 54
4.5.2 CPSC-R *in vivo* model 55
4.5.3 Clinical X-ray and computed tomography (CT) analyses 57
4.5.4 Histological slides preparation and analysis 58
4.5.5 Serum biochemical markers evaluations 60
4.5.6 PCR array analysis 61
Chapter 5: RESULTS AND DISCUSSION I: CALCIUM SILICATE CEMENT AS A RA-DDS 63
5.1 RA-added CSC material characterization 63
5.2 Release kinetics of RA from CSC 67
5.3 Biocompatibility of the RA-containing CSCs 71
5.4 Discussion 72
Chapter 6: RESULTS AND DISCUSSION II: CPSC EFFECTS ON OSTEOBLASTIC PROLIFERATION AND IN VIVO OSTEOGENESIS 76
6.1 CPSC material characterization 76
6.2 *In vitro* analysis of CPSC biocompatibility 80
6.3 *In vivo* analysis of CPSC osteogenic effects in rabbits 85
6.4 Discussion 95

Chapter 7: RESULTS AND DISCUSSION III: ANTI-OSTEOPOROTIC AND ENHANCED OSTEOGENIC EFFECTS OF RA-ADDED CPSC 99

7.1 Material characterizations 99

7.2 *In vitro* biocompatibility 104

7.3 Global anti-osteoporotic effects 108

7.4 Local osteogenic effects shown by X-ray and CT 116

7.5 Local osteogenic effects shown by histopathology 119

7.6 Local osteogenic effects shown by PCR analysis 122

7.7 Discussion 129

Chapter 8: CONCLUSIONS AND FUTURE WORK 141

8.1 Conclusions 141

8.2 Future work 147

REFERENCES 150

APPENDICES 163

Appendix A List of equipment 163

Appendix B Experimental protocols 166

B.1 Protocol for total RNA isolation from cells 166

B.2 Protocol for extracted RNA stabilization 167

B.3 Protocol for cDNA reverse transcription 168

B.4 Protocol for real-time PCR 169

B.5 Protocol for total RNA isolation from bone fragments 169

B.6 Protocol for PCR array 171

Appendix C Long-term daily monitoring log 174

Appendix D Post-surgery monitoring sheet 175

Appendix E Supplementary data 176

E.1 Supplementary radiographic images 176

E.2 Supplementary histological images 226

E.3 Supplementary PCR array results 249

List of Tables

Table 5.1: Quantitative analysis of the crystalline phases of CSC, CSC01, CSC05R and CSC10R after 7 days of setting using the Rietveld refinement. 64

Table 5.2: Average porosity and tortuosity of each sample. Standard deviation is given in brackets (n = 4). 67

Table 5.3: Theoretical release fractions over 28 days based upon the tortuosity found in our samples between 3 and 4..... 73

Table 6.1: Porosity calculated from μCT visualization. Data are presented as mean value ± standard deviation. (n = 4) 77

Table 7.1: Porosity measured by gas sorption and μCT methods. The results are presented as average ± standard deviation. (n = 4)..... 100

Table 7.2: 84 genes analyzed by PCR array given by the manufacturer 125

Table 7.3: Genes up-regulated in CPSC10 as compared to the sham control. 95% confidence interval (CI) is given in the bracket. 126

Table 7.4: Genes up-regulated in CPSC10-05R as compared to the sham control. 95% confidence interval (CI) is given in the bracket.. 127

List of Figures

Figure 2.1: Schematic drawing of pyrophosphates 13

Figure 2.2: Schematic drawing of a generic bisphosphonate and of risedronate, the third generation bisphosphonate drug used for this research. 14

Figure 2.3: Schematic drawing of effective drug concentration region 20

Figure 2.4: Schematic drawing of drug release from a planar surface 22

Figure 2.5: Schematic drawing of drug release in three dimensions 24

Figure 2.6: Representation threshold cycle (C_t) obtained from real time PCR analysis 30

Figure 2.7: Cell population plotted by forward scattered (FSC) and side scattered (SSC) fluorescent signals. 33

Figure 2.8: Representation of the relative quantities of G1, S and G2 phases in cell cycle analysis. Green arrow indicates the mathematical profile calculated by ModFitLT and the blue arrows indicate a histogram of cell numbers. 33

Figure 2.9: Illustration of biochemical markers related to bone remodelling. OPG (osteoprotegerin) is secreted from mature osteoblast cells and bound to RANKL (receptor activator of nuclear factor NF-κB ligand) in serum to prevent its binding with RANK on the osteoclast precursors and maturation of precursors. BALP (bone-specific alkaline phosphatase) and OCN (osteocalcin) are released from osteoblast cells and TRACP-5b (tartrate-resistant acid phosphatase-5b isoform) is secreted from the osteoclast cells as biomarkers for bone formation and resorption, respectively. Collagenous proteins, PYD (pyridinoline crosslinks), DPD (deoxypyridinoline crosslinks), OHP (hydroxyproline), NTX (N-terminal telopeptide) and CTX (C-terminal telopeptide), are released during bone matrix breakdown and used as biomarkers for bone resorption 37

Figure 3.1: Schematic drawing of experimental methods utilized to address objective 1 (refer to the list of abbreviation for symbols details)..... 40
Figure 3.2: Schematic drawing of experimental methods utilized to address objective 2 (refer to the list of abbreviation for symbols details)..... 41
Figure 4.1: Graphic illustration of the CPSC animal study schedule..... 55
Figure 4.2: Graphic illustration of the CPSC-R animal study schedule..... 56
Figure 4.3: A representation of the histological study. An area of 1 cm × 1 cm is observed under the light microscope. A histological slide has a thickness of 5 μm..... 59
Figure 5.1: Setting times of risedronate-added and risedronate-free CSC as a function of risedronate concentration (n = 4)..... 64
Figure 5.2: Compressive strength changes as a function of risedronate concentration (n = 10) after hardening for 3 and 7 days at 37 °C and 100% RH..... 65
Figure 5.3: XRD patterns of CSC and risedronate-containing CSC01R, CSC05R and CSC10R after 7 days of setting. The characteristic $Ca(OH)_2$ peaks (*) are reduced with increasing RA amount. Unidentified peaks are primarily attributed to dicalcium silicate..... 65
Figure 5.4: Scanning electron micrographs of CSC (a), CSC01R (b), CSC05R (c), and CSC10R (d) after 7 days of setting. One bar equals to 5 μm..... 66
Figure 5.5: FTIR scans of both (a) outer and (b) inner surfaces of CSC pellets with 10 wt% of RA. Characteristic peaks of POO^- stretching at 960 cm^{-1} are used to plot RA distribution (red spots). Each IR image represents an area of 10 μm × 10 μm. One bar equals to 1 mm..... 66
Figure 5.6: FTIR spectra of risedronic acid, risedronate calcium and calcium silicate cement sample with 10% risedronic acid preloaded. Sample powders were mixed (4 wt%) with dehydrated KBr and compressed into tablets..... 68

Figure 5.7: RA release curves of CSC01R, CSC05R and CSC10R in PBS up to 28 days in molar units (a) and up to 6 months as a fraction of the total initial RA amount (b). 69
Figure 5.8: RA adsorption onto hardened CSC after milling in RA saturated PBS solutions and RA desorption from these samples in PBS (*n* = 3). 70
Figure 5.9: Cell viability of osteoblast cells after incubation with the extracts of the different cements collected after 1, 3, and 7 days. Drug-free PBS served as the control, whereas 60 mg phenol/mL of media was used as the toxicity reference. The relative viability was calculated as optical density 570 (OD_{570}) of treatment group/OD_{570} of the control group. 71
Figure 6.1: Setting times (*n* = 4) and compressive strengths (*n* = 8) of CPSC5, CPSC10 and CPSC15. Error bar represents one standard deviation. 77
Figure 6.2: (a) X-ray diffraction (XRD) patterns of raw CSC powder, CPSC5, CPSC10 and CPSC15 samples after 3 and 7 days of hydration (*n* = 4). Peaks of calcium hydroxide (P), tricalcium silicate (T) and dicalcium silicate (D) are identified. (b) Rietveld refinement analysis of CPSC5, CPSC10 and CPSC15. Error bar represents 95% confidence interval. 78
Figure 6.3: Fourier transformation infrared (FTIR) spectra of CPSC5, CPSC10 and CPSC15 samples after 7 days of hydration. 79
Figure 6.4: µCT scans of 1 cm height sections of hardened CPSC to reveal their microstructure and macroporosity: (a) CPSC5; (b) CPSC10; (c) CPSC15 (*n* = 4). The color bar represents the diameter of pores, from 5 µm for the smallest pores in blue (µCT resolution limit), to 135 µm for the largest pores in red. 79
Figure 6.5: Relative viability of osteoblast cells incubated in CPSC5, CPSC10 and CPSC15 extracts for 3 days in different dilutions of (a) 5% (1:19); (b) 10% (1:9); (c) 20% (1:4); and (d)

50% (1:1). PBS with 10%-FBS in DMEM served as the control group, while an aqueous phenol solution was used as toxicity reference (n = 5). Error bars represent one standard deviation..... 81

Figure 6.6: Representations of raw data of relative quantities of cells in each phase within one cell cycle analyzed by FCM. They are (a) the control, (b) CPSC5, (c) CPSC10 and (d) CPSC15. 82

Figure 6.7: Fractions of diploid and tetraploid DNA strands in osteoblast cells. (n = 3) The relative quantity of tetraploid of CK is significantly lower than those of CPSC5 and CPSC10 but insignificantly lower than that of CPSC15. Relative quantities of CPSC 5, CPSC10 and CPSC15 are insignificantly different between each other. ($p < 0.05$) Error bar represents one standard deviation..... 83

Figure 6.8: Representations of threshold cycles of genes amplified by PCR..... 84

Figure 6.9: mRNA expressions of ALP, runx2, TGF-β, and OPG genes in osteoblast cells harvesting in CPSC extracts for 3 days (n = 8). All expressions were normalized to the expressions of CSC. The level of ALP expression in CPSC15 is significantly lower than those in CPSC5 and CPSC10; the level of OPG expression in CPSC15 is significantly higher than those in CPSC5 and CPSC10; the levels of runx2 and TGF-β expressions are statistically indifferent among CPSC5, CPSC10 and CPSC15. ($p * < 0.05$) Error bar represents one standard deviation. 85

Figure 6.10: X-ray images of rabbit hind legs with cement implantation after (a) 2 months and (b) 3 months. One bar is equal to 1 cm. Regions of remnant cement (blue arrows) and new trabecular bone (red arrows) were enclosed by green curves and their areas were automatically measured by Osirix. These readings were used in semi-quantitative analyses..... 87

Figure 6.11: Calculate scores of (a) remnant cement from highly degraded (score 1) to mostly non-degraded (score 6) and (b) new trabecular bone formation from merely no bone formation (score 1) to significant formation (score 6) of CPSC and clinical CPC between 2 and 3 months (*n* = 7). Error bars represent one standard deviation. (*p* *< 0.05 *vs.* 2 month) 89

Figure 6.12: 3D reconstruction of implanted bones after 3 months (red circles indicate the remaining material) 90

Figure 6.13: CT scans of rabbit hind legs after 2-month implantation. Trabecular bones and newly formed cortical bones are indicated in green. The size bar is equal to 1 cm. 91

Figure 6.14: CT scans of rabbit hind legs after 3-month implantation. Trabecular bones and newly formed cortical bones are indicated in green. The size bar is equal to 1 cm. 92

Figure 6.15: Histological observations of (a) clinical CPC, (b) CPSC5, (c) CPSC10 and (d) CPSC15 after 3 months of implantation (40x). Inflammation by neutrophils infiltration (black arrows), proliferated adipose tissue (green arrows), tissue encapsulation (yellow arrows) and new bone formation (blue arrows) were indicated on the images. The size bar is equal to 0.25 mm.. 93

Figure 7.1: The setting time and compressive strength changes with risedronate concentration. (*n* = 4 for the setting time and *n* = 8 for compressive strength tests). The error bars represent one standard deviation. 100

Figure 7.2: The relative phase content of Portlandite, Ca_2SiO_4, apatite, CSH gel and the balance of amorphous phase in CPSC10, CPSC10-05R and CPSC10-10R (*n* = 4). 101

Figure 7.3: Microporosity visualization for (a) CPSC10, (b) CPSC10-05R and (c) CPSC10-10R. 101

Figure 7.4: FTIR spectra of CPSC10, CPSC10-05R and CPSC10-10R after 1-day hardening (*n* = 4). 102

Figure 7.5: Scanning electron micrographs of (a) CPSC10-core, (b) CPSC10-edge, (c) CPSC10-05R-core, (d) CPSC10-05R-edge, (e) CPSC10-10R-core and (f) CPSC10-10R-edge after 7 days of setting. One bar equals to 20 μm. 103

Figure 7.6: Osteoblast-like cell viabilities. Cells were treated with CPSC10-05R and CPSC10-10R after 1 and 3 days immersion in PBS. Error bar represents one standard deviation (n = 5). ($p^* < 0.05$ *vs.* the control group)..... 105

Figure 7.7: Fractions of diploid (DNA double strands) and tetraploid (DNA quadruple strands) in osteoblast cells. Cells were harvested from CPSC extracts for 3 days. Error bar represents one standard deviation (n = 3). 106

Figure 7.8: Osteoblastic marker gene expression by real-time PCR. mRNA expressions of (a) ALP, (b) OPG, (c) runx2 and (d) TGF-β genes in osteoblast cells are shown after incubation in cement extracts for 1 day. Error bar represents one standard deviation (n = 8). ($p^* < 0.05$ *vs.*CPSC10)..... 107

Figure 7.9: Serum levels of BALP after 4, 6, 8 and 10 weeks between sham control, CPSC10 and CPSC10-05R (n = 10 except for the 10th week n = 5). "+" sign indicates that the readings are statistically different between the sham control and CPSC10. "@" symbol indicates that the readings are statistically different between the sham control and CPSC10-05R. ($p < 0.05$)..... 109

Figure 7.10: Serum TRACP-5b levels 1, 14 and 28 days after osteoporosis induction measured by ELISA. Error bar represents one standard deviation (n = 6). ($p^* < 0.05$)..... 109

Figure 7.11: Serum levels of OCN after 4, 6, 8 and 10 weeks between sham control, CPSC10 and CPSC10-05R (n = 10 except for the 10th week n = 5). "+" sign indicates that the readings are statistically different between the sham control and CPSC10. "@" symbol indicates that the readings are statistically different between the sham control and CPSC10-05R. "#" symbol

indicates that readings are statistically different between the CPSC10 and CPSC10-05R groups. ($p < 0.05$)..... 110
Figure 7.12: Serum levels of OPG/RANKL after 4, 6, 8 and 10 weeks between sham control, CPSC10 and CPSC10-05R ($n = 10$ except for the 10th week $n = 5$). ($p < 0.05$)..... 110
Figure 7.13: Serum levels of NTX after 4, 6, 8 and 10 weeks between sham control, CPSC10 and CPSC10-05R ($n = 10$ except for the 10th week $n = 5$). "+" sign indicates that the readings are statistically different between the sham control and CPSC10. "@" symbol indicates that the readings are statistically different between the sham control and CPSC10-05R. ($p < 0.05$)..... 111
Figure 7.14: Serum levels of CTX after 4, 6, 8 and 10 weeks between sham control, CPSC10 and CPSC10-05R ($n = 10$ except for the 10th week $n = 5$). "+" sign indicates that the readings are statistically different between the sham control and CPSC10. "@" symbol indicates that the readings are statistically different between the sham control and CPSC10-05R. ($p < 0.05$)..... 111
Figure 7.15: Serum levels of PYD after 4, 6, 8 and 10 weeks between sham control, CPSC10 and CPSC10-05R ($n = 10$ except for the 10th week $n = 5$). "+" sign indicates that the readings are statistically different between the sham control and CPSC10. "@" symbol indicates that the readings are statistically different between the sham control and CPSC10-05R. "#" symbol indicates that readings are statistically different between the CPSC10 and CPSC10-05R groups. ($p < 0.05$)..... 112
Figure 7.16: Serum levels of DPD after 4, 6, 8 and 10 weeks between sham control, CPSC10 and CPSC10-05R ($n = 10$ except for the 10th week $n = 5$). "+" sign indicates that the readings are statistically different between the sham control and CPSC10. "@" symbol indicates that the readings are statistically different between the sham control and CPSC10-05R. "#" symbol

indicates that readings are statistically different between the CPSC10 and CPSC10-05R groups. ($p < 0.05$)..... 112
Figure 7.17: Serum levels of OHP after 4, 6, 8 and 10 weeks between sham control, CPSC10 and CPSC10-05R ($n = 10$ except for the 10th week $n = 5$). "+" sign indicates that the readings are statistically different between the sham control and CPSC10. "@" symbol indicates that the readings are statistically different between the sham control and CPSC10-05R. ($p < 0.05$)..... 113
Figure 7.18: Serum levels of BSP after 4, 6, 8 and 10 weeks between sham control, CPSC10 and CPSC10-05R ($n = 10$ except for the 10th week $n = 5$). "+" sign indicates that the readings are statistically different between the sham control and CPSC10. "@" symbol indicates that the readings are statistically different between the sham control and CPSC10-05R. "#" symbol indicates that readings are statistically different between the CPSC10 and CPSC10-05R groups. ($p < 0.05$)..... 113
Figure 7.19: Serum levels of GHYL after 4, 6, 8 and 10 weeks between sham control, CPSC10 and CPSC10-05R ($n = 10$ except for the 10th week $n = 5$). "+" sign indicates that the readings are statistically different between the sham control and CPSC10. "@" symbol indicates that the readings are statistically different between the sham control and CPSC10-05R. ($p < 0.05$)..... 114
Figure 7.20: Serum levels of PINP after 4, 6, 8 and 10 weeks between sham control, CPSC10 and CPSC10-05R ($n = 10$ except for the 10th week $n = 5$). "+" sign indicates that the readings are statistically different between the sham control and CPSC10. "@" symbol indicates that the readings are statistically different between the sham control and CPSC10-05R. "#" symbol indicates that readings are statistically different between the CPSC10 and CPSC10-05R groups. ($p < 0.05$)..... 114

Figure 7.21: Serum levels of PICP after 4, 6, 8 and 10 weeks between sham control, CPSC10 and CPSC10-05R (n = 10 except for the 10th week n = 5). "+" sign indicates that the readings are statistically different between the sham control and CPSC10. "@" symbol indicates that the readings are statistically different between the sham control and CPSC10-05R. "#" symbol indicates that readings are statistically different between the CPSC10 and CPSC10-05R groups. ($p < 0.05$)..... 115

Figure 7.22: Serum levels of TRACP-5b after 4, 6, 8 and 10 weeks between sham control, CPSC10 and CPSC10-05R (n = 10 except for the 10th week n = 5). "+" sign indicates that the readings are statistically different between the sham control and CPSC10. "@" symbol indicates that the readings are statistically different between the sham control and CPSC10-05R. "#" symbol indicates that readings are statistically different between the CPSC10 and CPSC10-05R groups. ($p < 0.05$)..... 115

Figure 7.23: X-ray images of the rabbits' right legs 8 and 10 weeks after implantation. One bar is equal to 1 cm. 117

Figure 7.24: CT images of the rabbits' right legs 8 and 10 weeks after implantation. One bar is equal to 1 cm. 118

Figure 7.25: Comparison of the new bone formation scores between CPSC and 0.5% RA-CPSC groups 8 and 10 weeks after implantation (n = 5). 119

Figure 7.26: Histological observations of (a) Control, (b) CPSC and (c) 0.5% RA-CPSC after 10 weeks of implantation (20x and 100x). Indicated on the images is inflammation as indicated by neutrophil infiltration (black arrows), proliferated adipose tissue (green arrows), tissue encapsulation (yellow arrows), new bone formation (blue arrows), osteoclasts (orange arrows) and osteoblast (red arrows) The size bar equals 0.25 mm. 120

Figure 7.27: Comparison of 84 genes analyzed by PCR array between CPSC10 and the sham control. Pink lines represent threshold fold changes (= 3). The data are presented by fold changes of genes in CPSC10 (y-axis) versus fold changes of genes in the sham control (x-axis) in logarithm scale (base = 2). (*n* = 4) 123
Figure 7.28: Comparison of 84 genes analyzed by PCR array between CPSC10-05R and the sham control. Pink lines represent threshold fold changes (= 3). The data are presented by fold changes of genes in CPSC10-05R (y-axis) versus fold changes of genes in the sham control (x-axis) in logarithm scale (base = 2). (*n* = 4) 124

List of Abbreviations

ALP	alkaline phosphatase
ATPs	adenosine triphosphates
BALP	bone-specific alkaline phosphatase
BMD	bone mineral density
BP(s)	bisphosphonate(s)
BSP	bone sialoprotein
C_2S	dicalcium silicate ($(CaO)_2SiO_2$)
C_3S	tricalcium silicate ($(CaO)_3SiO_2$)
CaSR	calcium sensing receptor
CH	calcium hydroxide ($Ca(OH)_2$)
CP	calcium phosphate
CPC	calcium phosphate cement
CPSC	calcium phosphate silicate cement
CPSC5	calcium silicate cement with 5 wt% of monocalcium phosphate
CPSC10	calcium silicate cement with 10 wt% of monocalcium phosphate
CPSC15	calcium silicate cement with 15 wt% of monocalcium phosphate
CPSC-R	calcium phosphate silicate cement containing risedronate
CPSC10-05R	calcium silicate cement with 10 wt% of monocalcium phosphate and 0.5 wt% risedronate
CPSC10-10R	calcium silicate cement with 10 wt% of monocalcium phosphate and 1.0 wt% risedronate

CS	calcium silicate
CSC	calcium silicate cement
CSC01R	calcium silicate cement with 0.1 wt% of risedronate
CSC05R	calcium silicate cement with 0.5 wt% of risedronate
CSC10R	calcium silicate cement with 1.0 wt% of risedronate
CSH	calcium silicate hydrate
CT	computed tomography
CTX	C-terminal telopeptide
DDS	drug delivery system
DMEM	Dulbecco's modified eagle's medium
DMSO	dimethyl sulfoxide
DNA	deoxyribonucleic acid
DPD	deoxypyridinoline crosslinks
DXA	dual x-ray absorptiometry
ECM	extracellular matrix
ELISA	enzyme-linked immunosorbent assays
FBS	fetal bovine serum
FCM	flow cytometry
FPPS	farnesyl diphophate synthase
FTIR	Fourier transform infrared
GHYL	galactosyl hydroxylysine
GI	gastrointestinal

HA	hydroxyapatite (Ca_{10} $(PO_4)_6(OH)_2$)
HPLC	high performance liquid chromatography
i.v.	intravenous
MCP	monocalcium phosphate
MTT	3-(4,5-dimethylthiazol-2-yl)-2,5-diphenyltetrazoliumbromide ($C_{18}H_{16}BrN_5S$)
NMR	nuclear magnetic resonance
NTX	N-terminal telopeptide
OCN	osteocalcin
OHP	hydroxyproline
OPG	osteoprotegerin
PBS	phosphate buffered saline
PCR	polymerase chain reaction
PMMA	poly (methyl methacrylate)
PTH	parathyroid hormone
PICP	carboxy-terminal propeptide of type I procollagen
PINP	amino-terminal propeptide of type I procollagen
PYD	pyridinoline crosslinks
RA	risedronate
RAC	risedronate-calcium complexes ($Ca_2C_7H_9NO_7P_2$)
RANK	receptor activator NF-κB
RANKL	receptor activator NF-κB ligand
RNA	ribonucleic acid

rt-PCR	real time polymerase chain reaction
runx2	runt-related transcription factor 2
SANS	small-angle neutron scattering
SAXS	small-angle x-ray scattering
SEM	scanning electron microscope (microscopic)
SRICI	Shenyang Research Institute of Chemical Industry
TGF-β	transforming growth factor-β
TRACP-5b	tartrate resistant acid phosphatase-5b isoform
XRD	x-ray diffraction
μCT	micro-computed tomography

Acknowledgements

First and foremost, I would like to express my sincere gratitude to my supervisors, Dr. Tom Troczynski, Dr. Urs Häfeli, Dr. Dorin Ruse and Dr. Quanzu Yang, for their valuable guidance during the course of this research work and preparation of this thesis and to Natural Sciences and Engineering Research Council of Canada (NSERC) for their financial supports. I would like also to express my appreciation to my supervisory committee member, Dr. Rizhi Wang, for his time and suggestions.

I would like to thank Dr. Zhiqin Wang, Ms. Yixi Zhang, Ms. Wei Yang, Ms. Shiyao Qiao and Mr. Yubiao Zhang at the Safety Evaluation Centre of Shenyang Research Institute of Chemical Industry for their contributions in the cell researches and animal studies.

I also appreciate the great supports from my friends Dr. Mingxiao Hou, Dr. Xinwei Liu, Dr. Yun`en Liu and Mr. Yu Wang at the General Hospital of Shenyang Military Command for their supports in animal studies.

I also want to thank Dr. Jingyu Wang, Dr, Hongying Zhang and Ms. Wenting Gao at the Comparative Medicine Center in Dalian Medical University for their helps in histopathological preparations and assessments and Dr. Zhihong Zheng and Dr. Wei Yang at the Comparative Medicine Center in China Medical University for their anesthesia supports. The histological slides observation and analysis were explicitly conducted at Dalian Medical University by Dr. Hongying Zhang.

Finally, I want to appreciate my parents in the course of my doctoral research. Their endless support and love motivates me to overcome many obstacles on the path to pursuing my dreams.

Dedication

To My Parents

Chapter 1: INTRODUCTION

Thanks to the advancements in healthcare, human life expectancy has been significantly extended in the last couple of decades, from 69 years in 1970s to 79 years in 2000s in North America. As a result, the aging population constitutes a large proportion in our society. By 2030, it is estimated that the number of adults of 65 years or older worldwide will grow from 550 million in 2000 to 973 million and, in the United States alone, the number of old people will double to 71 million [1]. An increasing aging population means greater pressures on our healthcare systems, as there are many chronic diseases and complications related with aging [2, 3]. Aging-related chronic diseases include Alzheimer disease, Parkinson disease, rheumatoid arthritis, atherosclerosis, cardiovascular diseases, muscular degeneration, diabetes and bone fractures, and among those common diseases, fractures resulted from osteoporosis in aging population most seriously affects health and quality of life [2]. According to Osteoporosis Canada, in 2010, the direct cost of osteoporotic fractures was more than $2.3 billion [4]. Osteoporotic fractures have a much higher prevalence rate than heart attacks, strokes and cancers and affect more women than men. They reduce mobility after fractures and decrease the self-esteem because patients typically need intensive medical care from other people. Moreover, increasing demands for hospital rooms and unaffordable costs of prosthesis implantation make osteoporotic fractures one of the biggest medical concerns all over the world. Therefore, how to successfully address osteoporotic fractures becomes a big challenge to improve longevity and life quality of our community.

Bone cements, as other implanted prosthesis, can be successfully used in bone fracture reconstruction [5-7]. The development of bone cement with proper mechanical strength and desirable biological responses took place over more than 40 years [8]. The earliest bone cement,

poly (methyl methacrylate, PMMA), is non-ceramic (organic polymer)-based and has been used clinically for half a century. However, its weaknesses, e.g. shrinkage, non-degradability and heat generation during setting, reduce its product safety and limit its clinical usefulness [9]. The development of revolutionary calcium phosphate cement (CPC) by LeGeros and Brown and Chow solved some of these disadvantages [10, 11]. Hydroxyapatite (HA, $Ca_{10}(PO_4)_6(OH)_2$) is formed after CPC implantation at the tissue-implant interface [12], promoting marrow stromal cell differentiation into osteoblast-like cells [13, 14]. Nevertheless, CPC has relatively low compressive strength (<10 MPa) and poor vascularization properties [15-19]. Calcium silicates (CS)-based bioceramics, like calcium silicate cement (CSC), have a long history of being used as implants [12, 13, 20, 21]. The bioactivity of CSC primarily attributes to SiO_4^{4-} ions promoting osteoblast cell proliferation and producing transforming growth factors [20, 22-24]. SiO_4^{4-} and Ca^{2+} ions can reinforce osteogenesis by upregulating genes controlling cell cycle induction and progression [25]. In recent years, it has been claimed that the calcium phosphate silicate cement (CPSC), developed by adding monocalcium phosphate (MCP) into CSC, can further improve CSC's low setting rate, poor degradation and high alkalinity after setting [18, 26-30]. These can be attributed to MCP reaction with calcium hydroxide (CH, $Ca(OH)_2$), a product of CS hydration, into HA, accelerating the CS hydration and reducing the pH [31-33]. Furthermore, CPSC has been proved to be osteoinductive (able to induce new bone growth), osteoconductive (able to attach bone tissues on implant surface) and more biocompatible than CSC [34, 35].

The effectiveness of bone cement to reconstruct bone is significantly compromised under the osteoporotic conditions because osteoporosis can cause poor osseointegration between implant and bone tissue and result in stress concentration on the newly formed fragile connections [36-39]. Typical anti-osteoporotic therapies include Vitamin-D and calcium

supplements, bisphosphonates (BPs), parathyroid hormone (PTH) therapy and estrogen replacement. BP therapy is inexpensive and has been used most widely [6, 40]. BPs have two replaceable positions, R1 and R2, and when substituted by a hydroxyl group and nitrogen containing substitute, respectively, will be strongly bonded with bone minerals and increase their anti-resorptive capacity significantly [41-44]. Risedronate (RA) and zoledronate are the third generation BPs with the highest anti-osteoporotic potency [45]. RA inhibits the formation of the farnesyl diphosphate synthase (FPPS), disrupts the mevalonate pathway and stops the prenylation of proteins within osteoclasts [41-43]. However, there have been several side effects and complications associated with orally taken or injected BPs [46-49]. Therefore, a local BP delivery system by bone cement might be promising in achieving the desirable bone repair characteristics and anti-osteoporotic properties at the same time [19].

In this doctoral study, a novel RA delivery system, including CPSC containing RA (CPSC-R in short), was designed and RA's impact on CPSC material properties was evaluated. In addition, the *in vitro* biocompatibility of CPSC-R system was evaluated based upon its effects on gene expressions. Furthermore, with the help of an osteoporotic animal model, the anti-osteoporotic and osteogenic effectiveness of the CPSC-R system was evaluated by investigating how CPSC-R can promote osseointegration under osteoporotic conditions.

With the help of these comprehensive and systemic analyses, the following research hypothesis will be answered: Calcium Phosphate Silicate Cement as a Risedronate Delivery System is Suitable and Appropriate to Help Restore Bone Fractures under Osteoporosis Conditions.

Chapter 2: LITERATURE REVIEW

2.1 Calcium phosphate cement (CPC)

Calcium phosphate cement (CPC), first introduced by LeGeros *et al*. and Brown and Chow [10, 11], has been demonstrated to be bioactive, degradable (resorbable), moldable and suitable for grafting and coatings. Compared to other calcium phosphate (CP)-based bioceramics, CPC paste can be filled into irregular shapes of bone fractures and set *in situ*. This advantage gives clinical practitioners more flexibility and confidence in treating bone fracture diseases. The first commercial CPC has been used for the treatment of maxillofacial deformities as well as for the treatment of bone fracture defects [50, 51]. After CPC powders are mixed with water, a series of reactions take place, from the dissolution of cement powders to precipitation (crystallization) of a new CP ceramic, mainly HA. During resorption, CPC releases calcium (Ca^{2+}) and phosphate (PO_4^{3-}) ions, which promote growth of bone tissues on and around scaffolds [24, 52, 53].

The advantages of CPC over traditional bone cement, such as poly (methyl methacrylate) (PMMA) bone cement, are less heat-generation and *in situ* shrinkage, both undesirable. It has been shown that local temperature around implant can exceed 60 °C, thermally damaging tissues around implant [9, 54]. The shrinkage of PMMA cement after implantation will cause loose contact between tissues and implants, causing potential implant failures.

2.2 Calcium silicate cement (CSC)

While CSC has been widely used in construction, in recent years its capability as dental biomaterial, and as a substitution of bone, has been demonstrated *in vitro*, *in vivo*, and commercially. Several studies have shown that silicate-based biomaterials demonstrate excellent

bioactivity and biocompatibility [13, 20, 21, 55, 56]. The primary component of hardened ("set") CSC, calcium silicate hydrate (CSH), has shown a transition into HA when cultured in simulated body fluid [12, 57]. Compared to CP-based biomaterials, CS owns some distinctive advantages, such as better toughness, high tensile and compressive strength, while being virtually non-resorbable or very slowly resorbable [28]. These features promise successful treatment especially in elderly patients because the rate of new bone tissue growth decreases with age. The slow rate of bone growth is suspected to result in new bone micro-fractures, which in the long-term may lead to serious consequences, such as osteoporosis and bone fracture. Grafts are degrading faster than growing bone tissues, leaving some spaces in the implant. These spaces will contribute to mechanical strength loss. It is therefore reasonable to conclude that CS-based implants would provide better mechanical and structure supports to fractural bones than CP-based implants.
It is widely believed that osteoblast cells can induce bone formation under the bone-tension condition. The higher the tensile force is (but within limits), the faster the bone formation will be. Therefore, CSC implanted patients can undergo higher loads of activities and therefore might see faster bone growth.

2.2.1 Composition and structure of CSC

CSC consists of tricalcium silicate ($(CaO)_3SiO_2$ (C_3S)) and/or dicalcium silicate ($(CaO)_2SiO_2$ (C_2S)) at various weight ratios. C_3S and C_2S react with water and form CSH gel and CH. Equations governing this reaction are listed below [58]:

$$2(CaO)_3(SiO_2) + 7H_2O \rightarrow (CaO)_3(SiO_2)_2 \cdot 4(H_2O) + 3Ca(OH)_2 \qquad \text{(Equation 2.1)}$$

$$2(CaO)_2(SiO_2) + 5H_2O \rightarrow (CaO)_3(SiO_2)_2 \cdot 4(H_2O) + Ca(OH)_2 \qquad \text{(Equation 2.2)}$$

The gel phase CSH has a typically disordered structure (partially amorphous); ideally crystalline tobermorite ($Ca_5Si_6O_{16}(OH)_2(H_2O)_4$) and jennite ($Ca_9Si_6O_{16}(OH)_6(H_2O)_8$) should form during hydrations (equation 2.1and 2.2) [58]. Naturally occurring CSH crystals have a monoclinic structure as in tobermorite [59, 60]. Merlino *et al.* have shown that the structure of 1.4-nm tobermorite comprises a central layer of Ca-O sheet that is ribbed on either side with single silicate tetrahedron and silicate chains repeating at intervals of three silicate tetrahedrons. Two tetrahedrons share two oxygen atoms with the central Ca-O sheet; while the third tetrahedron shares only one atom [60-63]. Unlike tobermorite, jennite has every other unit of three silicate tetrahedrons ("dreierkette") replaced by a row of OH^- groups [62]. As a result, jennite has a more corrugating Ca-O layer, and some oxygen atoms are relieved from this rigid structure of tobermorite and become water molecules and OH^- groups. Those newly formed OH^- groups are charge-balanced by free Ca^{2+} ions and, thus, create Ca–OH bonds.

In general, the less crystalline form of CSH can be divided in to three groups: CSH (I), (II) and (III). CSH (I) is formed in the reaction between CaO and SiO_2 [64], or between calcium salts and alkali silicates, or (under certain conditions) between C_3S/C_2S and water in dilute aqueous suspensions at room temperature [62]. If C_3S or C_2S reacts with excess amount of water, e.g., the CSH gel hardens during hydration (equations 2.1 and 2.2) and two products with distinctive gel morphologies form. The inner product has a very fine particulate morphology for an extended period of time, and a new phase CSH (II) forms [65-67]. Similarly to CSH (I), CSH (II) is a distorted version of tobermorite. CSH (II) is also considered as an alteration to jennite with Ca/Si ratio of 2 [62]. CSH (III) forms when the powder to liquid ratio is 2:1 and has two components, CSH gel and $Ca(OH)_2$ [64]. CSH (III) is less crystalline than CSH (I) and (II), and has a Ca/Si ratio of 1.7~1.8. Several studies hypothesize that CSH gel is initially a mixture of

tobermorite- and jennite-like crystals, whose outer product morphology strongly depends on the gel chemical compositions [68-75]. In general, particles in outer products are longer and thinner than inner ones [74].

2.2.2 Formation of CSH

Preparation of a single-phase CSH

It has been shown that a single phase CSH (i.e., free of CH) can be prepared either from reactions between CaO and SiO_2 or from the double decomposition of calcium salts and alkali silicates in aqueous solutions [67, 76-81]. However, a simple hydration between C_3S or C_2S and water results in a highly disordered mixed-phase product, known as CSH gel and CH, common components of hydrated Portland cement [64]. Chen *et al*. have demonstrated that a mature CSH gel has a relatively higher maximum Ca/Si ratio of 1.8 than 1.5 in a synthetic single-phase CSH [64]. CSH gel and CH prepared by hydration of C_3S have a mean Ca/Si ratio between 1.7 and 1.8 and this ratio remains unchanged with its gel's age [82].

Heat Treatment of CSH

Heat treatment of CSH can increase the degree of polymerization of silicate chains and reduce the saturated weight of paste by converting OH^- groups into water [83]. Moreover, heat treatment can increase the amount of capillary porosity at the cost of mesoporosity. In addition, Thomas *et al.* argue that some heat treatments could accelerate the rate of hydration and strengthen cement setting [83]. However, elevated temperatures may decrease long-term strength and increase permeability [84]. Heat treatment may also induce expansions of material because of changes in pore systems and releases of liquid water (depending on treating time and moisture

state of pore system) [83, 85]. Moreover, heat treatment may cause microcracks due to viscoelastic strains induced by dimensional changes [83].

Nucleation, hydration and aging of CSH

When C_3S powders are mixed with water, this mixture experiences an initial rapid reaction followed by a moderate rate interaction [84]. A hypothesis, proposed by Gartner *et al.* [86] and modeled by Thomas *et al.* [87, 88], explains that nuclei of CSH form shortly after mixing, and that the nucleation rate varies with powder's surface area [88], calcium concentration and temperature [89]. Subsequently, precipitated CSH gels start to grow outward and take up pore space. Once powders are covered by a thick layer of CSH, the rate of reaction will be controlled by the rate of diffusion and significantly reduced [84]. The initial high reaction rate, which is measured through hydration heat release, is attributed to the autocatalytic effect of CSH gel, because precipitations of CSH nanoparticles stimulate and accelerate new particle formation [84].

Water exists in CSH in three forms: free, chemically bound and constrained water. The constrained water consists of water adsorbed on the surface and confined in pores. This type of water is preliminarily associated with the CSH phase [90]. Water content of CSH is dependent on the relative humidity, age and other processing parameters. Some articles summarized the process of hydration in the following steps [91, 92]. The hydration of C_3S starts with rapid dissolution of powder in the first 30 seconds [91]. Correspondingly, the pH surges up from 7 to 12.0~12.5, and both calcium and silicate concentrations increase as well. In the second step, the "induction period", the dissolution rate significantly slows down. This is followed by an "acceleration period", characterized by an exponential increase in the reaction rate (still lower than that in Step 1) and subsequently the rate of hydration decreases again because of a

diffusion-control mechanism dominating the reaction and a reduction in the surface area [92]. In addition, the rate of hydration is sensitive to the amount of Ca^{2+} and OH^- ions present in the solution [91, 93, 94]. High porous and low-density phases are initially formed according to the boundary nucleation process, and available reaction volumes will be filled up by this phase [95]. As the reaction proceeds, there is no available space to form new products and, thus, previously formed products densify.

CSH gel aging is defined as changes in the structure and properties that occur under ambient or hydrothermal conditions [96]. Aging will result in CSH of higher microstructural resistance to permanent changes and induce a higher degree of polymerization of silicate chains [96, 97].

2.2.3 Surface area and porosity

The surface area of a porous material is defined as the total internal boundary between the solid phases and the pore system [98]. This quantity is a measurement of fine pores present and indicates potentials for reactions between solid phases and intruded active species [98]. Surface area, in the case of disordered porous microstructures, also indicates the tortuosity and permeability of the pore phase [98]. It is known that CSH paste is a reactive, porous material with high internal surface area of 200 m^2/g or higher [98]. The surface area of a given CSH gel increases with its hydration time and varies with respect to the processing variables, such as the cement composition, reaction temperature, and water-to-cement (w/c) ratio [98]. Three types of porosity measurements are commonly used, including gas sorption, small-angle scattering and nuclear magnetic resonance (NMR) relaxation [97]. The gas sorption method requires the specimen in a dry state; however, the elimination of water from its microstructure may alter its

structures, such as shrinkage or collapse of the gel pores, thus significantly altering surface area [98]. Besides gas sorption method, small-angle scattering, including small-angle neutron scattering (SANS) and small-angle x-ray scattering (SAXS), can be used to detect cement surface areas as well. SAXS surface area values are considerably higher than SANS values [98]. The last method in literature is the NMR method, in which completely dried sample is not required as an advantage to gas sorption method [98].

Cement paste can be viewed as a dense suspension of powders in a liquid medium, and this liquid medium forms a three-dimensional inter-connected pores structure [99]. This pore system ranges from a few nanometers to millimeters and is responsible for material properties such as stiffness and strength. The total volume of cement powder and water will decrease as the hydration reaction proceeds. Water space will be gradually replaced by cement paste [99], and spaces not filled by the solid products are called capillary pores. As the hydration continues, the amount of capillary porosity decreases correspondingly until the capillary pore system transforms into a disconnected space at a percolation transition [99].

On the other hand, CSH gel contains many very small pores, with pore sizes ranging from 15~20 nm on the first day to less than 5 nm after 59 days setting [100]. The gel pore system is dependent upon chemical composition and changes with relative humidity, temperature, and the applied load [99]. Porosity can influence cement's mechanical strength, creep, permeability and diffusion [99]. Feret's Law elaborates a simple relation between compressive strength and porosity as seen in the equation 2.3 below:

$$\sigma = B\left(\frac{c}{c+w+p}\right)^2 \qquad \text{(Equation 2.3)}$$

, where σ = compressive strength, B = constant, c = volume of cement, w = volume of water, p = volume of air (i.e., open pores). Accordingly, compressive strength is inversely related to the

open porosity volume**.** Permeability is an intrinsic property of cement allowing the diffusion of gaseous or aqueous media inside cement under a pressure gradient and depends upon capillary pore size, volume and morphology. Expansions of cement can be induced by environmental factors, such as moisture and temperature changes, sulfate exposure and thawing/freezing cycles [99].

2.3 Calcium phosphate silicate cements (CPSC)

HA is found to have a close similarity to human bones, and, thus, its applications in bone replacement have been well studied, e.g., in prosthetics and dental repairs [101, 102]. However, a biological apatite contains some additional elements and chemically differs from HA [103]. Experiments have shown that synthetic and biologically harvested HA is able to elicit apatite layer formations on the interface with bone tissues [89, 104-106]. CPC and other CP-based bioceramics, which are used to repair fractures bone under physiological conditions, are gradually transformed into HA. CPC is superior to other CP bioceramics owing to its great flexibility. CPC can virtually fit for any shapes of fracture voids and be easily incorporated with different types of drugs [107]. Although HA is proved to be osteoconductive in nature and can support osteogenic differentiation of marrow stromal cells, its bioactivity, biocompatibility, and biodegradation raise some concerns over its clinical applications [24, 52, 53, 108]. CPC has low mechanical strengths (~10 MPa compressive strength) and leaches OH^- in *in vitro* conditions [16, 17]. In addition, several papers have reported CPC inferior bioactivities to those of silicon-contained Bioglass [109-111]. CSC advantages as a bone cement have been discussed thoroughly in the previous section [26]. However, slow setting rate and low short-term mechanical strength

(up to 30 days) have been shown to be associated with CSC, making it unfit for some applications [28, 112].

The idea of using a combination of CPC and CSC, which is called CPSC, is originated to overcome individual shortcomings. Bioglass® was the first CS material showing to have excellent biocompatibility and osseointegration [15, 113]. Silicate ions (SiO_4^{4-}) encourage the proliferation of osteoblast cells and activate cells to produce transforming growth factors [20]. Moreover, liberations of SiO_4^{4-} and Ca^{2+} can reinforce osteogenesis by manipulating genes to regulate cell cycle induction and progression [22]. Further studies indicate that SiO_4^{4-} can promote bone metabolism as well [23, 114, 115]. Several experimental results proved that CPSC is better than either CPC or CSC and might generate expected clinical results [26, 34, 116, 117]. Higher compressive strengths were observed (>20 MPa for CPSC *vs.* <10 MPa for CPC), and a layer of homogeneous apatite was formed on the cement surface in simulated body fluid, indicating that CPSC excels in bioactivity [26]. Furthermore, low pH variations *in vitro*, cell proliferation *in vivo* and good biodegradability were also demonstrated with CPSC [26, 117]. In addition, Zhao *et al.* reported both osteoblast cell growth and differentiation on CPSC surfaces [34].

2.4 Bisphosphonates

2.4.1 Overview of bisphosphonates

In 1960s, Fleish *et al.* found, in human urine and plasma, substances that can inhibit CP precipitation [118]. The product is called pyrophosphate, a naturally occurring polyphosphate, which reduces calcium crystal formation and dissolution and can inhibit *in vivo* calcification [119]. Bisphosphonates (BPs) are analogous to pyrophosphates but, unlike pyrophosphates (Fig.

2.1), in which one oxygen atom is bonded to two phosphorous atoms, have one carbon atom replacing that oxygen atom, rendering BPs better resistant to biological degradation (hydrolysis) and making BPs more stable than pyrophosphates [119].

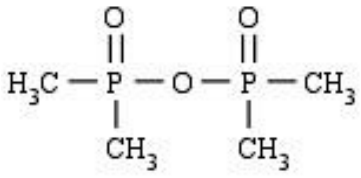

Figure 2.1: Schematic drawing of pyrophosphates

The molecular structure of BPs is shown in Fig. 2.2. Two side-chains are attached to the central carbon atom. Alterations of these side-chains bring BPs different chemical and physical properties and introduce various forms of BPs [119]. It has been shown that the presence of a hydroxyl group (-OH) can increase BPs' binding ability to bone minerals as compared to those without this functional group [119], as it provides tridentate instead of bidentate binding to chelate Ca^{2+} [120]. Sixty different forms of BPs have been synthesized based on different side chains substitutions and they can be grouped into nitrogen containing and non-nitrogen containing BPs [119]. The replacement of the second side-chain, R_2, gives rise to BPs different anti-resorptive potencies [119]. Risedronate (RA), as the third generation of BP (Fig. 2.2), has a nitrogen-containing heterocyclic ring at the R_2 location, which increases RA's anti-resorptive potency by 10,000 folds [119]. BPs anti-resorptive ability arises from the P-C-P structure rather than individual phosphonate groups [119]. However, high binding affinity does not necessarily mean high anti-resorptive potency. In addition, any alteration on phosphonate groups will change BPs affinity for minerals [119]. Therefore, binding affinity is attributed to the P-C-P moiety and

the OH group on R_1, but configurations on R_2 allow BPs exerting different biological activities and interactions with specific molecular targets [119].

Generic bisphosphonate **Risedronate**

Figure 2.2: Schematic drawing of a generic bisphosphonate and of risedronate, the third generation bisphosphonate drug used for this research.

Other than inhibiting calcium crystal formation and dissolution, BPs can reduce osteoclast-induced bone resorption, healing excessive bone resorption-related diseases, such as Paget's disease and malignancy-associated hypercalcemia and can be used as agents for bone imaging [119]. BPs are selectively taken up and adsorbed on the bone minerals, and preferably bind to bones having high turnover rate [119]. BPs' anti-resorptive actions can be grouped into 2 different types. Metabolites are formed between pyrophosphate analogous BPs and ATPs, and such metabolites accumulate inside osteoclast cells, impede osteoclast cell functions and induce osteoclast apoptosis [119]. Nitrogen-containing BPs have different mechanisms of anti-resorptive capacity. They affect other metabolic reactions, e.g., the mevalonate pathway, disrupt protein prenylation to interfere with signaling function of key regulatory proteins, and consequently reduce cellular activity and induce osteoclast apoptosis [119]. Current administration routes of BPs include oral and intravenous administrations. Though BPs are

widely used to treat osteoporosis and other chronic diseases, and though oral administration sounds like a good choice as it can provide uninterrupted pharmacotherapy to maintain desirable clinical outcomes, it has very poor adsorption from gastrointestinal tracts [46, 121]. Oral administration of BPs is also compromised by daily food intakes, especially those with high Ca^{2+} and Fe^{2+}, which form insoluble complexes that cannot absorbed [46]. Though intravenous (*i.v.*) method can avoid the low absorption rate, there are intrinsic problems associated with this method. Bioavailability of BPs varies, and those left in the body will remain probably for lifetime [46, 121]. After high *i.v.* dosage levels, BPs can be deposited in non-calcified tissues, e.g., the kidney [46], and cause other complications. The local delivery in the form of implants can solve these problems. It will achieve controlled release of BPs, avoid poisoning, and be target-specific, preventing irritations from other organs [46].

2.4.2 Risedronate

Risedronate (RA), also named risedronic acid, is a third generation nitrogen-containing BP. Its generic name is (1-hydroxy-2- (3-pyridinyl) ethylidene) BP with a chemical formula of $C_7H_{11}NO_7P_2$. The OH group at R_1 position (Fig. 2.2), increases RA's affinity for Ca^{2+}; while, on the R_2 position (Fig. 2.2), the nitrogen-containing ring enhances RA's anti-resorptive ability. Among 5 common BPs, RA, zoledronate, alendronate, etidronate and clodronate, RA has the medium bone affinity but the highest anti-resorptive potency [121].

RA is mainly used to treat postmenopausal osteoporosis, glucocorticoid-induced osteoporosis and Paget's diseases [119, 122]. Postmenopausal osteoporosis is a very common disease in women: 40% of Caucasian women are suffering from this disease after the menopausal period because of the deficiency of estrogen [123]. The deficiency of estrogen

results in the loss of bone mass and it is estimated that 10% of bone mass loss can increase the risk of fracture by 2 to 3 folds [124]. Several clinical trials have proved that RA can effectively increase the bone mineral density (BMD) compared to the placebo (no active ingredient) treatment [122]. One clinical study showed that, after 3 years of RA treatment (5 mg/day of oral intake), increases of BMD on lumbar spine, femoral trochanter, femoral neck and midshaft radius were 5.9, 6.4, 3.1 and 2.1% ($p < 0.001$ *vs.* placebo), respectively [125]. Another study reported that, after two years treatment with RA to prevent bone mass loss in recent menopausal women (i.e., within 6 months to 3 years), lumbar spinal and femoral neck BMD increased significantly as compared to the placebo group (5.4% *vs.* 1.1% on lumbar spine, 1.6% *vs.*1.2% on femoral neck, $p < 0.05$) [126]. A third study demonstrated that the combination of RA and estrogen replacement was more effective to prevent the bone mass loss than the estrogen replacement alone [127]. Glucocorticoids are widely used to treat inflammation, especially in the immunosuppression conditions; however, they can also cause bone mass loss and induce osteoporosis [122]. About 30 to 50% of patients who received glucocorticoid treatments for 6 months or longer suffered from osteoporotic fractures [128]. Though the exact mechanisms of glucocorticoid-induced osteoporosis are not yet clearly understood, it is believed that glucocorticoids can impair osteoblast cell activities [122]. In one study, in which RA (5 mg/day) was given to prevent glucocorticoid-induced osteoporosis (i.e., RA and glucocorticoid were given simultaneously), the mean BMD at the lumbar spine and femoral neck decreased by 3% ($p < 0.05$) after one year in the RA-free group compared to the RA treatment group [129]. In a study of 290 patients with low bone mass, RA significantly increased the mean BMD at the lumbar spine in the treatment group compared to the placebo group [130]. Paget's disease refers to the a localized increase of osteoclastic activity followed by the proliferation of osteoblast cells

and commonly occurs in elder people [122]. The bone formation in Paget's diseases by osteoblast cells has a thick but poor structure and pains are resulted from these deformed bones. After RA treatment of more than 2 months, all patients in the clinical study were relieved from pain [131]. Biomarker studies also showed that, after 6 months of RA treatment, bone turnover rates were significantly reduced compared to the placebo groups [131, 132].

RA's mechanism in bone resorption prevention is complex and includes the effects on osteoclast recruitment, differentiation, and resorptive activity [41-45, 133-138]. Only recently, the anti-resorptive mechanism of RA has become clearer [41-43]. It appears that RA inhibits the formation of the farnesyl diphosphate synthase (FPPS), disrupts the mevalonate pathway and stops the prenylation of osteoclast cell proteins [41]. Prenylation, also called lipidation, is a process to add hydrophobic prenyl functional groups to proteins. Without this particular function group, interactions between proteins are interrupted and osteoclast cells are unable to function properly without proper protein interactions. Eventually, apoptosis is induced in osteoclast cells. It is generally believed that RA can increase the proliferation and differentiation of osteoblast cells by upregulating several key genes expression within cells, e.g., runx2, ALP and OPG [35, 139, 140]. However, whether RA can also induce apoptosis of osteoblast cells is not known yet. It is only understood that RA at high concentrations can be cytotoxic (above 10^{-5} M) to osteoblast cells and the safe range of RA concentration is between 10^{-8} and 10^{-6} M [19, 141].

Oral intake RA's common side effect is gastrointestinal irritation (GI). One study found that among 219 patients who were given RA, 38% of them experienced GI, and 21% had adverse upper gastrointestinal events [142]. Another study showed that the overall GI incident rate among healthy menopausal women taking 5 mg/day RA for 2 weeks was 4.1% ($p < 0.001$) [143]. At higher dosage of RA (30 mg/day), gastric ulcers appeared more severe in RA treatment

groups than the placebo one [144]. In response to these findings, several researchers undertook the task of local delivery of other BPs [49, 54, 116].

There are fewer studies investigating release kinetics of BPs from local implants than those evaluating biological benefits resulted from local BPs delivery [145]. Slow release patterns (i.e., < 10% of BP loading released in the first few weeks) were observed for olpadronic acid, an earlier generation BP, released from porous hydroxyapatite implants into sodium chloride solution [146]. It was found that most of the release took place in the first 10 days of study. In addition, porosity effects on the release kinetics were also shown in this study [146]. The drug was released faster (i.e., 27.5% of the initially loaded BPs in 3 months) from the macroporous implants (20-30% porosity, pore sizes between 100 and 250 μm) than from the microporous ones (which released only 2.66% of the initially loaded BPs from the implant with 50-60% porosity, pore sizes between 1 and 5 μm). However, release was not detected from microporous implants with much lower porosity (3-5% porosity). This study showed that an initial rapid release of BPs was followed by a much slower, pseudo-steady release profiles [146]. Another study found that BPs release from hydroxyapatite was correlated with the rate of calcium dissolution from the implants [147].

Biological effects resulting from BPs local release, on the other hand, were well studied [116, 148-153]. *In vitro* studies of CPC doped with alendronate demonstrated its toxicity to osteoclast cells while promoting osteoblast cell proliferation and differentiation [49, 116]. In one study of radiolabeled zoledronate in porous tantalum implants, it was found that zoledronate quantity in peri-implant tissues was higher after 6 weeks than after 52 weeks (732.6 ng/g *vs.* 377.2 ng/g) and most of the released zoledronate was localized close to the implants [148]. Yoshinari *et al.* found that pamidronate-coated calcium phosphate implants improved bone

contact by 10% as compared to the non-coating implants ($p < 0.05$) [149]. In another study by Gou *et al.* on *in vivo* bone formation of zoledronate-loaded PLGA implants, bone mineral density and relative bone volume increased significantly compared to the control group (containing no zoledronate) ($p < 0.05$) [150]. In addition, the numbers of osteoclast and osteoblast cells found close to the implants were significantly affected by zoledronate release ($p < 0.05$). Histological studies suggested that early tissue growth and osseointegration with implants was improved by zoledronate-coated bone screws and local delivery of zoledronate did not cause adverse side-effects on osteoblast cells close to implants [151]. In another study focusing on the improvement of bone mechanical properties due to zoledronate-added PLGA implants, it was found that bone stiffness was significantly increased (i.e., by 15%) as compared to the zoledronate-free samples ($p < 0.01$) [152]. In one recent study of alendronate-doped calcium phosphate cement in osteoporosis animals, bone volume and new trabecular bone thickness were higher in alendronate-treated group than the control (CPC only) one ($p < 0.05$) [153]. It was also found that the thickness of original cortical bones close to implants was also increased by 30% in the alendronate-treated group, proving its anti-osteoporotic effects. However, there is no literature studying *in vivo* RA release from calcium phosphate silicate cement. In addition, the anti-osteoporotic effects of this particular drug delivery system also remain unknown.

2.5 Controlled drug release

Drug concentrations in the blood plasma can be divided into three distinct regions, namely, toxic, effective and ineffective levels, as schematically illustrated in Fig. 2.3. The difference between toxic and ineffective levels is called the "therapeutic window" [154]. When single drug doses are administrated into body, plasma concentrations will rapidly increase and then decrease. Hence, the time during which concentrations remain within the therapeutic window is very short [154]. To increase the time for the drug to be in the optimal dose range, the frequency of administration must be increased, which therefore requires more patient compliance. The term, controllable release, is interchangeable with sustained release or prolonged release [154], and a desirable drug delivery device should deliver drugs in controllable manners.

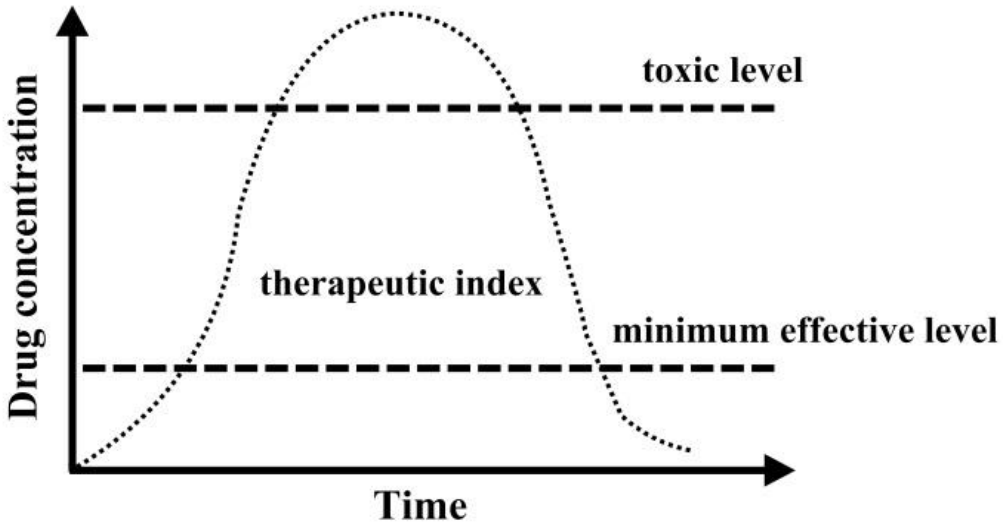

Figure 2.3: Schematic drawing of effective drug concentration region

Commonly encountered polymeric drug delivery systems (DDS) include diffusion-controlled, water penetration-controlled, chemically controlled, responsive and particulate DDS. In each system, special or unique properties of delivery materials are utilized to release drugs. For example, in the chemically controlled mechanism, drugs are either confined in or surrounded by biodegradable polymer membranes or homogeneously dispersed in biodegradable polymer matrices [154]. Confined by biodegradable membranes, drugs must diffuse out through membranes, while membranes initially retain their shapes but eventually degrade *in vivo*. Rates of drug release are thus dependent both on drug diffusivity and matrix degradation rate.

CPC has been used in drug delivery applications because of its abilities to incorporate several types of drugs and to deliver drugs to specific sites (target-specific) in controllable manners and also because CPC is biodegradable and injectable [107]. The drugs that have been delivered from CPC-based DDS include antibiotics, anti-inflammatory drugs and several bone growth factors [107]. The release kinetics from CPC in general follow diffusion-controlled processes, which allows for describing the drug release by Higuchi's law [107].

In my present study, Higuchi's law was used to describe the drug RA's release kinetics from hardened CSC and CPSC [155]. Such analyses were based upon a theoretical release model, in which several assumptions must be made: 1) the matrix retains its original shape; 2) no matrix dissolves; 3) there is homogeneous drug distribution in the matrix, and 4) the same release rate is observed at the surface and throughout the bulk [155].

In the Higuchi model, two release mechanisms are usually discussed [155]. In the simple diffusion model, drugs are first desorbed from solid surfaces, diffuse through matrices and eventually are leached into the surroundings (release environment) [155]. Alternatively, solvents in the release environment may penetrate into the matrices, dissolve drugs, and leach drugs out

of matrices. Several types of defects in matrices are responsible for drug delivery systems, i.e., pores, cracks, voids and intergranular (grain-boundary) spaces, which provide channels for the solvent diffusion [155]. Drugs dissolve and diffuse in the solvents, driven by the concentration gradient, instead of moving through matrices [155].

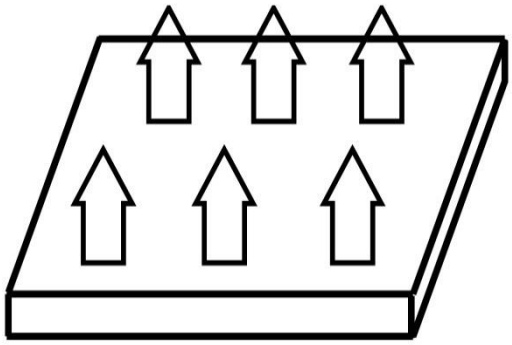

Figure 2.4: Schematic drawing of drug release from a planar surface

In this study, RA is strongly bound with Ca^{2+} and hardened CSC or CPSC [119]. If the first mechanism were valid, then RA would experience a very complicated release process. First, a concentration gradient would be established between the surface and core, and RA would start to diffuse through the matrix. RA's high affinity for Ca^{2+} would cause that RA, once desorbed from matrices, and would be rapidly re-adsorbed onto the matrix. If a significant release is observed, then it is reasonable to assume that the second mechanism dominates the RA release from CSC or CPSC. In the Higuchi model, two geometric systems are considered: unidirectional and three-dimensional. In the unidirectional geometry, drugs are released from a planar surface (Fig. 2.4) and equation 2.4 governs the amount of drug released with time [155]:

$$Q = [\frac{D\epsilon}{\tau}(2A - \epsilon C_s)c_s t]^{\frac{1}{2}} \qquad \text{(Equation 2.4)}$$

, where Q is the amount of drug release after time t per unit area; D is the diffusivity of the drug in the permeating solvent; τ is the tortuosity of the capillary system, which is roughly equal to 3

in the CSC or CPSC system; A is the total amount of drug present in the matrix; C_s is the solubility of drug in the solvent; ε is the porosity of the matrix. One assumption of equation 2.4 is that A is greater than C_s by a factor of 3 to 4; if not, the drug will dissolve in the solvent too fast to be modeled in a controllable release pattern.

It is necessary to discuss the porosity factor ε in more detail. Porosity (ε) used in equation 2.4 refers to the those filled with solvents in the pellet [155]. Hence, $\varepsilon = \varepsilon_o + KA$, where K is the specific volume of the drug (=1/density), and ε_o is the initial porosity. If RA is homogenously distributed in the pellet, ε is roughly equal to KA. Therefore, equation 2.4 can be reduced to:

$$Q = A[\frac{DK}{\tau}(2 - KC_s)C_s t]^{\frac{1}{2}} \qquad \text{(Equation 2.5)}$$

$$S = [\frac{DK}{\tau}(2 - KC_s)C_s t]^{\frac{1}{2}} \qquad \text{(Equation 2.6)}$$

, where the fraction of drug release $S = Q/A$. From equation 2.6, it is concluded that the fraction of drug release is independent of the initial amount of drug loading [155].

In a three dimensional geometry, drugs are leached from a pellet or tablet in all directions (Fig. 2.5). This geometry is more realistic for release kinetics from insoluble pellets [155], and thus analyses based upon this geometry dominate RA release kinetics from CSC or CPSC. Equation 2.7 governs the drug release in the 3D geometry:

$$(1-\alpha) + 2\left(\frac{a'}{a_o}\right)^3(1-\alpha) - \left(\frac{a'}{a_o}\right)^2(3-4\alpha) - \alpha\left(\frac{a'}{a_o}\right) + \alpha ln\left(\frac{a'}{a_o}\right) = \frac{6DKC_s t}{\tau a_o^2} \qquad \text{(Equation 2.7)}$$

, where a' is the radius of unleached portion; a_o is the radius of the entire pellet; $\alpha = \varepsilon C_s/A$ and $\varepsilon \approx KA$, so $\alpha \approx KC_s$. If α is much smaller than 1, equation 2.7 can be simplified to:

$$1 + 2\left(\frac{a'}{a_o}\right)^3 - 3\left(\frac{a'}{a_o}\right)^2 = \frac{6DKC_s t}{\tau a_o^2} \qquad \text{(Equation 2.8)}$$

, where $\left(\frac{a'}{a_o}\right)^3$ represents the remaining fraction of drugs loaded into a matrix.

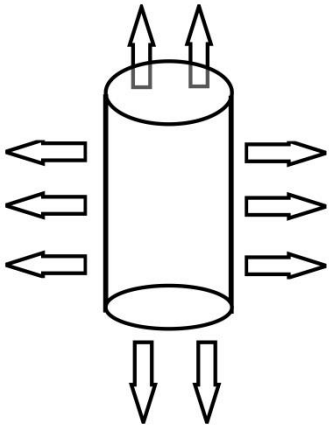

Figure 2.5: Schematic drawing of drug release in three dimensions

2.6 Osteoporosis and osteoporotic fracture

Osteoporosis, characterized by bone mineral (or bone mass) loss and microarchitecture deterioration, produces unmatched rates of bone formation and resorption [7, 40]. Osteoporosis is typically diagnosed based upon bone mineral density (BMD) by dual x-ray absorptiometry (DXA). A patient has osteoporosis if his/her T-score (subject's bone density) is 2.5 standard deviations below the average of young adults [40]. Though diagnosis of osteoporosis though BMD by DXA is a widely acceptable method, there are some concerns regarding the accuracy of this method [40]. The DXA method does not take into account bone geometry and fails to identify bone types, e.g., compact bones and spongy bones [40]. Therefore, high resolution CT is increasingly used to diagnose the early phases of osteoporosis because it can utilize 3-D volumetric data to predict both bone shapes and risk factors [40].

Two types of cells are involved in osteoporosis development, osteoblasts and osteoclasts. Osteoblast cells are derived from mesenchymal stem cells and exclusively responsible for the bone formation [40]. Osteoblasts, after differentiating from precursors, secret extracellular matrix (ECM) containing type-1 collagen and some non-collagenous proteins [40]. The mineralization of ECM can be enhanced by vitamin D, calcium and phosphate in the serum [40]. The bone formation can be enhanced by vitamin D and parathyroid hormone (PTH) but suppressed by glucocorticoid intakes. PTH can maintain the serum calcium level within a narrow range through the calcium sensing receptor (CaSR) on the parathyroid gland [40]. Osteoblast cells eventually undergo programmed cell death (apoptosis) or differentiate into osteocytes [156], and the differentiation is controlled by the Wnt/β-catenin pathway [157].

On the other hand, multinucleated osteoclast cells are differentiated from haemopoietic stem cells under the control of various factors such as receptor activator NF-κB ligand (RANKL) and macrophage-colony-stimulating factor (M-CSF) [40]. RANKL can activate its receptor, RANK, on osteoclasts and induce various key regulatory transcription factors to promote differentiation, multinucleation, activation and survival of osteoclasts [40]. The role of osteoclasts in bone resorption is to attach onto bone surfaces and create a highly acidic and enclosed environment [40], and subsequently cathepsin K is responsible for degrading collagen and resorbing bones.

Typical therapies of osteoporosis include anti-resorptive and anabolic drugs in addition to changes of bad life styles (smoking, alcohol consumption and physically inert) and vitamin D and calcium supplementations. Anti-resorptive drugs refer to those preventing or delaying bone resorption and include BP, denosumab, odanacatib, ONO-5334, saracatinib and BPs [40]. These drugs target different mechanisms to prevent osteoclastic bone resorption. Among these anti-

resorptive drugs, BPs are the most commonly used ones because of their relatively low cost and broad spectrum of osteoporosis treatments [40]. On the other hand, anabolic drugs stimulate and promote bone formation. This class of drugs is quite limited and the most commonly used is full-length PTH (1-84) or its N-terminal fragments (1-34) [40]. Other anabolic drugs, e.g., calcilytic drugs (MK-5442), sclerostin antibodies, and DKK-1 antibodies (BHQ-880), are still under development and waiting for approvals from different health authorities [40].

Compared to fractures caused by trauma or overuse, fractures resulting from osteoporosis have an increased risk of re-fractures, which decrease patient quality of life significantly [7, 40]. In addition, the excess time in the hospital resulted from these subsequent fractures increases the risk of life-threatening complications, such as pneumonia and thromboembolic diseases, which can be caused by the immobilization on bed [158]. In addition, osteoporotic fractures most commonly occur in wrist, spine and hip bones and found to be prevalent in older people [159].

Osteoporosis can both cause the bone fractures and delay the healing. It used to be thought that osteoporosis would not impair fracture reconstruction and was not the main factor resulting in subsequent fractures [160]. However, recent studies have found that not only is osteoporosis a key risk factor for fractures but it also results in delays in fracture healing [7, 36-38]. Recent studies found that in the osteoporosis group, bone forming-related gene expressions were decreased and osseointegration with implants was significantly reduced compared to the healthy one [36].

Osteoporosis can affect both the primary (short-term) and biological (long-term) stabilities of implants [7]. In particular, the loss of the primary stability may result in the implant failure rapidly. The poor osseointegration of implant and bone tissue results in low strength of bone-implant connections and, because the stresses tend to be concentrating at intersections with

low contacting areas, the implant stability is significantly impaired. The loss of the long-term stability is resulted from insufficient osteoblastic activity that prevents the long-term integration of implants with bone tissue and consequently compromises the biological stability [7].

2.7 *In vitro* evaluation of biocompatibility of biomaterials

2.7.1 Cytotoxicity of biomaterials

Cytotoxicity test is the most commonly used method to evaluate the biocompatibility of a biomaterial [161]. Other evaluation methods, e.g., PCR, western blotting and flow cytometry, are also commonly used. A comparison is made between the cytotoxicity of any given biomaterial and that of a control (non-toxic) material, on the same cell line(s). The selection of the cell line(s) is based upon type and location of the interaction of a biomaterial with the tissue, e.g., the cytotoxicity of an artificial blood vessel is evaluated against blood cells or that of a bone implant is evaluated against bone cells (osteoblast and osteoclast) [161]. There are two methods to evaluate the cytotoxicity, extract and direct contact method [161]. In the extract method, a biomaterial is immersed in a solution, e.g., phosphate buffer solution (PBS), for a period of time (the duration is dependent upon the study) and then removed. The solution is called an "extract" and is co-cultured with the cell line. After a period of time (typically 1 or 3 days), the viability of cells is measured. In the direct contact method, a biomaterial is directly co-cultured with the cell line and the viability of viable cells is measured. MTT assay is a common used assay to measure the cell viability. Soluble tetrazolium salts in 3-(4,5-dimethylthiazol-2-yl)-2,5-diphenyltetrazoliumbromide (MTT) react with oxidoreductase enzymes in viable cells to form insoluble purple Formazan dyes. The addition of dimethyl sulfoxide (DMSO) can dissolve these Formazan dyes into colored solution. A spectrophotometer is used to measure the absorption of

light of this color solution at a particular wavelength between 500 nm to 600 nm and the absorption depends on the concentration of the dissolved dyes. Relative viability instead of absolute viability is usually used to compare the cytotoxicity between a biomaterial and control to save efforts to construct the calibration curve. The relative viability is defined as the mean absorption of the sample material over the mean absorption of the control sample at the same wavelength. For example, if the mean absorption value of material A extract is 1.5 (unitless) and that of the control is 1.2, the relative viability is 1.25 or 125%. This value indicates that the number of viable cells cultured in material A extract is 25% higher than the number of viable cells cultured in the control, which implying that the material A is biocompatible or non-cytotoxic compared to the control, according to the ISO10993-5 standard.

2.7.2 Real time polymerase chain reaction (PCR)

Polymerase chain reaction (PCR) is another method to evaluate the *in vitro* biocompatibility of a biomaterial based upon its effects on certain genes regulation in cells [162]. Deoxyribonucleic acids (DNAs) in cells carry important genic information for cells to function properly, i.e., proliferation and differentiation. DNAs are first translated into ribonucleic acids (RNAs) and RNAs are used to control the synthesis of proteins. One RNA molecule carries genetic codes (target genes) of different proteins and, in any particular study, only one or a few target gene(s) in this molecule is typically of interest. The expression of this specific code, or the number of RNA molecules that carry this code, determines the potential number of this specific protein production in the cell and the biocompatibility of a biomaterial can be related to this expression of this gene.

However, the quantification of this gene is virtually impossible without amplification because the quantity is too low. PCR is used to amplify the quantity of RNA molecules that carry this gene (target RNA) [162]. Target RNAs have to be translated to complementary DNAs (cDNAs) in a process called reverse transcription and then cDNAs are used as templates to replicate DNA molecules in a polymerase chain reactor, which can accelerate the replication by heating the environment. After each thermal cycle, the number of DNA double strands is expected to double. In the real time PCR, a fluorescent dye is also added and bonded with DNA double strands to illuminate fluorescence signals. The intensity of fluorescence signals is correlated to the number of DNA double strands. A threshold value of signal intensity is arbitrarily defined and, once it's reached, a corresponding thermal cycle number, threshold cycle (C_t), is recorded after thermal amplification of cDNA (Fig. 2.6). In the typical thermal amplification display (Fig. 2.6, generated in the course of this research), relative fluorescence units (RFU, a unitless value indicting the fluorescence intensity coming from the amplified DNA strands) are plotted versus the number of the cycles that have been thermally completed. RFU correlates with DNA quantity and each curve in Fig. 2.6 represents the real-time change in the quantity of DNA stands in one well that is being amplified by PCR. The intersection between the threshold level and one green curve is the threshold cycle (C_t). The comparison of C_t values between the sample and control groups, which indicate the gene expression between these two groups, will imply the biocompatibility of a biomaterial.

The following example illustrates how to calculate gene expression in PCR. One research team developed a drug to increase cell B proliferation and TGF-β, which controls cell proliferation, and is the gene of interest in this study [35]. After DNA amplification with PCR, two C_t values are important, the C_t values of TGF-β in cells treated with drug and in the control

(no drug), donated as $C_{t\ TGF\text{-}\beta,\ drug}$ and $C_{t\ TGF\text{-}\beta,\ control}$, respectively. For example, if the $C_{t\ TGF\text{-}\beta,\ drug}$ is 4 and $C_{t\ TGF\text{-}\beta,\ control}$ is 9, the relative expression can be calculated as $2^{\Delta Ct}$. ΔC_t is equal to $C_{t\ TGF\text{-}\beta,\ control}$ - $C_{t\ TGF\text{-}\beta,\ drug}$, which is 5, and the $2^{\Delta Ct}$ is equal to 32. This value indicates that TGF-β gene expression in cells treated with drug is 32 times higher as the expression in cells treated with the control. Alternatively, it can be stated that the TGF-β expression in cells treated with drug is un-regulated 32-fold compared to the control.

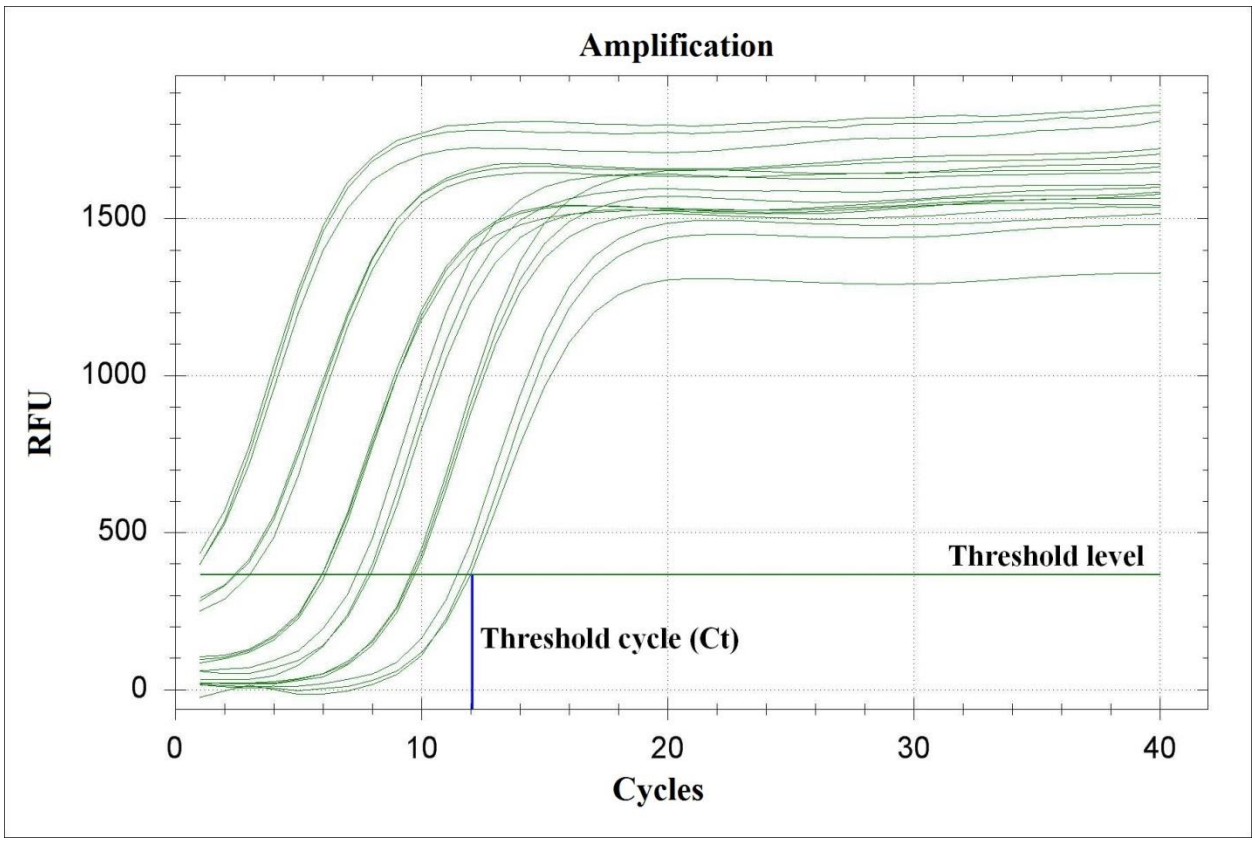

Figure 2.6: Representation threshold cycle (C_t) obtained from real time PCR analysis

2.7.3 Flow cytometry (FCM)

Compared to cytotoxicity evaluation and real time PCR, flow cytometry (FCM) is a less commonly used technique to study biocompatibility of a biomaterial [163], but it can accurately determine several parameters related to cell functions such as cell cycle, cell apoptosis, inflammation and microbial biology [163-165]. In my doctoral research, only cell cycle analysis was investigated by FCM. There are five main phases within one cell cycle, which are named G0, G1, S, G2 and M [163, 166]. G0 phase is the quiescent state of the cell and for most differentiated cells. S phase is the period when cells are replicating chromosomes. M phase is the period when cells are undergoing mitosis and become two identical cells. G1 phase is the period between G0 and S, and G2 phase is the period between S and M.

FCM measures cells in suspension when this suspension flows though the laser detector in a fluid stream (PBS-based) [163]. To be detectable by the laser beam, cells have to be stained with proper dyes. In the cell cycle analysis, cells are stained with propidium iodine (PI). This dye can bond with nucleic acids (both DNA and RNA) and therefore RNase A (the enzyme to digest RNA) must be added to breakdown RNA and eliminate error signals generated by RNA molecules. DNA bonded with PI can generate fluorescent signals, which can be detected by the laser probe. Two types of signals are used to plot cell population, as shown in Fig. 2.7, and commercial software, e.g., ModFitLT, is used to analyze relative quantities of cells in each phase. FCM identifies cell population by assessing the differences in cell morphology and the signals of FSC and SSC fluorescence are proportional to the cell size and granularity, respectively [167]. Therefore, the cell population is plotted by the intensity (unitless) of side scattered (SSC) fluorescent signal (y-axis) against that of forward scattered (FSC) fluorescent signal (x-axis). According to the FCM operating manual provided by the manufacturer, intact

cells are enclosed by the black line and cell debris and aggregates are excluded. Relative quantities of cells in each phase are calculated based upon the number of chromosomes (or DNA molecules) in each phase and the number of chromosomes is proportional to the intensity of signals collected by the laser detector [163]. After defining the proper cell population (e.g., refer to the typical Fig. 2.7, generated in the course of this research; these type of results are presented and discussed later in Chapters 5.2 and 5.3), the data are analyzed using commercial software such as ModFitLT. Figure 2.8, also generated in this research, presents an example of the histogram of cell numbers (y-axis) plotted versus states in one cell cycle (x-axis), which is indicated by the signals from the conjugates channels. Subsequently, a mathematical profile that can best match the histogram is generated by ModFitLT and the relative quantities of each phase within one cell cycle are calculated based upon this mathematical profile by integrating the areas underneath this profile curve. As shown in Fig. 2.8, three phases can be identified from this particular result and the lower and higher peaks refer to G1 and G2 phases, respectively. In addition, the saddle valley between these two peaks represents the relative quantity of cells in S phase.

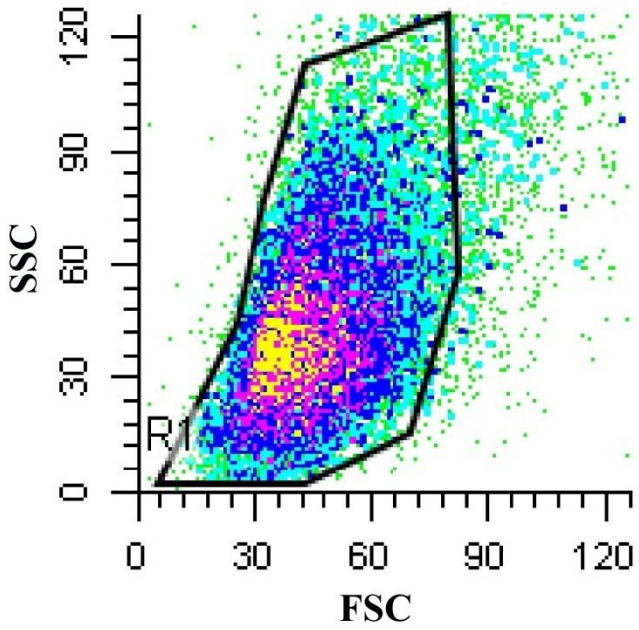

Figure 2.7: Cell population plotted by forward scattered (FSC) and side scattered (SSC) fluorescent signals.

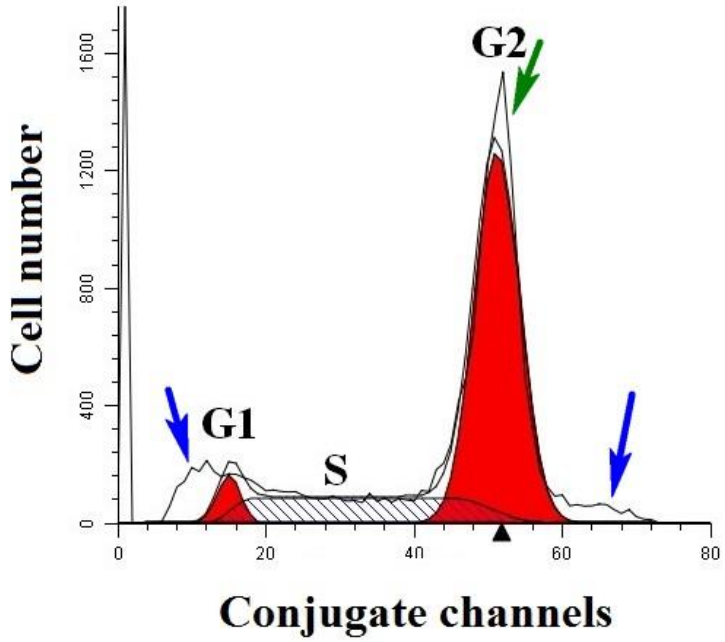

Figure 2.8: Representation of the relative quantities of G1, S and G2 phases in cell cycle analysis. Green arrow indicates the mathematical profile calculated by ModFitLT and the blue arrows indicate a histogram of cell numbers.

2.8 *In vivo* evaluation of biomaterials

In vivo tests of biomaterials are used to assess biomaterials' or biomedical devices' biocompatibility in the biological environment. In a broad definition, the biocompatibility refers to the ability of biomaterials to performed their intended purposes and functions [161]. To assess biocompatibility, material composition, locations of biomaterials' intended uses, degree of interaction between the biomaterial and local tissues, frequency and duration of biomaterials uses must be known to design proper *in vivo* evaluation [161]. In general, *in vivo* tests can be classified according to two different categories [161]. In terms of contact with tissues, biomaterials can be classified into surface biomaterials (e.g., artificial skins), external communicating device (e.g., blood circulating systems in hemodialysis for renal failure patients) and implants (e.g., total hip replacement prosthesis). Alternatively, biomaterials can be grouped into limited (or short term, <24 hours), prolonged (or intermediate, above 24 hours but less than 30 days) and permanent (long-term, > 30 days) medical devices. This classification system also helps in the proper design of *in vivo* evaluations [161]. For example, in my research, a drug delivery system was designed by incorporating drugs in bone cements. Therefore, according to the first category, my device is an implant and, according to the second category, my device was designed for long-term use.

There are many government agencies (e.g., FDA and Health Canada) and regulatory bodies (e.g., ASTM and ISO) publishing guidelines to conduct *in vivo* evaluations [161]. According to these guidelines, *in vivo* biocompatibility evaluations include, but are not limited to, the following tests: sensitization, irritation, acute toxicity, chronic toxicity, genotoxicity, carcinogenicity, hemocompatibility, reproductive toxicity, implantation , biodegradation and immune response [161]. Sensitization and irritation tests are similar and used to evaluate

potential allergic, irritating, and sensitizing responses in body when it is in contact with biomaterials [161]. Acute and chronic toxicity measure toxic effects to body when it is not in direct contact with biomaterials [161]. Acute toxicity tests measure toxic responses within 24 hours of exposures to biomaterials and chronic toxicity test evaluate response of long term exposures from 28 days to 90 days [161]. Genotoxicity and carcinogenicity tests assess potential genotoxic (DNA mutation) and tumorigenic (causing cancers) effects of biomaterials, respectively [161]. When biomaterials are intended to interact with the blood system, hemocompatibility test is performed [161] and includes evaluations of thrombosis (blood clots inside blood vessels), coagulation (blood clotting) and inflammation (leukocytes migration). As its name implies, reproductive toxicity assess whether biomaterials have potential toxic effect on reproductive functions [161]. Implantation tests are performed if biomaterials are intended to be implanted in the body and, if biomaterials can be degraded inside body, biodegradation tests evaluate toxicity of those degrading products [161]. Finally, immune response tests assess whether biomaterials can cause any adverse immune responses, e.g. hypersensitivity, inflammation, immunosuppression and immunestimulation [161].

When proper *in vivo* tests are decided, the next step is to choose the animal models. Animals used for *in vivo* tests can be rats, mice, rabbits, pigs, sheep, dogs, cats and nonhuman primates [161]. Depending on intended purposes of medical devices, different kinds of animals are used [161]. For example, rabbits are usually used to evaluating contact lenses and pigs and dogs are used more other than other animals when vascular grafts are evaluated [161]. In my study, female rabbits were selected as the animal model because of their relative short duration to reach skeletal maturity and close mineral composition of bone to human bone [168]. Rabbits typically have life spans of 9 to 12 yeas and are suitable for medium to long term (> 1 month)

studies. Lastly, gender bias can be avoided in the experiment by just using the same gender animals.

2.9 Biochemical markers related to bone resorption

As discussed previously, multinucleated giant osteoclast cells create enclosed acidic environment on bone surface to dissolve bone minerals and the release of Cathepsin K from osteoclast cells degrades collagenous and non-collagenous proteins in the extracellular matrix [40]. Meanwhile, several biochemical markers are released into blood and the measurement of these biomarkers can be used to evaluate the degree of bone resorption (Fig. 2.9). During the bone remodeling process, bone-specific alkaline phosphatase (BALP) and osteocalcin (OCN) are released from osteoblast cells [169, 170]. Elevated BALP and OCN levels in serum are corresponding with high bone turnover and resorption [169]. During the bone resorption, type I collagen is broken down by enzyme cathepsin K synthesized by mature osteoclasts [169, 171]. N- and C- terminus at the non-helical regions on type I collagens are called N- and C-telopeptide, respectively, and crosslinks are formed in these regions. After collagen breakdown, crosslinks are present in two forms: peptide bound and free forms [169]. The peptide bound forms include (N-terminal cross-linked telopeptide of Type I collagen (NTX) and C-terminal cross-linked telopeptide of Type I collagen (CTX); while, pyridinoline crosslinks (PYD) and deoxypyridinoline crosslinks (DPD) are free forms. During the collagen breakdown, another protein, hydroxyproline (OHP), was free from collagens and released into blood [172]. This protein is formed by post-translational hydroxylation in this peptide chain and accounts for 13-14 % of the amino acid quantity in collagens [172]. Elevated levels of NTX, CTX, PYD, DPD and OHP in blood serum clearly indicate the elevated level of bone resorption. Tartrate-resistant acid

phosphatase (TRACP) has two isoforms, 5a and 5b, with different molecular weights, TRACP-5b, secreted by osteoclast during the bone resorption process [173]. The level of TRACP-5b in blood serum indicates the level of osteoclastic activity and hence measures the degree of bone resorption by osteoclast cells.

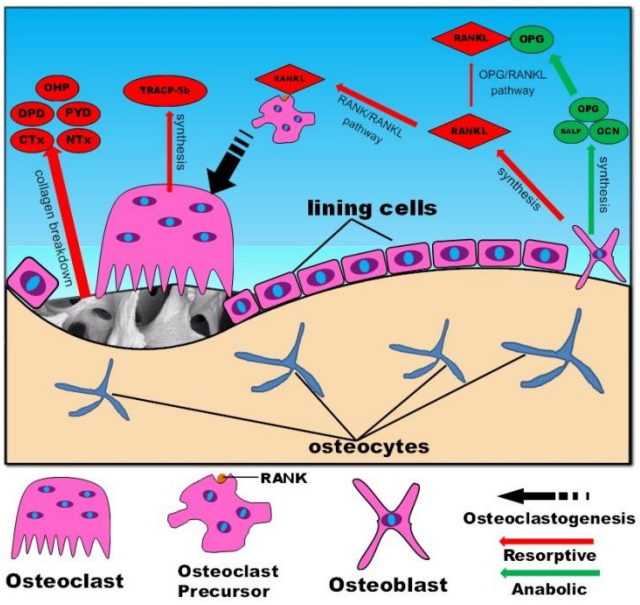

Figure 2.9: Illustration of biochemical markers related to bone remodelling. OPG (osteoprotegerin) is secreted from mature osteoblast cells and bound to RANKL (receptor activator of nuclear factor NF-κB ligand) in serum to prevent its binding with RANK on the osteoclast precursors and maturation of precursors. BALP (bone-specific alkaline phosphatase) and OCN (osteocalcin) are released from osteoblast cells and TRACP-5b (tartrate-resistant acid phosphatase-5b isoform) is secreted from the osteoclast cells as biomarkers for bone formation and resorption, respectively. Collagenous proteins, PYD (pyridinoline crosslinks), DPD (deoxypyridinoline crosslinks), OHP (hydroxyproline), NTX (N-terminal telopeptide) and CTX (C-terminal telopeptide), are released during bone matrix breakdown and used as biomarkers for bone resorption.

Chapter 3: SCOPE AND OBJECTIVES

As discussed, regenerative bone cement must be engineered to possess adequate mechanical strength, suitable setting rate and appropriate biological responses when used *in vivo*. When used as a potential DDS, the cements must additionally release drugs in a controllable fashion. Furthermore, their clinical response should be predictable, prevent diseases, treat existing illnesses and stimulate tissue growth. Since the mission of this doctoral project is to devise a RA-DDS with CSC or CPSC for the treatment of osteoporotic bone fractures, the specific objectives within this project are designed to achieve this goal:

- Prepare and characterize CSC as a RA-DDS, and then measure its release kinetics and *in vitro* biocompatibility;
- Evaluate CPSC that promotes osteoblastic proliferation and *in vivo* osteogenesis;
- Measure anti-osteoporotic and enhanced osteogenic effects of RA-added CPSC;

Objective 1: Prepare and characterize CSC as a RA-DDS, and measure its release kinetics and *in vitro* biocompatibility:

The CSC principal hydration product, the CSH gel, provides the hardened cement with sufficient mechanical strength (>20 MPa, typical compressive strength of cancellous bone) and large surface areas where drug molecules can be adsorbed. To better understand the experimental design in the first objective, a schematic flow chart is drawn here to visualize this concept (Fig. 3.1).

Part 1: Preparation and characterization of RA-added CSC

Setting time and mechanical strength are the two major properties of bone cements. To understand how RA changes CSC setting rate and mechanical strength, several characterization

techniques were used to investigate changes in the microstructure and hydration as a function of RA content. X-ray diffraction (XRD) and refinement analysis revealed how CSH gel changes with RA quantitatively and scanning electron microscopic (SEM) studies were helpful in understanding the microstructure changes with RA content in the cement. Eventually, Fourier transform infrared (FTIR) analyzed how RA is adsorbed onto CSH gel and its intervention mechanism on the hydration process.

Part 2: RA release kinetics from CSC

Drug release from any excipient can be diffusion- or degradation- dependent, or both. Many factors may affect the release kinetics, such as chemical and physical properties of drugs and interactions between drugs and excipients. Understanding RA release kinetics from CSC was helpful in achieving optimal profiles within the therapeutic window. *In vitro* drug release study was primarily conducted with high performance liquid chromatography (HPLC). FTIR microscope was used to analyze RA distribution within hardened CSC and porosity was measured by nitrogen gas sorption to assist the understanding of RA release mechanism from CSC with a well-established mathematical model.

Part 3: In vitro biocompatibility of RA-added CSC

It is generally accepted that *in vitro* biocompatibility is an important factor in determining the safety of biomaterials or biomedical devices. While CSC has been shown to be biocompatible with epithelial and osteoblastic cells, the addition of RA could influence the cement's biocompatibility and was evaluated by MTT (3-(4,5-dimethylthiazol-2-yl)-2,5-diphenyltetrazoliumbromide) cell viability assays.

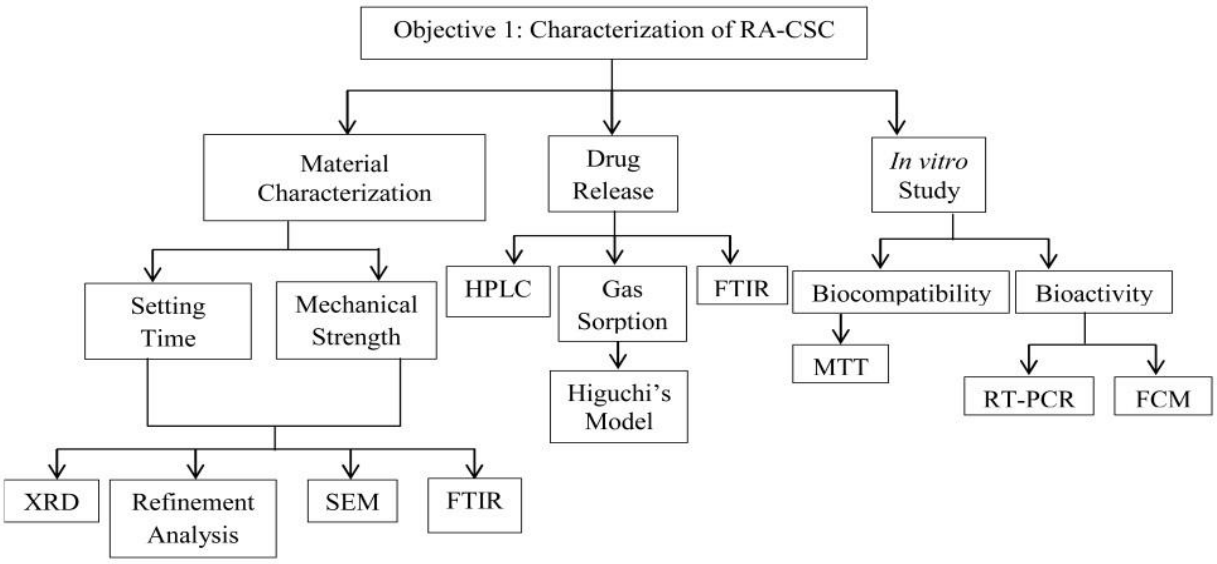

Figure 3.1: Schematic drawing of experimental methods utilized to address objective 1 (refer to the list of abbreviation for symbols details)

Objective 2: Evaluate CPSC that promotes osteoblastic proliferation and *in vivo* osteogenesis:

In this objective, CPSC was made by adding variable amounts of monocalcium phosphate (MCP) into CSC. The material properties of this new cement and its biocompatibility and bioactivity are not yet understood, and the following research topics were thus investigated: 1) how MCP affected CPSC material properties; 2) if CPSC was biocompatible and stimulated osteoblast cell proliferation *in vitro;* 3) if CPSC was osteogenic *in vivo* in rabbit models.

Part 1: Formulation and characterization of CPSC

It is known that MCP accelerates the hydration and alters the microstructure of CSC. Therefore, the changes in setting rate, compressive strength and porosity in dependence of various MCP concentrations in CSC must be investigated. To further explain these effects,

characterization techniques were again employed to explain the mechanism of MCP intervention. XRD and Rietveld refinement analysis were used to reveal and quantify the phase changes of CSH gel and apatites. SEM and micro-computed tomography (μCT) were used to observe cement microstructures. In addition, FTIR was applied to explain how MCP or apatite interacts with CSH gel.

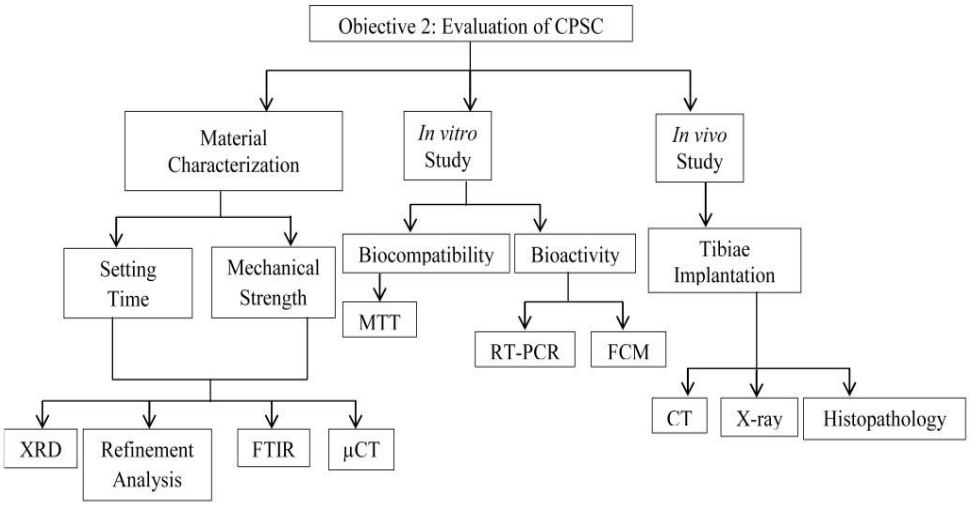

Figure 3.2: Schematic drawing of experimental methods utilized to address objective 2 (refer to the list of abbreviation for symbols details)

Part 2: In vitro investigation of the biocompatibility and proliferation effects of CPSC

In vitro analysis of CPSC biocompatibility and bioactivity was crucial to the subsequent *in vivo* studies. These *in vitro* tests gave insights on the safety of using CPSC in tissues and and also helped to determine the optimal phosphate content in CSC. The results were used to design the CPSC-R delivery system. Silimarly as in the first objective, osteoblast cells were selected to evaluate CPSC biocompatibility and bioactivity. Polymerase chain reaction (PCR) and flow cytometry (FCM) were employed to detect how CPSC affected osteoblast cell cyles and to investigate how CPSC promoted osteoblast cell prolifration.

Part 3: In vivo analysis of the osteogenic effects of CPSC in a rabbit model

In vivo results provided first-in-hand information regarding the effectiveness of osteoconduction and osteoinduction of CPSC and helped to determine the best composition of CPSC for RA delivery in the subsequent studies. Female rabbits were used as the animal model in this study because of three reseaons. Firstly, rabbits' bone strucutures and mineral compositions are very close to those of humans. Secondly, rabbits typically have life spans of 9 to 12 yeas and are suitable for medium to long term (>1 month) studies. Lastly, gender bias can be avoided in the experiment by just using females. At predetermined endpoints, X-ray and computed tomography (CT) radiographs were taken of the implantation sites and animals were sacrificed for the histological study.

Objective 3: Measure anti-osteoporotic and enhanced osteogenic effects of RA-added CPSC:

In this objective, a RA delivery system was designed by adding variable amounts of RA into CPSC. Although the biocompatibility and bioactivity of CPSC were clearly understood from the second objective, the impact of the drug RA on CPSC biocompatibility and bioactivity remained unknown. In this study, these parameters were investigated and the anti-osteoporotic effectiveness of CPSC-R was subsequently evaluated.

Part 1: In vitro investigation of the biocompatibility and proliferation effects of CPSC-R

The *in vitro* part of this study was intended: 1) to evaluate the biocompatibility of RA-added CPSC (CPSC-R) with osteoblast cells; 2) to understand the pathways affecting the bioactivity of CPSC-R on cells; 3) and to reveal how CPSC-R affected osteoblast cell proliferation and differentiation *ex vivo*. These results proved that CPSC-R was biocompatible with living tissues and able to promote tissue growth. The biocompatibility was tested by

comparing the cytotoxicity between CPSC and CPSC-R, and rt-PCR was used to determine osteoblastic differentiation-related gene expressions. Finally, flow cytometry (FCM) results demonstrated that cell cycle was affected by CPSC-R.

Part 2: In vivo analysis of anti-osteoporotic and osteogenic effects of CPSC-R

This *in vivo* study was used to evaluate the effectiveness of CPSC-R when used to repair osteoporotic bone fractures. Healthy female rabbits were used to create the osteoporotic model. Enzyme-linked immunosorbent assays (ELISA) were used to verify the effectiveness of osteoporosis and to evaluate the changes of major osteoporosis-related biomarkers after implantation. CT and X-ray were used to evaluate the degree of bone reconstruction at implant sites, and histology studies were intended to observe the relative growth of new bones into cement and any signs of inflammations. Furthermore, PCR arrays were used to investigate genes relating the osteoporosis treatment and osteogenesis and to reveal the pathways of CPSC-R in bone reconstruction.

Chapter 4: MATERIALS AND METHODS

4.1 Cement preparation

4.1.1 RA-added CSC preparation

Ground CSC powder of average particle size of ~50 μm, containing 50 mol% each of dicalcium silicate (C_2S) and tricalcium silicate (C_3S) (Innovative BioCeramix Inc., Vancouver, Canada), was combined with 0.1, 0.5 and 1.0 wt% of RA (Beta Pharma Inc**.,** Branford, U.S.A.). Since synthesis of CSC powder is not a significant part in this research, details on preparation and characterization can be found in previous doctoral thesis from our laboratory [174]. The reference CSC samples were prepared in the same way but contained no RA. These experimental cement materials are referred to CSC01R, CSC05R and CSC10R respectively, and simply CSC for the RA-free samples. To initiate the cement setting reaction, distilled water was added into the cement powders at a liquid-to-powder ratio of 0.5 by weight, and homogenized into cement paste by simply mixing with a pestle in a mortar.

4.1.2 CPSC preparation

MCP (5, 10 and 15 %) was purchased from Fisher Chemical (U.S.A.) and mixed with CSC, which is identical to that used in the first study. These materials are referred to as CPSC5, CPSC10 and CPSC15, respectively. To initiate the cement setting reaction, distilled water was added into the cement powders at a liquid-to-powder ratio of 0.5 by weight, and homogenized into cement paste by simply mixing with a pestle in a mortar.

4.1.3 RA-added CPSC preparation

CPSC containing 10% of MCP was prepared exactly as mentioned above and 0.5% and 1.0% RA (Beta Pharma, Branford, U.S.A.) were added into formulated CPSC. These samples are referred to as CPSC10 (RA-free), CPSC10-05R (0.5% RA) and CPSC10-10R (1.0% RA), respectively. To initiate the cement setting reaction, distilled water was added into the cement powders at a liquid-to-powder ratio of 0.5 by weight, and homogenized into cement paste by simply mixing with a pestle in a mortar.

4.2 Cement characterization

4.2.1 Setting time and compressive strength determination

The cement pastes were molded into 17 mm × 2 mm (diameter × height) and 6 mm × 12 mm polystyrene cylinders for the testing of setting time and compressive strength, respectively and stored in a 37 °C and 100% RH incubator. The cement setting time was determined in accordance with ASTM Standards Database (ASTM ID: C191-08). A 1 mm diameter, 7.8 g weight needle was rested on the flat surface of a cement sample for 1 to 2 seconds, and then lifted. The cement was considered set if no visible mark from the needle was observed on the surface. The time elapsed between the initial contact of cement and water and the endpoint with no visible mark was recorded as the final setting time. These experiments were repeated 4 times for each sample. The compressive test was carried out at a crosshead speed of 2.54 mm/min on an Instron 3369 (Grove City, Pennsylvania, U.S.A.) instrument equipped with a 50 kN load cell. The samples underwent compressive tests within 5 min after they were removed from the molds to avoid moisture evaporation from sample surfaces. After 3 and 7 days, compressive strength of samples was measured and each sample strength test was replicated 10 times.

4.2.2 Structural analysis of CSC

X-ray diffractometer (XRD, MultiFlex, Rigaku, Japan; source Cu-Kα at 40 kV at 20 mA), with a shutter and standard sample holder, was used to determine the progress of the cement hydration through monitoring the amount of CH, which is the byproduct of hydration of CSC, and the relative quantity of the unreacted CS. The XRD scans ranged from 10 to 60 degrees at a 2 deg/min speed. Each sample was replicated four times. Rietveld analysis was performed to analyze crystallinity of the hydrated samples ground to a particle size of less than 10 μm. Step-scan was carried out over a two-theta range of 3° - 80° with CoKa radiation on a Bruker D8 Focus Bragg-Brentano diffractometer equipped with an Fe monochromator foil, 0.6 mm (0.3°) divergence slit, incident- and diffracted-beam Soller slits and a LynxEye detector. The scan results were analyzed using the International Centre for Diffraction Database PDF-4 and Search-Match software by Siemens (Bruker) and refined with Rietveld program Topas 4.2 (Bruker AXS). In our study, XRD patterns of 7-day setting samples were obtained.

In the second and third studies, Rietveld refinement was performed on ball-milled samples (after 7 day setting) to reduce their particle size to <10 μm. Step-scan was carried out over a two-theta range of 10°-120° with 0.05 degree/step and 5 s/step (2^{nd} study) or of 10° - 100° with 0.02 degree/step and 1 s/step (3^{rd} study). The scan results were analyzed with the Inorganic Crystal Structure Database and diffraction patterns and refined with HighScore Plus (version 3.0, PANalytical, Netherlands).

Scanning electron microscope (SEM, Hitachi S-3000N, Hitachi Co., Japan), equipped with an EDX analyzer, was used to examine the samples' microstructures after 7 days of hydration. Surface area and pore size analyzer (Autosorb-1 series, Quantachrome Instruments, U.S.A.) was used to determine the samples (7 day) porosity and to calculate tortuosity. Pellets

were prepared in the same way as in compressive strength test and outgassed for 24 hours before test in 25 °C in glass tubes. Subsequently, tubes were transferred to test station and porosity was calculated by nitrogen absorbance method. Measurements were conducted isothermally at 25 °C.

Micro-computed tomography (μCT, MicroCT 100, SCANCO Medical AG, Bruettisellen, Switzerland) was used to visualize the materials' porosity after 7 day setting. Fourier transform infrared spectroscopy (FTIR, PE100 series, PerkinElmer, Massachusetts, U.S.A.) was used to detect HA interference with Si-O-Si bonds in the 7-day hydrated samples. The spectrum range was selected between 4000 cm^{-1} and 400 cm^{-1}. Dried sample powders were weighed and mixed with 4 wt% dehydrated KBr and the mixtures were compressed into tablets.

4.3 RA release analysis from CSC

4.3.1 Risedronate release detection

Cement pellets for RA release experiments were prepared the same way as in the compressive strength test. 3 hours after setting, the pellets were immersed in the phosphate buffer solution (10 mL, PBS, pH~7.4) in glass containers (20 mL). At predefined time points of 12 hours and then 1, 3, 7, 14, 21, 28 days, and 3 and 6 months, the solutions were taken out for analysis and the containers were replaced with new PBS solution. The mobile phase was an aqueous PBS (1.5 mM Na_2EDTA, 11 mM sodium phosphate and 5 mM tetrabutylammonium bromide as an ion-pair reagent) and methanol (V:V = 88:12, pH = 6.75). All reagents listed above were purchased from SinoPharm Chemical Reagent Co., Ltd (Shanghai, China). Separation of RA from the solution was obtained by using a reversed-phase column (Kromasil-C18, 4.6 mm × 250 mm, 5 μm) and a guard column, on an Agilent 1100 (Germany) high performance liquid chromatography (HPLC) at a 1 mL/min flow rate. The UV detection

wavelength was 262 nm and column temperature was set at 25 °C [175]. Each result was based upon 6 identical sample readings.

4.3.2 Adsorption/desorption analysis and kinetics of RA onto/from CSC pellets

After 7 day setting, hardened CSC samples of 9 g were milled in a mortal and equally dispersed in three 20 mL RA-saturated PBS solutions (pH = 5.6), and mixtures were magnetically stirred for 24, 48 and 72 hours, respectively, at 25 ^{o}C. Subsequently, mixtures were centrifuged at 3000 rpm for 3 min to separate supernatants and powders. RA concentrations in supernatants were analyzed by using the previously established HPLC method and plotted against time (24, 48 and 72 hours) to demonstrate RA adsorption process on milled CSC. Powders were dried in the 200 ^{o}C oven for 12 hours and analyzed by FTIR. Each sample was replicated three times.

Adsorbed CSC powders, each of 2 g, were dispersed into three 10 mL RA-free PBS solutions and magnetically stirred for 24, 48 and 72 hours, respectively. Subsequently, supernatants were separated by the centrifuge and RA concentrations in PBS were analyzed and plotted with time (24, 48 and 72 hours).

The RA release kinetics was analyzed with the help of the 3D Higuchi equation (equation 2.8);

$$1 + 2(a/a_0)^3 - 3(a/a_0)^2 = 6DKC_s t/\tau a_0^2 \qquad \text{(equation 2.8)}$$

, where t is the releasing time; D is the diffusivity of RA in PBS; τ is the tortuosity of the capillary system in the carrier material; C_s is the solubility of drug in PBS; a is the radius of unleached portion (RA remains unreleased in this region) of the test pellet; a_o is the radius of the entire pellet; K *is* RA's specific volume and is equal to 0.535 cm^3/g; and $(a/a_0)^3$ represents the

remaining fraction in the pellets [155]. The diffusivity of RA in PBS, $D_{RA,}$ can be estimated from the *Stokes-Einstein* equation as 2.2×10^{-6} cm^2/s [176]. τ can be calculated from the equation 4.1, $1/\tau = 1\text{-}2/3[(1 + \varepsilon)(1 - \varepsilon)^{2/3}]$, where ε is the porosity within the matrix [176].

4.3.3 Analysis of RA distribution in the CSC pellet

CSC pellets with 10% RA were prepared in the same method as for the compressive test. After 7 days of setting, pellets were broke into halves and the top and interior surfaces were scanned in an FTIR microscope (Spotlight 200 FTIR Microscope System, PerkinElmer, Massachusetts, U.S.A.). Based upon previous IR analysis, the peak at 960 cm^{-1}, characteristic for POO^- stretching, was selected to plot the RA distributions within set CSC samples.

4.4 *In vitro* biocompatibility analysis

4.4.1 Cell culture of osteoblast cells

Osteoblast cells were isolated from calvaria of neonatal (<2 days old) Sprague-Dawley rats by an enzymatic digestive process [177]. The rat calvaria were washed three times in PBS (pH = 7.4), minced into fragments of 1 mm in diameter, and then digested in 0.25% (w/v) trypsin-EDTA solution (20 min, 37 ºC) to eliminate fibroblastic contamination. Subsequently, they were treated with1 mg/mL collagenase (Sigma, U.S.A.) at 37 ºC for 90 min to release osteoblast cells. Supernatants were centrifuged at 1000 rpm for 10 min, suspended in cell culture media made of Dulbecco's modified eagle's medium (DMEM, Hyclone, U.S.A.) containing 10% (v/v) heat-inactivated fetal bovine serum (FBS, Hyclone, U.S.A.), 100 U/mL penicillin, and 100 mg/mL streptomycin (Hyclone, U.S.A.), and incubated in 25 cm^2 flasks at 37 ºC under a humidified atmosphere consisting of 5% CO_2. Culture media were

refreshed every 2 days during cell culture. Osteoblast cells used in my study were between their second and fourth passages.

4.4.2 MTT assay of RA-added CSC on osteoblast cells

To evaluate cytotoxicity of the cement pellets, they were initially set for 1 day at 37 ºC, placed in 10 mL PBS-containing tubes and incubated for 1, 3, and 7 days. Collected supernatants were sterilized by 0.22 µm filtration and stored in the refrigerator [178]. On the day preceding the cytotoxicity test, each well of 96-well plate was seeded with 5×10^3 osteoblast-like cells in 200 µL of 10%-FBS DMEM culture media, and incubated at 37 ºC in 5% CO_2 atmosphere. On the day of testing, culture media were removed and 4 µL of the supernatants or of RA-free PBS (for the control) together with 196 µL of culture media were added. A toxicity reference consisting of 200 µL of a 60 mg/mL phenol (C_6H_5OH) solution was also added to osteoblast-containing wells. Viable cell numbers were evaluated after 3 days of culturing by using an (3-(4,5-dimethylthiazol-2-yl)-2,5-diphenyltetrazoliumbromide (MTT, Sigma, U.S.A.) assay. For this purpose, 20 µL of a 5 mg/mL MTT/PBS solution was added into each well and cultured for another 4 hours at 37 ºC. After supernatants were removed, 150 µL of dimethyl sulfoxide (DMSO, Sigma, U.S.A.) was added into each well to completely dissolve the newly formed purple formazan. The absorbance of formazan was read at 570 nm by a multidetection microplate reader (Synergy™ HT, BioTek, U.S.A.) equipped with Gen51.10 software. The cell viability was defined as the sample absorption at 570 nm divided by the absorption of the control group at the same wavelength.

4.4.3 MTT assay of CPSC on osteoblast cells

Cement pellets after 1-day initial setting were put into 10 mL PBS-containing tubes for 3 days at 37ºC. Subsequently, the pellets were removed and PBS extracts were sterilized by 0.22 μm filtration and stored in the refrigerator for future use [178]. The extracts were diluted with DMEM and FBS to form 5%, 10% , 20% and 50% solutions with 10% FBS in media. Corresponding fresh PBS with 10%-FBS in DMEM served as the control groups. 60 mg/mL aqueous phenol solution was used as the toxicity reference. On the day preceding the test, each well of a 96-well plate was seeded with 5×10^3 osteoblast cells, added with 10%-FBS DMEM culture medium of 200 μL, and incubated at 37 ºC in an incubator kept at 5% CO_2. On the day of testing, 200 μL of the prepared extracts and/or controls were pipetted into the wells to replace culture media and cells were cultured for 3 days. Viable cells were evaluated with the help of MTT (3-(4, 5-dimethylthiazol-2-yl)-2, 5-diphenyltetrazoliumbromide, Sigma, U.S.A.) assays. For this purpose, 20 μL of a 5 mg/mL MTT solution was added into each well and cultured for 4 hours at 37 ºC. After removing the supernatants, 150 μL of dimethyl sulfoxide (DMSO, Sigma, U.S.A.) was added into each well to completely dissolve the formed purple formazan crystals. The absorbance of formazan was read at 570 nm by a Microplate Reader (Synergy^{TM} HT, BioTek, U.S.A.) equipped with Gen51.10 software. The viability was calculated as OD_{570} of treated group/OD_{570} of the control.

4.4.4 MTT assay of RA-added CPSC on osteoblast cells

Cement pellets after 1-day initial setting were put in 10mL PBS-contained tubes for 1 and 3 days at 37ºC. Subsequently, pellets were removed and PBS extracts were sterilized by 0.22 μm filters and stored in the refrigerator for future use. Extracts were diluted with DMEM at the ratio

of 1:1 and 10% FBS was then added in to extracts. Corresponding fresh PBS with 10%-FBS in DMEM served as the control groups. Aqueous phenol solution (60 mg/mL) was used as the toxicity reference. On the day preceding the test, each well of a 96-well plate was seeded with 5×10^3 osteoblast cells, added with 10%-FBS DMEM culture medium of 200 µL, and incubated at the 37 ºC and 5% CO_2 circumstance. On the day of testing, 200 µL of the prepared extracts and/or controls were pipetted into wells to replace culture media and cells were cultured for 3 days. Viable cells were evaluated with the help of MTT (3-(4,5-dimethylthiazol-2-yl)-2,5-diphenyltetrazoliumbromide, Sigma, U.S.A.) assays in the same method as mentioned above.

4.4.5 Gene expression analysis on RT-PCR

Osteoblast-specific genes, alkaline phosphatase (ALP), osteoprotegerin (OPG), runt-related transcription factor 2 (Runx2) and transforming growth factor-β (TGF-β), were evaluated in this study and β-actin gene was used as the housekeeping gene. Primer designs of interested genes and the housekeeping gene were based upon a published study [35]. Total RNA from cells cultured in extracts or DMEM for 3 days was isolated by RNeasy Mini Kit (Qiagen, Texas, U.S.A.), and RNA quality and concentration were monitored by µ-UV spectrophotometer at 230, 260 and 280 nm wavelengths. Complementary DNA (cDNA) was synthesized from 2 µL RNA using reverse transcriptase (TaKaRa, Dalian, China) and stored at -80 ºC for future use. A total volume of 25 µL cDNA mixture per well was amplified on real-time PCR (CFX96 Real-Time System, Bio-Rad, U.S.A.) as follows: 95 ºC initialization for 2 min, 94 ºC denaturing for 30 s, 55 ºC annealing for 30 s, 68 ºC extension for 30 s, repeated for 40 cycles, and melting point analysis from 55 ºC to 95 ºC. In the second study, relative gene expressions of each sample were first calculated from the $2^{\Delta\Delta Ct}$ equation and then normalized to gene expressions of the pure CSC

sample; while in the third study, levels of gene expression were calculated from the $2^{\Delta\Delta Ct}$ equation directly.

4.4.6 Cell cycles analysis on flow cytometer

Cells were cultured with extracts or DMEM for 1 day and subsequently collected by centrifugation. Cells were washed twice with cold PBS and fixed in 75% ethanol at 4 °C overnight. On the following day, cells were collected, washed with cold PBS, and stained by 500 μL 50 μg/mL PI-PBS solution of 100 μg/mL RNeasy A. Subsequently, cells were incubated at 4 °C for 30 min and analyzed on the flow cytometer (BD FACSCantoII, BD bioscience, U.S.A.). Results were analyzed on ModFit LT 3.6 (Verity Software House, U.S.A.). Each group was repeated 3 times.

4.4.7 Statistical analysis

IBM® SPSS® Statistical software v.19.0 (SPSS Inc., Chicago, Illinois, U.S.A.) was used to analyze our data. The results are reported as mean ± standard deviation. After testing the homogeneity of variance, one-way ANOVA ($p < 0.05$) was performed to compare the values among individual groups. If variances of individual groups are assumed equal, least significant difference (LSD) *post hoc* multiple comparison test was used; otherwise, Tamhane's (T2) *post hoc* multiple comparison test was used to detect significance levels.

4.5 *In vivo* study

Animal studies were approved by both the animal welfare committee of Safety Evaluation Centre in Shenyang Research Institute of Chemical Industry (SRICI, permit

No.:K002) and the animal care committee at the University of British Columbia (permit not required).

4.5.1 CPSC *in vivo* animal model

Rabbits are frequently used in bone tissue engineering studies because they have relatively short duration to reach skeletal maturity [168]. Fifty-six female New Zealand White rabbits, 5 - 9 months and 1.5 - 2.1 kg, were randomly divided into 4 groups and used for this study. Calcium phosphate cement (CPC, chronOS-Inject, SYNTHES, Switzerland) was used as the internal control to compare with CPSC, and the sham operation (no implantation) group was also used as the operation control. To simulate bone cement in non-load bearing applications, epiphyses on tibiae from both hind legs were used as implantation or perforation (drilling the hole) sites. In CPSC15/CPC, CPSC10/CPC, CPSC5/CPC groups, right tibiae were implanted with CPSC and left tibiae were implanted with CPC; while in the control group both tibiae were drilled without implantation. Two endpoints were chosen for this study at 8 weeks (n = 7) and 12 weeks (n = 7). Upon sacrifice of the animals, clinical X-ray and computed tomography (CT) scans were performed and the tissue samples were prepared for histological evaluations. A graphic illustration of the study schedule is presented in Fig. 4.1.

Rabbits were acclimatized for 7 days and surgery was then performed at the Safety Evaluation Centre in SRICI. Food and water were removed 12 hours before surgery. The rabbits were stabilized on the rack and anesthetized by the *i.v.* injection of pentobarbital sodium (2%, 1 mL/kg). Bilateral medial tibiae were clipped free of fur below and above the joint and cleansed with iodophor. Perforations (d = 6 mm, $ø$ = 3 mm) were created by a blunt sterilized manual drill and phosphate buffer saline (pH = 7.4) was irrigated to avoid necrosis. Cement pastes were

injected into holes and bone wax was applied on top to stop cement paste movement and bleeding from marrow cavity. Cefalexin powder was dusted onto tissues and incisions to minimize bacterial infection. Each rabbit was kept in a single cage after surgery, and food and water were accessed *ad libitum*. Antibiotics (0.5 mL per animal/day, Synulox, Pfizer, U.S.A.) were intramuscularly injected daily for three days after surgery. Incisions were purposely left open to remove possible fester growth underneath incisions and skins were closed by sutures after 1 day.

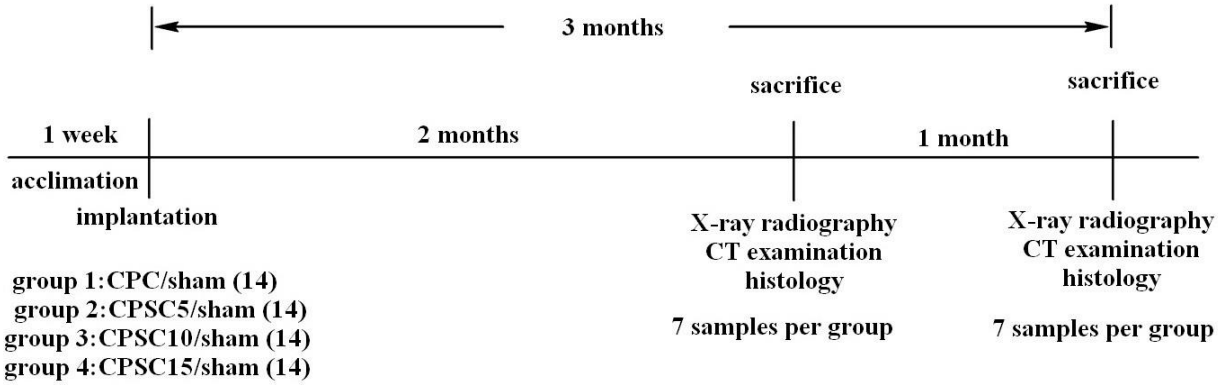

Figure 4.1: Graphic illustration of the CPSC animal study schedule.

4.5.2 CPSC-R *in vivo* model

Thirty female New Zealand rabbits, aged about 6 months and weighted between 1.5 and 2.1 kg, were randomly divided into 3 groups and used for this study, namely sham group (control), CPSC10 (RA-free, 10% MCP) and CPSC10-05R (0.5% RA, 10% MCP), respectively. All animals were bilaterally ovariectomized (castration) after one-week acclimation period and, two weeks later after castration, were injected of methylprednisolone (1 mg/day/kg, Solu-Medrol, Pfizer, U.S.A.) for 4 weeks to induce osteoporosis as previously described [179]. Two

endpoints were designed in this study, 8 weeks (n = 5) and 10 weeks (n = 5). A graphic illustration of the study schedule is presented in Fig. 4.2.

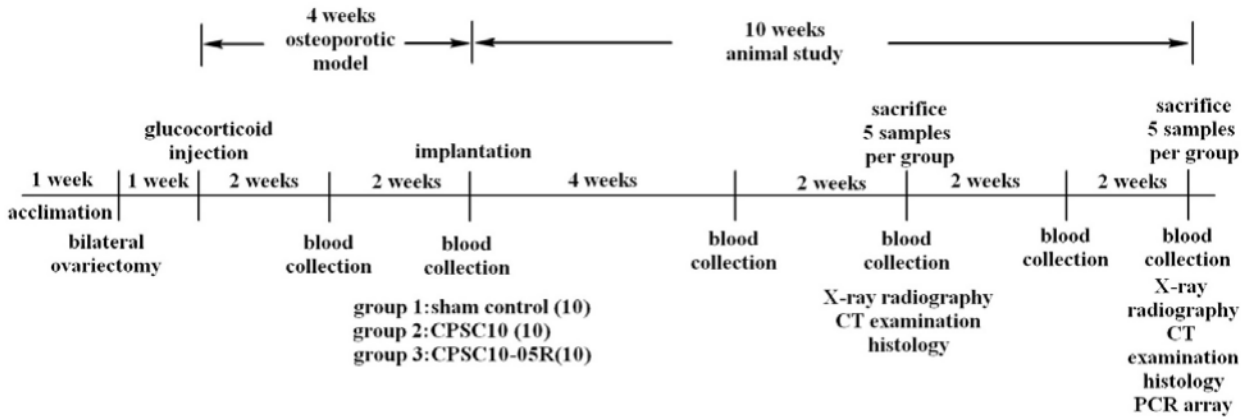

Figure 4.2: Graphic illustration of the CPSC-R animal study schedule.

Both bilateral ovariectomy and implantation surgeries rigorously followed aseptic procedures. The operation room was sterilized with ultraviolet lighting for two hours and food and water were removed 12 hours before surgery. All surgery tools, including consumables and materials were sterilized one night before by autoclaving except of those that cannot be sterilized by autoclaving being sterilized at 200 °C for 3 hours. Rabbits were positioned supinely on the rack and anesthetized by *i.v.* injection of pentobarbital sodium (2%, 1ml/kg). Right medial tibiae were clipped free of fur below and above the joint and cleansed with iodophor. Dislocated incisions were made to minimize risks of infection, and perforations (d = 6 mm, $ø$ = 3 mm) were created by a blunt manual drill. During drilling, phosphate buffer saline (pH = 7.4) was irrigated to avoid necrosis. For CPSC and CPSC-R groups, cement paste were injected into holes and bone wax was applied to stop paste movement and bleeding; for the sham group, bone wax was inserted to stop bleeding. Cefalexin powder was sowed on tissues surrounding holes and

incisions. Each rabbit was kept in a single cage after surgery, and food and water were accessed *ad libitum*. Antibiotics (0.5 ml per animal/day, Synulox, Pfizer, U.S.A.) were intramuscularly injected for 3 days after surgery. Incisions were purposely left unsutured until fester growing underneath was removed after 24 hours and skins were sutured to close.

4.5.3 Clinical X-ray and computed tomography (CT) analyses

At the pre-determined endpoints, rabbits were subject to clinical X-ray and CT scans before being sacrificed for histological studies. After transported to hospitals, the rabbits were anesthetized by pentobarbital sodium (2%, 1 mL/kg), scanned by clinical X-ray (Kodak DirectView DR7500, Carestream Health, Rochester, U.S.A., 50 kVp, 160mA, 10 mS) and CT (Discovery CT750 HD, GE Healthcare, Waukesha, U.S.A., 100 kV, 20 mA, 0.625 mm) systems. All images were saved in DICOM ("Digital Imaging And Communications In Medicine") format and subsequently analyzed with open-source Osirix imaging software (32-bit, free version, PIXMEO, Switzerland) [180]. In X-ray image analyses, the images were displayed in black and white style and the minimum background greyvalue (the brightness of each pixel on image) was defined at 2000. Newly formed bone and the remnant cement were differentiated based upon the differences in greyvalue, i.e., the remnant cement had higher greyvalue than the newly formed trabecular bone and therefore appeared brighter on the images, following the commonly used procedures in medical imaging [181]. In CT image analyses, the images were displayed in spectrum cult (color-coding). Therefore, the cortical bone or the remnant cement with higher density appeared in red, the newly formed trabecular bone or cancellous bone with similar density (i.e. less dense than the cortical bone) appeared in green and soft tissues (of lowest density) appeared in blue on these CT images.

4.5.4 Histological slides preparation and analysis

After radiographic examinations, rabbits were sacrificed by CO_2 inhalation, epiphyses on both tibiae were excised, and the surrounding soft tissues were removed (refer to the schematic Fig. 4.3 for more information on the samples collection for histology). The histological slide preparation followed a well-established method [182]. After collection, the specimens were immediately fixed in 10% neutral buffered formalin solution for 1 week and washed in distilled water for another 2 hours. Subsequently, the specimens were decalcified in formic acid-sodium citrate solution for 2 weeks and again washed in distilled water for 2 hours. After decalcification, the specimens were dehydrated in graded series of ethanol solutions (30%, 50% and 70%) for at least 36 hours in each and embedded in paraffin wax. Thereafter, the specimens were divided into two parts along the implant axis and three longitudinal ground-sections 5 µm thick were prepared for each half. All sections were stained with hematoxylin–eosin and examined under light microscope. Histopathological evaluation parameters included signs of inflammation, encapsulation, presences of osteoblast and osteoclast cells, new bone formation, and bone remodeling [183]. All histological analyses were performed at Dalian Medical University, under the direction of Dr. Hongying Zhang.

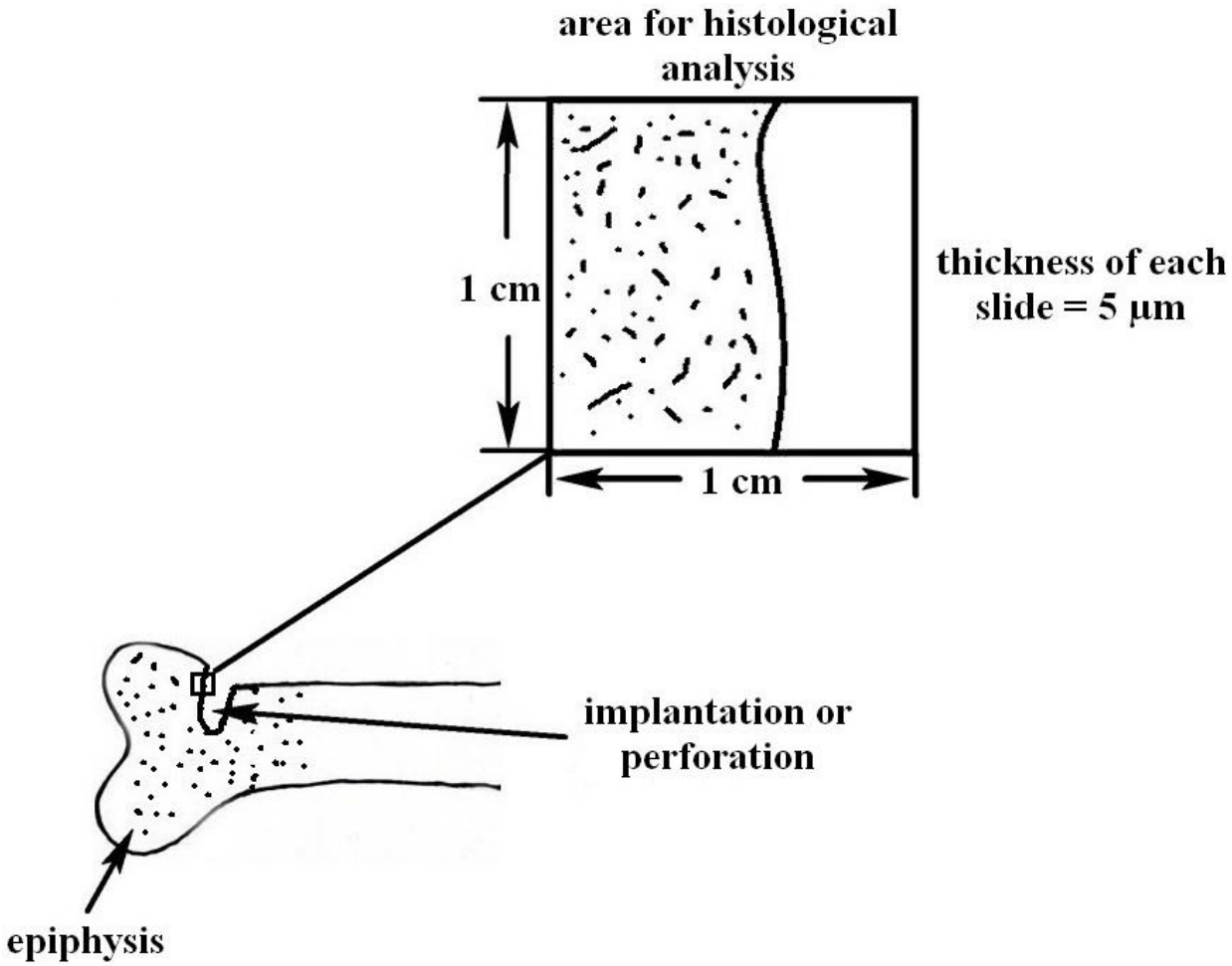

Figure 4.3: A representation of the histological study. An area of 1 cm × 1 cm is observed under the light microscope. A histological slide has a thickness of 5 μm.

4.5.5 Serum biochemical markers evaluations

In the CPSC-R *in vivo* study, at the 4^{th}, 6^{th}, 8^{th} and 10^{th} week after surgery, 2 mL blood samples (n = 10 for week 4, 6 and 8, and n = 5 for week 10) were collected from each rabbit in the ear artery and stored in blood tubes (Vacutainer, BD Biosciences, U.S.A.) at room temperature undisruptedly for 30 min to clot. Afterwards, the tubes were centrifuged at 3000 rpm for 10 min and the supernatants (blood serum) were separated and stored at -20 °C for future use. Collected serum samples from the same group were pooled together and then divided into aliquots of 2 mL each.

Serum levels of bone-specific alkaline phosphatase (BALP), osteocalcin (OCN), osteoprotegerin (OPG), receptor activator of nuclear factor NF-κB ligand (RANKL), tartrate resistant acid phosphatase-5b isoform (TRACP-5b), pyridinoline crosslinks (PYD), deoxypyridinoline crosslinks (DPD), hydroxyproline (OHP), carboxy-terminal propeptide of type I procollagen (PICP) and amino-terminal propeptide of type I procollagen (PINP), galactosyl hydroxylysine (GHYL), bone sialoprotein (BSP), N-terminal telopeptide (NTX) and C-terminal telopeptide (CTX) were detected by the enzyme-linked immunosorbent assay (ELISA) kits. (n = 8, technical replicates)

In addition, during the osteoporotic model creation period, blood samples were collected before 2 weeks and 4 weeks after glucocorticoid injections and treated in the exactly same way as the abovemetioned protocol and only TRACP-5b in serum was measured to validate the osteoporotic model.

4.5.6 PCR array analysis

PCR arrays were used to quantify and evaluate osteogenesis-related gene expressions in perforated or implanted tibiae from osteoporotic rabbits between the sham control, CPSC10 and CPSC10-05R groups. Immediately after euthanasia of the animals after 10 weeks, bone fragments from epiphyses were collected, immersed in RNA stabling reagents (RNAlater RNA stabilization reagent, Qiagen, U.S.A.) overnight and stored at -80 °C for future use. To effectively isolate total RNA from bone fragments, the fragments (10 mg) were milled in the liquid nitrogen thoroughly and treated with 5 mL trizol (QIAzol, Qiagen, U.S.A.). The mixtures were standing for 10 min, treated with 1 mL chloroform and shaken rigorously. Subsequently, the mixtures were left uninterruptedly for another 15 min and centrifuged at 4 °C for 15 min. Top clear layers were transferred to new tubes and total RNAs were isolated by the RNeasy Plus Mini Kit (Qiagen, Texas, U.S.A.). For each group, total RNAs from each sample were pooled (biological replicates, $n = 5$) and stored in the -80 °C refrigerator for future use. Three micro litters of defrozen RNA solution was used to reversely transcribe into 102 µL of cDNA and this amount of cDNA was mixed with supplied reagents to form a 2400 µL PCR component before PCR analysis (refer to Appendix B.6 for more details). Twenty-five micro litters of PCR component was added into each well in the PCR array (RT² Profiler PCR Array osteogenesis for rabbit, Qiagen, Texas, U.S.A.) and amplified on real-time PCR (CFX96 Real-Time System, Bio-Rad, U.S.A.) as follows: 95 ºC initialization for 10 min, 95 ºC amplifying for 15 s, 60 ºC collecting data for 60 s, repeated for 40 cycles,. Each group included 4 PCR arrays (technical replicates, $n = 4$). After thermal amplification and data collection, C_t (threshold cycle) values were exported into an Excel file and uploaded to the web-based data analysis tool provided by the manufacturer (http://pcrdataanalysis.sabiosciences.com/pcr/arrayanalysis.php). The results

were analyzed using this web-based tool and discussed based on the comparison of gene expressions between CPSC10 or CPSC10-05R and the sham control group. For more information on this PCR array, please refer to the manufacturer website. (http://www.sabiosciences.com /rt_pcr_product/HTML/ PANZ-026Z.html#resource)

Chapter 5: RESULTS AND DISCUSSION I: CALCIUM SILICATE CEMENT AS A RA-DDS

5.1 RA-added CSC material characterization

Both CSC setting time (Fig. 5.1) and compressive strength (Fig. 5.2) were adversely affected by the addition of RA beyond 0.5%. CSC with 1.0% RA had the average setting time about twice that of RA-free CSC and their mean compressive strength was less than 1 MPa. However, CSC containing 0.1% RA was barely affected, whereas those containing 0.5% RA had perceivable longer setting time and lower strength than RA-free CSC. XRD analysis (Fig. 5.3) and Rietveld refinement (Table 5.1) were conducted to explain the RA effect on cement properties. Since CH is one of the hydration products which is well crystallized, following development of CH peaks indicates the progress of hydration of the CS to CH and thus formation CSH gel (which is poorly crystallized and difficult to follow precisely through XRD data). It is seen in Fig. 5.3 that CH intensity progressively decreases with RA content increase, indicating that the CSH gel, responsible for the progress of setting and mechanical properties development of cement, was much lower (3.6%) in the highest RA sample than the RA-free sample (20.8%). SEM micrographs in Fig. 5.4 confirm the XRD results. In CSC10R sample in Fig. 5.4d, unlike CSC or CSC01R (Fig. 5.4a or b), CSH gel particles appeared to be much smaller in size, i.e., mostly smaller than 3 μm. Gel structures became less connected from CSC to CSC05R (Fig. 5.4a to Fig. 5.4c) and completely disconnected in CSC10R (Fig. 5.4d).

The RA, however, seemed to be homogeneously distributed in the entire cement pellet, based on FTIR scans performed both on the outer and inner surfaces of a pellet (Fig. 5.5).

Table 5.1: Quantitative analysis of the crystalline phases of CSC, CSC01, CSC05R and CSC10R after 7 days of setting using the Rietveld refinement.

Sample Name	Mineral Phase Quantity (%)				
	Dicalcium Silicate (Ca_2SiO_4)	Tricalcium Silicate (Ca_3SiO_5)	Portlandite ($Ca(OH)_2$)	C-S-H gel ($CaO{\cdot}SiO_2{\cdot}H_2O$)	Total
CSC	48.5	14.8	15.9	20.8	100
CSC01R	49.6	15.7	20.1	14.6	100
CSC05R	53.0	19.5	19.3	8.2	100
CSC10R	53.4	29.2	13.8	3.6	100

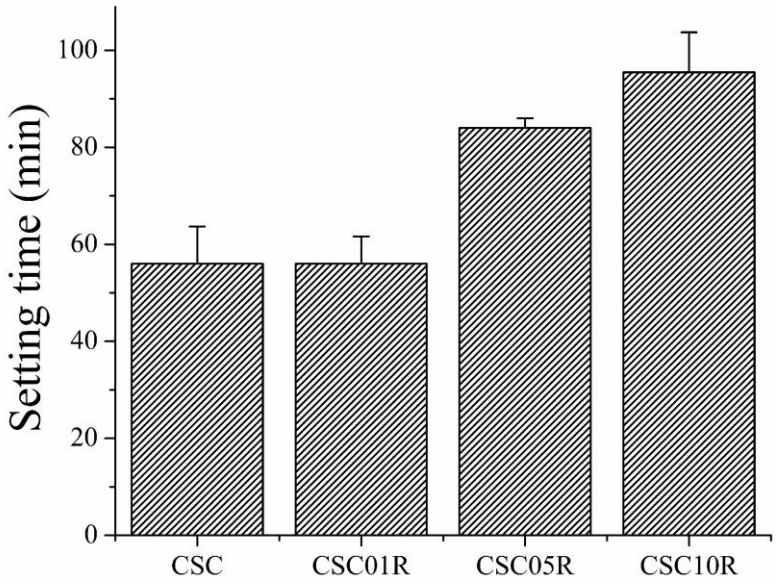

Figure 5.1: Setting times of risedronate-added and risedronate-free CSC as a function of risedronate concentration (*n* = 4).

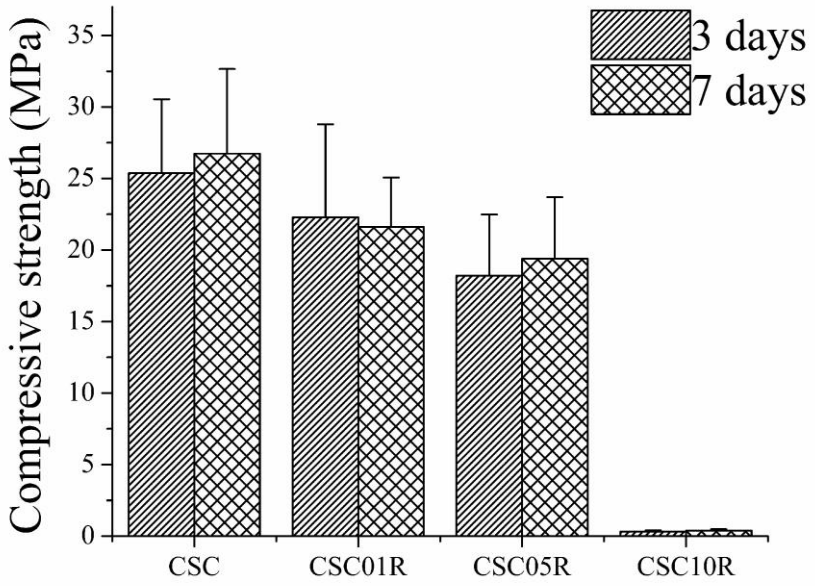

Figure 5.2: Compressive strength changes as a function of risedronate concentration (*n* = 10) after hardening for 3 and 7 days at 37 °C and 100% RH.

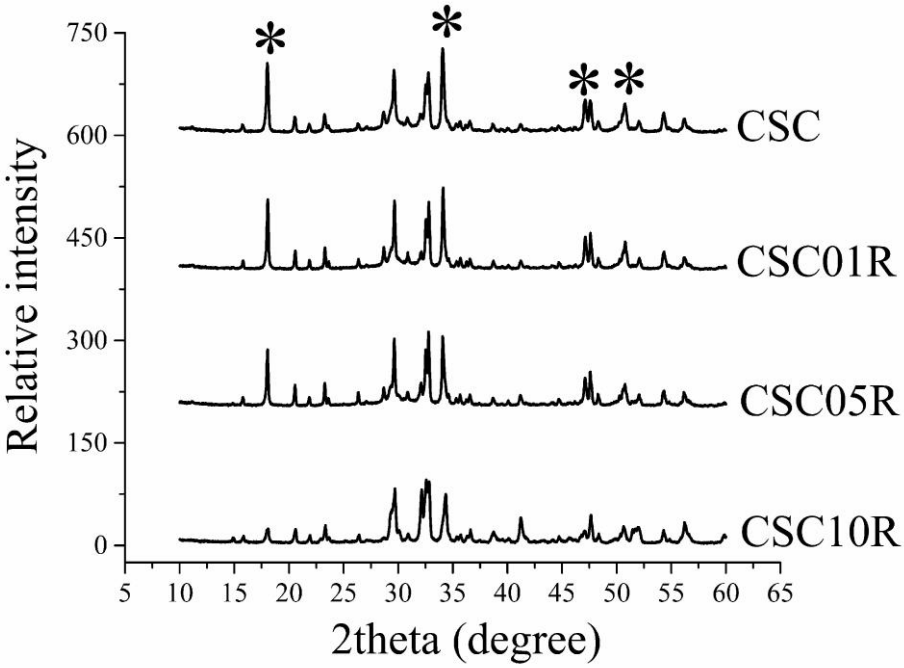

Figure 5.3: XRD patterns of CSC and risedronate-containing CSC01R, CSC05R and CSC10R after 7 days of setting. The characteristic $Ca(OH)_2$ peaks (*) are reduced with increasing RA amount. Unidentified peaks are primarily attributed to dicalcium silicate.

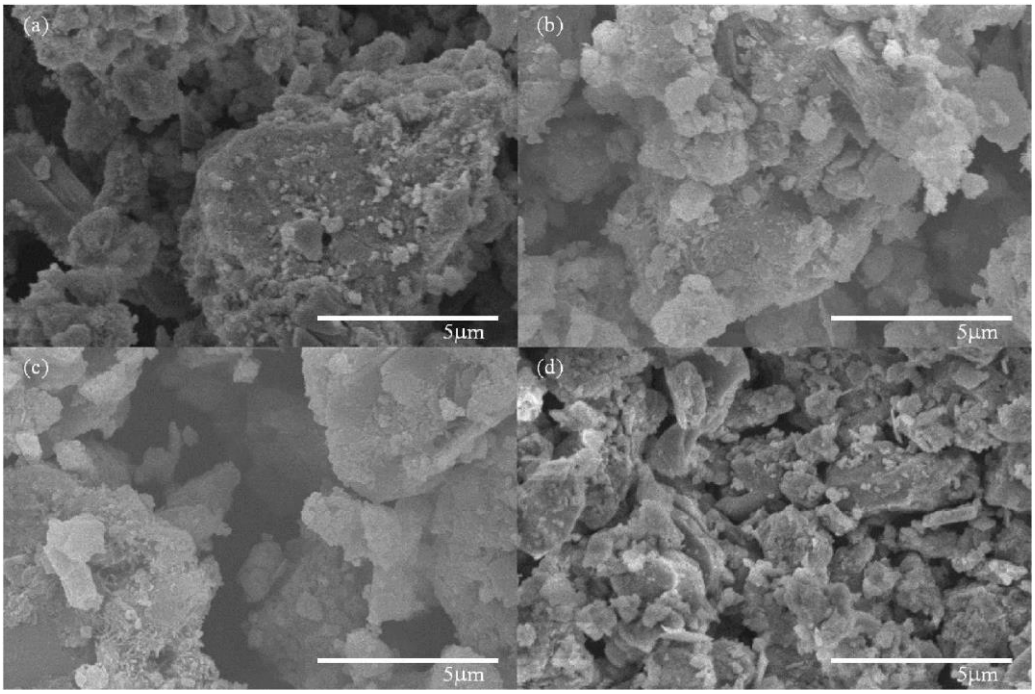

Figure 5.4: Scanning electron micrographs of CSC (a), CSC01R (b), CSC05R (c), and CSC10R (d) after 7 days of setting. One bar equals to 5 µm.

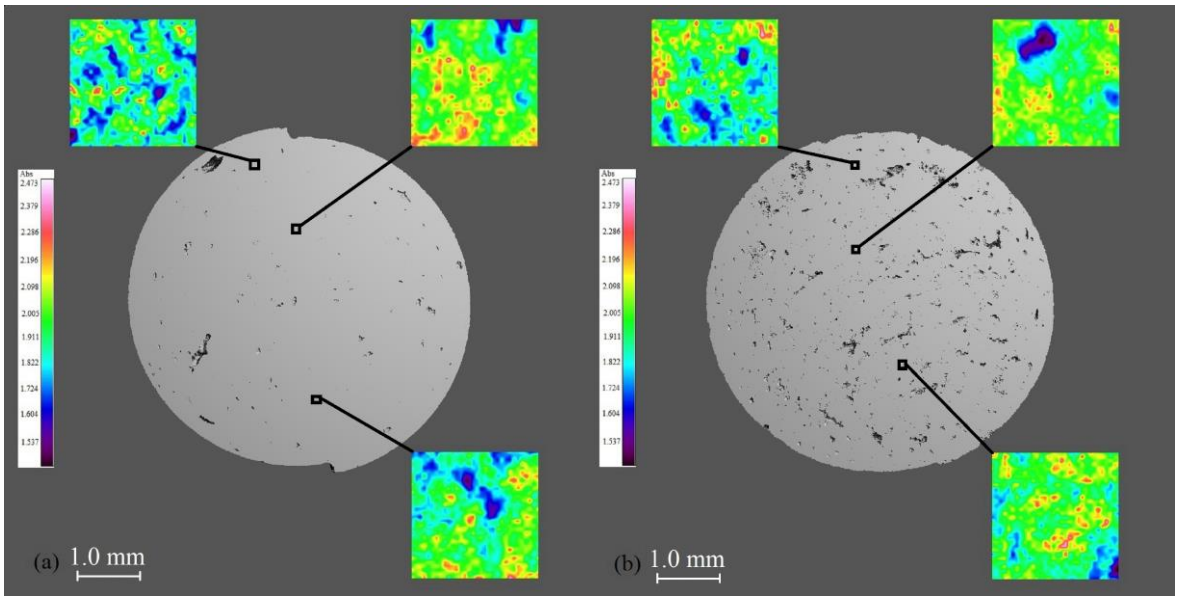

Figure 5.5: FTIR scans of both (a) outer and (b) inner surfaces of CSC pellets with 10 wt% of RA. Characteristic peaks of POO^- stretching at 960 cm^{-1} are used to plot RA distribution (red spots). Each IR image represents an area of 10 µm × 10 µm. One bar equals to 1 mm.

5.2 Release kinetics of RA from CSC

FTIR spectra (Fig. 5.6) reveal that the phosphonate group (POO^-) which stretches at 951 cm^{-1} and 887 cm^{-1} in RA, shifts to higher wavenumbers of 893 cm^{-1} and 999 cm^{-1} in calcium-RA complexes, in agreement with previous infrared studies of metal-RA ligands [184]. In the 10% RA-CSC sample, POO^- stretches at 937 cm^{-1} and 879 cm^{-1} indicate that RA formed calcium salts in hydrated cements [184]. Therefore, it is anticipated that RA calcium (RAC) instead of RA had been leached from the CSC-RA samples. In order to apply Higuchi's equation to analyze our release results, the solubility of RAC and cement tortuosity must be known. The solubility of RAC, $C_{RAC,}$ was measured by HPLC as 2.3×10^{-4} g/mL, equivalent to 7.165×10^{-4} M. The average tortuosity was calculated based upon average porosity and listed in Table 5.2.

Table 5.2: Average porosity and tortuosity of each sample. Standard deviation is given in brackets (*n* = 4).

	Sample Name			
	CSC	CSC01R	CSC05R	CSC10R
Porosity (ε)	0.103 (0.008)	0.114 (0.003)	0.091 (0.016)	0.070 (0.001)
Tortuosity (τ)	3.164 (0.009)	3.176 (0.003)	3.150 (0.019)	3.122 (0.001)

The cumulative release profiles (Fig. 5.7) reveals that the release of RA is proportional to the initial content of RA in the CSC (Fig. 5.7a). Only the two highest RA concentrations showed an initial burst release, followed by a slow release phase beyond the first 2 days. As a fraction of the incorporated amount of RA, CSC05R showed the largest release (9.3% cumulative on day 28), followed by CSC01R with a release of 7.6% on day 28, and finally followed by CSC10R with a release of 6.3% on day 28. In the long-term, RA continued to be leached out from the cement pellets at a very slow rate, increasing by about 1% over the next 5 months.

Figure 5.8 demonstrates that RA strongly adsorbs on hydrated CS. After adding milled hardened CSC powders to a saturated RA solution, the RA concentration dropped to zero within 24 hours. Fig. 5.8 also shows that the desorption of RA from CS is too low to be detected by HPLC.

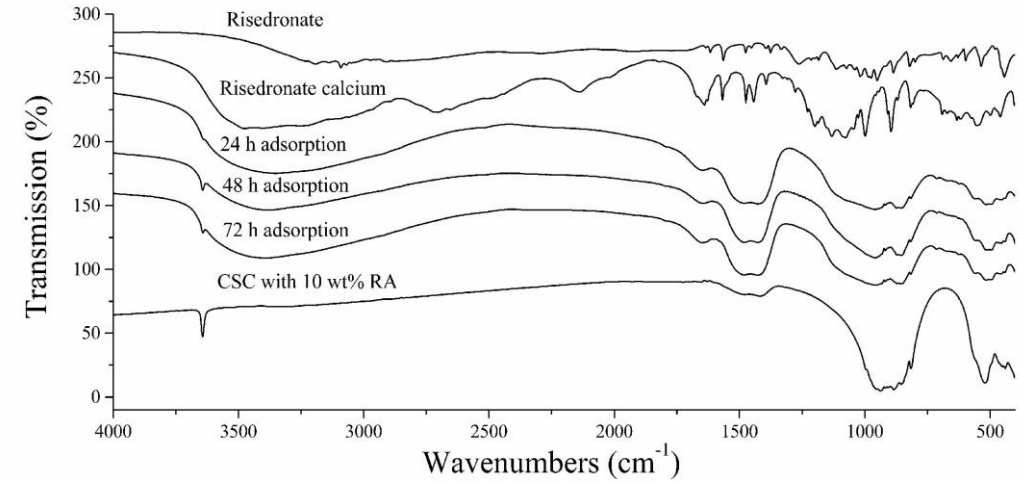

Figure 5.6: FTIR spectra of risedronic acid, risedronate calcium and calcium silicate cement sample with 10% risedronic acid preloaded. Sample powders were mixed (4 wt%) with dehydrated KBr and compressed into tablets.

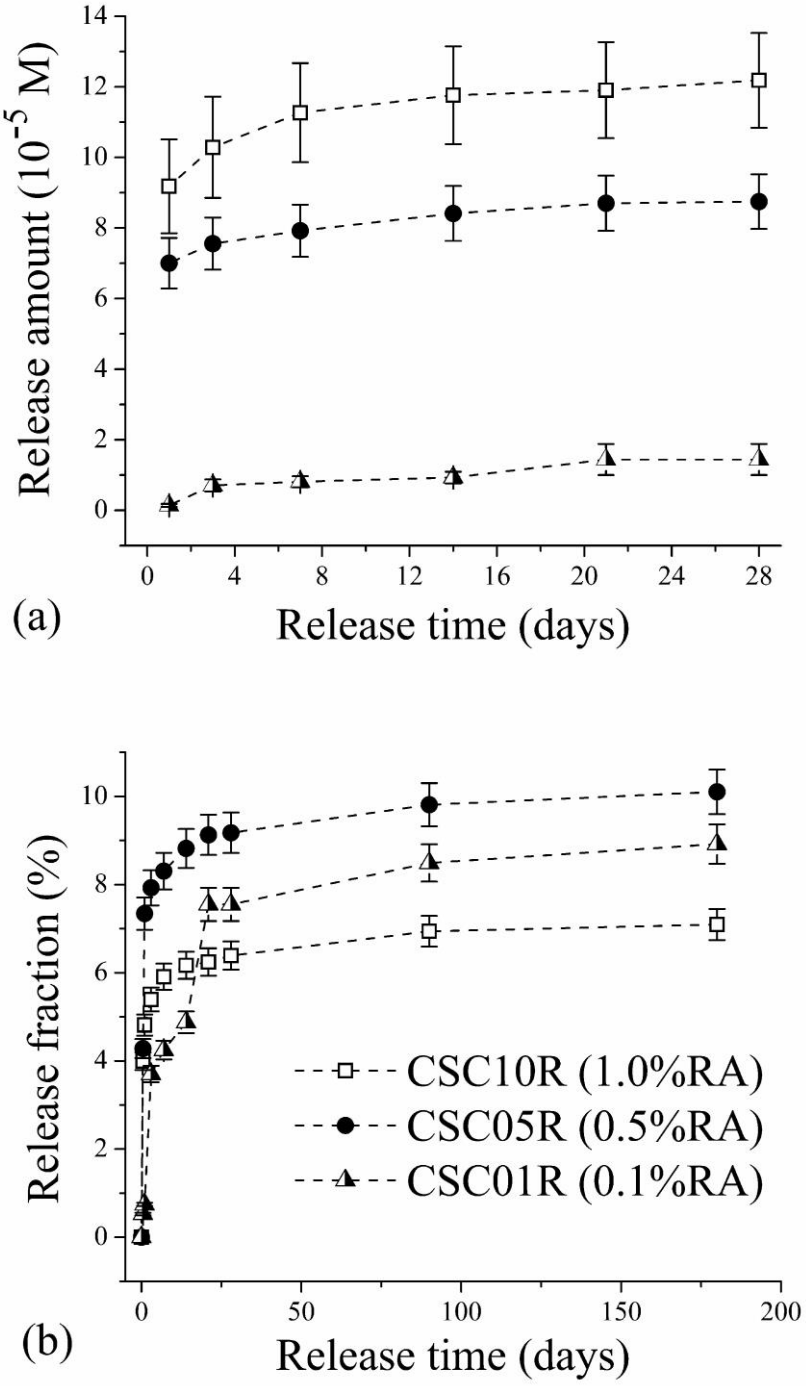

Figure 5.7: RA release curves of CSC01R, CSC05R and CSC10R in PBS up to 28 days in molar units (a) and up to 6 months as a fraction of the total initial RA amount (b).

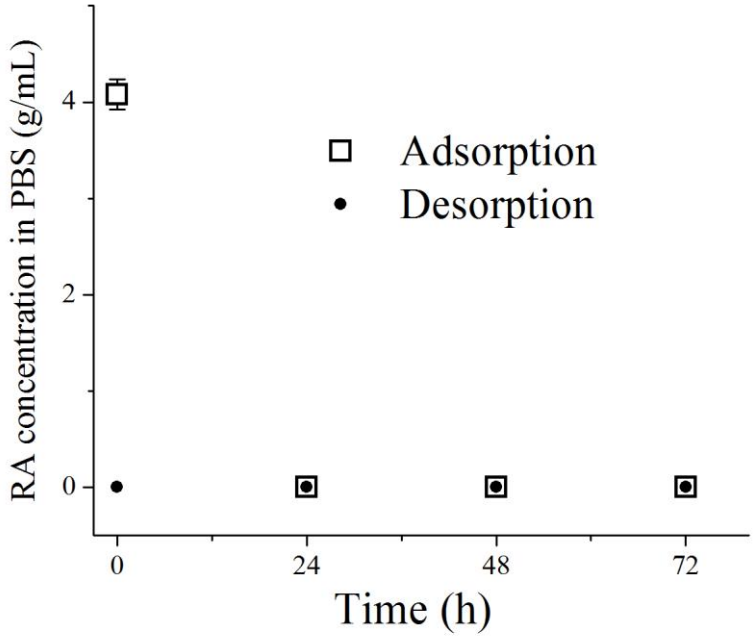

Figure 5.8: RA adsorption onto hardened CSC after milling in RA saturated PBS solutions and RA desorption from these samples in PBS (*n* = 3).

5.3 Biocompatibility of the RA-containing CSCs

Figure 5.9 clearly shows that the osteoblast cells were not negatively impacted by the RA and/or other compounds released into the incubation media. Cell viability of all RA-containing CSC samples was not significantly reduced compared to the control and close to 100% cell viability. According to the ISO10993-5 standard, a relative viability reduction of less than 30% is considered safe and biocompatible. The tested RA-containing CSCs thus seem to be safe and biocompatible.

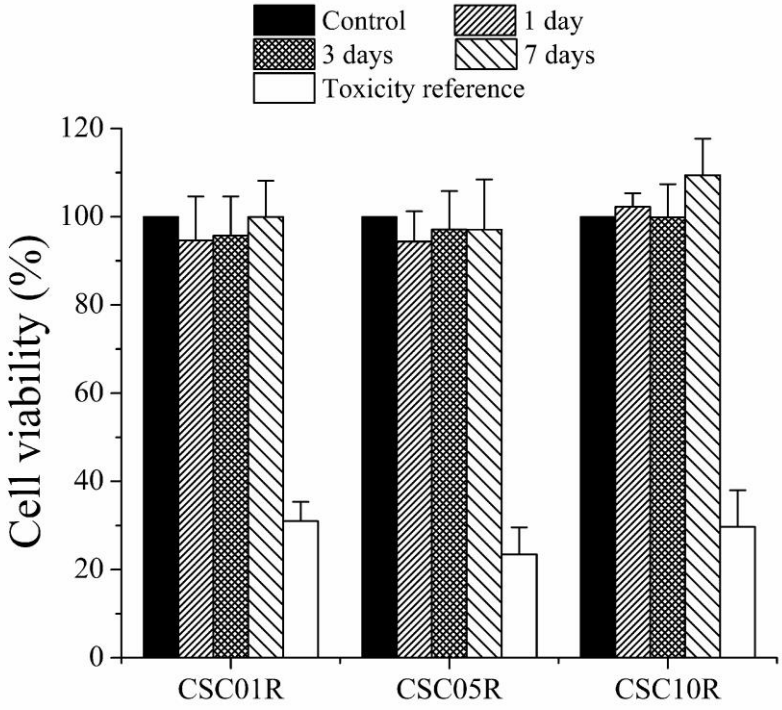

Figure 5.9: Cell viability of osteoblast cells after incubation with the extracts of the different cements collected after 1, 3, and 7 days. Drug-free PBS served as the control, whereas 60 mg phenol/mL of media was used as the toxicity reference. The relative viability was calculated as optical density 570 (OD_{570}) of treatment group/OD_{570} of the control group.

5.4 Discussion

The setting time and compressive strength data clearly demonstrates that RA modifies CSC hydration mechanism. These effects were also witnessed by other researchers and attributed to RA high affinity to calcium ions [46-48, 54, 116, 185]. However, RA has a limited impact on CSC cement properties below 0.5%, and a negligible impact at 0.1%. XRD and Rietveld refinement analyses demonstrate that CSH gel, the phase providing mechanical strengths to hydrated CSC cements, decreased with increased RA amount, implying that RA hinders the hydration reaction. It appears that semi-crystalline CSH gel particles (Fig. 5.5) are reduced in size and became disconnected in the samples with higher RA concentration, e.g., CSC10R. These morphological changes support the loss of mechanical properties of CSC rich in RA. The IR spectrum (Fig. 5.6) of the hardened CSC samples with 10% RA is notably different from that of pure RA or RAC ($Ca_2C_7H_9NO_7P_2$), which was obtained by reacting RA with $CaCl_2$ solution. This implies that the formation of risedronic calcium complexes in CSC is not a simple reaction with risedronic acid and CH. The subsequent adsorption/desorption tests proved this hypothesis. Within 24 hours of immersion of hardened CSC powders in RA saturated PBS solutions, RA was completely adsorbed onto CSH gels, the hydrated product of CSC. Similar results have also been observed between alendronate, another form of BP, and calcium deficient apatite [54]. RA-adsorbed CSC powders, however, have similar IR transmission spectra as CSC samples with 10% RA. These results indicate that RA is progressively adsorbed onto CSH surfaces, not only progressively inhibiting further growth and entanglement of CSH gels but also leading to a more complicated RA-calcium complex structure, which is a stoichiometrically different and thermodynamically stable form of RAC ($Ca_2C_7H_9NO_7P_2$) [48, 186].

Table 5.3: Theoretical release fractions over 28 days based upon the tortuosity found in our samples between 3 and 4.

Tortuosity (τ)	Release Time (d)						
	0.5	1	3	7	14	21	28
3 (low)	2.77%	3.91%	6.73%	10.19%	14.27%	17.34%	19.89%
4 (high)	2.40%	3.39%	5.84%	8.85%	12.41%	15.10%	17.34%

The release of RAC increased with RA concentration in agreement with previous findings for similar CPC-based DDS [107]. Fractional releases of RAC from CSC, however, were much lower compared to the previous results for CPC or other apatites [187, 188], where more than 20% of alendronate was released after 3 weeks. In contrast, another study reported that the cumulative zoledronate release from commercial HA and CPC was in the 10^{-6} M range [189].These opposing results may be attributed to different inorganic phases and BPs loading methods used in these studies, and also to vastly different detection methods. The longer term cumulative release, however, was similar between these studies and our study – the drug release after one month had plateaued [187-189]. Our long-term fractional release curve (Fig. 5.7b) showed only a 1% increase beyond 30 days.

As determined previously (and confirmed here) RA is toxic for concentrations above 10^{-5} M to osteoblast cells [141], and the high release rate may provide local RA concentrations above the toxicity limit. Since osteoporosis is a chronic disease and requires a continuous long-term treatment plan [190], release must be slowed down to match the therapeutic index. One way of doing this is by increasing tortuosity. However, the change of tortuosity values is negligibly small (Table 5.2) compared to release time in the Higuchi's equation and is therefore expected to have very limited impacts on release kinetics. The release predicted according to 3D Higuchi's law (Table 5.3) reaches 10% in one week and keeps increasing afterwards. Actual releases seemed to cease at that level after one month. Higuchi's law assumes that there is abundant and

continuous dissolution of drugs. The solubility of RAC is 7.165×10^{-4} M, which is much greater than RA released concentration in PBS (Fig. 5.7a). This implies that low RA amount in PBS is not controlled by RAC solubility. Our adsorption/desorption test revealed RA can be strongly bonded to CSH gels and, once adsorbed, are very difficult to be detached from CSH surfaces. The removal of RA from CSH surfaces can be explained by the exchange between phosphate ions in PBS and phosphonate groups on RA [191, 192]. The displacement of RA by phosphate ions results into the gradual release RA into PBS. It is found that RA is homogeneously distributed within CSC pellets (Fig. 5.8) and, therefore, only a small fraction of RA can be found on pore surfaces, where were accessible by PBS. Since hardened CSC is non-degradable within a short period, e.g. one year, RAC trapped inside cement matrices cannot be reached by PBS without matrix degradation. Therefore, only pore-surface adsorbed RAC can be displaced by phosphate ions in PBS and responsible for the release and the rest of RAC is still trapped inside cementitious matrix until the degradation takes place. It is known that chronic diseases, such as osteoporosis, need long-term treatment, but sometimes patients are not willing to comply with administrations [193]. Implanted RA-added CSC system, based upon current release studies, could be capable of delivering RA for the long-term treatment of osteoporosis. Furthermore, it will increase patient compliance since it does not require patients' active involvement in RA administration.

RA toxic levels on osteoblast cells and releasing curves are well correlated. Sun *et al.*'s recently showed that BPs above 10^{-5} M are toxic to cells, and that the safe range is between 10^{-6} M and 10^{-8} M [141]. In our present study, the RA concentrations in the MTT assays were between 0.003×10^{-5} M and 0.225×10^{-5} M, which are well below the toxic level (10^{-5} M) and within the safe range (10^{-6} M~10^{-8} M). Our study indicates that RA-loaded CSC can be

biocompatible if the system is engineered to deliver RA at local concentrations well below the toxic limit. It is expected that the normal blood flow and diffusion reduces local RA concentrations rapidly *in vivo* below such toxic concentrations. Therefore, in the future, *in vivo* pharmacokinetics and pharmacodynamics tests should be conducted in implants to determine local (near the implant) and systemic (in the body) RA (or RAC) concentrations, and further implementations may be needed to improve the design to better fit clinical requirements.

Chapter 6: RESULTS AND DISCUSSION II: CPSC EFFECTS ON OSTEOBLASTIC PROLIFERATION AND IN VIVO OSTEOGENESIS

6.1 CPSC material characterization

Both setting time and compressive strength of CPSC decreased with MCP content, as shown in Fig. 6.1, indicating an increasing setting rate and hydration reaction with the higher MCP content. The average strength of CPSC15 was approximately one third of CPSC5's, implying that MCP has a profound impact on CSC hydrations. Crystalline structures of hardened cement were analyzed by XRD (Fig. 6.2a) and Rietveld refinement (Fig. 6.2b). Calcium hydroxide was produced during hydration and, unlike calcium silicate hydrate (CSH) gel, was more easily detectable from the XRD patterns. Calcium hydroxide progressively reacted with MCP to form hydroxyapatite and this reaction explained both the lower amount of calcium hydroxide present in higher MCP samples and the baseline broadening around 33° in Fig. 6.2a. It was also revealed that the time effects on the hydration were negligible: regardless of MCP content, calcium hydroxide or C_2S peak heights were invariable between 3-day and 7-day samples. Unlike C_3S reacting rapidly with water, C_2S tended to slowly hydrate and its amount was indifferent among these samples. FTIR peaks (Fig. 6.3) at 1477 cm^{-1} and at 1035 and 874 cm^{-1} correspond to OH deformations and Si-O-Si vibrations, respectively [194]. The OH deformation peak indicated that formation Si-OH group and its reflection decreased with MCP content. On the other hand, the double peaks at 1035 and 874 cm^{-1} refer to siloxane (Si-O-Si) bonds and the peak intensity at 1035 cm^{-1} increased with MCP content [194].

Microporosity (Fig. 6.4, and porosity was given in Table 6.1) was also found to increase with the MCP concentration and appeared more inter-connected in CPSC15 than in CPSC5. Similar effect observed previously was linked to *in situ* water release upon reaction of MCP with

calcium hydroxide during cement setting [31]. While this phenomenon appears to increase the final porosity of set cement (and consequently to decrease its strength), it is also providing additional water necessary for cement setting *in situ*, i.e., without the need for additional setting water. This may prove important when CPSC sets in confined spaces deficient in water.

Table 6.1: Porosity calculated from μCT visualization. Data are presented as mean value ± standard deviation. (*n* = 4)

	Sample		
	CPSC5	CPSC10	CPSC15
porosity	2.46% ± 0.54%	5.66% ± 0.49%	12.86% ± 8.24%

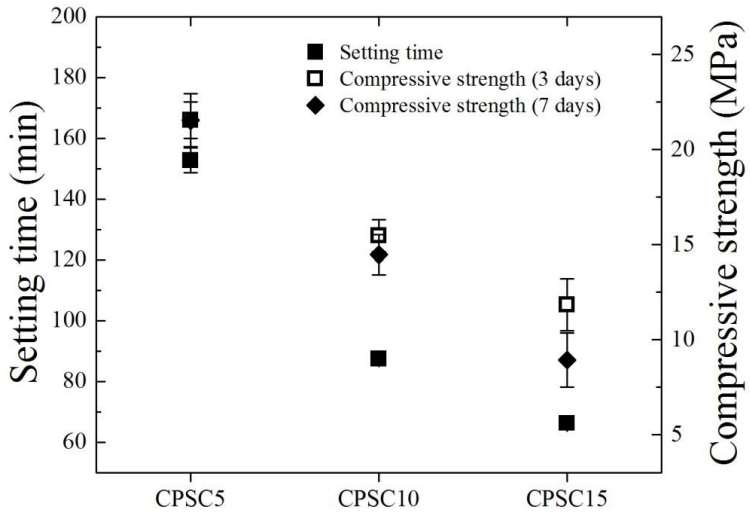

Figure 6.1: Setting times (*n* = 4) and compressive strengths (*n* = 8) of CPSC5, CPSC10 and CPSC15. Error bar represents one standard deviation.

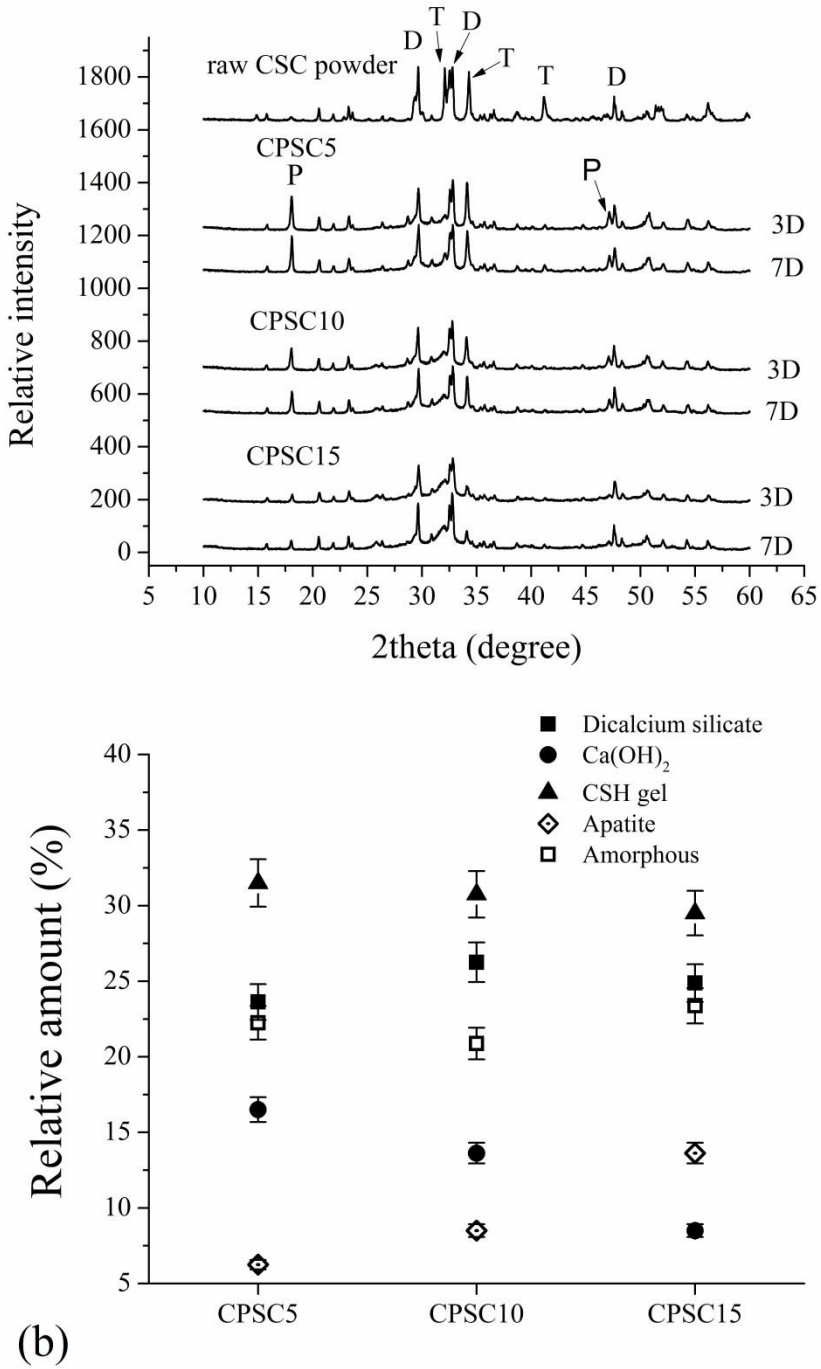

Figure 6.2: (a) X-ray diffraction (XRD) patterns of raw CSC powder, CPSC5, CPSC10 and CPSC15 samples after 3 and 7 days of hydration (*n* = 4). Peaks of calcium hydroxide (P), tricalcium silicate (T) and dicalcium silicate (D) are identified. (b) Rietveld refinement analysis of CPSC5, CPSC10 and CPSC15. Error bar represents 95% confidence interval.

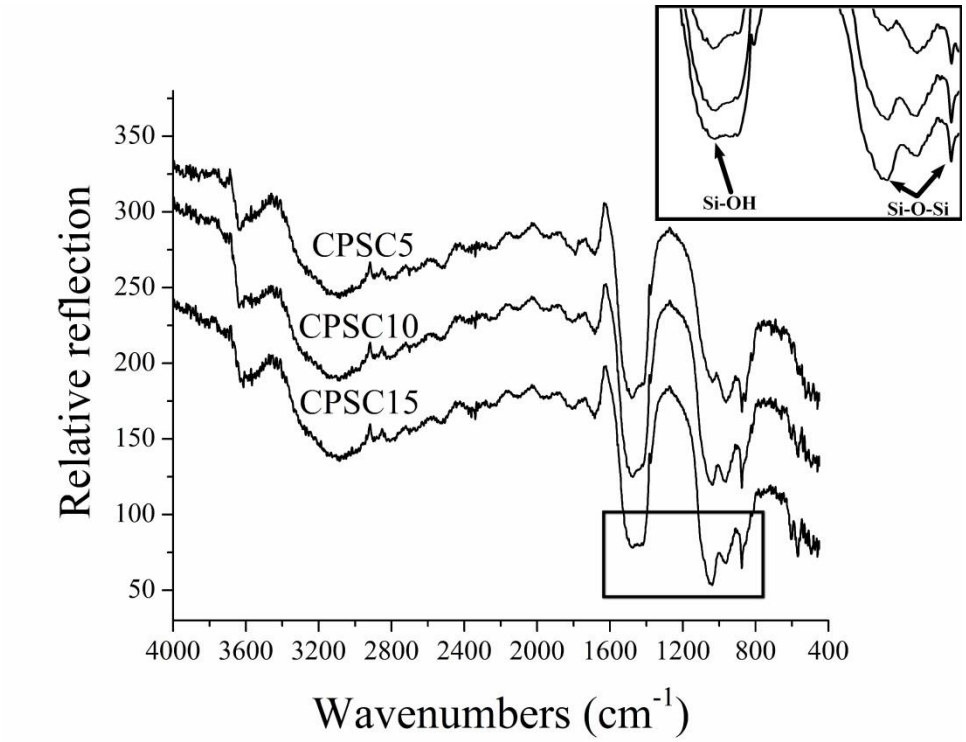

Figure 6.3: Fourier transformation infrared (FTIR) spectra of CPSC5, CPSC10 and CPSC15 samples after 7 days of hydration.

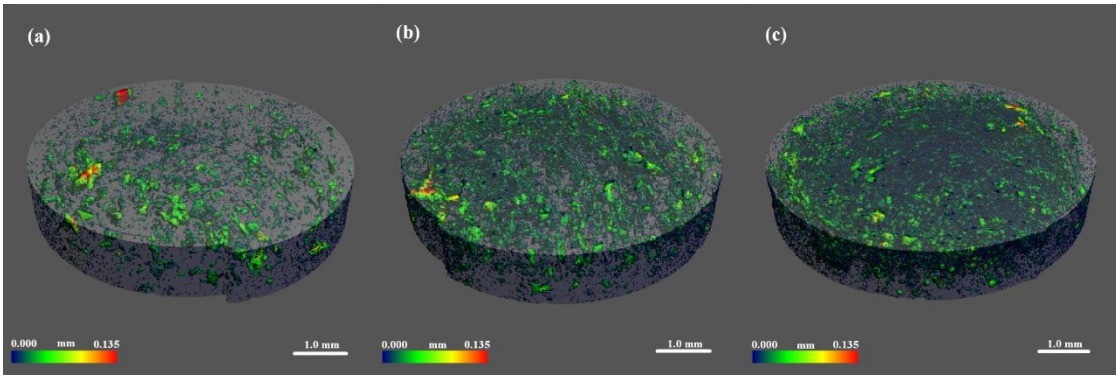

Figure 6.4: µCT scans of 1 cm height sections of hardened CPSC to reveal their microstructure and macroporosity: (a) CPSC5; (b) CPSC10; (c) CPSC15 (*n* = 4). The color bar represents the diameter of pores, from 5 µm for the smallest pores in blue (µCT resolution limit), to 135 µm for the largest pores in red.

6.2 *In vitro* analysis of CPSC biocompatibility

Cytotoxicity results shown in Fig. 6.5 clearly indicate that CPSC extracts significantly increased osteoblast cell viabilities as compared to CSC extract. Regardless of the dilution levels, CPSC extracts had positive effects on osteoblast cell proliferation; however, at the lowest dilution level (50%), the CSC extracts slightly reduced osteoblast viability. Flow cytometry confirmed these results. Raw data (Fig. 6.6) of relative quantities of cells in each state within one cell cycle were analyzed by FCM and final results were compiled into the bar chart (Fig. 6.7). DNA diploids (double strands) are doubled after each cell cycle to accomplish the mitosis. In Fig. 6.7, cells treated by CPSC extracts tended to have larger quantity of tetraploid (DNA quadruple strands) than untreated cells. This data indicate that cell proliferation was enhanced by CPSC extracts. Threshold cycles of genes amplified by PCR were depicted in Fig. 6.8 and used to calculated relative gene expressions in Fig. 6.9. Genetic analysis (Fig. 6.9) shows the levels of expression of osteoblast-specific genes in osteoblast cells. The results were normalized with respect to the reference CSC sample by dividing the fold changes in the CSC-treated ones. It is found that the levels of expression of ALP and OPG genes in CPSC15 were statistically different from those in CPSC5 or CPSC10; however, runx2 and TGF-β expressions were statistically indifferent between CPSC5, 10 and 15. In addition, only TGF-β expressions in all three samples were above 1, indicating that the other genes were down-regulated in CPSC extracts compared to CSC extracts.

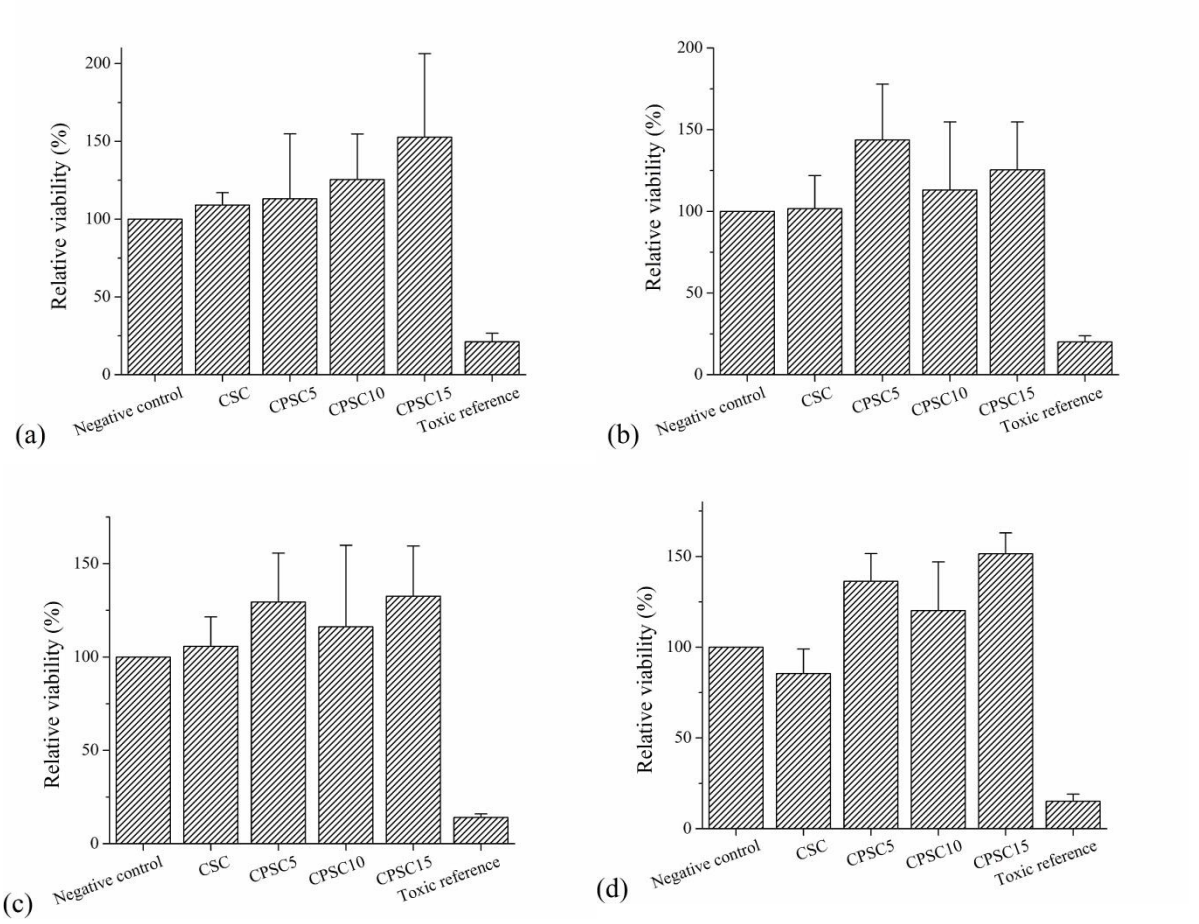

Figure 6.5: Relative viability of osteoblast cells incubated in CPSC5, CPSC10 and CPSC15 extracts for 3 days in different dilutions of (a) 5% (1:19); (b) 10% (1:9); (c) 20% (1:4); and (d) 50% (1:1). PBS with 10%-FBS in DMEM served as the control group, while an aqueous phenol solution was used as toxicity reference (n = 5). Error bars represent one standard deviation.
(a) The viability for CSC is only significantly lower than that for CPSC15; the viabilities for CPSC5, 10 and 15 are insignificantly different between each other. ($p < 0.05$)
(b) The viability for CSC is significantly lower than that for CPSC5; the viabilities for CPSC5, 10 and 15 are insignificantly different between each other. ($p < 0.05$)
(c) Viabilities for CSC, CPSC5, 10 and 15 are insignificantly different between each other. ($p < 0.05$)
(d)) The viability for CSC is significantly lower than those of CPSC5, 10 and 15; the viabilities for CPSC5, 10 and 15 are insignificantly different between each other, except of those between CPSC10 and 15. ($p < 0.05$)

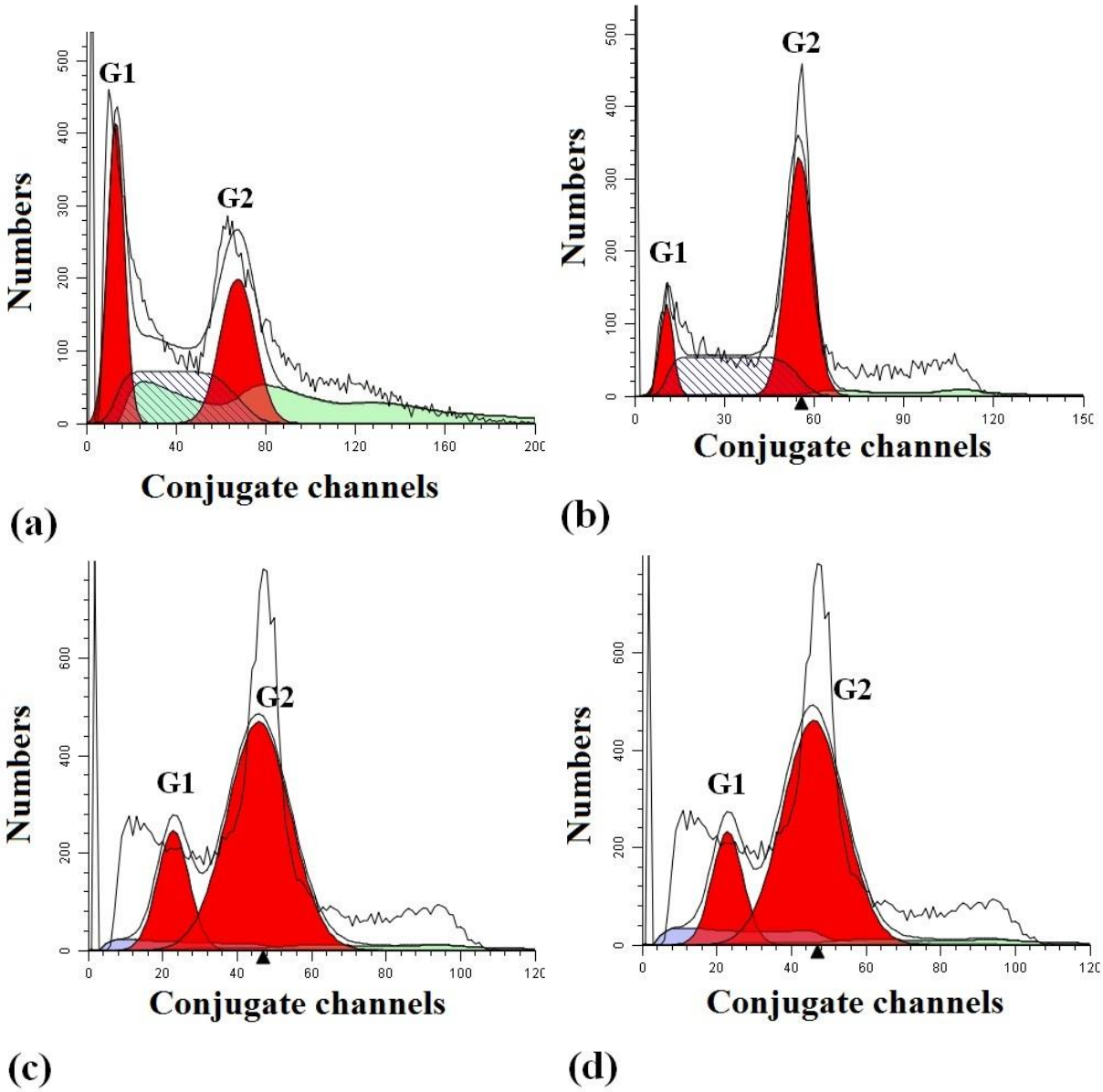

Figure 6.6: Representations of raw data of relative quantities of cells in each phase within one cell cycle analyzed by FCM. They are (a) the control, (b) CPSC5, (c) CPSC10 and (d) CPSC15.

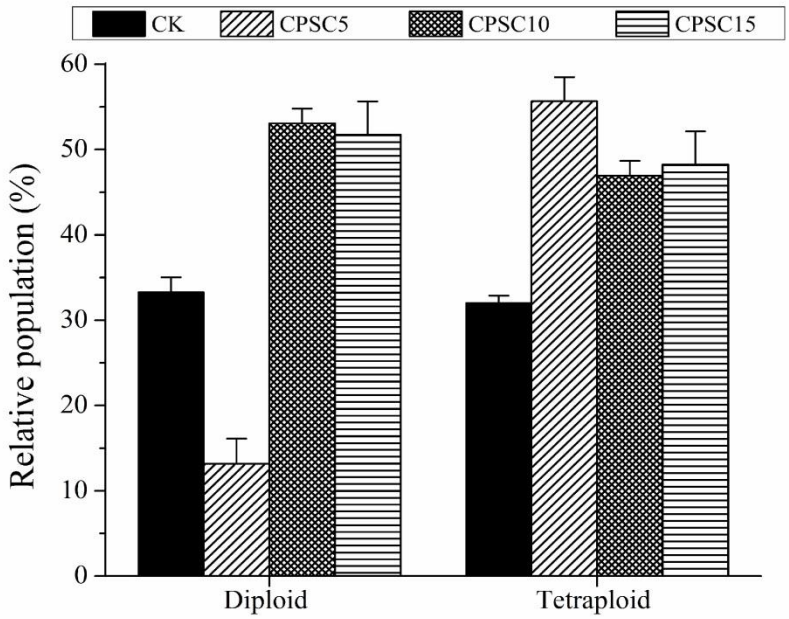

Figure 6.7: Fractions of diploid and tetraploid DNA strands in osteoblast cells. (n = 3) The relative quantity of tetraploid of CK is significantly lower than those of CPSC5 and CPSC10 but insignificantly lower than that of CPSC15. Relative quantities of CPSC 5, CPSC10 and CPSC15 are insignificantly different between each other. (p < 0.05) Error bar represents one standard deviation.

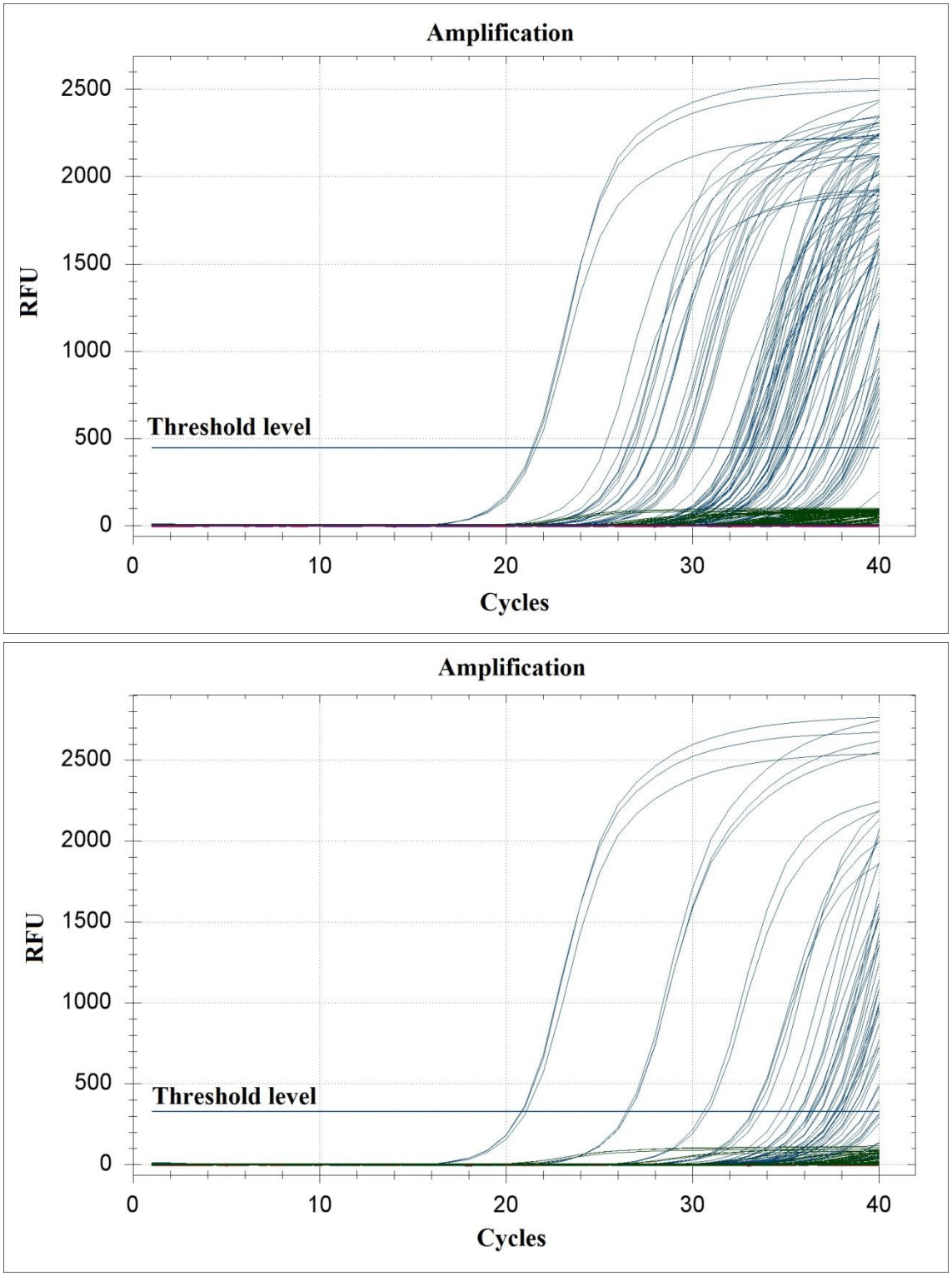

Figure 6.8: Representations of threshold cycles of genes amplified by PCR

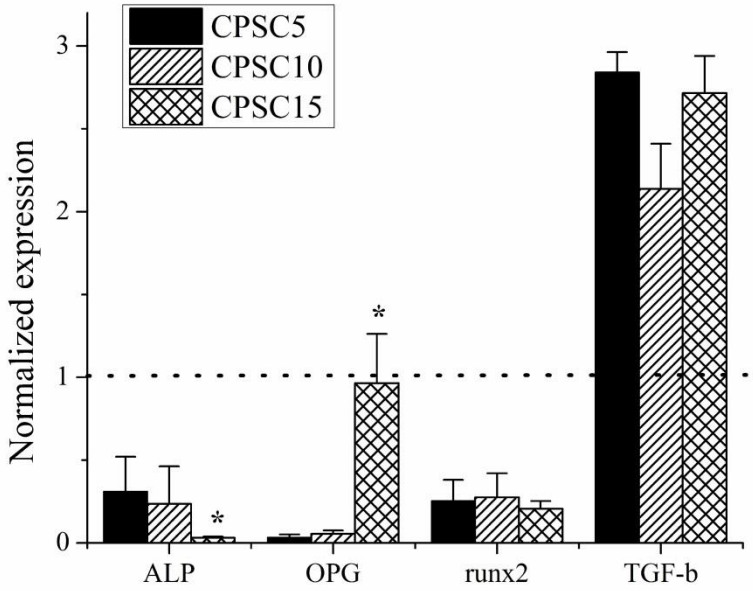

Figure 6.9: mRNA expressions of ALP, runx2, TGF-β, and OPG genes in osteoblast cells harvesting in CPSC extracts for 3 days (n = 8). All expressions were normalized to the expressions of CSC. The level of ALP expression in CPSC15 is significantly lower than those in CPSC5 and CPSC10; the level of OPG expression in CPSC15 is significantly higher than those in CPSC5 and CPSC10; the levels of runx2 and TGF-β expressions are statistically indifferent among CPSC5, CPSC10 and CPSC15. (*p* * < 0.05) Error bar represents one standard deviation.

6.3 *In vivo* analysis of CPSC osteogenic effects in rabbits

X-rays graphs (Fig. 6.10a and b) indicate that new trabecular bone was formed around and inside implants, implying that both CPC and CPSC were osteoconductive. However, CPSC appeared to degrade slower than CPC. Semi-quantitative analyses (Fig. 6.11a and b) provided support for such observations. It was shown (Fig. 6.11a) that both CPC and CPSC had *in vivo* degradation from 2 to 3 months; CPC *in vivo* degradation, however, was faster than CPSC and statistically significant ($p < 0.05$). On the other hand, new trabecular bone formation around and inside implants (Fig. 6.11b) appeared to be higher in CPSC than CPC and such osseointegration appeared to increase with time in CPSC samples. Contrarily, osseointegration of new bone formation appeared to decrease with time significantly ($p < 0.05$) in CPC. The above

observations strongly indicated that CPSC appeared to be more osteoconductive than clinical CPC. CT scans further proved the results of semi-quantitative analyses. As indicated in Fig. 6.13, both CPC and CPSC promoted some new trabecular bone formation around remnant implants after 2 months of implantation; however, at the end of 3 months, Fig. 6.14, CPC resorbed faster than CPSC. In addition, all CPSC samples showed significant trabecular bone formation around and inside remnant materials; CPC, however, became isolated from cortical bones, in between there was much less new trabecular bone formed. Histological studies (Fig. 6.15) showed that layered bone matrix deposition was witnessed in both CPC and CPSC samples, implying that CPSC was as osteoconductive as clinical CPC. After 3 months, neutrophil-based inflammatory cell infiltration was observed as well and an encapsulation of fibrous tissues composed of collagen fibers, fibroblasts and fibrocytes was also observed around perforation. Furthermore, some bone marrow tissues were replaced by adipose tissues. However, histological slides were unable to provide reliable information regarding the comparison between clinical CPC and CPSC in terms of bone formation and inflammation.

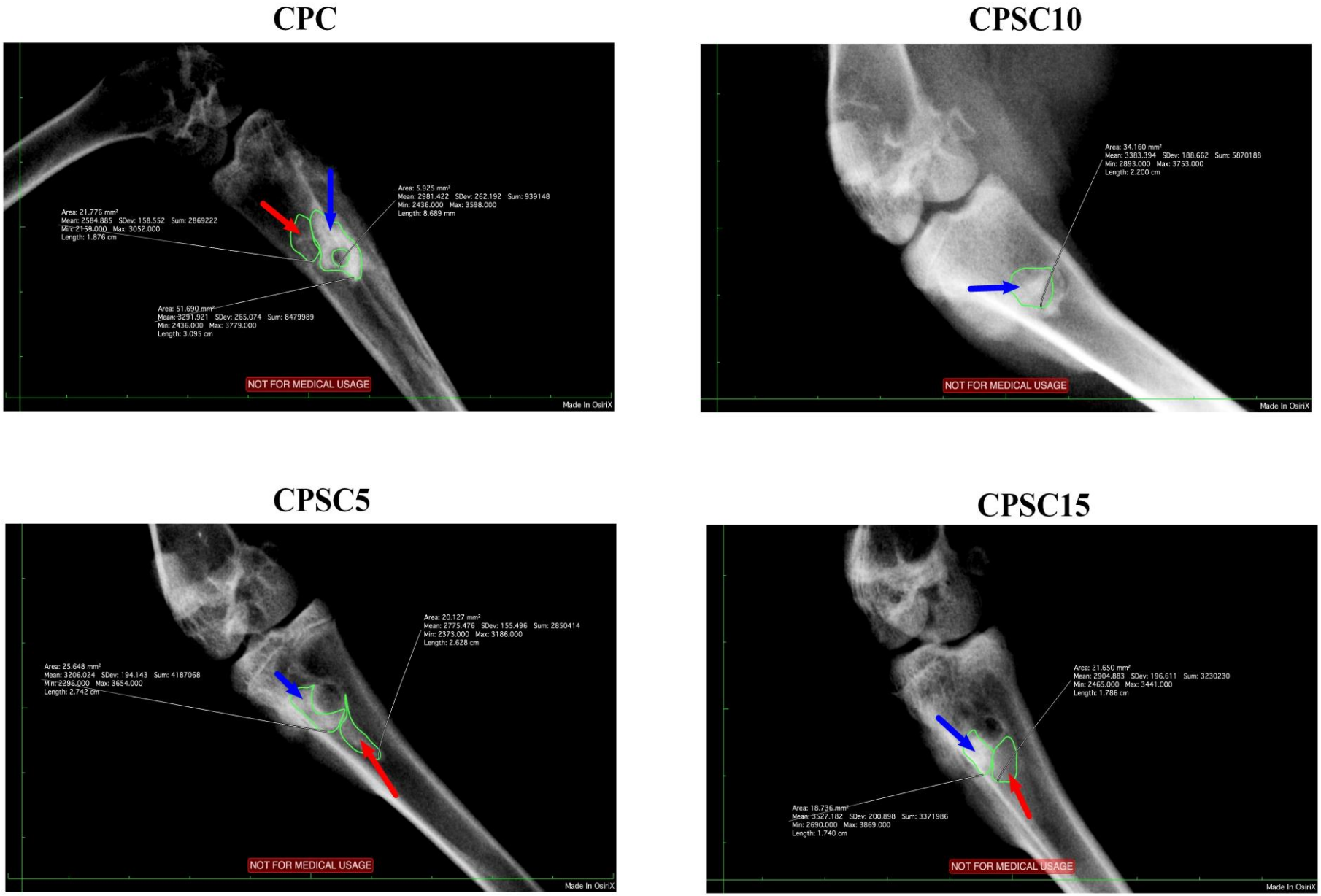

Figure 6.10: X-ray images of rabbit hind legs with cement implantation after (a) 2 months and (b) 3 months. One bar is equal to 1 cm. Regions of remnant cement (blue arrows) and new trabecular bone (red arrows) were enclosed by green curves and their areas were automatically measured by Osirix. These readings were used in semi-quantitative analyses

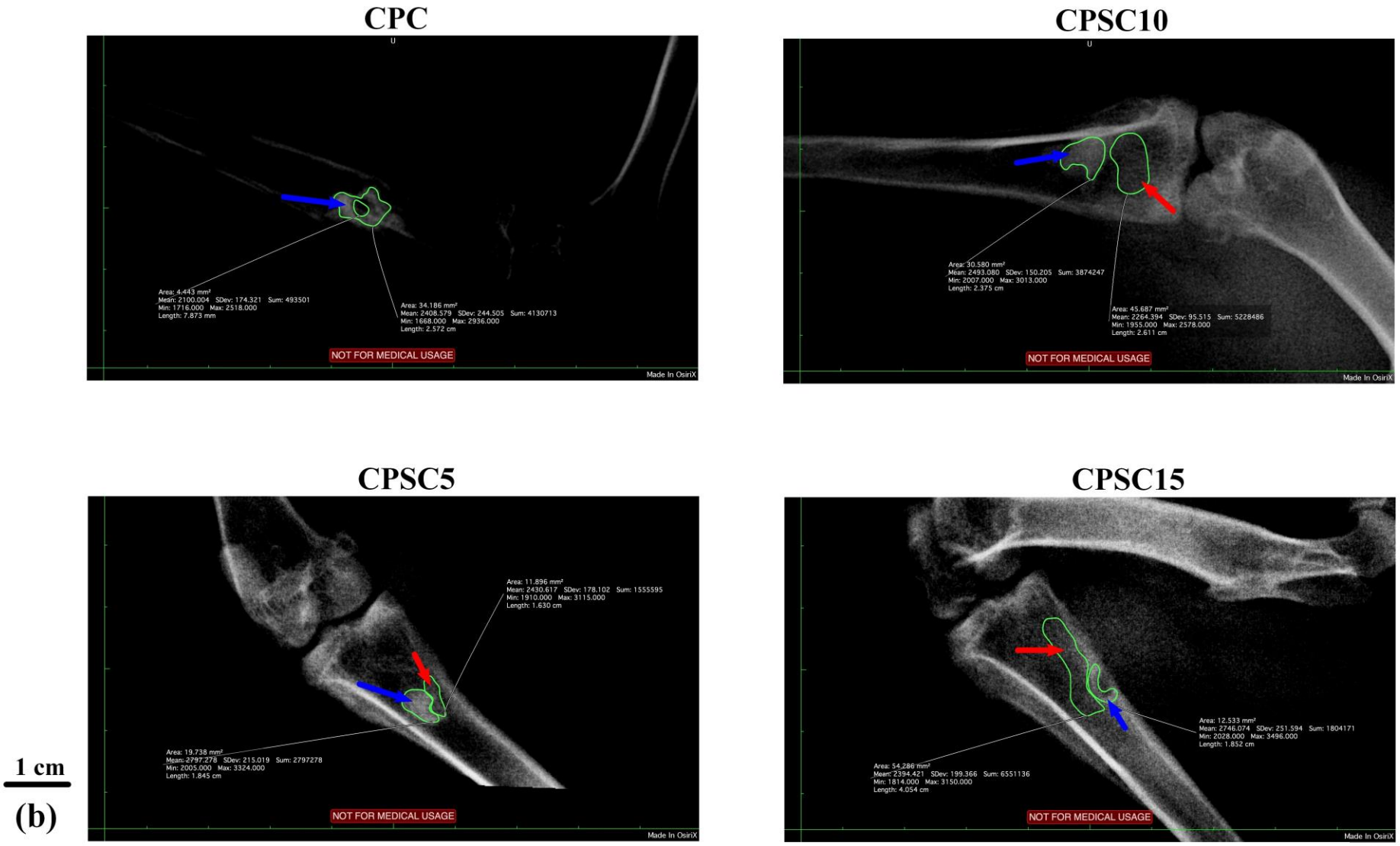

Figure 6.10 (continued): X-ray images of rabbit hind legs with cement implantation after (b) 3 months. One bar is equal to 1 cm. Regions of remnant cement (blue arrows) and new trabecular bone (red arrows) were enclosed by green curves and their areas were automatically measured by Osirix. These readings were used in semi-quantitative analyses.

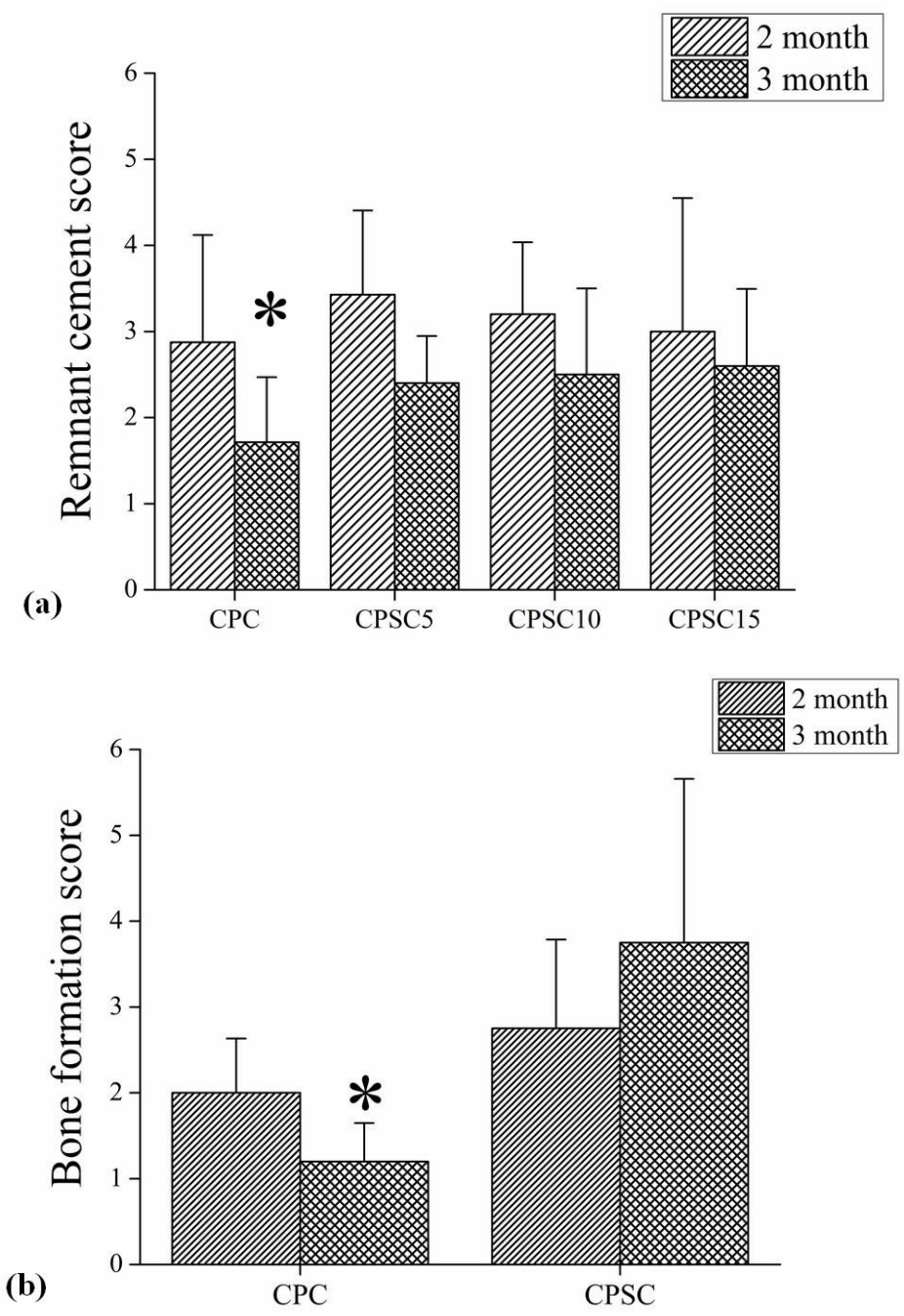

Figure 6.11: Calculate scores of (a) remnant cement from highly degraded (score 1) to mostly non-degraded (score 6) and (b) new trabecular bone formation from merely no bone formation (score 1) to significant formation (score 6) of CPSC and clinical CPC between 2 and 3 months (n = 7). Error bars represent one standard deviation. (p *< 0.05 *vs.* 2 month)

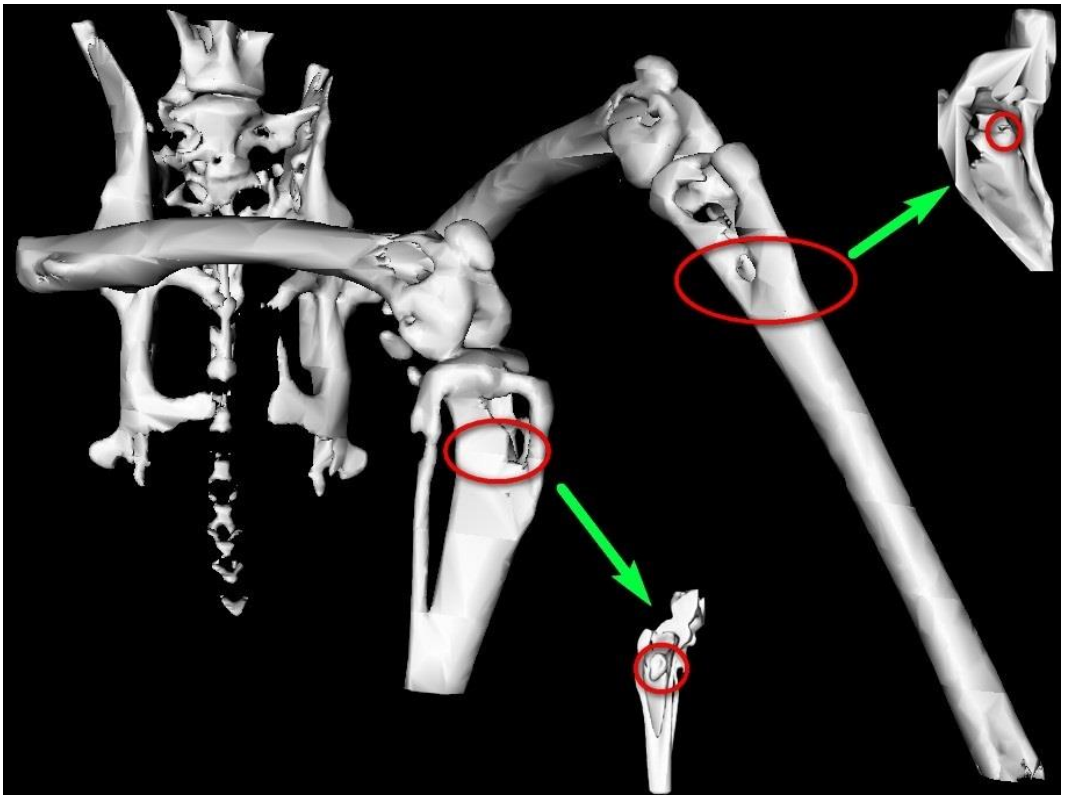

Figure 6.12: 3D reconstruction of implanted bones after 3 months (red circles indicate the remaining material)

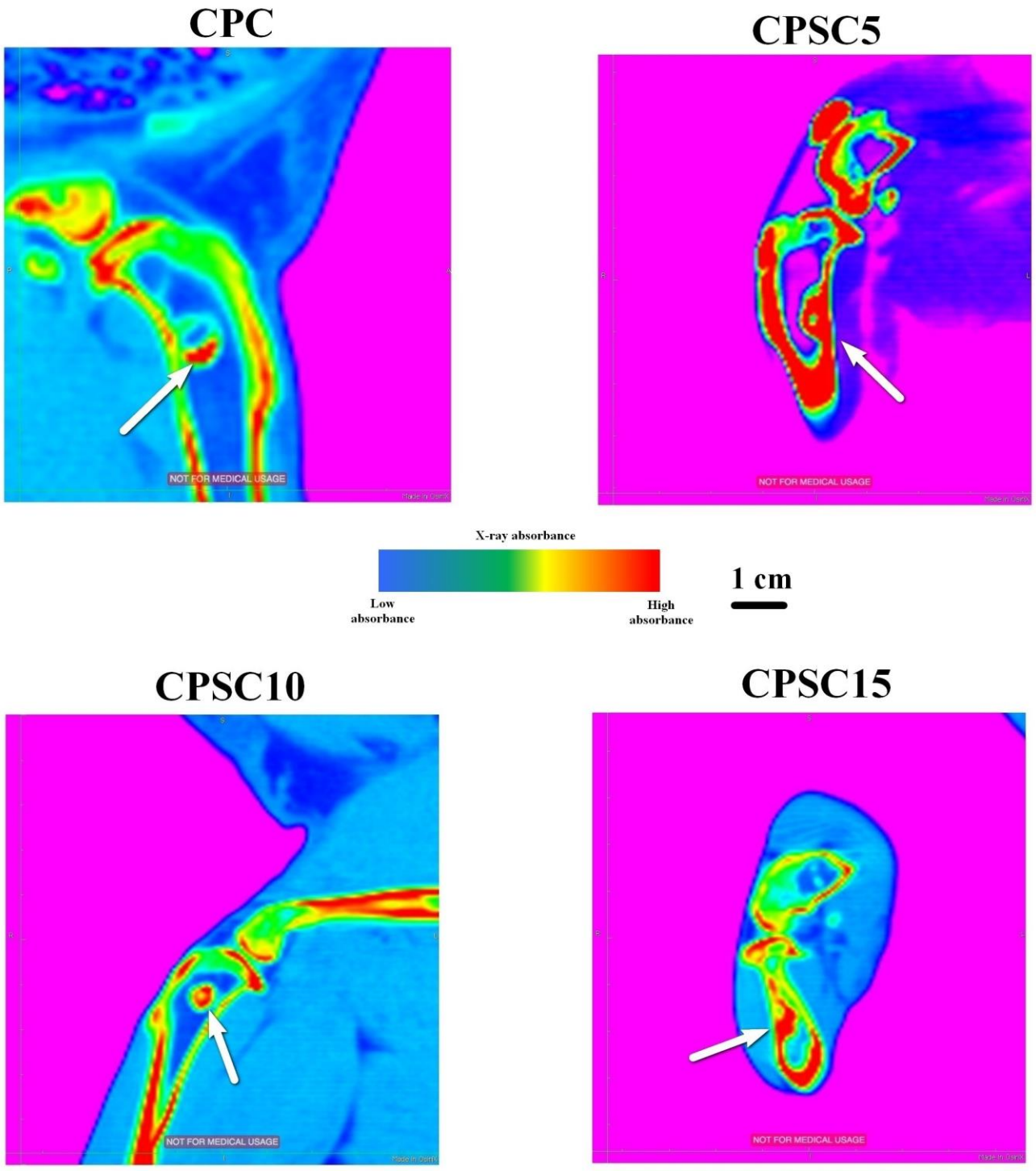

Figure 6.13: CT scans of rabbit hind legs after 2-month implantation. Trabecular bones and newly formed cortical bones are indicated in green. The size bar is equal to 1 cm.

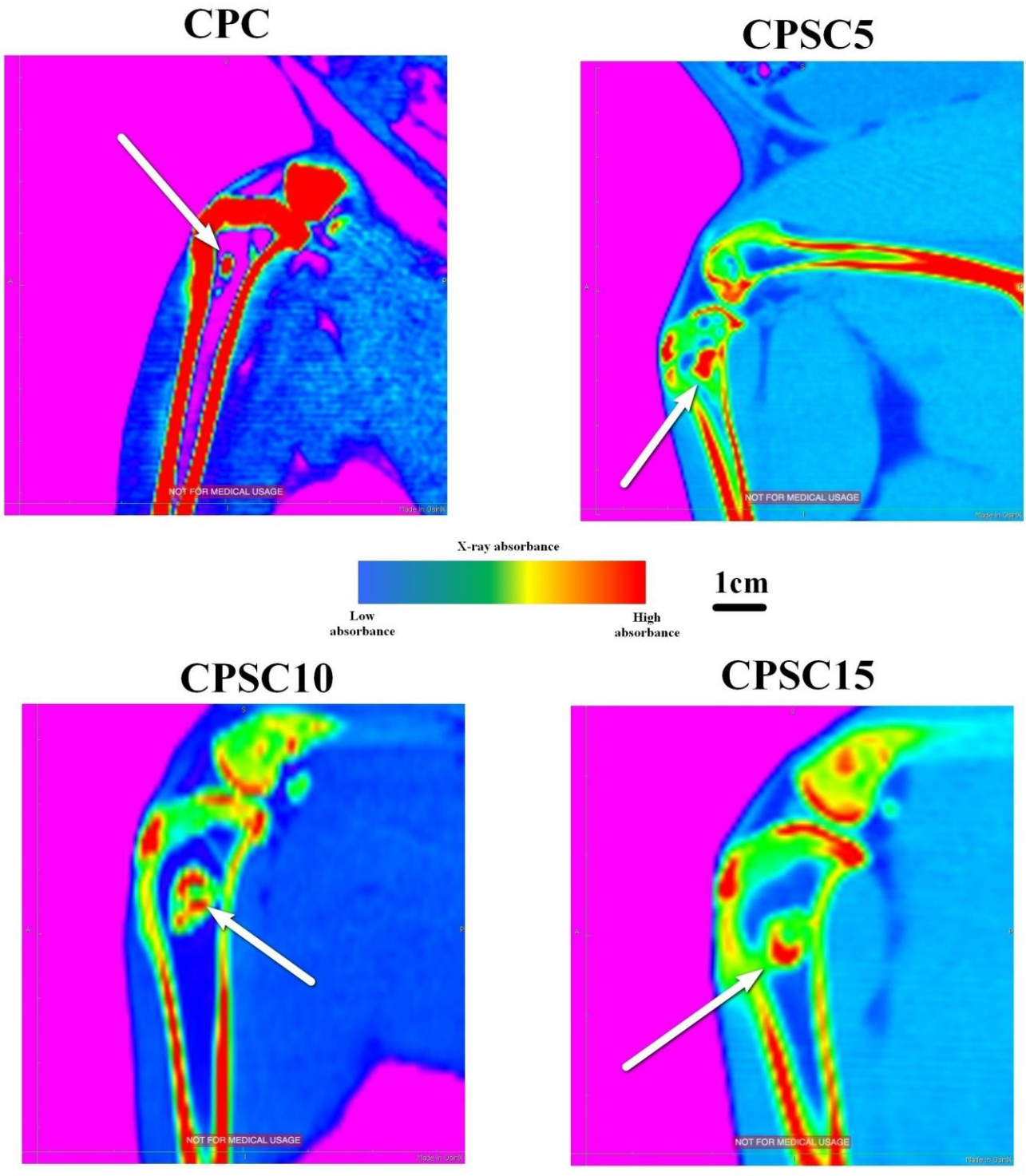

Figure 6.14: CT scans of rabbit hind legs after 3-month implantation. Trabecular bones and newly formed cortical bones are indicated in green. The size bar is equal to 1 cm.

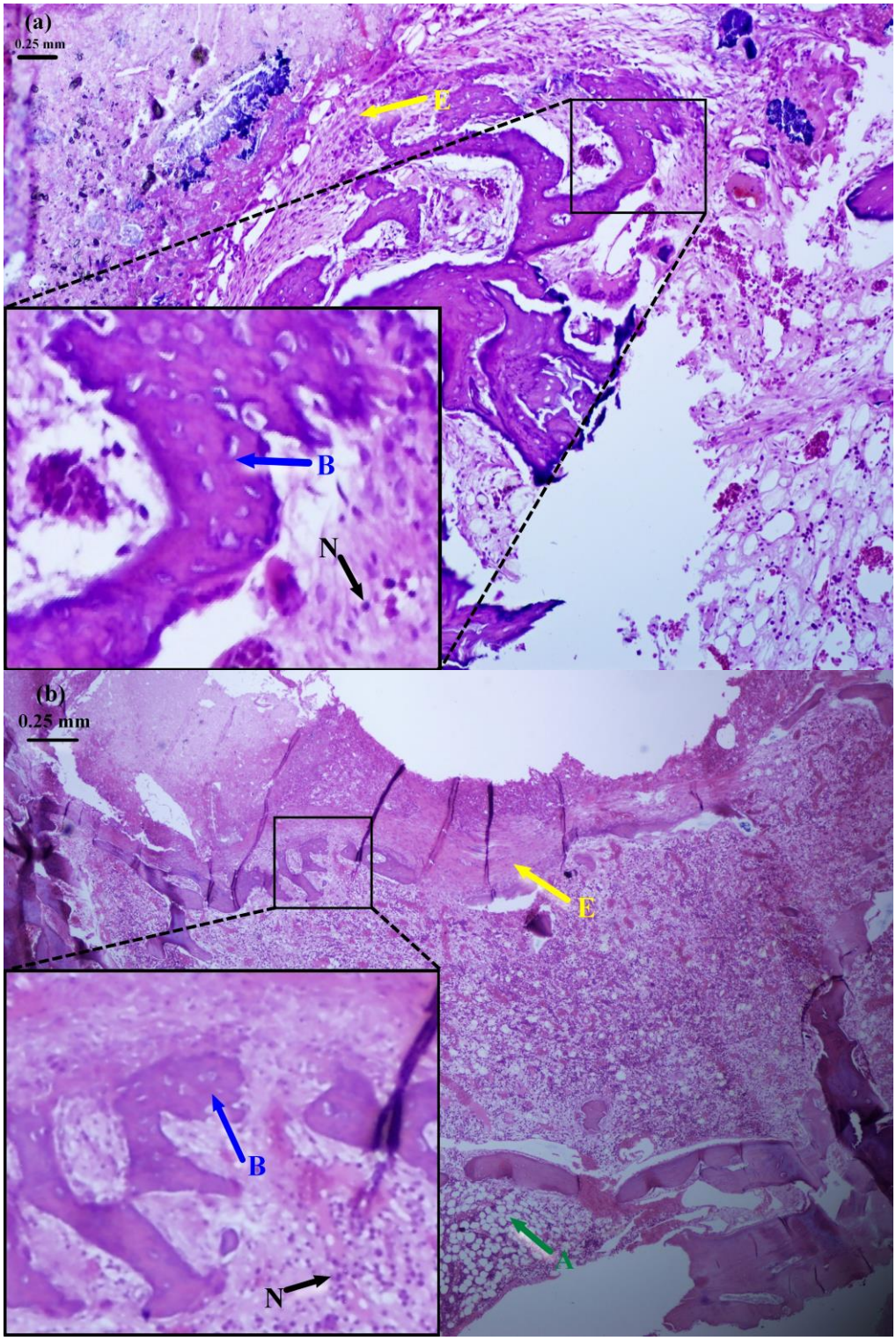

Figure 6.15: Histological observations of (a) clinical CPC, (b) CPSC5, (c) CPSC10 and (d) CPSC15 after 3 months of implantation (40x). Inflammation by neutrophils infiltration (black arrows), proliferated adipose tissue (green arrows), tissue encapsulation (yellow arrows) and new bone formation (blue arrows) were indicated on the images. The size bar is equal to 0.25 mm.

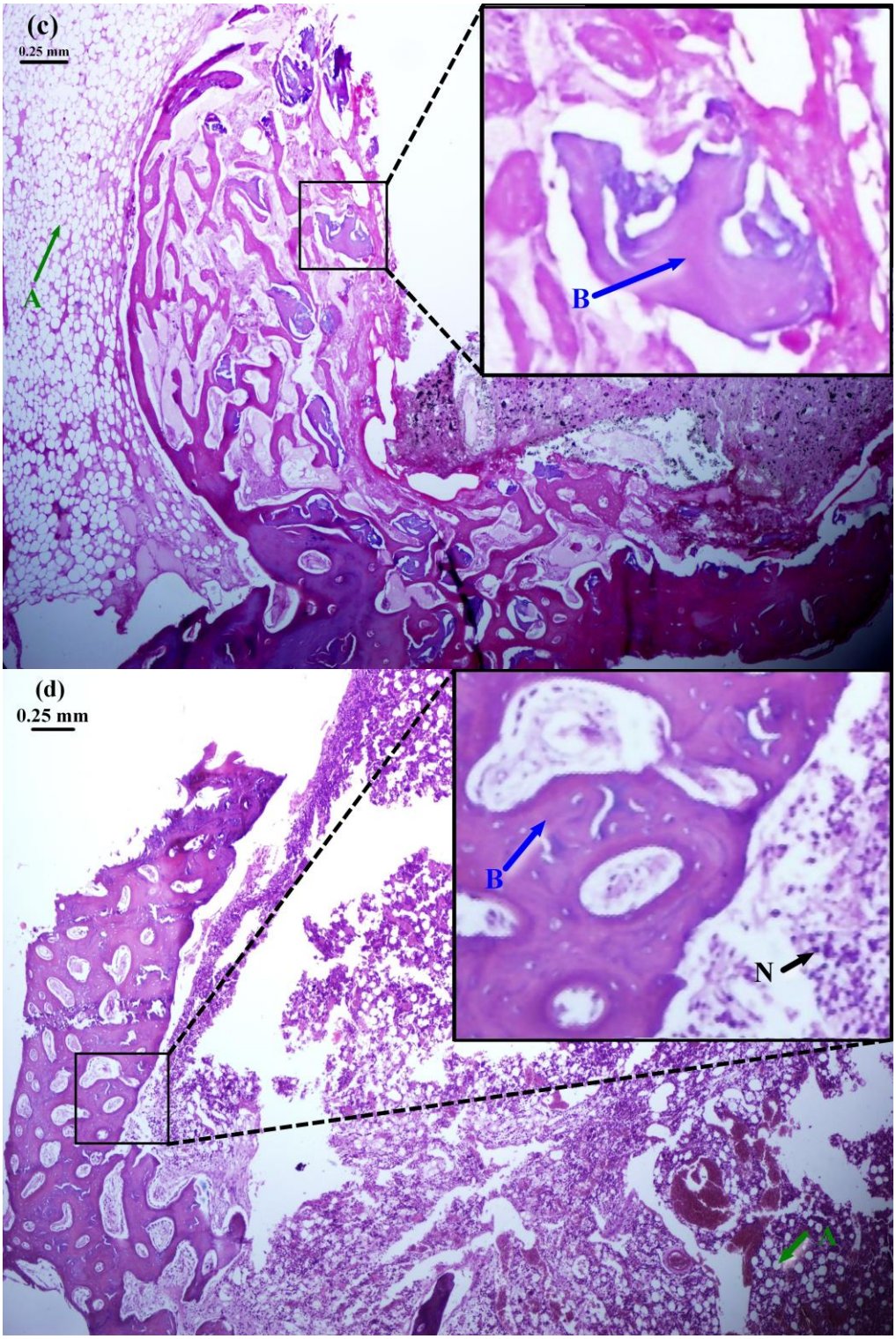

Figure 6.15 (continued): Histological observations of (c) CPSC10 and (d) CPSC15 after 3 months of implantation (40x). Inflammation by neutrophils infiltration (black arrows), proliferated adipose tissue (green arrows), tissue encapsulation (yellow arrows) and new bone formation (blue arrows) were indicated on the images. The size bar is equal to 0.25 mm.

6.4 Discussion

A suitable implant biomaterial must be biocompatible, functional (i.e., able to express its desirable functions properly), and structurally stable, including stability over time. Furthermore, for clinically useful bone cements, setting time and compressive strength must be optimized: a too short setting time is undesirable because it may not allow enough time to inject and fit the cement paste perfectly into the bone cavity; a too long setting time would not provide sufficient mechanical support after completion of the cement placement. Although bone cement is typically designed for use in non-load bearing applications, poor mechanical support arising from too long setting time and low compressive strength may make implants more prone to faster-than-usual degradation, causing peri-implant instability and implant failures [195]. MCP has shown to impact the CPSC hydration reactions by reducing both setting time and compressive strength, confirming previous observations [33]. MCP can react with the calcium hydroxide formed from calcium silicate hydration, producing *in situ* apatite and excess water, according to the equation 6.1, $6CaHPO_4 \cdot 2H_2O + 4Ca(OH)_2 = Ca_{10}(PO_4)_6(OH)_2 + 18H_2O$ [19, 33]. This mechanism explains why less calcium hydroxide was found in higher MCP samples, Fig. 6.2, but also their higher porosity (due to the excess water) and thus lower strength. The setting of CPSC is attributed to the CSH gel polymerization. XRD in our study reveals that C_3S is the primary source of the CSH gel. According to Collepardi and Massidda [196], the reduction in setting time could be attributed to the formation of a porous CSH gel layer covering the unreacted calcium silicate because of the formation of apatite and *in situ* formation of water. Therefore, water could more easily access the unreacted C_3S and thus the hydration process accelerates and apatite content increases with MCP content,

explaining the peak base broadening at 33º, Fig. 6.2a. CSH gel formed during hydration is responsible for cement compressive strength [62, 83]. The lower amount of CSH in CPSC15, and higher porosity (due to excess water formation) thus results in their poorer mechanical strength.

μCT reveals that micropores tend to be more interconnected in CPSC15 than in CPSC5. These microstructural changes further explain why CPSC samples with higher MCP content showed reduced mechanical strength due to interconnected porous microstructures. FTIR (Fig. 6.3) reveals that the peak intensity of Si-OH group at 1477 cm^{-1} decreased with MCP amount and the peak was barely seen in CPSC15. This may be attributed to the formation of apatite in CPSC. The presence of apatite disrupted the crystallinity of CSH gel and resulted in Si-OH groups undetectable by IR spectrum [194]. Siloxane bonds formed during the hydration of calcium silicate and its IR reflection intensity increased with porosity [194]. On Fig. 6.3, the peak at 874 cm^{-1} merely changed; however, the other peak at 1035 cm^{-1} increased significantly with MCP content. μCT (Fig. 6.4) studies have shown that porosity increased with MCP content. Therefore, the IR results are in a good agreement with μCT observations. The presence of MCP accelerates the hydration process and increases the setting rate; however, the concurrent formation of apatite and water might disrupt the continuity of CSH gel and create more porosity. Therefore, CPSC compressive strength was compromised.

The CPSC system tested in this work was found to be more biocompatible than the previously evaluated CSC system [19]. It appears that the presence of MCP increased osteoblast viabilities, which were similar to that of cells treated only by the culture medium. Osteoblast cells used in our research were isolated from neonatal SD rats and retained osteoblastic phenotypes in culture [197], which means that mature osteoblast cells can undergo osteogenesis and transform into osteocytes. The cell viabilities evaluated by MTT assays, therefore, included the viabilities of

both osteoblasts and osteocytes. Osteoblastic cell cycles and osteoblast-specific genes expressions were examined. It is known that, within a cell cycle, cell differentiation and proliferation are exclusive to each other [198]. Flow cytometry data showed that proliferation of osteoblast was enhanced by CPSC, while expressions of differentiation-regulating genes, such as ALP and runx2, were downregulated compared to CSC, confirming previous results by Fei *et al.* [35]. Transforming growth factor β (TGF-β) promotes osteoblast proliferations [199], and our results suggested that CPSC-treated osteoblast cells enhanced proliferation, not differentiation. In a preliminary *in vitro* study of CPSC system, calcium (Ca^{2+}), phosphate (PO_4^{3-}) and silicate (SiO_4^{4-}) ions were found abundant in the extract solutions [31, 35]. The high Ca^{2+} concentrations in the extract solutions in our study may be responsible for this improved proliferation because Ca^{2+} can bind to G-protein coupled extracellular calcium sensing receptors [199]. OPG is the antagonist to RANKL, which is responsible for differentiation and recruitment of osteoclast cells and initiation of bone resorption [200], and its level determines the osteoclastogenetic activity of osteoclast cells. It was found that increasing MCP content in CSC is accompanied by an increase in OPG expression because of higher Ca^{2+} and PO_4^{3-} concentrations in solution released by CPSC15 [201, 202].

CPSC demonstrates better osteoconductivity than clinical CPC. As CPSC resorbed slower than CPC (Fig. 6.10 to 6.14), it is expected that CPSC could provide more mechanical and structural support to the fractural sites [203]. As discussed, a suitable biomaterial should have matched rates between implant degradation and osseointegration [204-206]. In this study, CPSC demonstrated better osseointegration with longer resorption than CPC. Though CPC promoted some new trabecular bone formation within the first 2

months of implantation, newly formed bone was resorbed again by osteoclast cells within the next month, making the remnant CPC unable to provide enough mechanical support to fractured bone due to poor osseointegration between implant and bone. In addition, CPSC showed a slower degradation and better osseointegration than CPC. The setting processes determine the different *in vivo* degradation rates between CPC and CPSC. CPC is set by the precipitation and entanglement of hydroxyapatites; while, our particular CPSC is set by the hydration of calcium silicate to form CSH gel. The relatively slow degradation of CPSC can better control the release of bone formation stimulating ions, e.g., SiO_4^{4-} and Ca^{2+}, to achieve the prolonged osteogenic effects, and to increase the biocompatibility by limiting the sudden increase in local pH. Histopathological results also indicated that new bone was formed around and inside CPSC (Fig. 6.15). Leukocytes (predominately neutrophils in this study) indicated that decreasing acute inflammation was associated with both CPSC and clinical CPC, but there were no signs of chronic inflammation [207]. Neutrophils dominate the acute inflammation stage and shortly die, and foreign materials (i.e., bone cements) cause the migration of leukocytes and acute inflammation [207]. Neutrophils and macrophages are recruited to phagocytize foreign particles in body; bone cements, however, cannot be phagocytized by neutrophils because cement debris are commonly much larger than the size of neutrophils [207]. Instead, dissolution, or *in vivo* biodegradation, of cement can eventually remove it from body. In CPSC samples, the controlled release of $Ca(OH)_2$ may be helpful in maintaining the inflammation at the minimal level [208]. The longer release of osteogenic ions from CPSC than clinical CPC continuously enhanced bone formation near and inside CPSC implants and was expected to provide better bone restoration than clinical CPC in the long term.

Chapter 7: RESULTS AND DISCUSSION III: ANTI-OSTEOPOROTIC AND ENHANCED OSTEOGENIC EFFECTS OF RA-ADDED CPSC

7.1 Material characterizations

Both compressive strengths and setting time were more compromised at 1.0% RA than at 0.5% of RA (Fig. 7.1). The results have also shown that for most samples 3-day strengths were similar to 7-day strengths (12-13 MPa), with the exception of the sample CPSC10-10R which was ~50% weaker after 3 days of setting. The crystallinity results (Fig. 7.2) demonstrated that the content of calcium silicate hydrate (CSH) gel and apatite formations declined with RA amount, while the content of the amorphous phases increased. μCT and gas sorption porosity data (Fig. 7.3 and Table 7.1) reveal that the overall porosity fraction > 5 μm in size for CPSC10-10R and CPSC10-05R were similar (about 3-4%) and smaller than for CPSC10 (about 5%). Table 7.1 also compares the samples porosity determined by μCT method with the results obtained with the gas sorption methods. FTIR results (Fig. 7.4) demonstrated that in the 1400 cm^{-1} to 1500 cm^{-1} region the double-peak of phosphonate groups in RA was more distinguishable in CPSC10-10R than in CPSC10-05R and within the region between 800 cm^{-1} and 1200 cm^{-1} triple peaks assigned to Si-O-Si were clearly identified. Cross-sections of CPSC10, CPSC10-05R and CPSC10-10R samples after 7-day setting were examined under SEM and their micrographs are in Fig. 7.5. Both edges and cores on these cross-sections were examined and it is found that there was less porosity on the edge than in the core regardless of sample types (Fig. 7.5a and b, c and d, e and f). In addition, the CSH gel crystallinity looked the most continuous in CPSC10 and the least in CPSC10-10R (Fig. 7.5a, c and e).

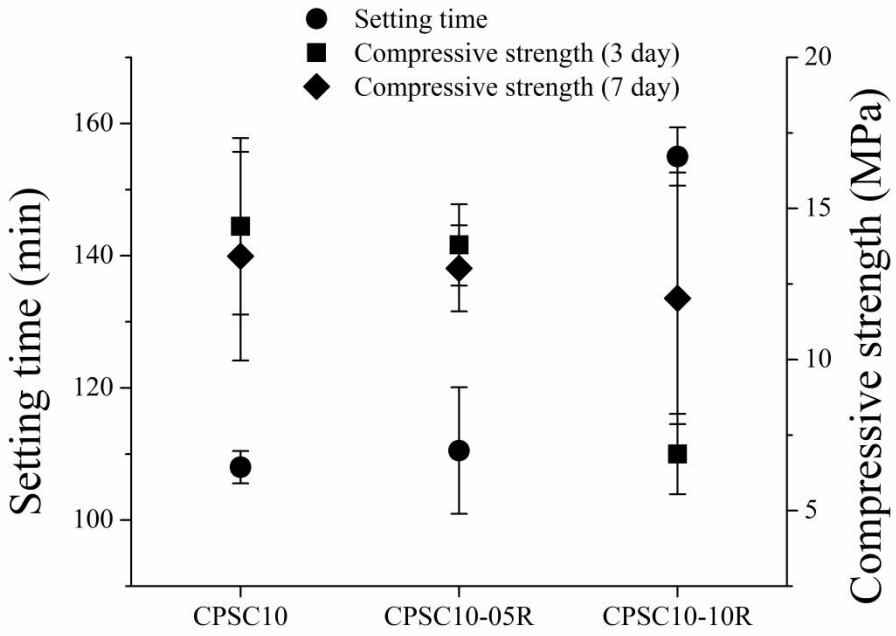

Figure 7.1: The setting time and compressive strength changes with risedronate concentration. (*n* = 4 for the setting time and *n* = 8 for compressive strength tests). The error bars represent one standard deviation.

Table 7.1: Porosity measured by gas sorption and µCT methods. The results are presented as average ± standard deviation. (*n* = 4)

	Sample		
	CPSC10	CPSC10-05R	CPSC10-10R
Gas sorption	23.2% ± 5.2%	14.4% ± 1.9%	12.4% ± 2.8%
µCT	5.7% ± 0.5%	3.4% ± 0.6%	3.9% ± 0.3%

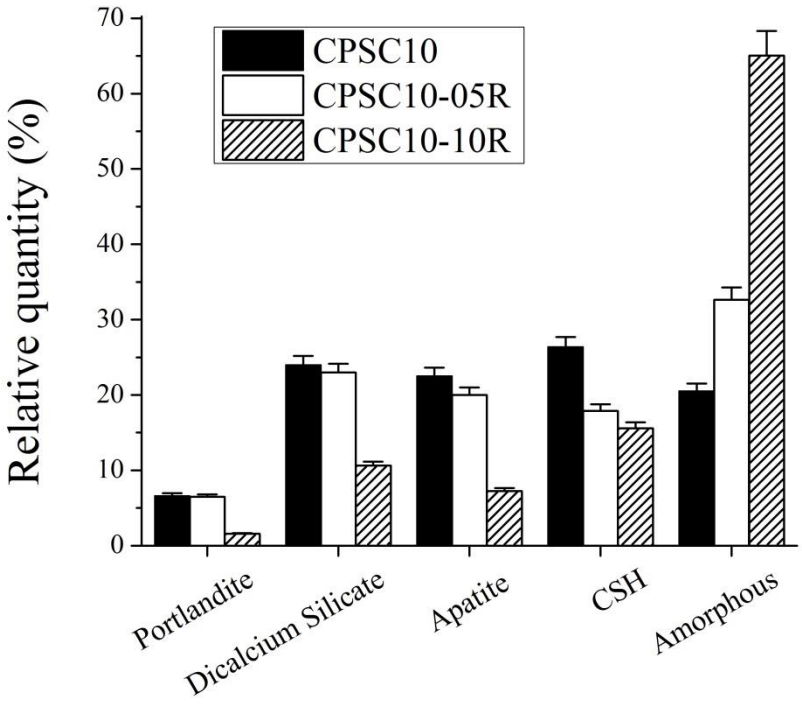

Figure 7.2: The relative phase content of Portlandite, Ca_2SiO_4, apatite, CSH gel and the balance of amorphous phase in CPSC10, CPSC10-05R and CPSC10-10R (*n* = 4).

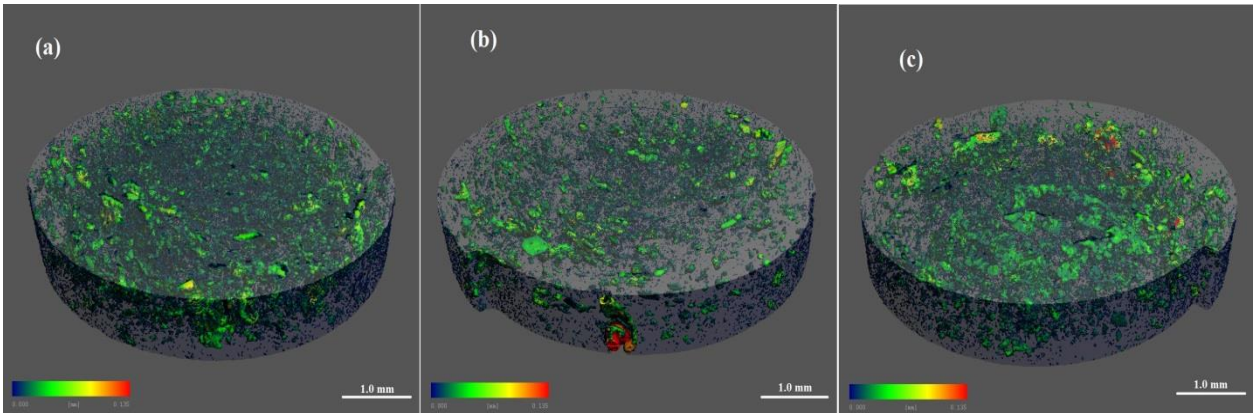

Figure 7.3: Microporosity visualization for (a) CPSC10, (b) CPSC10-05R and (c) CPSC10-10R.

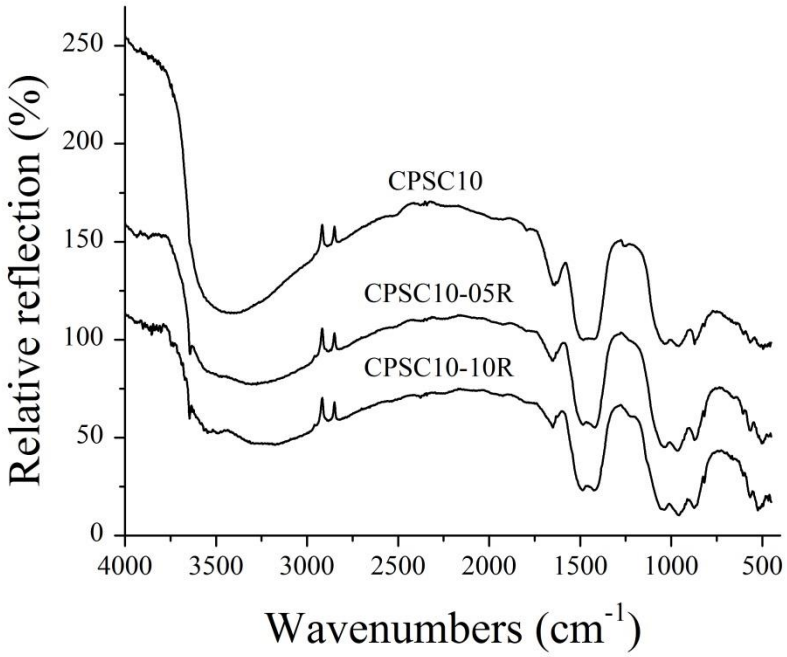

Figure 7.4: FTIR spectra of CPSC10, CPSC10-05R and CPSC10-10R after 1-day hardening (*n* = 4).

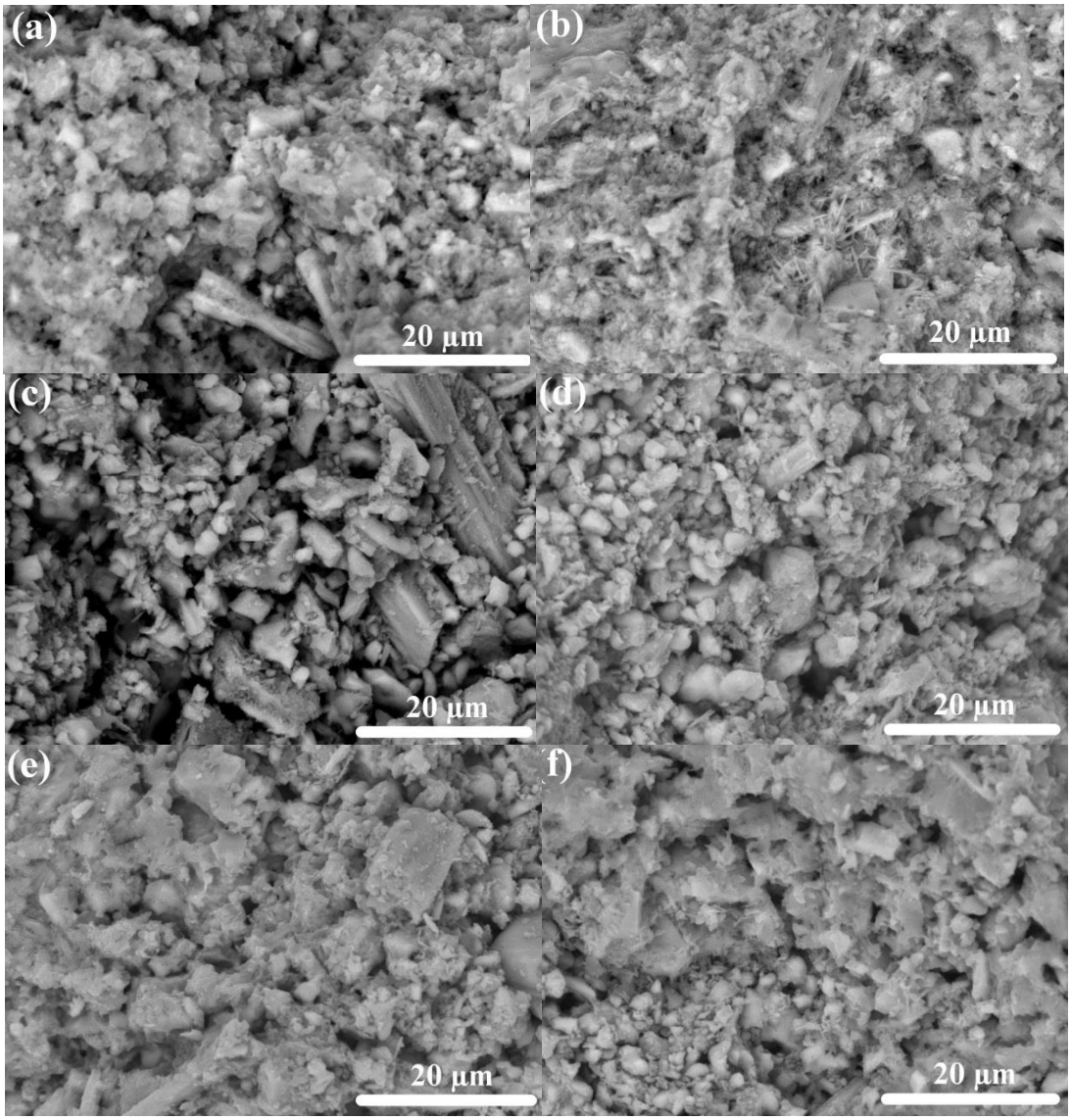

Figure 7.5: Scanning electron micrographs of (a) CPSC10-core, (b) CPSC10-edge, (c) CPSC10-05R-core, (d) (d) CPSC10-05R-edge, (e) CPSC10-10R-core and (f) CPSC10-10R-edge after 7 days of setting. One bar equals to 20 µm.

7.2 *In vitro* biocompatibility

Cytotoxicity results (Fig. 7.6) demonstrated that osteoblasts viabilities of control were significantly lower than 1-day cement extracts of CPSC10-05R and CPSC10-10R but insignificantly lower than the 3-day results. In general, the 3-day extracts were more toxic than 1-day extracts. Cell cycle results by FCM, shown in Fig. 7.7, revealed that CPSC10, CPSC10-05R and CPSC10-10R had comparable effects on regulation of cell cycles and on promoting osteoblastic proliferation and differentiation. Gene expressions tests were carried out on four commonly used osteoblast-specific genes. From Fig. 7.8a to c, ALP, OPG and runx2 expressions in CPSC10-05R were significantly higher than those in either CPSC10 or CPSC10-10R. However, TGF-β expressions (Fig. 7.8d) were seen to significantly decrease with RA content. With the exception of ALP expressions, significant differences were observed between CPSC10 and CPSC10-10R.

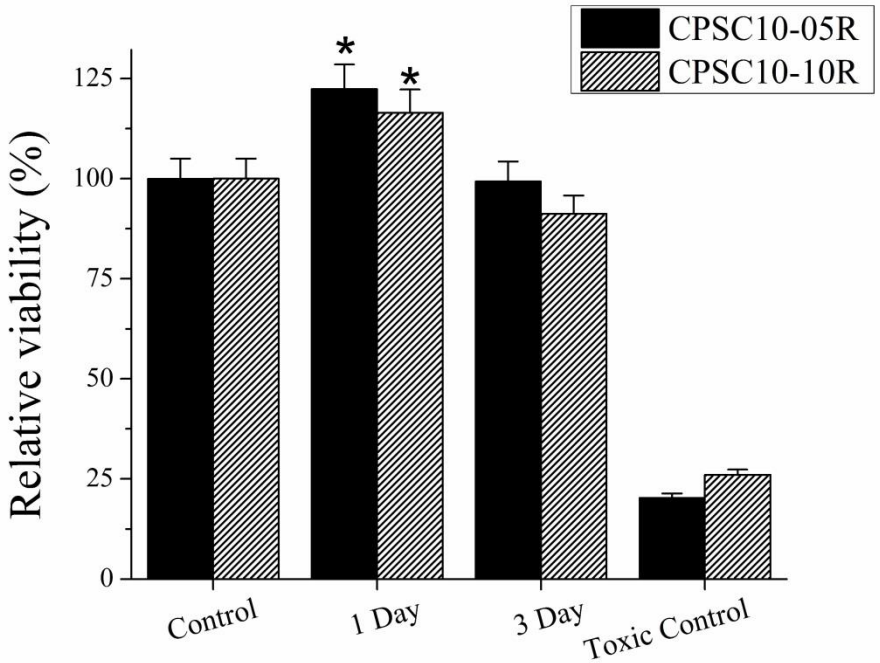

Figure 7.6: Osteoblast-like cell viabilities. Cells were treated with CPSC10-05R and CPSC10-10R after 1 and 3 days immersion in PBS. Error bar represents one standard deviation (n = 5). ($p^* < 0.05$ *vs.* the control group)

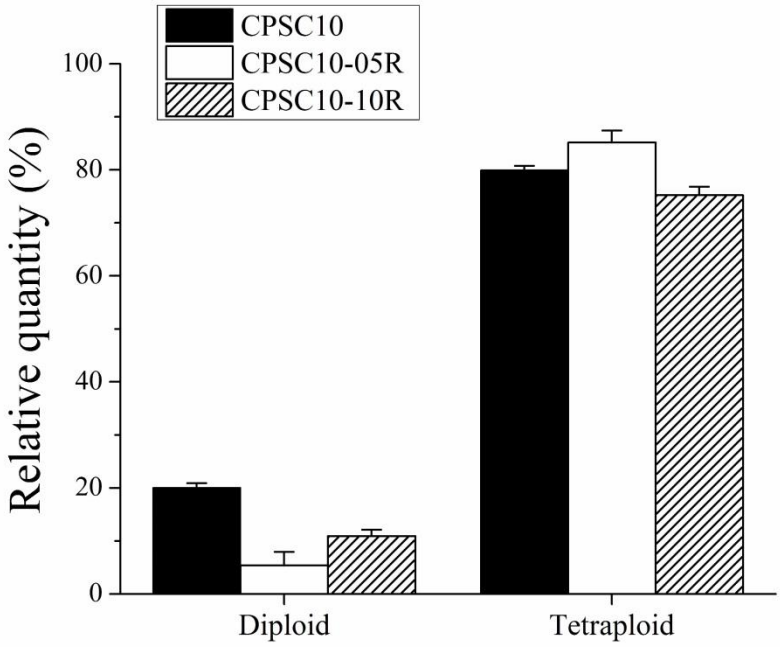

Figure 7.7: Fractions of diploid (DNA double strands) and tetraploid (DNA quadruple strands) in osteoblast cells. Cells were harvested from CPSC extracts for 3 days. Error bar represents one standard deviation (*n* = 3).

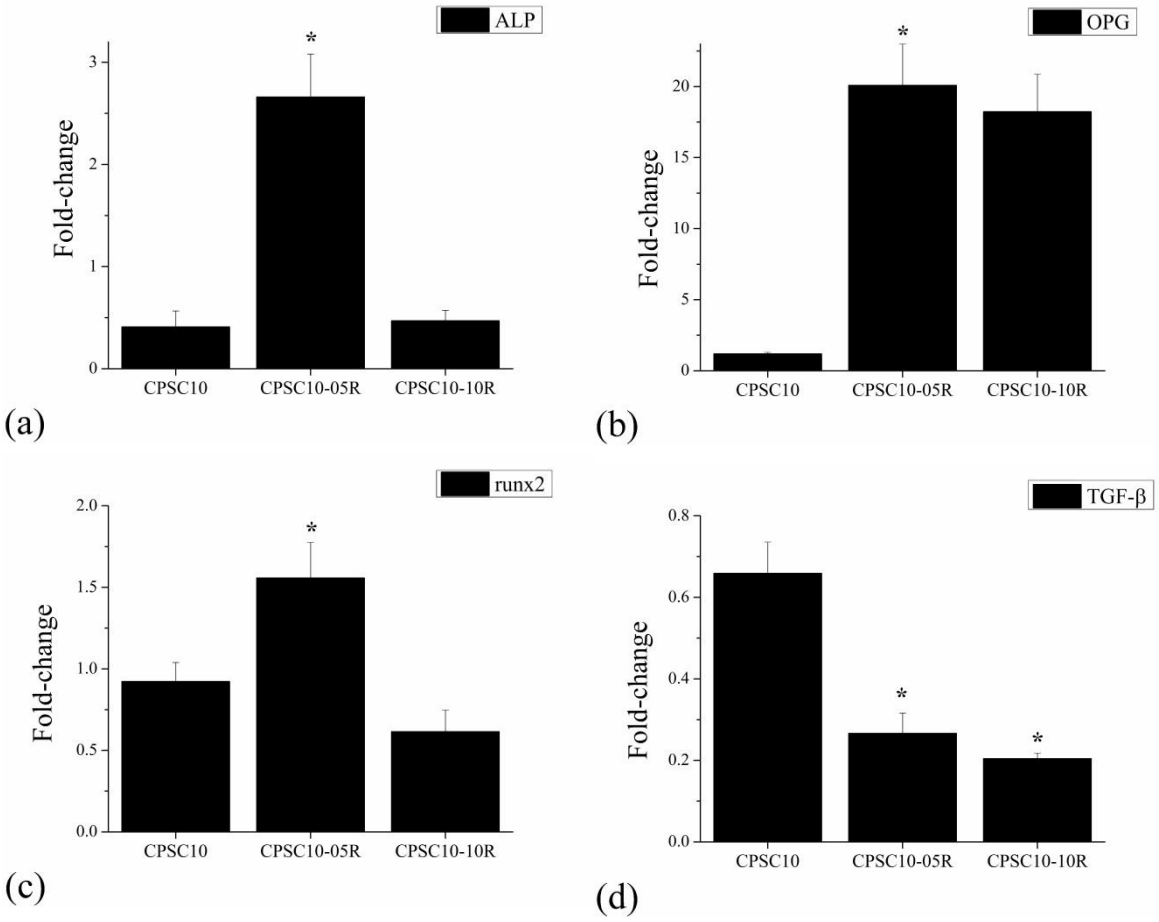

Figure 7.8: Osteoblastic marker gene expression by real-time PCR. mRNA expressions of (a) ALP, (b) OPG, (c) runx2 and (d) TGF-β genes in osteoblast cells are shown after incubation in cement extracts for 1 day. Error bar represents one standard deviation (*n* = 8). (*p < 0.05 *vs.*CPSC10)**

7.3 Global anti-osteoporotic effects

Serum TRACP-5b level results strongly imply that osteoclastic activities in all rabbits were significantly elevated due to the treatment of glucocorticoid injection as well as the bilateral ovariectomy. As shown in Fig. 7.9, the TRACP-5b serum level increased with treatment time and the serum level after 4 weeks was significantly ($p < 0.05$) higher than the baseline level on the 1st day of injection.

Bone-specific ALP and OCN levels were significantly ($p < 0.05$) decreased in CPSC10 and CPSC10-05R as compared to the sham control group (Fig. 7.10 and 7.11). In the sham control group, serum levels reached the maximum at the 8th week and dropped afterwards. In Fig. 7.12, serum levels of OPG/RANKL were statistically indifferent between the sham control, CPSC10 and CPSC10-05R groups.

Biomarkers related to bone resorption were significantly lower in CPSC10 or CPSC10-05R groups than the sham control ($p < 0.05$). Figure 7.22 shows serum TRACP-5b level changes in all three groups from the 4th to 10th week. It is clearly demonstrated that the serum level in CPSC10-05R was the lowest among the three groups. Statistical analysis results showed that serum level in CPSC10-05R and the sham control were significantly ($p < 0.05$) different between each other; however, serum levels in CPSC10 were not significantly lower in CPSC10 than the sham control ($p < 0.05$).

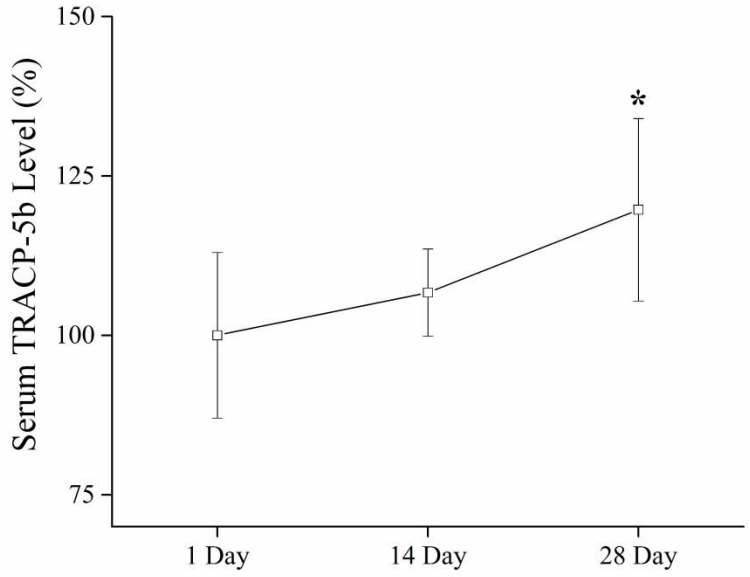

Figure 7.10: Serum TRACP-5b levels 1, 14 and 28 days after osteoporosis induction measured by ELISA. Error bar represents one standard deviation (n = 6). (p^* < 0.05)

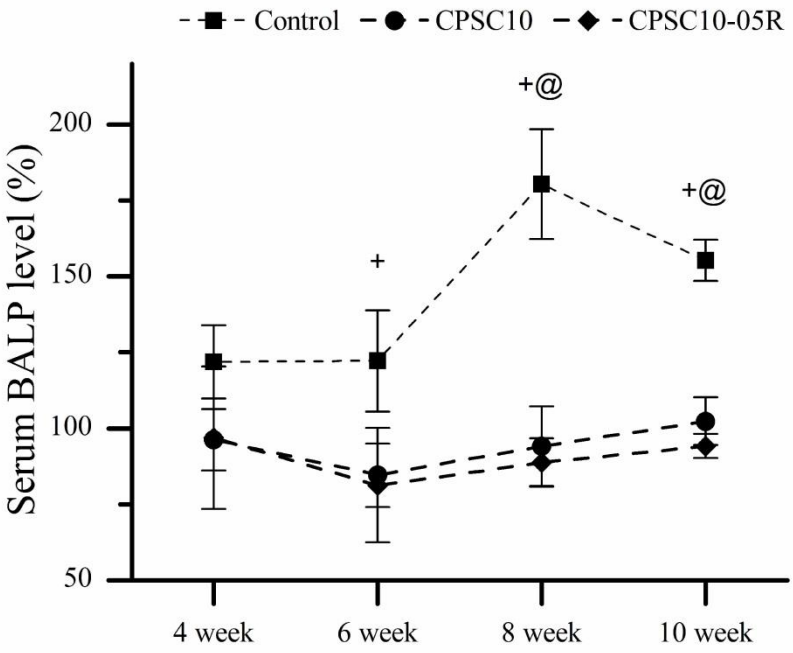

Figure 7.9: Serum levels of BALP after 4, 6, 8 and 10 weeks between sham control, CPSC10 and CPSC10-05R (n = 10 except for the 10th week n = 5). "+" sign indicates that the readings are statistically different between the sham control and CPSC10. "@" symbol indicates that the readings are statistically different between the sham control and CPSC10-05R. (p < 0.05)

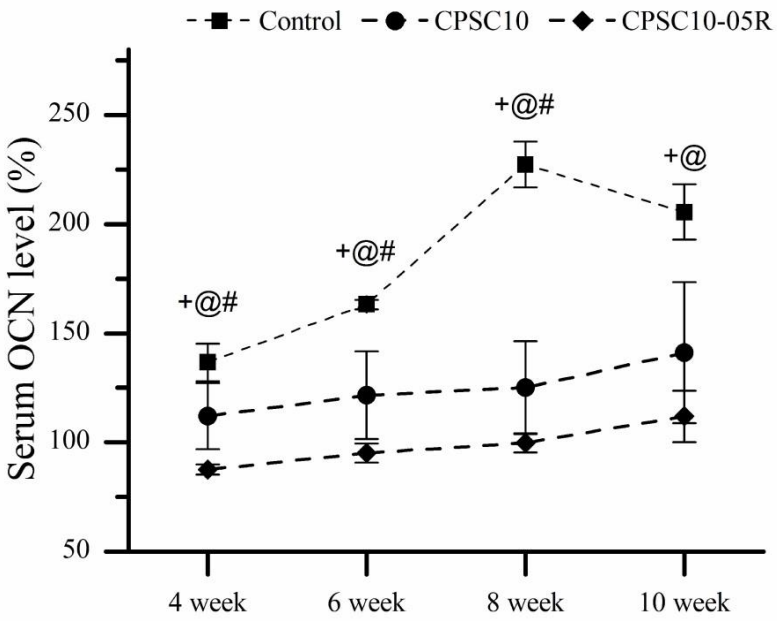

Figure 7.11: Serum levels of OCN after 4, 6, 8 and 10 weeks between sham control, CPSC10 and CPSC10-05R (*n* = 10 except for the 10th week *n* = 5). "+" sign indicates that the readings are statistically different between the sham control and CPSC10. "@" symbol indicates that the readings are statistically different between the sham control and CPSC10-05R. "#" symbol indicates that readings are statistically different between the CPSC10 and CPSC10-05R groups. ($p < 0.05$)

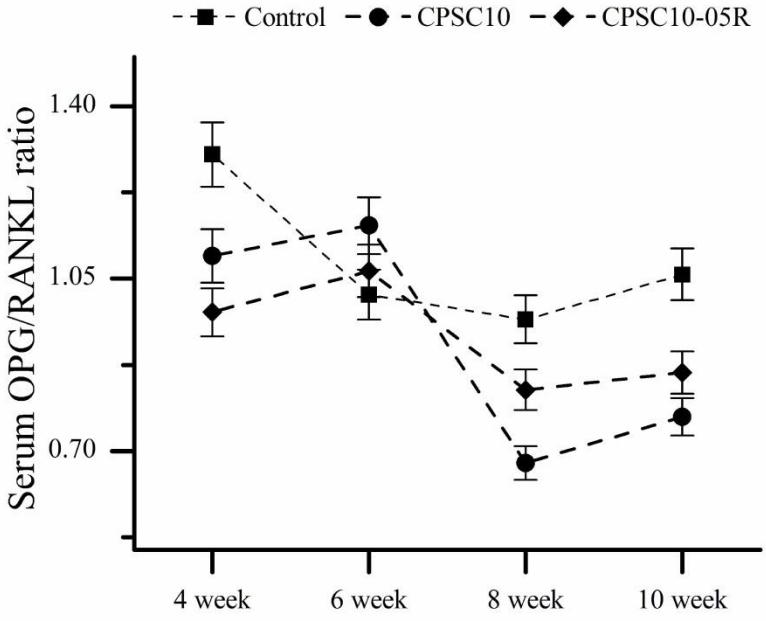

Figure 7.12: Serum levels of OPG/RANKL after 4, 6, 8 and 10 weeks between sham control, CPSC10 and CPSC10-05R (*n* = 10 except for the 10th week *n* = 5). ($p < 0.05$)

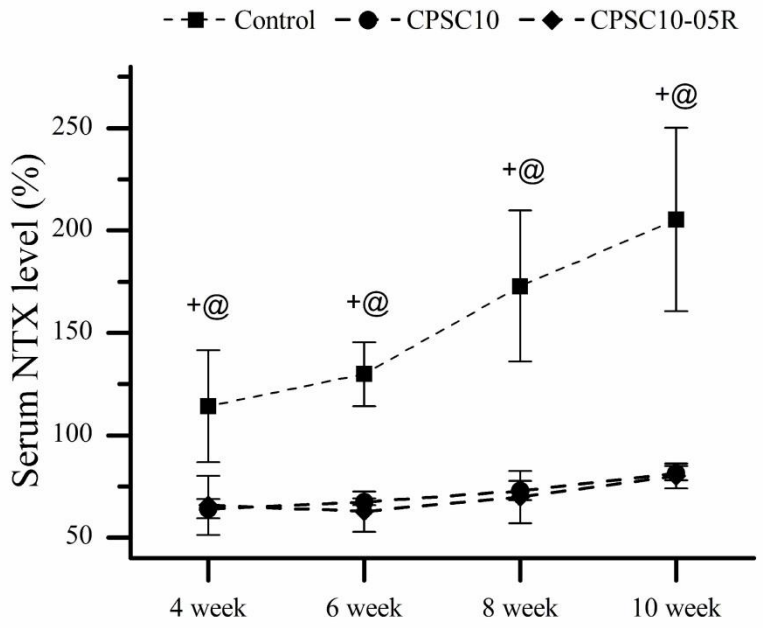

Figure 7.13: Serum levels of NTX after 4, 6, 8 and 10 weeks between sham control, CPSC10 and CPSC10-05R (*n* = 10 except for the 10th week *n* = 5). "+" sign indicates that the readings are statistically different between the sham control and CPSC10. "@" symbol indicates that the readings are statistically different between the sham control and CPSC10-05R. ($p < 0.05$)

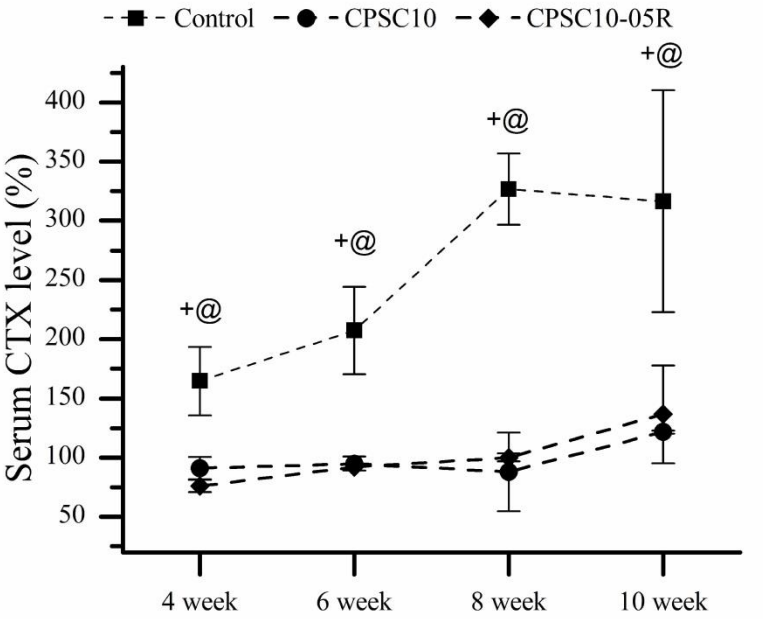

Figure 7.14: Serum levels of CTX after 4, 6, 8 and 10 weeks between sham control, CPSC10 and CPSC10-05R (*n* = 10 except for the 10th week *n* = 5). "+" sign indicates that the readings are statistically different between the sham control and CPSC10. "@" symbol indicates that the readings are statistically different between the sham control and CPSC10-05R. ($p < 0.05$)

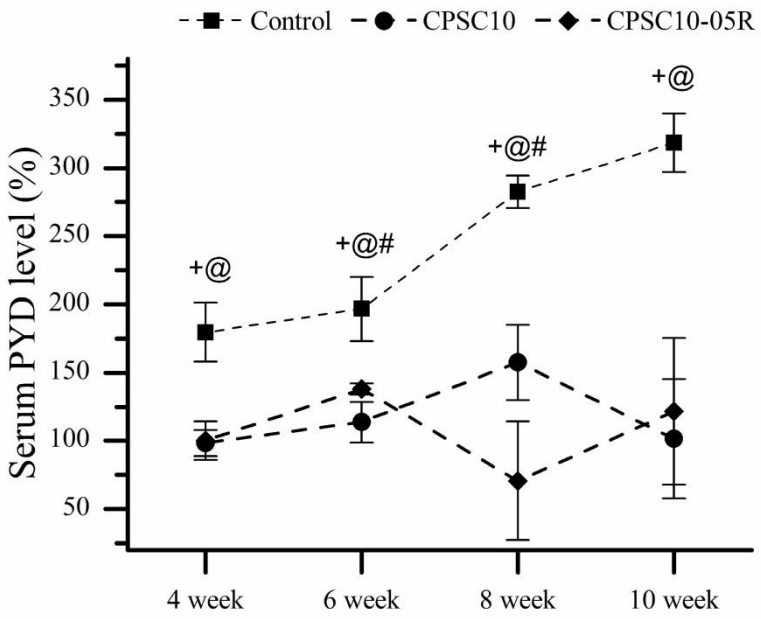

Figure 7.15: Serum levels of PYD after 4, 6, 8 and 10 weeks between sham control, CPSC10 and CPSC10-05R (*n* = 10 except for the 10th week *n* = 5). "+" sign indicates that the readings are statistically different between the sham control and CPSC10. "@" symbol indicates that the readings are statistically different between the sham control and CPSC10-05R. "#" symbol indicates that readings are statistically different between the CPSC10 and CPSC10-05R groups. ($p < 0.05$)

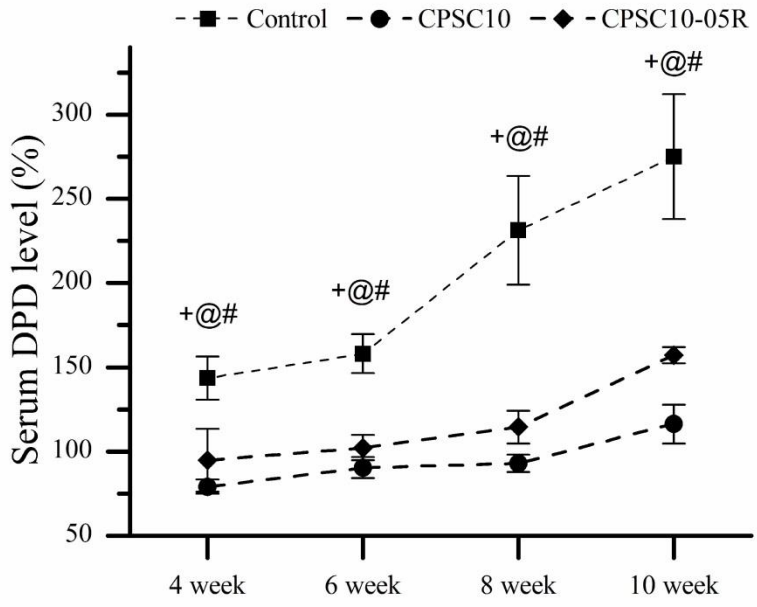

Figure 7.16: Serum levels of DPD after 4, 6, 8 and 10 weeks between sham control, CPSC10 and CPSC10-05R (*n* = 10 except for the 10th week *n* = 5). "+" sign indicates that the readings are statistically different between the sham control and CPSC10. "@" symbol indicates that the readings are statistically different between the sham control and CPSC10-05R. "#" symbol indicates that readings are statistically different between the CPSC10 and CPSC10-05R groups. ($p < 0.05$)

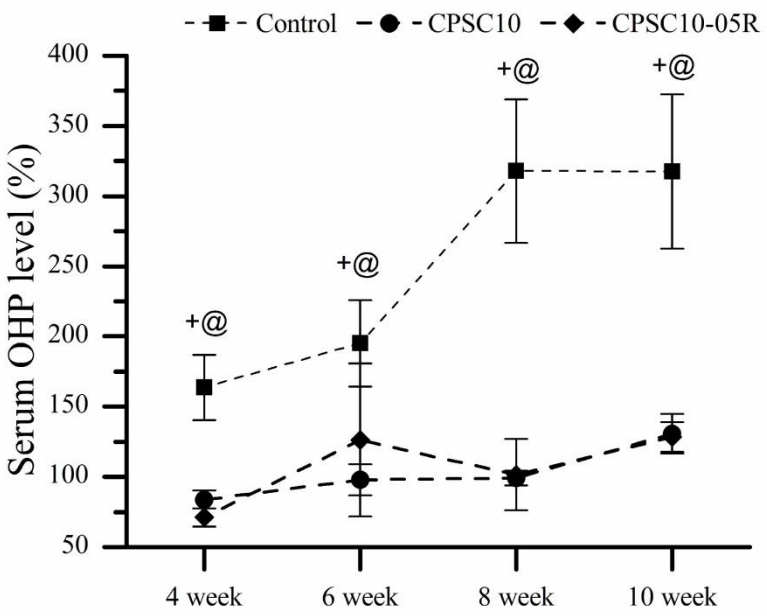

Figure 7.17: Serum levels of OHP after 4, 6, 8 and 10 weeks between sham control, CPSC10 and CPSC10-05R (*n* = 10 except for the 10th week *n* = 5). "+" sign indicates that the readings are statistically different between the sham control and CPSC10. "@" symbol indicates that the readings are statistically different between the sham control and CPSC10-05R. ($p < 0.05$)

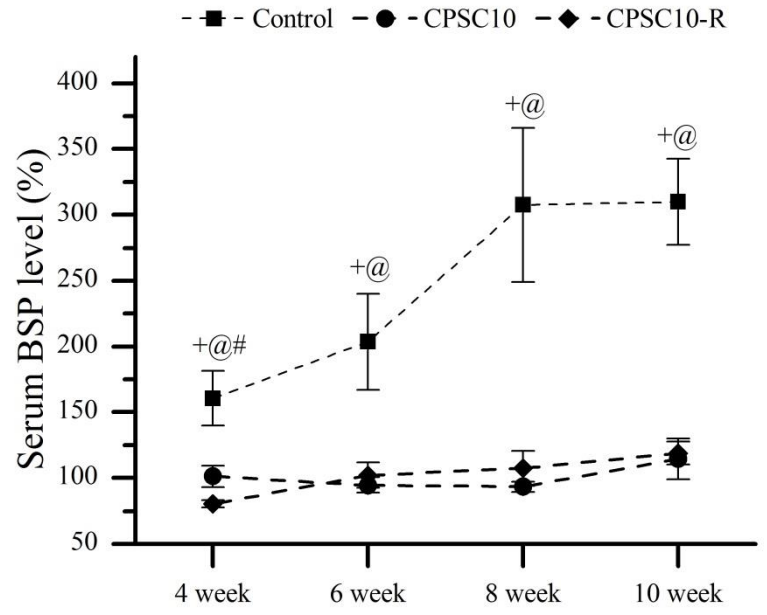

Figure 7.18: Serum levels of BSP after 4, 6, 8 and 10 weeks between sham control, CPSC10 and CPSC10-05R (*n* = 10 except for the 10th week *n* = 5). "+" sign indicates that the readings are statistically different between the sham control and CPSC10. "@" symbol indicates that the readings are statistically different between the sham control and CPSC10-05R. "#" symbol indicates that readings are statistically different between the CPSC10 and CPSC10-05R groups. ($p < 0.05$)

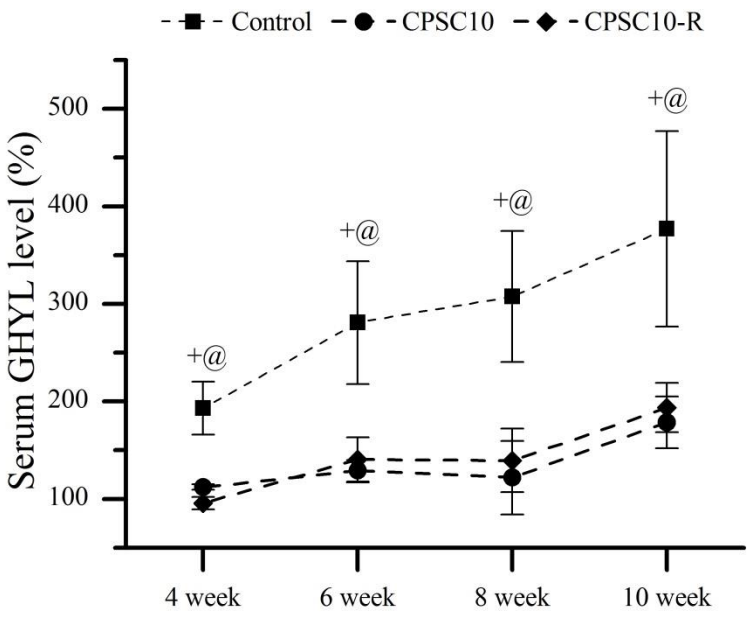

Figure 7.19: Serum levels of GHYL after 4, 6, 8 and 10 weeks between sham control, CPSC10 and CPSC10-05R (*n* = 10 except for the 10th week *n* = 5). "+" sign indicates that the readings are statistically different between the sham control and CPSC10. "@" symbol indicates that the readings are statistically different between the sham control and CPSC10-05R. (*p* < 0.05)

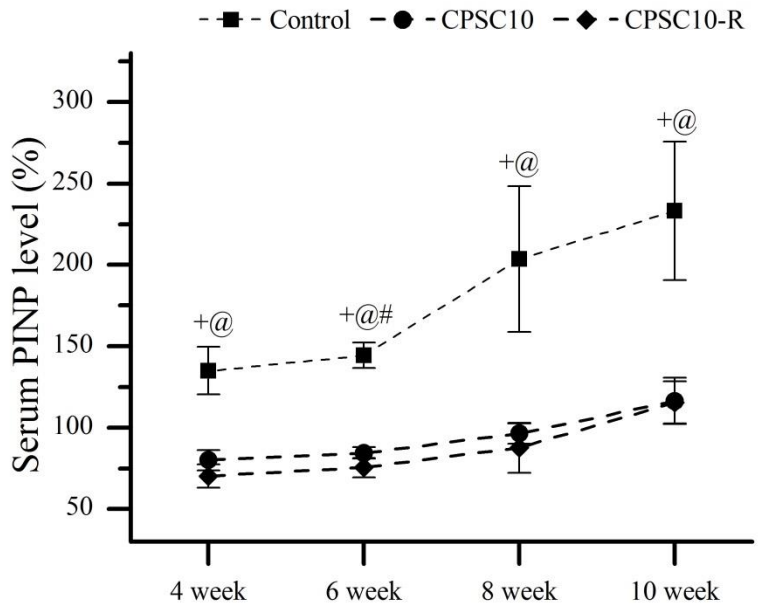

Figure 7.20: Serum levels of PINP after 4, 6, 8 and 10 weeks between sham control, CPSC10 and CPSC10-05R (*n* = 10 except for the 10th week *n* = 5). "+" sign indicates that the readings are statistically different between the sham control and CPSC10. "@" symbol indicates that the readings are statistically different between the sham control and CPSC10-05R. "#" symbol indicates that readings are statistically different between the CPSC10 and CPSC10-05R groups. (*p* < 0.05)

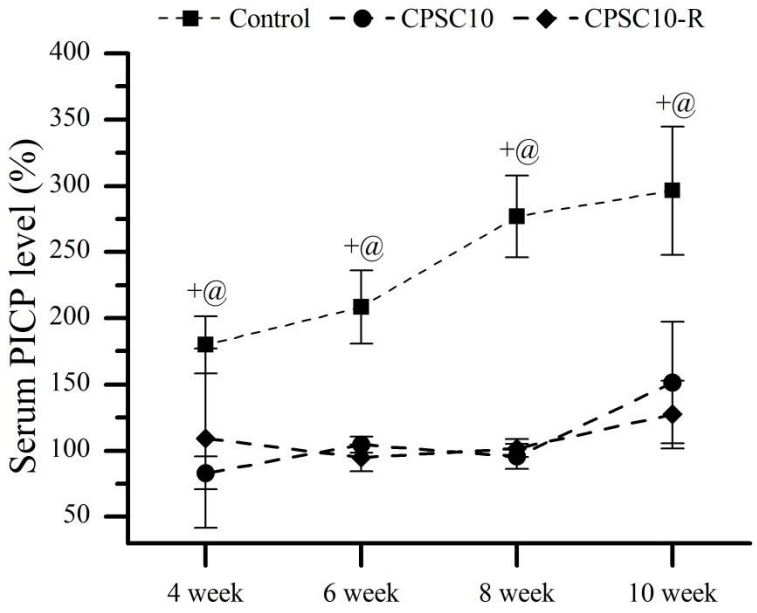

Figure 7.21: Serum levels of PICP after 4, 6, 8 and 10 weeks between sham control, CPSC10 and CPSC10-05R (*n* = 10 except for the 10th week *n* = 5). "+" sign indicates that the readings are statistically different between the sham control and CPSC10. "@" symbol indicates that the readings are statistically different between the sham control and CPSC10-05R. "#" symbol indicates that readings are statistically different between the CPSC10 and CPSC10-05R groups. (*p* < 0.05)

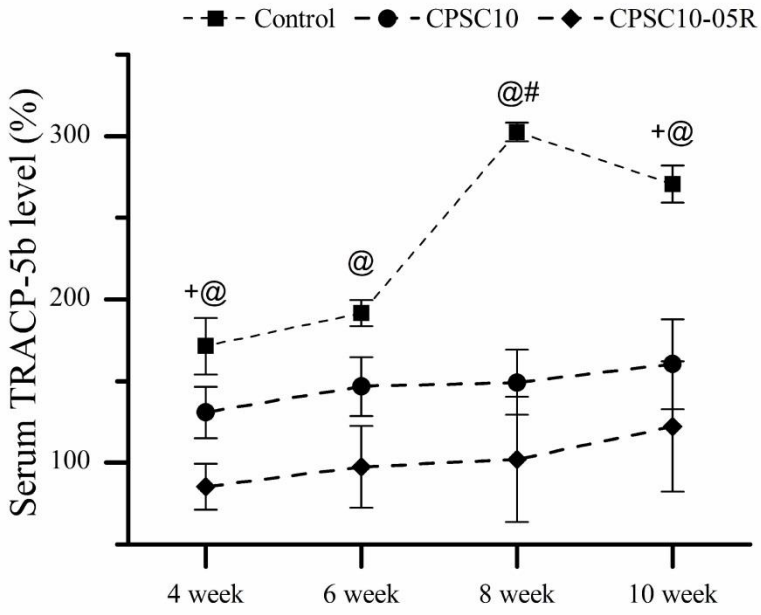

Figure 7.22: Serum levels of TRACP-5b after 4, 6, 8 and 10 weeks between sham control, CPSC10 and CPSC10-05R (*n* = 10 except for the 10th week *n* = 5). "+" sign indicates that the readings are statistically different between the sham control and CPSC10. "@" symbol indicates that the readings are statistically different between the sham control and CPSC10-05R. "#" symbol indicates that readings are statistically different between the CPSC10 and CPSC10-05R groups. (*p* < 0.05)

7.4 Local osteogenic effects shown by X-ray and CT

Clinical X-ray and CT images show that there was more trabecular bone formation after 10 weeks of implantation of RA-CPSC than CPSC. Figure 7.23 shows X-ray radiographs after 8and 10 weeks of implantation for each treatment group. Newly formed trabecular bone was indifferent between CPSC and RA-CPSC groups after 8 weeks of implantation. After 10 weeks, there seemed to be more newly formed trabecular bone in RA-CPSC group than in CPSC, although this is a non-quantitative observation. CT scans (Fig. 7.24) also indicated that there was more bone formation (green color) around cement (red color) in RA-CPSC than CPSC after 10 weeks. A semi-quantitative analysis (Fig. 7.25) shows a trend towards more trabecular bone formation in RA-CPSC than in CPSC. After 8 weeks of implantation, new bone formation was only slightly higher in RA-CPSC than in CPSC. After 10 weeks of implantation, however, more bone formation in the RA-CPSC group was found.

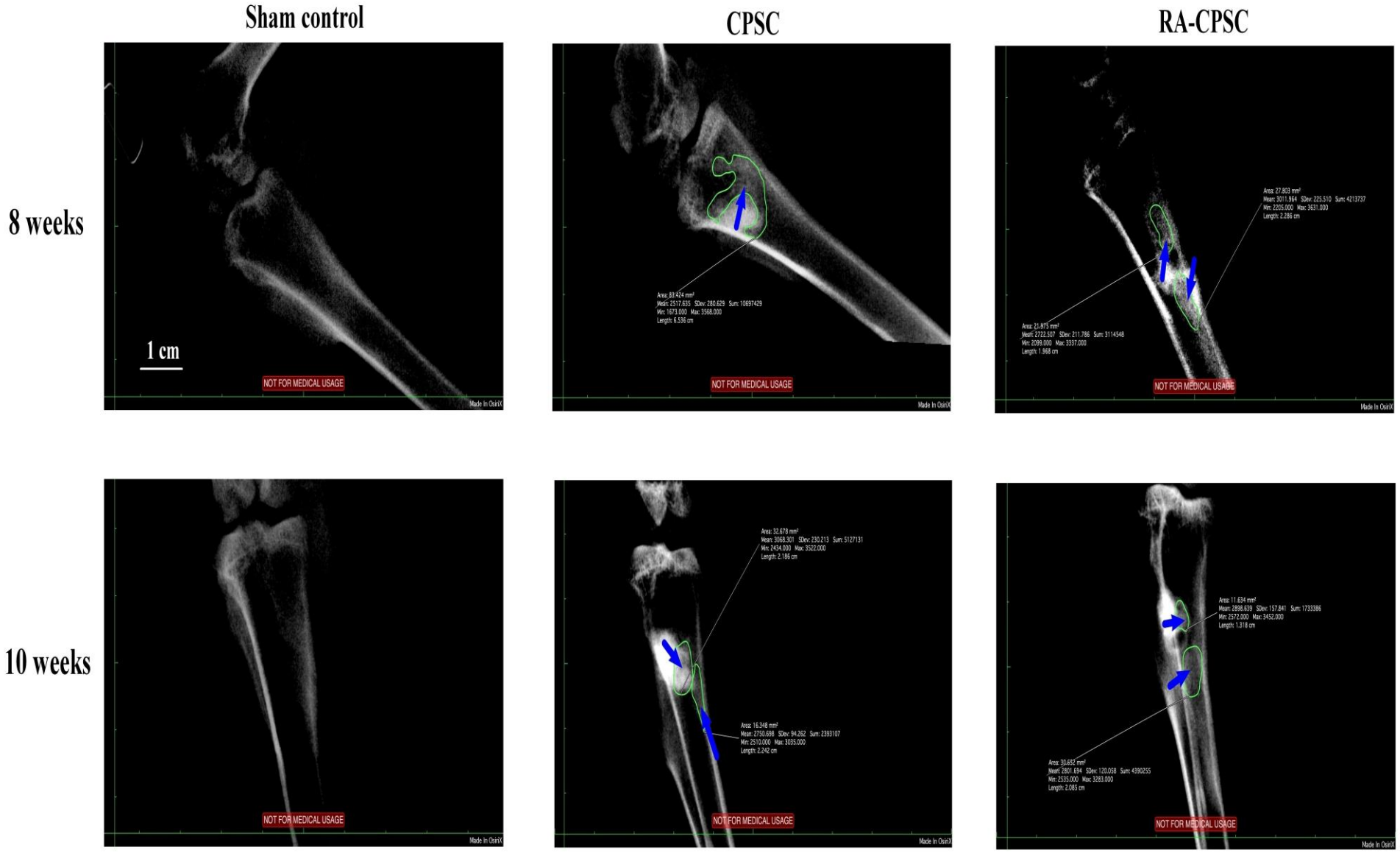

Figure 7.23: X-ray images of the rabbits' right legs 8 and 10 weeks after implantation. One bar is equal to 1 cm.

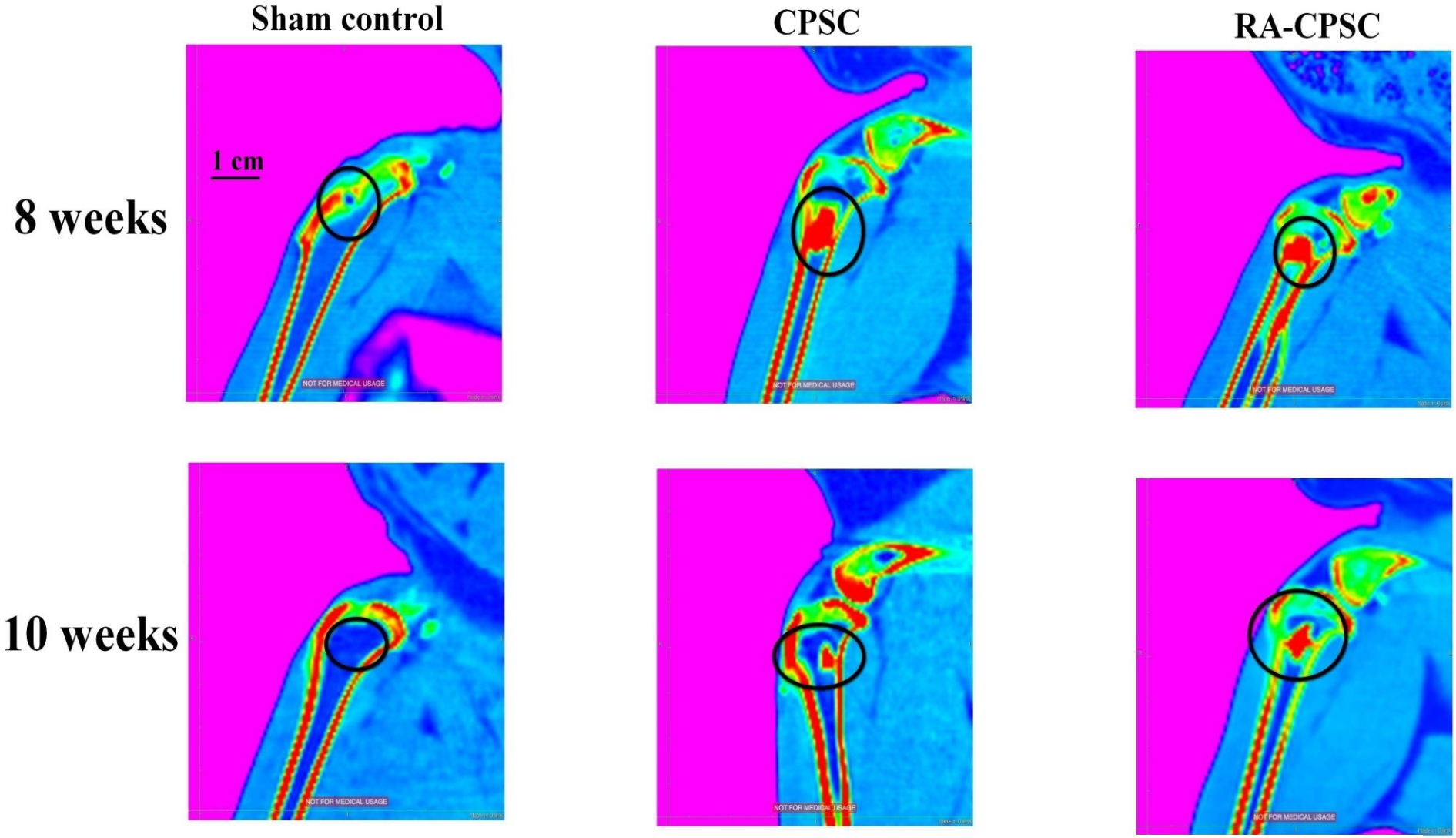

Figure 7.24: CT images of the rabbits' right legs 8 and 10 weeks after implantation. One bar is equal to 1 cm.

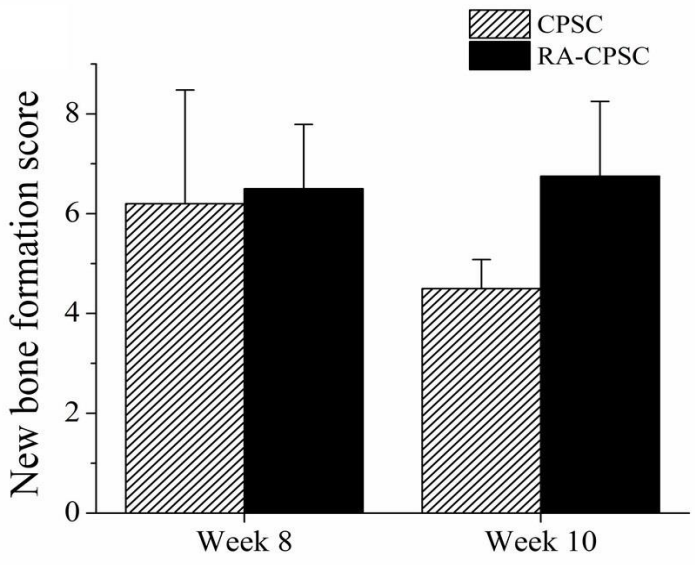

Figure 7.25: Comparison of the new bone formation scores between CPSC and 0.5% RA-CPSC groups 8 and 10 weeks after implantation (n = 5).

7.5 Local osteogenic effects shown by histopathology

Histological observations showed better bone restoration and healing in the 0.5% RA-CPSC group than the CPSC alone group (Fig. 7.26). In the control group (Fig. 7.26a), there was no newly formed bone in the vicinity of the perforation. Instead, a band of proliferative connective tissue was observed. The perforation formed an elliptical structure, which consisted of proliferative connective tissue, granulation tissue and fibrous tissue composed of collagen fibers, fibroblasts, and fiber cells. In addition, adipose tissue, neutrophils and osteoclasts were also present. In the CPSC group, basic bone restoration was evidenced in the form of a thin a layer of lamellar bone (Fig. 7.26b). In addition, osteoblasts were present, which were absent from the control. In the 0.5% RA-CPSC group (Fig. 7.26c), a larger amount of newly formed bone shaped in long strips or irregular sheets was observed. Compared to both the control and CPSC groups, there was more bone formation and less bone marrow replaced by adipose tissue.

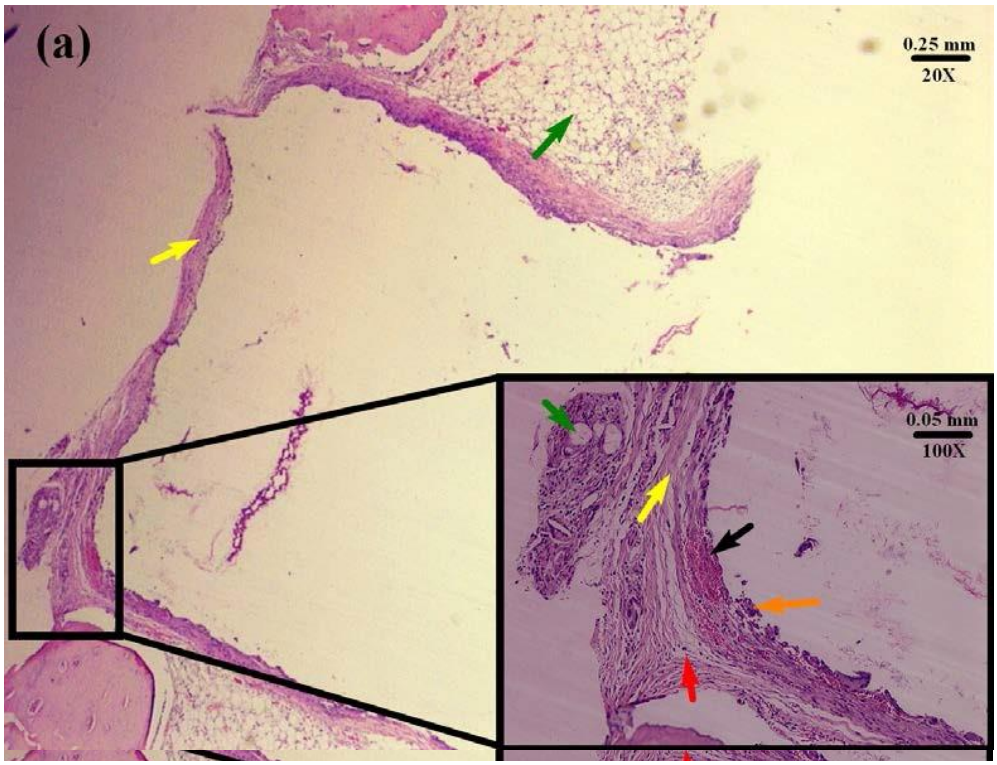

Figure 7.26: Histological observations of (a) Control, (b) CPSC and (c) 0.5% RA-CPSC after 10 weeks of implantation (20x and 100x). Indicated on the images is inflammation as indicated by neutrophil infiltration (black arrows), proliferated adipose tissue (green arrows), tissue encapsulation (yellow arrows), new bone formation (blue arrows), osteoclasts (orange arrows) and osteoblast (red arrows) The size bar equals 0.25 mm.

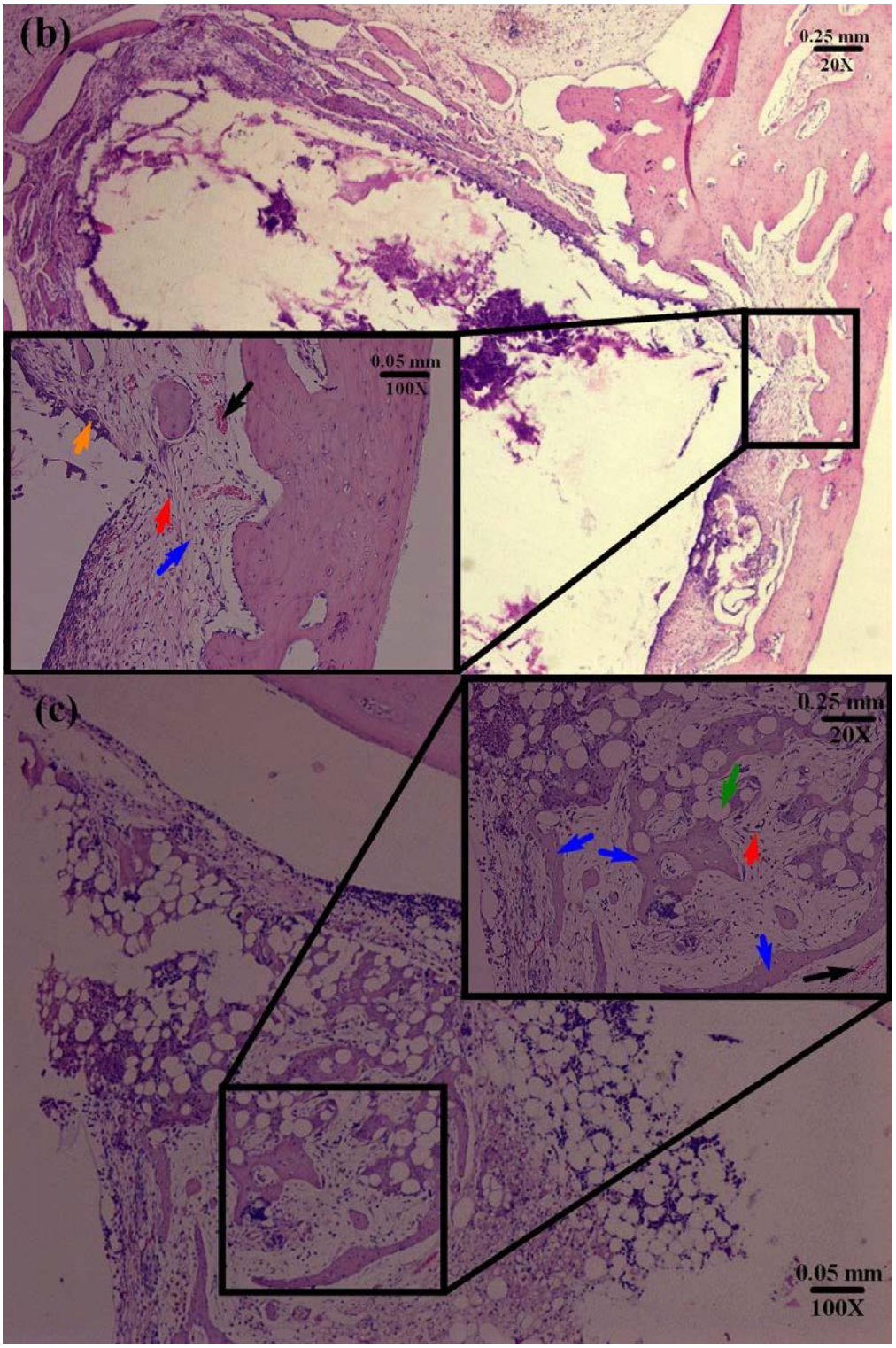

Figure 7.26 (continued): Histological observations of (b) CPSC and (c) 0.5% RA-CPSC after 10 weeks of implantation (20x and 100x). Indicated on the images is inflammation as indicated by neutrophil infiltration (black arrows), proliferated adipose tissue (green arrows), tissue encapsulation (yellow arrows), new bone formation (blue arrows), osteoclasts (orange arrows) and osteoblast (red arrows) The size bar equals 0.25 mm.

7.6 Local osteogenic effects shown by PCR analysis

The comparisons of 84 osteogenesis-related gene expressions (refer to Table 7.2) between CPSC10 (and CPSC10-05R) and the sham control are shown in Fig. 7.27 and 7.28. The data are presented by fold changes (i.e., how many times the expression of any particular gene increases in relation to the housekeeping gene in the same sample) of genes in CPSC10 or CPSC10-05R (y-axis) versus fold changes of genes in the sham control (x-axis) in logarithmic scale (base = 2). Two purple lines were the threshold expression (=3) and divided the graph into three regions. The region above the upper threshold lime indicates that the genes were up- regulated in either CPSC10 or CPSC10-05R as compared to the sham control and the region below the lower threshold line indicates that the genes were down-regulated in CPSC10 or CPSC10-05R compared to the sham control. Genes outside the threshold lines are considered biological significant.

Tables 7.3 and 7.4 show gene full names and their fold changes in CPSC10 and CPSC10-05R as compared to the sham control [209-218]. It is found that 15 genes of BMP5, CD36, CTSK, FN1, ITGA1. ITGB1, LOC100009177, LOC100342904, LOC100344425, LOC100345812, LOC100348414, MMP2, MMP9, MMP13 and SPP1 (gene codes given and refer to Table 7.3 or 7.4 for full names) were up-regulated in both CPSC10 and CPSC10-05R as compared to the shame control. In addition, Table 7.4 indicates that additional 6 genes of COL1A2, COL2A1, LOC100338577, LOC100340503, LOC100347598 and SMAD2 were only up-regulated in the CPSC10-05R group compared to the sham control. Fold changes ranged from 9 to 98 times.

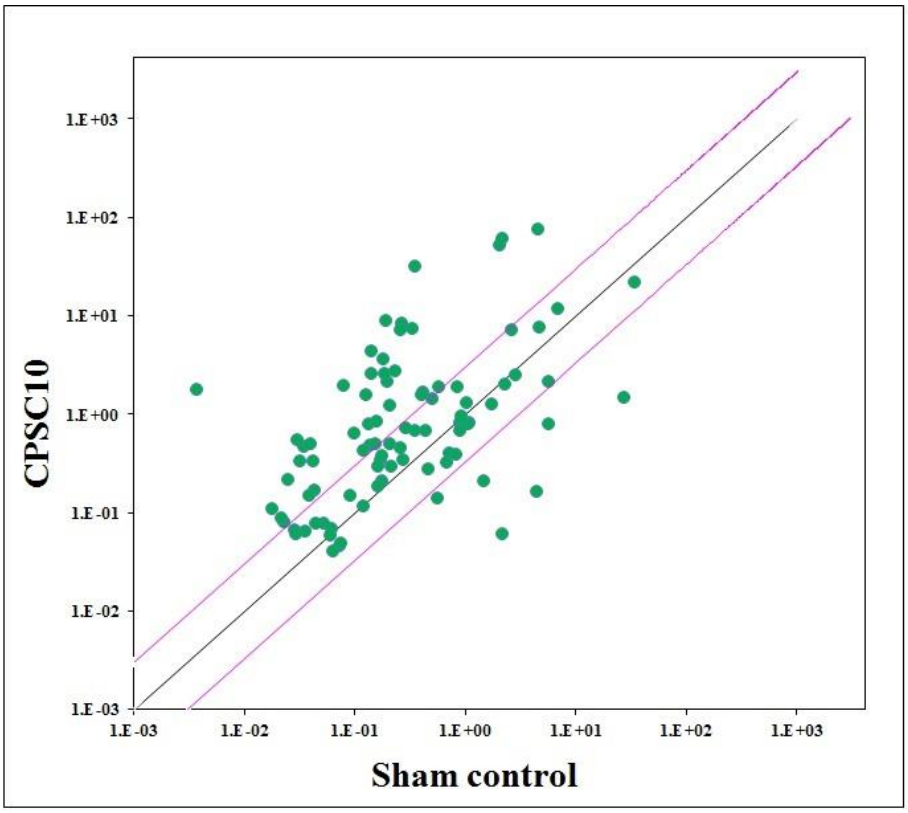

Figure 7.27: Comparison of 84 genes analyzed by PCR array between CPSC10 and the sham control. Pink lines represent threshold fold changes (= 3). The data are presented by fold changes of genes in CPSC10 (y-axis) versus fold changes of genes in the sham control (x-axis) in logarithm scale (base = 2). (*n* = 4)

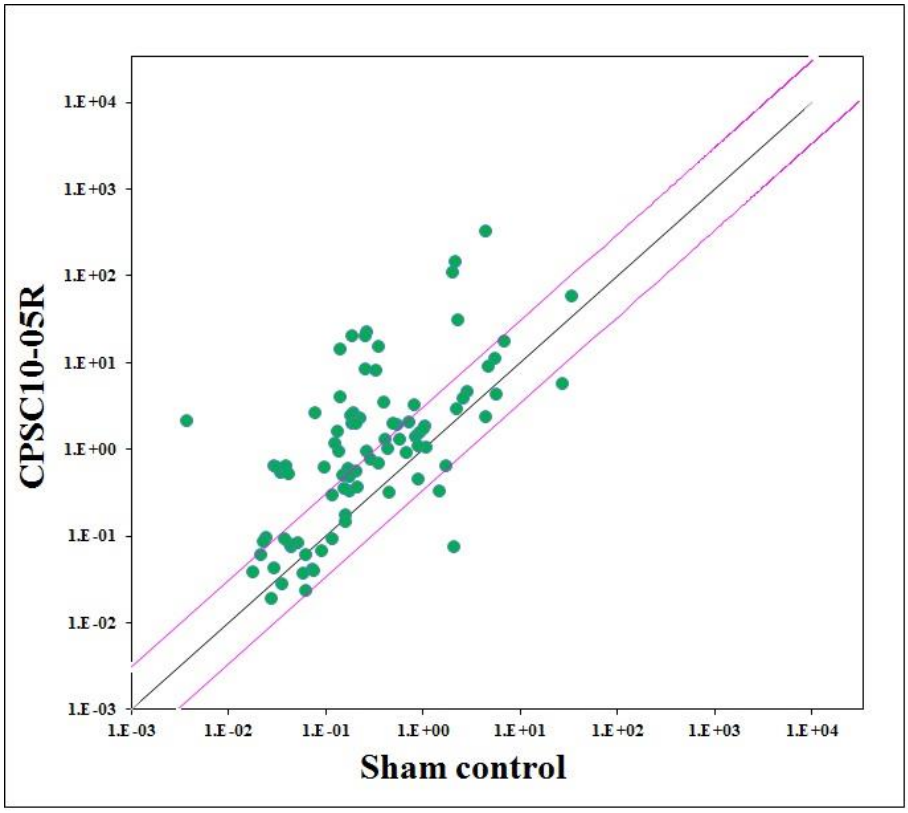

Figure 7.28: Comparison of 84 genes analyzed by PCR array between CPSC10-05R and the sham control. Pink lines represent threshold fold changes (= 3). The data are presented by fold changes of genes in CPSC10-05R (y-axis) versus fold changes of genes in the sham control (x-axis) in logarithm scale (base = 2). (*n* = 4)

Table 7.2: 84 genes analyzed by PCR array given by the manufacturer

Skeletal development	
Cartilage condensation	BMPR1B, COL2A1, LOC100356758 (BMP1), MGP, SOX9
Ossification	AHSG, BMP-2, BMP4, BMP5, BMP7, BMPR1A, BMPR1B, BMPR2, CDH11, CHD, COL2A1, CTSK, DLX5, FGF2 (bFGF), FGFR2, GLI1, IGF1, IGF2, LOC100008806 (EGFR), LOC100008942 (IHH), LOC100144342 (IGF1R), LOC100338577 (MCSF), LOC100339156 (RUNX2), LOC100340503 (Osteocalcin), LOC100341009 (TNFSF11), LOC100344425 (IBSP), LOC100347598 (COL1A1), LOC100348414 (BMP3), LOC100355119 (ACVR1), LOC100356758 (BMP1), LOC100356871 (SP7), LOC100358460 (NOG), MGP, MMP2, MMP9, SHH, SMAD1, SOX9, SPP1 (Osteopontin), TGFB1, TGFB2, TGFB3
Osteoclast differentiation	LOC100338577 (MCSF), LOC100340503 (Osteocalcin), LOC100341009 (TNFSF11), TNF
Osteoblast differentiation	BMP-2, BMP4, BMP7, BMPR1A, BMPR1B, BMPR2, CHD, DLX5, FGF2 (bFGF),FGFR2, GLI1, IGF1, LOC100008942 (IHH), LOC100339156 (RUNX2), LOC100340503 (Osteocalcin), LOC100341629 (SOX2), LOC100347598 (COL1A1), LOC100348897 (IGFBP5), LOC100351309 (PTH), LOC100355119 (ACVR1), LOC100356871 (SP7), LOC100358460 (NOG), NF1, PTHLH, SMAD1, SPP1 (Osteopontin)
Other genes	CTNNB1, FGFR1, IL6, LOC100341109 (ALPL), LOC100344335 (TGFBR2), LOC100345812 (TGFBR1)
Bone mineral metabolism	
Bone mineralization	AHSG, BMP-2, BMP4, BMP7, BMPR1A, BMPR1B, BMPR2, FGFR2, IGF1, LOC100340503 (Osteocalcin), LOC100351309 (PTH), LOC100355119 (ACVR1), MGP, MMP13, PTGS2 (COX2), PTHLH, SOX9, TGFB1, TGFB3.
Calcium ion binding and homeostasis	CALCR, CDH11, FGF2 (bFGF), ITGB1, LOC100008808 (EGF), LOC100008907 (VDR), LOC100340503 (Osteocalcin), LOC100342904 (ANXA5), MMP2, TGFB1
Extracellular matrix (ECM) molecules:	
Collagens	COL10A1, COL14A1, COL15A1, COL1A2, COL2A1, COL5A1, LOC100009177 (COL3A1), LOC100347598 (COL1A1)
ECM protease inhibitors	AHSG, SERPINH1
ECM proteases	CTSK, MMP2, MMP9, MMP13
Other genes	BGN, FLT1, LOC100341109 (ALPL)
Cell adhesion molecules	
Cell-cell adhesion	BMPR1B, CDH11, COL14A1, COL2A1, ITGB1, LOC100008806 (EGFR), LOC100008942 (IHH), LOC100341009 (TNFSF11), LOC100356758 (BMP1), SOX9, TGFB1, TNF, VCAM-1
Cell-matrix adhesion	CD36, ITGA1, ITGAM, ITGB1, LOC100009177 (COL3A1), LOC100101621 (ITGA2), LOC100338577 (MCSF).
Other genes	COL15A1, COL5A1, FN1, LOC100340503 (Osteocalcin), TNF
Growth factors	GMCSF, FGF1, FGF2 (bFGF), IGF1, IGF2, LOC100008808 (EGF), LOC100352388 (PDGFA), LOC100356652 (GCSF), VEGFA
Transcription factors	GLI1, LOC100339156 (RUNX2), LOC100340325 (NFKB1), LOC100341629 (SOX2), LOC100342616 (SMAD5), SMAD1, SMAD2, SOX9

Table 7.3: Genes up-regulated in CPSC10 as compared to the sham control. 95% confidence interval (CI) is given in the bracket.

Gene code	Gene full name [209-218]	Gene functions [209-218]	Fold changes	95% CI
BMP5	bone morphogenetic protein 5	Ossification	13.21	(12.55, 13.87)
CD36	cluster of differentiation 36	Cell-Matrix Adhesion	24.46	(23.24, 25.69)
CTSK	cathepsin K	Ossification,ECM Proteases	30.54	(29.01, 32.06)
FN1	fibronectin 1	Cell Adhesion	11.67	(11.09, 12.26)
ITGA1	integrin, alpha 1	Cell-Matrix Adhesion	18.00	(17.10, 18.90)
ITGB1	integrin, beta 1	Calcium Ion Binding and Homeostasis,Cell-Cell Adhesion, Cell-Matrix Adhesion	18.00	(17.10, 18.90)
LOC100009177	collagen, type III, alpha 1	Collagens,Cell-Matrix Adhesion	89.26	(84.80, 93.73)
LOC100342904	annexin A5	Calcium Ion Binding and Homeostasis	10.67	(10.13, 11.20)
LOC100344425	integrin-binding sialoprotein	Ossification	28.05	(26.65, 29.45)
LOC100345812	transforming growth factor, beta receptor 1	Skeletal Development	12.58	(11.95, 13.20)
LOC100348414	bone morphogenetic protein 3	Ossification	20.05	(19.05, 21.06)
MMP13	matrix metallopeptidase 13	Bone Mineralization,ECM Proteases	30.22	(28.71, 31.73)
MMP2	matrix metallopeptidase 2	ECM Proteases	12.32	(11.70, 12.93)
MMP9	matrix metallopeptidase 9	Ossification,ECM Proteases	13.52	(12.85, 14.20)
SPP1	secreted phosphoprotein 1	Ossification,Osteoblast Differentiation	27.86	(26.46, 29.25)

Table 7.4: Genes up-regulated in CPSC10-05R as compared to the sham control. 95% confidence interval (CI) is given in the bracket.

Gene code	Gene full name [209-218]	Gene functions [209-218]	Fold changes	95% CI
BMP5	bone morphogenetic protein 5	Ossification	15.45	(14.68, 16.22)
CD36	cluster of differentiation 36	Cell-Matrix Adhesion	32.36	(30.74, 33.98)
COL1A2	collagen, type I, alpha 2	Collagens	52.39	(49.77, 55.01)
COL2A1	collagen, type II, alpha 1	Cartilage Condensation,Ossification, Collagens,	11.96	(11.36, 12.56)
CTSK	cathepsin K	Cell-Cell Adhesion Ossification,ECM Proteases	84.08	(79.88, 88.29)
FN1	fibronectin 1	Cell Adhesion	9.93	(9.43, 10.42)
ITGA1	integrin, alpha 1	Cell-Matrix Adhesion	21.09	(20.04, 22.15)
ITGB1	integrin, beta 1	Calcium Ion Binding and Homeostasis,Cell-Cell Adhesion, Cell-Matrix Adhesion	28.27	(26.86, 29.68)
LOC100009177	collagen, type III, alpha 1	Collagens,Cell-Matrix Adhesion	43.52	(41.35, 45.70)
LOC100338577	colony stimulating factor 1 (macrophage)	Ossification,Osteoclast Differentiation,Cell-Matrix Adhesion	19.68	(18.70, 20.67)
LOC100340503	bone gamma-carboxyglutamate (gla) protein	Ossification, Osteoclast Differentiation, Osteoblast Differentiation, Bone Mineralization,Calcium Ion Binding and Homeostasis,Cell Adhesion	72.07	(68.46, 75.67)

Gene code	Gene full name [209-218]	Gene functions [209-218]	Fold changes	95% CI
LOC100342904	annexin A5	Calcium Ion Binding and Homeostasis	13.17	(12.51, 13.82)
LOC100344425	integrin-binding sialoprotein	Ossification	79.27	(75.31, 83.24)
LOC100345812	transforming growth factor, beta receptor 1	Skeletal Development	16.27	(15.45, 17.08)
LOC100347598	collagen, type I, alpha 1	Ossification,Osteoblast Differentiation,Collagens	13.21	(12.55, 13.87)
LOC100348414	bone morphogenetic protein 3	Ossification	13.61	(12.93, 14.30)
MMP13	matrix metallopeptidase 13	Bone Mineralization,ECM Proteases	97.93	(93.04, 102.83)
MMP2	matrix metallopeptidase 2	ECM Proteases	9.07	(8.62, 9.52)
MMP9	matrix metallopeptidase 9	Ossification,ECM Proteases	10.42	(9.90, 10.94)
SMAD2	SMAD family member 2	Transcription Factor	12.56	(11.94, 13.19)
SPP1	secreted phosphoprotein 1	Ossification,Osteoblast Differentiation	64.95	(61.70, 68.20)

7.7 Discussion

Material properties of CPSC are primarily attributed to the hydration of calcium silicate in CPSC and the formation of CSH gel. The reduction in compressive strength and setting rate are corresponding to the decrease in CSH gel content and increase in the amorphous phase content (Fig. 7.1 and 7.2). In our previously published study, it was reported that RA is progressively adsorbed onto the unreacted CS surfaces and this may interfere with further hydration [19]. Therefore, the increase of RA concentration from 0.5% to 1.0% significantly affects the CSH gel formation in the hardened CPSC. At the relatively low RA concentration level of 0.5%, the setting rate and compressive strength decrease insignificantly as compared to CPSC, i.e., by 2.3% and 3.0% (7-day strength) respectively. While the 7-day and 3-day compressive strengths of CPSC10 and CPSC10-05R are similar, these values are different for CPSC10-10R, i.e., 3-day setting sample strength is only about half of that setting for 7 days. This may be attributed to the fact that interference on CSH crystal structure due to the apatite precipitation and amorphous phase formation is time-dependent and RA-content dependent. It was previously shown that MCP reacts with $Ca(OH)_2$ to precipitate apatite within CSH gel [33]. CPSC10-10R is exceptional because initially the hydration reaction is impeded by RA and hydration proceeds slowly, resulting in higher compressive strengths only after 7 days [19].

Porosity larger than 5 μm for the three types of 7-days set cement samples is visualized by μCT evaluations in Fig. 7.3, and quantified in Table 7.1. However majority of pores in calcium-silicate based cements are below 1 μm [219]. It is understandable therefore that the porosity measured by μCT is far below that determined by gas sorption. The general trend is that CPSC10 had the highest average porosity among the three types of samples regardless of the measurement methods. However, the gas sorption method determines the porosity fraction in the

range of about 13-23%, i.e., 3-4 times higher than the μCT method. Clearly, there is a significant fraction (8-17%) of porosity < 5 μm in all samples, which is typical to calcium silicate-based cements. The micrograph results (Fig 7.5) are in a good agreement with μCT visualization. As discussed, the interference of RA on CPSC hydration disrupted the crystal structures of CSH gel and creates large size (> 5 μm) porosity. Therefore, the compressive strengths of CPSC10-10R were reduced compared to those of CPSC10 and CPSC10-05R.

In the FTIR spectrum (Fig. 7.4), the shift of the double peaks of phosphonate groups in RA to higher wavenumbers (between 1400 cm^{-1} and 1500 cm^{-1}). It was previously reported that the double peaks of phosphonate groups of RAC (i.e., RA-calcium complex) in the RA-added CSC shifted to higher wavenumbers as compared to pure RA (around 800 cm^{-1}) or RAC made by reacting RA with calcium salts (around 900 cm^{-1}) [19]. Such changes indicate that RAC present in CPSC10 is likely neither pure RA nor pure RAC and such RAC can be bonded to apatite or CSH crystals. It is anticipated therefore that during the degradation of CPSC10 *in vivo*, RAC would be released to the close vicinity tissue, effectively to achieve a controllable release pattern as previously indicated [19].

In vitro cytotoxicity measures the biocompatibility of a biomaterial. In this study (Fig. 7.6), the effects of RA (between 0.5% and 1.0% RA) on CPSC cytotoxicity were analyzed. It was demonstrated that CPSC was non-cytotoxic to osteoblast cells in Chapter 6. In this study, it was further proved that RA incorporation in CPSC (up to 1.0%) showed no cytotoxic effects on osteoblast cells. This finding well agrees with our observation in Chapter 5, in which a RA delivery system by CSC was evaluated based upon its cytotoxicity on osteoblast cells. In Chapter 6, it was also shown that CPSC improved osteoblast cells proliferation. In this study, the DNA tetraploid amount was compared between osteoblast cell samples treated by CPSC10, CPSC10-

05R RA and CPSC10-10R and proved that CPSC has slightly higher proliferating effects on osteoblast than CPSC10-10R but slightly lower than CPSC10-05R. However, these differences are not statistically significant. This proves that CPSC-R has the same proliferating effects on osteoblast cells as pure CPSC.

In Fig. 7.8, 4 osteoblast-specific genes expressions were compared between CPSC10, CPSC10-05R and CPSC10-10R. As a mediator, runx2 plays an important role in osteoblast differentiation [35]. It has been observed that CSPS10-05R significantly increases the expression of runx2 in osteoblasts compared to CPSC10 and CPSC10-10R. RA up-regulating effects on runx2 expression have been also observed in another study, in which it was shown that such upregulating effects were time and concentration-dependent [140]. This explains the down-regulation of runx2 expression in CPSC10-10R. The transcription factor,runx2, regulates the expression the ALP, which is responsible for osteoblast differentiation, and the up-regulation of ALP gene in CPSC10-05R compared to the other two groups well agrees with the runx2 expressions [35]. OPG is a decoy receptor to RANKL and RANK and inhibits the recruitment of osteoclast cells [139, 220]. The up-regulation of OPG expressions in RA-added samples proved that RA has a profound effect on osteoblast differentiation and anti-osteoclastogenesis. In both OPG and ALP expressions, it has been found that CPSC10-10R expressions are lower than CPSC10-05R because RA has concentration-dependent effects on these genes' expressions [139, 221, 222]. However, TGF-β expressions are down-regulated with RA in Fig. 7.8d. This may be attributed to the SiO_4^{4-} ion concentration difference among these samples. TGF-β expression is highly depending on the SiO_4^{4-} concentration, and RA high affinity for CSH gel and apatite prevents the dissolution of SiO_4^{4-} into extracts [19, 223]. Based upon these quantitative studies on *in vitro* CPSC-R effects on osteoblast cells, it can be implied that CPSC-R system can

promote both osteoblastic proliferation and differentiation. RA is responsible for up-regulating differentiation-specific genes, i.e., improving osteoblast cells' differentiation into either osteocytes or lining cells [156]. On the other hand, Ca^{2+}, SiO_4^{4-} and PO_4^{3-} are released from CPSC cement to encourage osteoblast cells proliferation.

To proceed to *in vivo* evaluation of CPSC as a RA delivery system, CPSC with 0.5% RA was selected as the study sample because, based on the *ex vivo* studies, CPSC10-05R shows better mechanical properties and gene up-regulating effectiveness than CPSC10-10R. Unlike the *in vivo* study reported in Chapter 6, the animals used in this study had osteoporosis induced before the implantation or surgery. To induce osteoporosis in healthy rabbits, two-step treatments were performed, bilateral ovariectomy and glucocorticoid injection. Though osteoporotic model creation in rabbits is not as often studied as in rats and mice, Kaveh *et al.* have successfully induced osteoporosis in female rabbits [179]. Bilateral ovariectomy was aimed to result in estrogen deficiency in female rabbits, which is similar to estrogen removal in women after menopausal period. Estrogen deficiency activates osteoclast cell precursors differentiating into mature osteoclast cells and increases osteoclast activities [224]. Meanwhile, the injection of glucocorticoid affects both osteoblast and osteocytes because glucocorticoids can induce apoptosis of both osteoblasts and osteocytes and prevent osteoblasts from synthesizing ECM [225].

In this study, the biomarker TRACP-5b was measured at a 2-week interval (Fig. 7.9) during the model creation and the results indicates that the serum level was significantly elevated, i.e., by ~20% ($p < 0.05$). This result strongly implies that osteoclastic activities have been successfully increased in experimental animals [226]. After implantation of bone cement, this biomarker was also evaluated at the same intervals from the 4th week until the end of our

study. The results (Fig. 7.22) indicate that the animals treated with RA received a significant reduction in this biomarker, i.e., by more than 100% as compared to the sham control after 10 weeks ($p < 0.05$). However, in the group of animals implanted with CPSC10 but not treated by RA, the biomarker reduction was not statistically ($p < 0.05$) significant as compared to the sham control group. Therefore, it is reasonable to conclude that RA-added CPSC10 has positive effects in treating osteoporosis by reducing osteoclastic activities and decreasing the number of osteoclast cells [41-45, 133-138].

In our study, both serum BALP and OCN levels (Fig. 7.10 and 7.11) were significantly reduced in CPSC10-05R groups as compared to the sham control after 10 weeks by 50% ($p < 0.05$) and 100% ($p < 0.05$), respectively, agreeing with a previous study demonstrating that RA effectively reduced BALP levels in Paget's disease patients [125]. Bone-specific alkaline phosphatase (BALP) and osteocalcin (OCN) are released from osteoblast-like cells and their elevated levels are strongly related to high bone turnover [169, 170]. In addition, it is also found that CPSC10 significantly decreased serum BALP and OCN levels as well ($p < 0.05$). These results indicate that CPSC as RA delivery system could effectively reduce the bone turnover rate and therefore effectively treat osteoporosis because a high turnover rate is linked to osteoporosis [227]. Though data showed that both ALP and OCN levels were lower in the CPSC10-05R group than CPSC10 group, the differences were not significant after 10 weeks ($p < 0.05$). This may imply that RA concentration in CPSC10 was too low (0.5%) to result in statistically significant differences.

In our study, it is found that OPG/RANKL ratio was statically indifferent between the sham control, CPSC10 and CPSC10R groups ($p < 0.05$). This result implies that neither RA nor CPSC has positive effects in reducing RANKL synthesis or promoting OPG synthesis within

osteoblast cells. RANKL (receptor activator of nuclear factor NF-κB ligand) belongs to the family of tumor necrosis factor family and secreted by osteoblast cells [228]. This protein binds with RANK on osteoclast precursors to activate the differentiation of mature osteoclast cells [228]. Osteoprotegerin is the antagonist to RANKL and also released from osteoblast cells. It can bind with RNAKL and prevent the pathway RANK/RANKL on osteoclast precursors to differentiate in mature osteoclast cells. Therefore, the ratio of OPG/RANKL strongly indicates osteoclastogenic activity.

During bone resorption, type I collagen is broken down by enzyme cathepsin K synthesized by mature osteoclasts [169, 171]. N- and C- terminus at the non-helical regions on type I collagens are called N- and C-telopeptide, respectively, and crosslinks are formed in these regions. After collagens breakdown, crosslinks are present in two forms: peptide bound and free forms [169]. The peptide bound forms include (N-terminal cross-linked telopeptide of Type I collagen (NTX) and C-terminal cross-linked telopeptide of Type I collagen (CTX); while, pyridinoline crosslinks (PYD) and deoxypyridinoline crosslinks (DPD) are free forms. In Fig. 7.13 to 7.16, CTX, NTX, DPD and PYD levels in serum were significantly elevated in the sham control group compared to treated groups ($p < 0.05$), which strongly indicates that bone resorption, or more specifically type I collagen breakdown, was significantly hampered by the implants. However, after 10 weeks, the DPD serum level was significantly ($p < 0.05$) higher in CPSC10-05R by 20% than CPSC10 group. This may be caused by different blood collection times from each group. All of these biomarkers are affected by physiological factors, such as diet, and their levels vary with time [229-232]. One study found that urine excretion of DPD was 61% higher in the night than in the morning [229]. Therefore, variations of these biomarkers between CPSC10 and CPSC10-05R may result from the above mentioned facts. In addition, it is

also implied that RA has no effect on preventing type I collagen breakdown. Therefore the only preventing effect, based upon these data, is from CPSC10.

Type I collagen is synthesized from the procollagen molecule, in which there are amino- and carboxy-terminal extension peptides [172]. Carboxy-terminal propeptide of type I procollagen (PICP) and amino-terminal propeptide of type I procollagen (PICP) are released into blood during bone formation and their levels are related to bone turnover rate [172, 233, 234]. In our study, it is found that both serum PICP and PINP levels were significantly decreased in CPSC10 and CPSC10-05R as compared to the sham control ($p < 0.05$). This finding implies that CPSC10 could effectively reduce bone turnover rate and treat osteoporosis. Based upon our data, it is not observed that RA had addition effects on PICP or PINP levels. Another clinical study, however, indicated BP can change PICP serum level significantly. This may be attributed to low (0.5%) RA concentration in CPSC10.

During the collagen breakdown in bone resorption, another protein, hydroxyproline (OHP), is also released and found in serum [172]. OHP is formed by post-translational hydroxylation in this peptide chain and accounts for 13-14% of the amino acid quantity in collagens [172]. Since OHP derived from collagen breakdown cannot be reutilized in collagen formation [172], it appears as a good indicator of bone resorption. Meanwhile, amino acids, hydroxylysine, are also freed from collagenous networks in the form of galactosyl hydroxylysine (GHYL) and can be found in serum [172]. Since GHYL cannot be metabolized in body, it is also an indicator of bone resorption [172]. Figure 7.17 shows serum OHP levels up to 10 weeks in all three samples. It is clearly indicated that the OHP level in the sham control was significantly elevated as compared to the CPSC10 and CPSC10-05R group ($p < 0.05$). Serum GHYL levels in CPSC10 and CPSC10-05R were significantly lower than the sham control ($p < 0.05$). However,

in both biomarkers, differences between CPSC10 and CPSC10-05R were not statistically significant. It was previously reported that oral intakes of BPs had profound effects in reducing serum OHP level by 50% [235]; however, in our study, this effect was not observed. This could be also attributed to low concentration of RA in CPSC10.

Bone sialoprotein (BSP) is the last biomarker tested in this study. It is synthesized by osteoblast cells and released during bone resorption [172]. However, practical studies of BSP found that it is actually more correlated with bone resorption than bone formation [236]. Therefore, in our study, BSP was also used as an indicator of bone resorption. In Fig. 7.18, serum BSP levels in both CPSC10 and CPSC10-05R were significantly lower than that in the sham control ($p < 0.05$), indicating that bone resorption was impeded by implantation. Similar to other biomarkers reported in this study, any significant effects from RA incorporation were not observed. Another clinical study, however, found that *i.v.* administration of bisphosphonate could rapidly reduce serum BSP level as few as 4 days [236]. These results can be also explained by the relatively low RA concentration in CPSC10 and the related low release rate of RA from CPSC10.

Based upon the abovemetioned biomarker analysis, it is reasonable to conclude that CPSC10, or CPSC bone cements in general, could significantly reduce the rate bone turnover and decrease the prevalence of abnormal bone resorption associated with osteoporosis. However, it could not be concluded that RA had some additional benefits in bone resorption prevention. One reason could be because of the low concentration of RA in CPSC10, i.e., too low to be significantly effective. In addition, most RA was trapped within slowly degrading CPSC10. It is expected however that the continued slow degradation of CPSC10 would release more RA and thus the results could be different in the long term. Nevertheless, even at this low concentration,

RA resulted in a significant reduction in osteoclastic activities (TRACP-5b) and demonstrated a potential for positive treatment of osteoporosis.

Radiographic studies (Fig. 7.23 to 7.25) and histological analyses (Fig. 7.26) indicated that there was more bone formation in RA-CPSC than in CPSC after 10 weeks of implantation. Semi-quantitative analyses based upon X-ray images (Fig. 7.23) showed that the difference of new bone formation scores between CPSC and RA-CPSC was larger after 10 weeks than after 8 weeks, indicating that the resorption of new bone was higher in CPSC than RA-CPSC [237, 238]. These results, however, are not statistically significant, implying that long term studies, for example 6 months or longer, are needed to achieve significant results. Histological observations confirmed that the number of osteoclast cells was reduced in RA-CPSC *vs.* CPSC after 10 weeks, implying that osteoclast survival and their activities were suppressed in RA-CPSC because of RA-induced osteoclast apoptosis[237]. The presence of granulation tissues indicated that the healing process started and was better in RA-CPSC and CPSC than the control group, indicating that fractural restoration was enhanced because of CPSC [238]. The above studies showed that, as a RA local delivery system, RA-CPSC could provide superior biological (longer-term) stability and osseointegration than CPSC. In addition, the differences in preventing bone resorption between local and systemic effects might be attributed to the slow release of RA from CPSC. It was attempted to analyze the RA *in vitro* release from CPSC in PBS up to 6 months. However, the concentration of the drug was below the resolution of the chromatographic method. RA was likely taken up by peri-implant bone minerals, resulting in significant local effects, but insignificant systemic effects.

The importance of PCR array is that all osteogenesis-related genes can be analyzed and compared simultaneously. In the PCR array results, two parameters determine the interpretation

of the results, the statistical significance and the biological significance. The statistical significance is easy to understand, i.e., through determination of the *p*-values of the results. The biological significance refers to the threshold fold changes in the data [239, 240]. This represents the upper and lower limits of indifferent gene expressions, within which gene expressions are considered not biologically up-regulated or down-regulated. The choice of this value is depending on particular diseases or pathways that PCR arrays analyze [239, 240]. In this study, the threshold value was 3 by default.

The relevant information on all genes analyzed in this study can be found from the website of National Centre of Biotechnology Information (NCBI, http://www.ncbi.nlm.nih.gov/). For example, BMP5 (bone morphogenetic protein 5) and LOC100348414 (bone morphogenetic protein 3) are responsible for encoding the member proteins in the bone morphogenetic protein family [209]. Bone morphogenetic proteins have the ability to induce endochondral osteogenesis *in vivo*. CD36 (cluster of differentiation 36) encodes the fourth major glycoprotein of the platelet surface, which serves as a receptor for thrombospondin in platelets and various cell lines. Because thrombospondins are involved in adhesive processes [210], gene CD36 plays an important role in cell-matrix adhesion. CTSK (cathepsin K) encodes the synthesis of protein, cathepsin K, which is responsible for degrading collagens in ECM [40]. FN1 (fibronectin 1) encodes the protein, fibronectin, in ECM, which can promote cell attachment migration and differentiation [211]. ITGA1 (integrin, alpha 1) and ITGB1 (integrin, beta 1) are responsible for encoding subunits of integrin receptor, alpha 1 and beta 1, respective. Integrin receptors with alpha 1 and beta 1 subunits can form cell-surface receptors for collagens [212]. LOC100009177 (collagen, type III, alpha 1) is used to encode type III collagen with alpha 1 chain [213]. LOC100342904 (annexin A5) is responsible for encoding proteins in annexin family, which can

bind Ca^{2+} ions from blood [214]. Other than these abovemetioned genes, there were another 6 genes also up-regulated in both CPSC10 and CPSC10-05R as compared to the sham control. The functions of these 15 genes cover ossification, cell matrix adhesion, calcium biding, mineralization, cell differentiation and ECM formation during osteogenesis, and up-regulations of these genes in both statistical and biological ways indicate that CPSC promoted osteogenesis because releases of Ca^{2+} , PO_4^{3-} and SiO_4^{4-} ions from CPSC degradation encourage bone formation [215].

There were additional 6 genes that were only up-regulated in the CPSC10-05R group as compared to the CPSC10 group. COL1A2 (collagen, type I, alpha 2), COL2A1(collagen, type II, alpha 1) and LOC100347598 (collagen, type I, alpha 1) are responsible for encoding collagens in osteoblast cells, which are subsequently forming the organic matrix in ECM [213], and especially COL2A1 is an important marker of chondrocyte differentiation, which converts immature proliferating chondrocytes into hypertrophying chondrocytes and facilitate the endochondral ossification [241-243]. LOC100338577 (colony stimulating factor 1 (macrophage) encodes macrophage colony stimulating factor 1 protein, which is less synthesized in osteoporotic conditions [216]. LOC100340503 (bone gamma-carboxyglutamate (gla)) encodes the synthesis of bone gamma-carboxyglutamate (gla) protein. This protein is mainly found in blood plasma and plays an important role in blood coagulation [217]. SMAD2 (SMAD family member 2) controls the synthesis of protein in the SMAD family. SAMD family proteins are important transcription factors controlling the transforming growth factor β pathways [218]. The up-regulations of these 6 genes can be explained by the incorporation of RA in CPSC [217, 244, 245], and these results strongly indicate that RA had additional benefits in promoting osteogenesis under the osteoporotic conditions.

In conclusion, the PCR array analyzes results were in a good agreement with radiographic and histological observations. Though, from the global point of view, it was inconclusive to imply any benefits of RA in bone resorption prevention, the local bone formation studies including radiography, histology and PCR array indicates that RA could improve bone formation and prevent resorption of bone close to CPSC-R implants, possibly because the amount of RA released was small and mostly absorbed by bone close to implants [148].

Chapter 8: CONCLUSIONS AND FUTURE WORK

8.1 Conclusions

The important discovery of this research is that both risedronic acid (RA) and mono-calcium phosphate (MCP) have significant impact on calcium silicate cement (CSC) hydration process and thus also on the set material properties. Increasing the amount of RA loaded into CSC affected CSC properties in a concentration-dependent manner. In particular, the addition of RA increased the setting time of RA-free CSC from 58 min to 95 min and reduced its compressive strength to below 1 MPa when RA concentration was 1.0 wt%. However, when RA concentration was limited to 0.5 wt%, the setting time and compressive strength of the cement were 84 min and 19.4 MPa (7-day), respectively. This is a clear indication that RA interferes with CSC hydration reactions. Based on FTIR and adsorption/desorption studies, RA was found to be progressively adsorbed onto the unreacted calcium silicate (CS) to prevent further CS hydration. This mechanism changed the calcium-silicate-hydrate (CSH) gel microstructure and decreased hardened cement crystallinity. For example, compared to the pure CSC, the CSC10R (i.e., CSC with 1% addition of RA) had a discontinuous CSH microstructure, where CSH crystals were significantly smaller (i.e., 0.5 to 3 μm), as compared to the CSH crystals in RA-free cements (i.e., up to 8 μm). Rietveld refinement based upon X-ray diffraction showed that the volume fraction of CSH gel in CSC10R was only about one fifth of that in CSC, for the same setting time of 7 days.

The addition of MCP also affected CSC material properties. Both setting time and compressive strength of CPSC were reduced with MCP content. The setting time decreased from more than 150 min in CPSC5 (i.e., containing 5 wt% of MCP) to about 70 min in CPSC15 and both 3 and 7 day compressive strengths reduced from 22 MPa in CPSC5 to 10 MPa in CPSC15.

Although the presence of MCP increased CSC hydration rate, FTIR and Rietveld refinement analysis revealed that simultaneous formation of the apatite could have interrupted the continuity of the resulting CSH gel microstructure. In addition, μCT visualization of CPSC porosity demonstrated that excess water produced from the reaction between MCP and $Ca(OH)_2$ evaporated and thus increased the set CSC porosity (2.46% *vs.*12.86%, CPSC5 *vs.*CPSC15). Consequently, the excessive porosity was responsible for strength reduction of the hardened CPSC15 to 8.93MPa (*vs.*21.54 MPa for CPSC5, after 7 days setting).

When RA was added into CSC with 10% MCP, it was found that both the setting time and compressive strength were affected as well in a concentration-dependent manner. When 1.0% of RA was added, the setting time of CPSC10 increased by more than 40 min and the 3-day compressive strength of CPSC10 was nearly halved. Like RA in CSC, CSH gel formation and microstructure of CPSC were also compromised. Rietveld refinement found that RA resulted in increased content of the amorphous phase of CSH gel. Based upon FTIR study and previously determined RA impact on pure CSC, it is concluded that the adsorbed RA prevented further hydration of the unreacted CS in CPSC, thus disrupted the hydration process and therefore also changed the setting time and compressive strength.

Our study indicates that RA can be released from CSC in a sustainable and controllable manner. It appears that the overall RA release rate is determined to a large extent by the resorption rate of the carrier cement. Only ~10% of RA was released from CSC within the first month and, in the following 5 months, the release was almost equal to zero. The FTIR study found that RA formed RA-calcium complex, RAC in short. HPLC measurements revealed that RAC had a much smaller (i.e., by a factor of $10^4 \sim 10^5$) solubility in phosphate buffer solution (PBS) than RA. The experimental RA release profiles agreed well with the theoretical

predictions from the Higuchi model, providing the solubility of RAC was used in the calculations (rather than the solubility of RA). The release pattern of RA from CSC into PBS could be in general described as an initial burst in the first week, followed by a pseudo-steady state which slowed down significantly after 2 weeks. In total, 80% ~ 90% of the total RA release took place within that period. However, after 4 weeks of release, more than 90% of the initially loaded RA still remained inside the non-resorbed CSC, implying that the RA release from CSC was mainly degradation-controlled, rather than diffusion-controlled. It can be therefore anticipated that, when implanted in body, RA will be released into body with the rate limited by the relatively slow degradation of CSC. While this work did not generate sufficient volume of data to quantify *in vivo* degradation rate of CSC, it is anticipated that CPSC degradation rate could be up to ~10X slower than the degradation rate of calcium phosphate cements (CPC). It is also important to emphasize that such CSC-based drug delivery system (DDS) will not cause any adverse toxic side effects due the sudden increase of RA concentration in blood plasma.

This work demonstrated that the CPSC-based RA delivery system was biocompatible and enhanced *in vitro* osteoblast cell proliferation and differentiation. MTT assays proved that RA-added CSC, RA-free CPSC, and RA-added CPSC were non-cytotoxic to osteoblast cells as compared to cells treated by the control medium (purely nutrients). Genetic analyses provided evidence for up-regulation of TGF-β expression and down-regulations of ALP, runx2 and OCN expressions, suggesting that CPSC stimulates osteoblast cell proliferation. Flow cytometry data demonstrated that CPSC significantly increased the relative quantity of proliferating cells as compared to the control ($p < 0.05$), also implying that CPSC enhanced *in vitro* osteoblast proliferation. When RA was added into CPSC, differentiation-specific genes, such as ALP, runx2 and OCN, in osteoblast cells were significantly ($p < 0.05$) up-regulated by CPSC10-05R

(0.5% RA) as compared to CPSC10. These results prove that CPSC-R could improve *in vitro* osteoblast differentiation. Flow cytometry data showed that the relative quantities of the cells undergoing mitosis (i.e., proliferating) was statistically indifferent ($p < 0.05$) between CPSC and CPSC-R, implying that CPSC-R systems could improve *in vitro* osteoblast proliferation as much as CPSC.

In the *in vivo* study of CPSC, clinically used calcium phosphate cement (CPC) was the control (reference) material. Radiographic examinations of the implantation sites were performed after 2 and 3 months of material implantation. The histology studies were carried out after animal euthanasia to evaluate new bone formation and inflammation in regions close to implant or perforation. The X-ray images showed that CPSC degraded significantly slower than the reference CPC and had more newly formed trabecular bone after 3 months of implantation. CT images agreed well with the X-ray observations. These results imply that CPSC could provide better osseointegration than the current clinically CPC. However, due to the relatively low resolution of the X-ray images (80 μm per pixel) and the CT images (0.625 mm per layer) images, the volumes of the remnant implants and the newly formed trabecular bone could not be accurately differentiated and determined. As a result, the semi-quantitative studies attempted to quantify the differences in the *in vivo* material degradation and bone formation rates between CPSC and CPC failed. The histological slides analysis demonstrated that CPSC appeared to accelerate the local bone formation rate as compared to CPC and both CPSC and CPC appeared to enhance bone formation as compared to the sham control group.

The quantitative biomarker study in the i*n vivo* evaluation of CPSC as local a drug delivery system of RA demonstrated that CPSC-R could significantly reduce the prevalence of osteoporosis but insignificantly prevent bone turnover and collagen breakdown as compared to

CPSC-treated rabbits. Serum TRACP-5b levels were significantly lower in the CPSC10-05R group than the sham control one by ~100% ($p < 0.05$); however, serum TRACP-5b levels in the CPSC10 group did not reduced significantly as compared to the sham control ($p < 0.05$). These results imply that CPSC as a local delivery system of RA could effectively reduce osteoclast cell activities and therefore also treat osteoporosis. Biomarkers, such as BSP, BALP and OCN are good indicators of bone turnover rate and these biomarkers were significantly lower in both CPSC10 and CPSC10-05R groups than in the sham control group ($p < 0.05$). However, the differences between the serum levels in CPSC10 and CPSC10-05 groups were not statically significant ($p < 0.05$). The above results suggest that CPSC as an implant could effectively reduce bone turnover rate in osteoporotic patients. The answer to question whether RA could result in additional effects in preventing bone remolding was inconclusive, possible because the RA concentration in CPSC10-05R was too low (i.e., only 0.5%) to be significantly effective. Furthermore, the biomarkers related to collagen breakdown during bone resorption, such as NTX, CTX, DPD, PYD, PICP, PINP, OHP and GHYL, were significantly lower in both CPSC10 and CPSC10-05R groups than in the sham control group ($p < 0.05$), implying that CPSC as an implant could effectively prevent collagen breakdown. Unfortunately, the assessment of RA effects in the prevention of collagen breakdown remained inconclusive, possibly also because RA concentration in CPSC10-05R was too low to be significantly effective

Radiographic examinations in the *in vivo* study of CPSC-R were performed after 8 and 10 weeks of material implantation and histology studies were carried out after animal euthanasia to evaluate new bone formation in the areas close to implant or perforation. The qualitative study on both X-ray and CT images showed that CPSC10-05R improved osseointegration of implant with the newly formed trabecular bone after 10 weeks as compared to the CPSC10 group. It is

suggested that this is because RA was locally released and prevented osteoclast cells from resorbing new trabecular bone. However, semi-quantitative studies could not be performed because the resolutions of the clinical X-ray and CT systems were too low (80 μm per pixel and 0.625 mm per layer, respectively) to accurately determine the volumes of remnant implants and newly formed trabecular bones. Histological observations demonstrated that there appeared to be more newly formed trabecular bone in CPSC10-05R than CPSC10 possibly because RA improved local bone formation.

Quantitative analyses of osteogenesis-related gene expressions in CPSC10 and CPSC10-095R as compared to the sham control were performed with PCR arrays. PCR array results showed that 15 genes were significantly up-regulated in both CPSC10 and CPSC10-05R groups as compared to the sham control ($p < 0.05$). These up-regulations of gene expression were from the lowest of 9.07-fold (MMP2, CPSC10-05R *vs.* the sham control) to the highest of 97.93-fold (MMP13, CPSC10-05R *vs.* the sham control). In addition, there were 6 more genes that were significantly up-regulated only in CPSC10-05R, (and not in CPSC10), as compared to the sham control ($p < 0.05$). These additional up-regulations of gene expressions were attributed to effects of local RA release from CPSC10. These results indicate that both CPSC and CPSC-R had positive effects in promoting bone formation under the osteoporotic conditions. Because of the local release of RA from CPSC, the CPSC-R appeared to be superior to CPSC in improving osteogenesis.

In summary, this research provided the initial indications that CPSC could act as a potential RA delivery system for the more effective bone loss and/or fracture restoration. This might be especially true for patients with osteoporosis. Based upon our results, it is concluded that CPSC-R drug delivery system could effectively improve local bone formation and

osteogenesis and prevent bone resorption. However, from the systemic (global) point of view, while CPSC as the RA drug delivery system effectively reduced osteoclastic activities, it could not be concluded that CPSC-R also prevented collagen breakdown and reduced bone turnover rates.

8.2 Future work

The present work generated only preliminary results for the complex CPSC-R bone cement as a possible drug delivery system for general use as well as for osteoporotic patients. Therefore there are many issues related to CPSC bone cement and its drug incorporation, which remain to be evaluated and resolved.

The particular area requiring significant improvement relates to the cement material properties, in particular for the cements containing larger amounts of RA. The work should explore the kinetics and mechanisms of RAC complexes formation and absorption within the cements structure, thus elucidating the possibilities for avoiding the decreased hydration rate and decreased strength of CPSC-R systems. Alternatively, the search for biocompatible hydration rate accelerators should be initiated. Bone cements are usually injected into fracture bones in the paste form under the guidance of X-rays. Therefore, the injectability of CPSC-R is another research topic requiring particular attention if mechanically strong implants are of interest. As these are ceramic materials, any defect (e.g., pore or crack) produced during cement injection will affect the implant strength. X-ray visualization of such implants is one way to monitor *in situ* such defects formation. ZrO_2 is typically used as an additive to increase the radio-opacity under the X-ray guidance. The effects of radio-opacifier on cement properties, both structural and biological, should be initiated in the future.

As determined in this work, RA significantly affects CPSC material properties by increasing the setting time and reducing the compressive strength. Therefore, alternative methods of RA loading into the cement, while avoiding the decrease of the cement strength (and without compromising its drug loading capacity), are needed. One possibility could be to formulate microspheres of drugs encapsulated within biodegradable polymers and then to incorporate such microspheres within the cement. Such research would also have to evaluate the impact of the microspheres on cement properties.

CPSC drug loading capacity, and the quantitative specifics of drug release mechanism, is an important research area for future work, both for direct RA loading (explored in this work) as well as indirect drug loading through the admixed microspheres. In addition, there is increasing interest in adding protein-based bone growth factors into bone cements. However, CPSC is highly alkaline and thus will destroy the structure and functionality of these proteins. How to incorporate the proteins in CPSC without compromising the protein efficacy is another research topic concerning the broad issue of the application of CPSC in drug delivery systems.

Recent studies argue the safety of X-rays exposure, i.e., in terms of permanent damage to tissues and organs in surgery operators. There is increasing interest to use magnetic resonance to replace X-rays as the visualization method. Therefore, the future work should look into the modifications to CPSC to achieve acceptable response to magnetic fields.

Finally, more *in vivo* studies are required to help better understanding CPSC as the RA local delivery system. As discussed in the previous sections, semi-quantitative analyses attempting to quantify the rates of *in vivo* CPSC degradation and new bone formation based upon clinical X-rays and CT systems failed because of too low image resolutions. In future, it is proposed to use 3D micro-CT to quantify the bone formation as well as material degradation.

μCT has a much higher resolution (5 μm) than the clinical CT systems (0.625 mm). This high resolution could enable non-invasive visualization of the implant as well as the tissue around implant and quantitatively determine the parameters important in evaluating implant *in vivo* performance, such as rates of implant degradation, rates of new bone formation, degrees of osseointegration and contact areas between the implants and trabecular bones.

The current studies were inconclusive in indicating that RA locally released from CPSC may additionally help in preventing high bone turnover and collagen breakdown. In the future studies, RA concentrations in CPSC should be increased in a stepwise manner until it can be observed that RA results in significant changes in the prevention of collagen breakdown. Furthermore, large animals studies are needed to evaluate the long-term effects of CPSC-R in bone restoration and osteoporosis treatment as well as the potential hazards to immune systems. Long-term study (> 1 year) of both intra- and post implantation effects, e.g., biosafety and bioactivity, of implants on host animals is needed. Finally, clinical trials must be commenced to observe CPSC-R biological performance in human beings, i.e., whether CPSC-R could meet the rigorous requirements of safety and positive clinical expectations (effectiveness).

REFERENCES

[1] US Census Bureau: International database. Table 094. Midyear population, by age and sex. (government document)2010.
[2] Prasad S, Sung B, Aggarwal BB. Age-associated chronic diseases require age-old medicine: role of chronic inflammation. Prev Med. 2012;54 Suppl:S29-37.
[3] Schneider EL, Guralnik JM. The aging of America. Impact on health care costs. Jama. 1990;263:2335-2340.
[4] Osteoporosis Canada 2014. Available from: https://www.osteoporosis.ca/osteoporosis-and-you/what-is-osteoporosis/.
[5] Li JP, Li P, Hu J, Dong WY, Liao NN, Qi MC, *et al.* Early healing of hydroxyapatite-coated implants in grafted bone of zoledronate acid treated osteoporotic rabbits. J Periodontol. 2014:1-12.
[6] Qi MC, Zhou XQ, Hu J, Du ZJ, Yang JH, Liu M, *et al.* Oestrogen replacement therapy promotes bone healing around dental implants in osteoporotic rats. Int J Oral Maxillofac Surg. 2004;33:279-285.
[7] Arcos D, Boccaccini AR, Bohner M, Diez-Perez A, Epple M, Gomez-Barrena E, *et al.* The relevance of biomaterials to the prevention and treatment of osteoporosis. Acta Biomater. 2014;10:1793-1805.
[8] Benum P. The use of bone cement as an adjunct to internal fixation of supracondylar fractures of osteoporotic femurs. Acta orthop scand. 1977;48:52-56.
[9] Lopez-Heredia MA, Kamphuis GJ, Thune PC, Oner FC, Jansen JA, Walboomers XF. An injectable calcium phosphate cement for the local delivery of paclitaxel to bone. Biomaterials. 2011;32:5411-5416.
[10] Brown WE, Chow LC. A new calcium phosphate setting cement. J Dent Res. 1983;62:672-672.
[11] LeGeros R, Chohayeb A, Shulman A. Apatitic calcium phosphates: possible dental restorative materials. J Dent Res. 1982;61:343.
[12] Xu S, Lin K, Wang Z, Chang J, Wang L, Lu J, *et al.* Reconstruction of calvarial defect of rabbits using porous calcium silicate bioactive ceramics. Biomaterials. 2008;29:2588-2596.
[13] Ni S, Chang J, Chou L, Zhai W. Comparison of osteoblast-like cell responses to calcium silicate and tricalcium phosphate ceramics in vitro. J Biomed Mater Res B Appl Biomater. 2007;80:174-183.
[14] Tuna EB, Dincol ME, Gencay K, Aktoren O. Fracture resistance of immature teeth filled with BioAggregate, mineral trioxide aggregate and calcium hydroxide. Dent Traumatol. 2011;27:174-178.
[15] Obata A, Kasuga T. Cellular compatibility of bone-like apatite containing silicon species. J Biomed Mater Res A. 2008;85:140-144.
[16] el-Briak H, Durand D, Nurit J, Munier S, Pauvert B, Boudeville P. Study of a hydraulic dicalcium phosphate dihydrate/calcium oxide-based cement for dental applications. J Biomed Mater Res. 2002;63:447-453.
[17] Michailesco P, Kouassi M, El Briak H, Armynot A, Boudeville P. Antimicrobial activity and tightness of a DCPD-CaO-based hydraulic calcium phosphate cement for root canal filling. J Biomed Mater Res B Appl Biomater. 2005;74:760-767.
[18] Yu L, Li Y, Zhao K, Tang Y, Cheng Z, Chen J, *et al.* A novel injectable calcium phosphate cement-bioactive glass composite for bone regeneration. PloS one. 2013;8:e62570.

[19] Gong T, Wang Z, Zhang Y, Sun C, Yang Q, Troczynski T, *et al.* Preparation, characterization, release kinetics, and in vitro cytotoxicity of calcium silicate cement as a risedronate delivery system. J Biomed Mater Res A. 2014;102:2295-2304.
[20] Liu X, Ding C, Wang Z. Apatite formed on the surface of plasma-sprayed wollastonite coating immersed in simulated body fluid. Biomaterials. 2001;22:2007-2012.
[21] Siriphannon P, Kameshima Y, Yasumori A, Okada K, Hayashi S. Formation of hydroxyapatite on CaSiO3 powders in simulated body fluid. J Eur Ceram Soc 2002;22:511-520.
[22] Hench LL, Xynos ID, Edgar AJ, Buttery LDK, Polak JM, Zhong JP, *et al.* Gene activating glasses. Journal of Inorganic Materials. 2002;17:897-909.
[23] Maroothynaden J, Hench LL. Bioglass (R) stimulation of embryonic long-bones in altered loading environments. J Gravit Physiol. 2001;8:79-80.
[24] Santos JD, Jha LJ, Monteiro FJ. Surface modifications of glass-reinforced hydroxyapatite composites. Biomaterials. 1995;16:521-526.
[25] Skalny J, Gebauer J, Odler I. Materials science of concrete: special volume: calcium hydroxide in concrete (book): Wiley-Blackwell; 2001.
[26] Huan Z, Chang J. Calcium-phosphate-silicate composite bone cement: self-setting properties and in vitro bioactivity. J Mater Sci Mater Med. 2009;20:833-841.
[27] Schweitzer JS, Livingston RA, Rolfs C, Becker HW, Kubsky S. Ion beam analysis of the hydration of tricalcium silicate. Nuclear Instruments & Methods in Physics Research Section B-Beam Interactions with Materials and Atoms. 2003;207:80-84.
[28] Zhao W, Wang J, Zhai W, Wang Z, Chang J. The self-setting properties and in vitro bioactivity of tricalcium silicate. Biomaterials. 2005;26:6113-6121.
[29] Zhao W, Chang J. Sol–gel synthesis and in vitro bioactivity of tricalcium silicate powders. Mater Lett 2004;58:2350-2353.
[30] Sadiasa A, Sarkar SK, Franco RA, Min YK, Lee BT. Bioactive glass incorporation in calcium phosphate cement-based injectable bone substitute for improved in vitro biocompatibility and in vivo bone regeneration. J Biomater Appl. 2014;28:739-756.
[31] Zhou S, Ma J, Shen Y, Haapasalo M, Ruse ND, Yang Q, *et al.* In vitro studies of calcium phosphate silicate bone cements. J Mater Sci Mater Med. 2013;24:355-364.
[32] Li J, Qiu ZY, Zhou L, Lin T, Wan Y, Wang SQ, *et al.* Novel calcium silicate/calcium phosphate composites for potential applications as injectable bone cements. Biomed Mater. 2008;3:044102.
[33] Huan Z, Chang J. Novel tricalcium silicate/monocalcium phosphate monohydrate composite bone cement. J Biomed Mater Res B Appl Biomater. 2007;82:352-359.
[34] Zhao Q, Qian J, Zhou H, Yuan Y, Mao Y, Liu C. In vitro osteoblast-like and endothelial cells' response to calcium silicate/calcium phosphate cement. Biomed Mater. 2010;5:35004.
[35] Fei L, Wang C, Xue Y, Lin K, Chang J, Sun J. Osteogenic differentiation of osteoblasts induced by calcium silicate and calcium silicate/beta-tricalcium phosphate composite bioceramics. J Biomed Mater Res B Appl Biomater. 2012;100:1237-1244.
[36] Mori H, Manabe M, Kurachi Y, Nagumo M. Osseointegration of dental implants in rabbit bone with low mineral density. J Oral Maxillofac Surg. 1997;55:351-361.
[37] Becker W, Hujoel PP, Becker BE, Willingham H. Osteoporosis and implant failure: an exploratory case-control study. J Periodontol. 2000;71:625-631.
[38] Ozawa S, Ogawa T, Iida K, Sukotjo C, Hasegawa H, Nishimura RD, *et al.* Ovariectomy hinders the early stage of bone-implant integration: histomorphometric, biomechanical, and molecular analyses. Bone. 2002;30:137-143.

[39] Taxel P, Ortiz D, Shafer D, Pendrys D, Reisine S, Rengasamy K, *et al.* The relationship between implant stability and bone health markers in post-menopausal women with bisphosphonate exposure. Clin Oral Invest 2014;18:49-57.
[40] Rachner TD, Khosla S, Hofbauer LC. Osteoporosis: now and the future. Lancet. 2011;377:1276-1287.
[41] Rogers MJ, Crockett JC, Coxon FP, Monkkonen J. Biochemical and molecular mechanisms of action of bisphosphonates. Bone. 2011;49:34-41.
[42] Russell RG. Bisphosphonates: the first 40 years. Bone. 2011;49:2-19.
[43] Russell RG, Watts NB, Ebetino FH, Rogers MJ. Mechanisms of action of bisphosphonates: similarities and differences and their potential influence on clinical efficacy. Osteoporosis International. 2008;19:733-759.
[44] Ebetino FH, Hogan AM, Sun S, Tsoumpra MK, Duan X, Triffitt JT, *et al.* The relationship between the chemistry and biological activity of the bisphosphonates. Bone. 2011;49:20-33.
[45] Russell R. Determinants of structure–function relationships among bisphosphonates. Bone. 2007;40:S21-S25.
[46] Ezra A, Golomb G. Administration routes and delivery systems of bisphosphonates for the treatment of bone resorption. Adv Drug Deliv Rev. 2000;42:175-195.
[47] Gutta R, Louis PJ. Bisphosphonates and osteonecrosis of the jaws: science and rationale. Oral Surg Oral Med Oral Pathol Oral Radiol Endod. 2007;104:186-193.
[48] Boanini E, Torricelli P, Gazzano M, Fini M, Bigi A. The effect of zoledronate-hydroxyapatite nanocomposites on osteoclasts and osteoblast-like cells in vitro. Biomaterials. 2012;33:722-730.
[49] Panzavolta S, Torricelli P, Bracci B, Fini M, Bigi A. Functionalization of biomimetic calcium phosphate bone cements with alendronate. J Inorg Biochem. 2010;104:1099-1106.
[50] Kamerer DB, Hirsch BE, Snyderman CH, Costantino P, Friedman CD. Hydroxyapatite cement: a new method for achieving watertight closure in transtemporal surgery. Am J Otol. 1994;15:47-49.
[51] Constantz BR, Ison IC, Fulmer MT, Poser RD, Smith ST, VanWagoner M, *et al.* Skeletal repair by in situ formation of the mineral phase of bone. Science. 1995;267:1796-1799.
[52] Santos JD, Jha LJ, Monteiro FJ. In vitro calcium phosphate formation on SiO_2-Na_2O-CaO-P_2O_5 glass reinforced hydroxyapatite composite: A study by XPS analysis. J Mater Sci Mater Med. 1996;7:181-185.
[53] Tancred DC, Carr AJ, McCormack BA. The sintering and mechanical behavior of hydroxyapatite with bioglass additions. J Mater Sci Mater Med. 2001;12:81-93.
[54] Schnitzler V, Fayon F, Despas C, Khairoun I, Mellier C, Rouillon T, *et al.* Investigation of alendronate-doped apatitic cements as a potential technology for the prevention of osteoporotic hip fractures: critical influence of the drug introduction mode on the in vitro cement properties. Acta Biomater. 2011;7:759-770.
[55] de Aza PN, Guitian F, de Aza S. Bioactivity of wollastonite ceramics: In vitro evaluation. Scr Metall Mater. 1994;31:1001-1005.
[56] Hench LL, Wilson J. An introduction to bioceramics (book): World Scientific; 1993.
[57] Lin K, Chang J, Cheng R. In vitro hydroxyapatite forming ability and dissolution of tobermorite nanofibers. Acta Biomater. 2007;3:271-276.
[58] Richardson IG. The calcium silicate hydrates. Cement and Concrete Research. 2008;38:137-158.
[59] Gard J, Taylor H, Cliff G, Lorimer G. A reexamination of jennite. Am Mineral. 1977;62:365-368.

[60] Merlino S, Bonaccorsi E, Armbruster T. Tobermorites: Their real structure and order-disorder (OD) character. Am Mineral. 1999;84:1613-1621.
[61] Megaw HD, Kelsey CH. Crystal structure of tobermorite. Nature. 1956;177:390-391.
[62] Chen JJ, Thomas JJ, Taylor HFW, Jennings HM. Solubility and structure of calcium silicate hydrate. Cement and Concrete Research. 2004;34:1499-1519.
[63] Hamid S. Thecrystal structure of the 11 A natural tobermorite. Crystalline Materials. 1981;154:189-198.
[64] Lequeux N, Morau A, Philippot S, Boch P. Extended x-ray absorption fine structure investigation of calcium silicate hydrates. J Am Ceram Soc 1999;82:1299-1306.
[65] Taylor HW. Hydrated calcium silicates. Part I. Compound formation at ordinary temperatures. J Chem Soc. 1950:3682-3690.
[66] Gard J, Taylor H. Calcium silicate hydrate (II). Cement and Concrete Research. 1976;6:667-677.
[67] Yu P, Kirkpatrick RJ, Poe B, McMillan PF, Cong X. Structure of calcium silicate hydrate (C-S-H): near-, mid-, and far-infrared spectroscopy. J Am Ceram Soc 1999;82:742-748.
[68] Sueur L. Chemical and morphological studies of the hydration of tricalcium silicate. Proc Br Ceram Soc (conference) 1984. p. 177.
[69] Rayment D, Majumdar A. The composition of the CSH phases in portland cement pastes. Cement and Concrete Research. 1982;12:753-764.
[70] Grutzeck MW, Roy DM. Electron microprobe studies of the hydration of 3CaO. SiO_2 (book)1969.
[71] Taylor HFW, Newbury DE. An electron-microprobe study of a mature cement paste. Cement and Concrete Research. 1984;14:565-573.
[72] Richardson IG, Groves GW. Microstructure and microanalysis of hardened ordinary portland-cement pastes. J Mater Sci. 1993;28:265-277.
[73] Dent Glasser L, Lachowski E, Mohan K, Taylor H. A multi-method study of C_3S hydration. Cement and Concrete Research. 1978;8:733-739.
[74] Richardson I. The nature of CSH in hardened cements. Cement and Concrete Research. 1999;29:1131-1147.
[75] Groves G, Sueur P, Sinclair W. Transmission electron microscopy and microanalytical studies of ion-beam-thinned sections of tricalcium silicate paste. J Am Ceram Soc 1986;69:353-356.
[76] Cong X, Kirkpatrick RJ. ^{17}O MAS NMR investigation of the structure of calcium silicate hydrate gel. J Am Ceram Soc 1996;79:1585-1592.
[77] Thomas JJ, Chen JJ, Jennings HM, Neumann DA. Ca-OH bonding in the CSH gel phase of tricalcium silicate and white portland cement pastes measured by inelastic neutron scattering. Chem Mater 2003;15:3813-3817.
[78] Taylor HF. Cement chemistry (book): Thomas Telford; 1997.
[79] Allen AJ, Thomas JJ, Jennings HM. Composition and density of nanoscale calcium-silicate-hydrate in cement. Nat Mater. 2007;6:311-316.
[80] Klur I, Pollet B, Virlet J, Nonat A. CSH structure evolution with calcium content by multinuclear NMR. Nuclear Magnetic Resonance Spectroscopy of Cement-Based Materials (book):Springer;1998. p. 119-141.
[81] Cong X, Kirkpatrick RJ. ^{29}Si MAS NMR study of the structure of calcium silicate hydrate. Adv Cem Based Mater. 1996;3:144-156.

[82] Grutzeck M, Benesi A, Fanning B. Silicon-29 magic angle spinning nuclear magnetic resonance study of calcium silicate hydrates. J Am Ceram Soc 1989;72:665-668.
[83] Thomas JJ, Jennings HM. Effect of heat treatment on the pore structure and drying shrinkage behavior of hydrated cement paste. J Am Ceram Soc. 2002;85:2293-2298.
[84] Tennis PD, Jennings HM. A model for two types of calcium silicate hydrate in the microstructure of Portland cement pastes. Cement and Concrete Research. 2000;30:855-863.
[85] Sabri S, Illston JM. Immediate and delayed thermal-expansion of hardened cement paste. Cement and Concrete Research. 1982;12:199-208.
[86] Ramachandran VS. Differential thermal method of estimating calcium hydroxide in calcium silicate and cement pastes. Cement and Concrete Research. 1979;9:677-684.
[87] Thomas JJ, Jennings HM, Chen JJ. Influence of nucleation seeding on the hydration mechanisms of tricalcium silicate and cement. Journal of Physical Chemistry C. 2009;113:4327-4334.
[88] Ai H, Young J. Volume stability of densified cement pastes. Mat Sci Conc. 1998:493-507.
[89] Goller G, Demirkiran H, Oktar FN, Demirkesen E. Processing and characterization of bioglass reinforced hydroxyapatite composites. Ceram Int 2003;29:721-724.
[90] Thomas JJ, FitzGerald SA, Neumann DA, Livingston RA. State of water in hydrating tricalcium silicate and portland cement pastes as measured by quasi-elastic neutron scattering. J Am Ceram Soc 2001;84:1811-1816.
[91] Bullard JW. A determination of hydration mechanisms for tricalcium silicate using a kinetic cellular automaton model. J Am Ceram Soc 2008;91:2088-2097.
[92] Gartner EM, Gaidis JM. Hydration mechanisms: I. Mat Sci Conc. 1989;95.
[93] Damidot D, Bellmann F, Möser B, Sovoidnich T. Calculation of the dissolution rate of tricalcium silicate in several electrolyte compositions. Cement Wapno Beton. 2007;74:56-67.
[94] Damidot D, Nonat A, Barret P. Kinetics of tricalcium silicate hydration in diluted suspensions by microcalorimetric measurements. J Am Ceram Soc. 1990;73:3319-3322.
[95] Thomas JJ, Allen AJ, Jennings HM. Hydration kinetics and microstructure development of normal and $CaCl_2$-accelerated tricalcium silicate pastes. Journal of Physical Chemistry C. 2009;113:19836-19844.
[96] Thomas JJ, Jennings HM. A colloidal interpretation of chemical aging of the CSH gel and its effects on the properties of cement paste. Cement and Concrete Research. 2006;36:30-38.
[97] Thomas JJ, Allen AJ, Jennings HM. Structural changes to the calcium–silicate–hydrate gel phase of hydrated cement with age, drying, and resaturation. J Am Ceram Soc 2008;91:3362-3369.
[98] Thomas JJ, Jennings HM, Allen AJ. The surface area of hardened cement paste as measured by various techniques. Concr Sci Eng. 1999;1:45-64.
[99] Jennings HM, Bullard JW, Thomas JJ, Andrade JE, Chen JJ, Scherer GW. Characterization and modeling of pores and surfaces in cement paste: Correlations to processing and properties. J Adv Concr Technol. 2008;6:5-29.
[100] Halperin WP, Jehng JY, Song YQ. Application of spin-spin relaxation to measurement of surface area and pore size distributions in a hydrating cement paste. Magn Reson Imaging. 1994;12:169-173.
[101] Francis MD. The inhibition of calcium hydroxyapatite crystal growth by polyphosphonates and polyphosphates. Calc Tiss Res. 1969;3:151-162.
[102] Akao M, Aoki H, Kato K. Mechanical properties of sintered hydroxyapatite for prosthetic applications. J Mater Sci 1981;16:809-812.

[103] Radev L, Hristov V, Michailova I, Samuneva B. Sol-gel bioactive glass-ceramics Part I: Calcium Phosphate Silicate/Wollastonite glass-ceramics. Cent Eur J Chem. 2009;7:317-321.
[104] Xin R, Leng Y, Chen J, Zhang Q. A comparative study of calcium phosphate formation on bioceramics in vitro and in vivo. Biomaterials. 2005;26:6477-6486.
[105] Knowles JC, Bonfield W. Development of a glass reinforced hydroxyapatite with enhanced mechanical properties. The effect of glass composition on mechanical properties and its relationship to phase changes. J Biomed Mater Res. 1993;27:1591-1598.
[106] Oktar FN, Goller G. Sintering effects on mechanical properties of glass-reinforced hydroxyapatite composites. Ceram Int 2002;28:617-621.
[107] Ginebra MP, Traykova T, Planell JA. Calcium phosphate cements as bone drug delivery systems: a review. J Control Release. 2006;113:102-110.
[108] Shimaoka H, Dohi Y, Ohgushi H, Ikeuchi M, Okamoto M, Kudo A, *et al.* Recombinant growth/differentiation factor-5 (GDF-5) stimulates osteogenic differentiation of marrow mesenchymal stem cells in porous hydroxyapatite ceramic. J Biomed Mater Res A. 2004;68:168-176.
[109] del Real RP, Ooms E, Wolke JG, Vallet-Regi M, Jansen JA. In vivo bone response to porous calcium phosphate cement. J Biomed Mater Res A. 2003;65:30-36.
[110] Comuzzi L, Ooms E, Jansen JA. Injectable calcium phosphate cement as a filler for bone defects around oral implants: an experimental study in goats. Clin Oral Implan Res 2002;13:304-311.
[111] Sanzana ES, Navarro M, Macule F, Suso S, Planell JA, Ginebra MP. Of the in vivo behavior of calcium phosphate cements and glasses as bone substitutes. Acta Biomater. 2008;4:1924-1933.
[112] Kenny SM, Buggy M. Bone cements and fillers: a review. J Mater Sci Mater Med. 2003;14:923-938.
[113] Cho SB, Nakanishi K, Kokubo T, Soga N, Ohtsuki C, Nakamura T, *et al.* Dependence of apatite formation on silica-gel on its structure: effect of heat treatment. J Am Ceram Soc. 1995;78:1769-1774.
[114] Schwarz K, Milne DB. Growth-promoting effects of silicon in rats. Nature. 1972;239:333-334.
[115] Carlisle EM. Silicon: a possible factor in bone calcification. Science. 1970;167:279-280.
[116] Panzavolta S, Torricelli P, Bracci B, Fini M, Bigi A. Alendronate and pamidronate calcium phosphate bone cements: setting properties and in vitro response of osteoblast and osteoclast cells. J Inorg Biochem. 2009;103:101-106.
[117] Guo H, Wei J, Yuan Y, Liu C. Development of calcium silicate/calcium phosphate cement for bone regeneration. Biomed Mater. 2007;2:S153-159.
[118] Fleish H, Neuman WF. Mechanisms of calcification: role of collagen, polyphosphates, and phosphatase. Am J Physiol. 1961;200:1296-1300.
[119] Russell RGG, Rogers MJ. Bisphosphonates: from the laboratory to the clinic and back again. Bone. 1999;25:97-106.
[120] Ebetino FH, Francis MD, Rogers MJ, Russell RGG. Mechanisms of action of etidronate and other bisphosphonates. Rev Contemp Pharmaco. 1998;9:233-243.
[121] Papapoulos SE. Bisphosphonates: how do they work? Best Pract Res Cl En. 2008;22:831-847.
[122] Dunn CJ, Goa KL. Risedronate: a review of its pharmacological properties and clinical use in resorptive bone disease. Drugs. 2001;61:685-712.

[123] Melton J. Perspectives: how many women have osteoporosis now? J Bone Miner Res. 1995;10:175-177.
[124] Cummings SR, Black DM, Nevitt MC, Browner W, Cauley J, Ensrud K, *et al.* Bone-density at various sites for prediction of hip-fractures. Lancet. 1993;341:72-75.
[125] Reginster J, Minne HW, Sorensen OH, Hooper M, Roux C, Brandi ML, *et al.* Randomized trial of the effects of risedronate on vertebral fractures in women with established postmenopausal osteoporosis. Vertebral Efficacy with Risedronate Therapy (VERT) Study Group. Osteoporosis International. 2000;11:83-91.
[126] Hooper MJ, Ebeling PR, Roberts AP, Graham JJ, Nicholson GC, D'Emden M, *et al.* Risedronate prevents bone loss in early postmenopausal women: a prospective randomized, placebo-controlled trial. Climacteric. 2005;8:251-262.
[127] Harris ST, Wasnich R, Ettinger M, Weiss S, Davidson M, Bosch L, *et al.* The effects of risedronate plus estrogen compared with estrogen alone in postmenopausal women. J Bone Miner Res. 1999;14:S410-S410.
[128] Adinoff AD, Hollister JR. Steroid-induced fractures and bone loss in patients with asthma. N Engl J Med. 1983;309:265-268.
[129] Cohen S, Levy RM, Keller M, Boling E, Emkey RD, Greenwald M, *et al.* Risedronate therapy prevents corticosteroid-induced bone loss: a twelve-month, multicenter, randomized, double-blind, placebo-controlled, parallel-group study. Arthritis Rheum. 1999;42:2309-2318.
[130] Reid DM, Hughes RA, Laan RF, Sacco-Gibson NA, Wenderoth DH, Adami S, *et al.* Efficacy and safety of daily risedronate in the treatment of corticosteroid-induced osteoporosis in men and women: a randomized trial. European Corticosteroid-Induced Osteoporosis Treatment Study. J Bone Miner Res. 2000;15:1006-1013.
[131] Hosking D, Eusebio R, Chines A. Paget's disease of bone: reduction of disease activity with oral risedronate. Bone. 1998;22:51-55.
[132] Siris ES, Chines AA, Altman RD, Brown JP, Johnston CC, Jr., Lang R, *et al.* Risedronate in the treatment of Paget's disease of bone: an open label, multicenter study. J Bone Miner Res. 1998;13:1032-1038.
[133] Sato M, Grasser W, Endo N, Akins R, Simmons H, Thompson DD, *et al.* Bisphosphonate action. Alendronate localization in rat bone and effects on osteoclast ultrastructure. J Clin Invest. 1991;88:2095-2105.
[134] Sahni M, Guenther HL, Fleisch H, Collin P, Martin TJ. Bisphosphonates act on rat bone resorption through the mediation of osteoblasts. J Clin Invest. 1993;91:2004-2011.
[135] Hughes DE, Wright KR, Uy HL, Sasaki A, Yoneda T, Roodman GD, *et al.* Bisphosphonates promote apoptosis in murine osteoclasts in vitro and in vivo. J Bone Miner Res. 1995;10:1478-1487.
[136] Lin JH. Bisphosphonates: a review of their pharmacokinetic properties. Bone. 1996;18:75-85.
[137] Hughes DE, MacDonald BR, Russell RG, Gowen M. Inhibition of osteoclast-like cell formation by bisphosphonates in long-term cultures of human bone marrow. J Clin Invest. 1989;83:1930-1935.
[138] Leu CT, Luegmayr E, Freedman LP, Rodan GA, Reszka AA. Relative binding affinities of bisphosphonates for human bone and relationship to antiresorptive efficacy. Bone. 2006;38:628-636.

[139] Koch FP, Merkel C, Ziebart T, Smeets R, Walter C, Al-Nawas B. Influence of bisphosphonates on the osteoblast RANKL and OPG gene expression in vitro. Clin Oral Invest 2012;16:79-86.
[140] Koch FP, Merkel C, Al-Nawas B, Smeets R, Ziebart T, Walter C, *et al.* Zoledronate, ibandronate and clodronate enhance osteoblast differentiation in a dose dependent manner–A quantitative in vitro gene expression analysis of Dlx5, Runx2, OCN, MSX1 and MSX2. J Cranio Maxill Surg. 2011;39:562-569.
[141] Sun J, Song F, Zhang W, Sexton BE, Windsor LJ. Effects of alendronate on human osteoblast-like MG63 cells and matrix metalloproteinases. Arch Oral Biol. 2012;57:728-736.
[142] Hamilton B, McCoy K, Taggart H. Tolerability and compliance with risedronate in clinical practice. Osteoporosis International. 2003;14:259-262.
[143] Lanza FL, Hunt RH, Thomson AB, Provenza JM, Blank MA. Endoscopic comparison of esophageal and gastroduodenal effects of risedronate and alendronate in postmenopausal women. Gastroenterology. 2000;119:631-638.
[144] Lanza F, Schwartz H, Sahba B, Malaty HM, Musliner T, Reyes R, *et al.* An endoscopic comparison of the effects of alendronate and risedronate on upper gastrointestinal mucosae. Am J Gastroenterol. 2000;95:3112-3117.
[145] Su K, Shi X, Varshney RR, Wang DA. Transplantable delivery systems for in situ controlled release of bisphosphonate in orthopedic therapy. Expert Opin Drug Deliv. 2011;8:113-126.
[146] Denissen H, van Beek E, Lowik C, Papapoulos S, van den Hooff A. Ceramic hydroxyapatite implants for the release of bisphosphonate. Bone Miner. 1994;25:123-134.
[147] Seshima H, Yoshinari M, Takemoto S, Hattori M, Kawada E, Inoue T, *et al.* Control of bisphosphonate release using hydroxyapatite granules. J Biomed Mater Res B Appl Biomater. 2006;78:215-221.
[148] McKenzie K, Dennis Bobyn J, Roberts J, Karabasz D, Tanzer M. Bisphosphonate remains highly localized after elution from porous implants. Clin Orthop Relat Res. 2011;469:514-522.
[149] Yoshinari M, Oda Y, Inoue T, Matsuzaka K, Shimono M. Bone response to calcium phosphate-coated and bisphosphonate-immobilized titanium implants. Biomaterials. 2002;23:2879-2885.
[150] Gou W, Wang X, Peng J, Lu Q, Wang Y, Wang A, *et al.* Controlled delivery of zoledronate improved bone formation locally in vivo. PloS one. 2014;9:e91317.
[151] Arnoldi J, Alves A, Procter P. Early tissue responses to zoledronate, locally delivered by bone screw, into a compromised cancellous bone site: a pilot study. Bmc Musculoskel Dis. 2014;15:97.
[152] Greiner SH, Wildemann B, Back DA, Alidoust M, Schwabe P, Haas NP, *et al.* Local application of zoledronic acid incorporated in a poly(D,L-lactide)-coated implant accelerates fracture healing in rats. Acta Orthop. 2008;79:717-725.
[153] Verron E, Pissonnier M-L, Lesoeur J, Schnitzler V, Fellah BH, Pascal-Moussellard H, *et al.* Vertebroplasty using bisphosphonate-loaded calcium phosphate cement in a standardized vertebral body bone defect on an osteoporotic sheep model. Acta Biomater. 2014.
[154] Ratner BD, Hoffman AS, Schoen F, Lemons JE. (book). San Diego, California2004.
[155] Higuchi T. Mechanism of sustained-action medication. theoretical analysis of rate of release of solid drugs dispersed in solid matrices. J Pharm Sci. 1963;52:1145-1149.
[156] Bonewald LF. The amazing osteocyte. J Bone Miner Res. 2011;26:229-238.
[157] Shahnazari M, Yao W, Corr M, Lane NE. Targeting the Wnt signaling pathway to augment bone formation. Curr Osteoporos Rep. 2008;6:142-148.

[158] Center JR, Nguyen TV, Schneider D, Sambrook PN, Eisman JA. Mortality after all major types of osteoporotic fracture in men and women: an observational study. Lancet. 1999;353:878-882.
[159] Burge R, Dawson-Hughes B, Solomon DH, Wong JB, King A, Tosteson A. Incidence and economic burden of psteoporosis-related fractures in the United States, 2005–2025. J Bone Miner Res. 2007;22:465-475.
[160] Stromsoe K. Fracture fixation problems in osteoporosis. Injury. 2004;35:107-113.
[161] Ratner BD. Biomaterials science: an introduction to materials in medicine (book): Academic press; 2004.
[162] Kolmodin LA, Birch DE. PCR Cloning Protocols. Polymerase Chain Reaction (book):Springer;2002. p. 3-18.
[163] Lopes MA, Knowles JC, Kuru L, Santos JD, Monteiro FJ, Olsen I. Flow cytometry for assessing biocompatibility. J Biomed Mater Res. 1998;41:649-656.
[164] Kamiya I, Okuda K, Hara K. Flow-cytometric identification and detection of Porphyromonas gingivalis by a LPS specific monoclonal antibody. J Periodontol. 1994;65:309-315.
[165] Corver WE, Cornelisse CJ, Fleuren GJ. Simultaneous measurement of two cellular antigens and DNA using fluorescein-isothiocyanate, R-phycoerythrin, and propidium iodide on a standard FACScan. Cytometry. 1994;15:117-128.
[166] Alberts B. Molecular Biology of the Cell: Reference edition (book): Garland Science; 2008.
[167] Givan AL. Principles of flow cytometry: an overview. Method Cell Biol. 2000;2001:19-50.
[168] Pearce AI, Richards RG, Milz S, Schneider E, Pearce SG. Animal models for implant biomaterial research in bone: a review. Eur Cell Mater. 2007;13:1-10.
[169] Brown JE, Chow E. Bone Metastases. Bone biomarkers in research and clinical practice (book):Springer;2009. p. 93-116.
[170] Koizumi M, Maeda H, Yoshimura K, Yamauchi T, Kawai T, Ogata E. Dissociation of bone formation markers in bone metastasis of prostate cancer. Brit J Cancer. 1997;75:1601.
[171] Holzer G, Noske H, Lang T, Holzer L, Willinger U. Soluble cathepsin K: a novel marker for the prediction of nontraumatic fractures? Lab Clin Med. 2005;146:13-17.
[172] Swaminathan R. Biochemical markers of bone turnover. Clinica Chimica Acta. 2001;313:95-105.
[173] Halleen JM, Tiitinen SL, Ylipahkala H, Fagerlund KM, Vaananen HK. Tartrate-resistant acid phosphatase 5b (TRACP 5b) as a marker of bone resorption. Clin Lab 2006;52:499-509.
[174] Zhou S. Synthesis and characterization of calcium phosphate silicate bio-cements 2014.
[175] Jia HJ, Li W, Zhao K. Determination of risedronate in rat plasma samples by ion-pair high-performance liquid chromatography with UV detector. Anal Chim Acta. 2006;562:171-175.
[176] Saltzman WK. Drug delivery: engineering principles for drug therapy (book). US: Oxford University Press; 2001.
[177] Bellows CG, Aubin JE, Heersche JNM, Antosz ME. Mineralized bone nodules formedin vitro from enzymatically released rat calvaria cell populations. Calcif Tissue Int 1986;38:143-154.
[178] Friedman RL, Iglewski BH, Miller RD. Identification of a cytotoxin produced by Legionella pneumophila. Infect Immun. 1980;29:271-274.
[179] Ibrahim TA, AbuBakar MZ, Ibrahim R, Kaveh K. Osteoporosis induction in animal model. Am J Anim Vet Sci. 2010;5.
[180] Rosset A, Spadola L, Ratib O. OsiriX: an open-source software for navigating in multidimensional DICOM images. Journal of Digital Imaging. 2004;17:205-216.

[181] Buckland-Wright JC, Lynch JA. Radiographic measurement of bone turnover: microfocal radiography. Methods in Bone Biology (book):Springer;1998. p. 251-272.
[182] Morse A. Formic Acid-Sodium Citrate Decalcification and Butyl Alcohol Dehydration of Teeth and Bones for Sectioning in Paraffin. J Dent Res. 1945;24:143-153.
[183] Verrier S, Hughes L, Alves A, Peroglio M, Alini M, Boger A. Evaluation of the in vitro cell-material interactions and in vivo osteo-integration of a spinal acrylic bone cement. Eur Spine J. 2012;21 Suppl 6:S800-809.
[184] Demoro B, Caruso F, Rossi M, Benitez D, Gonzalez M, Cerecetto H, *et al.* Risedronate metal complexes potentially active against Chagas disease. J Inorg Biochem. 2010;104:1252-1258.
[185] Lin JH, Chen IW, Duggan DE. Effects of dose, sex, and age on the disposition of alendronate, a potent antiosteolytic bisphosphonate, in rats. Drug Metab Dispos. 1992;20:473-478.
[186] Hayakawa T, Furuya N, Yasuoka S, Katoh T, Fukushima T. Computational analysis of bisphosphonates and bisphosphonate / calcium complexes. J Oral Tiss Eng. 2010;8:107-114.
[187] Jindong Z, Hai T, Junchao G, Bo W, Li B, Qiang WB. Evaluation of a novel osteoporotic drug delivery system in vitro: alendronate-loaded calcium phosphate cement. Orthopedics. 2010;33:546-561.
[188] Kim CW, Yun YP, Lee HJ, Hwang YS, Kwon IK, Lee SC. In situ fabrication of alendronate-loaded calcium phosphate microspheres: controlled release for inhibition of osteoclastogenesis. J Control Release. 2010;147:45-53.
[189] Sorensen TC, Arnoldi J, Procter P, Robioneck B, Steckel H. Bone substitute materials delivering zoledronic acid: physicochemical characterization, drug load, and release properties. J Biomater Appl. 2013;27:727-738.
[190] Delmas PD. Treatment of postmenopausal osteoporosis. Lancet. 2002;359:2018-2026.
[191] Peter B, Gauthier O, Laib S, Bujoli B, Guicheux J, Janvier P, *et al.* Local delivery of bisphosphonate from coated orthopedic implants increases implants mechanical stability in osteoporotic rats. J Biomed Mater Res A. 2006;76:133-143.
[192] Queffelec C, Petit M, Janvier P, Knight DA, Bujoli B. Surface modification using phosphonic acids and esters. Chem Rev. 2012;112:3777-3807.
[193] Huybrechts KF, Ishak KJ, Caro JJ. Assessment of compliance with osteoporosis treatment and its consequences in a managed care population. Bone. 2006;38:922-928.
[194] Leonor IB, Balas F, Kawashita M, Reis RL, Kokubo T, Nakamura T. Biomimetic apatite deposition on polymeric microspheres treated with a calcium silicate solution. J Biomed Mater Res B Appl Biomater. 2009;91:239-247.
[195] Sorensen TC, Arnoldi J, Procter P, Beimel C, Jonsson A, Lenneras M, *et al.* Locally enhanced early bone formation of zoledronic acid incorporated into a bone cement plug in vivo. J Pharm Pharmacol. 2013;65:201-212.
[196] Collepardi M, Massidda L. Hydration of tricalcium silicate. J Am Ceram Soc 1971;54:419-422.
[197] Yamamoto N, Furuya K, Hanada K. Progressive development of the osteoblast phenotype during differentiation of osteoprogenitor cells derived from fetal rat calvaria: model for in vitro bone formation. Biol Pharm Bull. 2002;25:509-515.
[198] Alborzi A, Mac K, Glackin CA, Murray SS, Zernik JH. Endochondral and intramembranous fetal bone development: osteoblastic cell proliferation, and expression of alkaline phosphatase, m-twist, and histone H4. J Cran Genet Dev Bio. 1995;16:94-106.

[199] Xynos ID, Edgar AJ, Buttery LD, Hench LL, Polak JM. Gene-expression profiling of human osteoblasts following treatment with the ionic products of Bioglass® 45S5 dissolution. J Biomed Mater Res 2001;55:151-157.
[200] Hadjidakis DJ, Androulakis, II. Bone remodeling. Ann N Y Acad Sci. 2006;1092:385-396.
[201] Uemura H, Yasui T, Umino Y, Niki H, Takikawa M, Saito S, *et al.* Circulating osteoprotegerin in women during GnRH-agonist treatment and their relationships with mineral components and biomarkers of bone turnover. Bone. 2003;33:860-866.
[202] Bosetti M, Cannas M. The effect of bioactive glasses on bone marrow stromal cells differentiation. Biomaterials. 2005;26:3873-3879.
[203] Zhou L, Hu CJ, Xu GP, Yan JL. In vitro and in vivo study of calcium polyphosphate fiber/calcium phosphate cement/micromorselized bone composite for bone defect repair. J Biomed Mater Res B Appl Biomater. 2012;100:1190-1197.
[204] Burg KJ, Porter S, Kellam JF. Biomaterial developments for bone tissue engineering. Biomaterials. 2000;21:2347-2359.
[205] Brown KL, Cruess RL. Bone and cartilage transplantation in orthopaedic surgery. A review. J Bone Joint Surg Am. 1982;64:270-279.
[206] Enneking WF, Eady JL, Burchardt H. Autogenous cortical bone grafts in the reconstruction of segmental skeletal defects. J Bone Joint Surg Am. 1980;62:1039-1058.
[207] Anderson JM. Biological responses to materials. Ann Rev Mater Res 2001;31:81-110.
[208] Aminabadi NA, Maljaei E, Erfanparast L, Aghbali AA, Hamishehkar H, Najafpour E. Simvastatin versus calcium hydroxide direct pulp capping of human primary molars: a randomized clinical trial. J Dent Res Dent Clin Dent Pros. 2013;7:8.
[209] Chen D, Zhao M, Mundy GR. Bone morphogenetic proteins. Growth factors. 2004;22:233-241.
[210] Lawler J. The structural and functional properties of thrombospondin. Blood. 1986;67:1197-1209.
[211] Colvin RB. Fibronectin in wound healing (book): Newyork: Academic press; 1989.
[212] Ignatius MJ, Large TH, Houde M, Tawil JW, Barton A, Esch F, *et al.* Molecular cloning of the rat integrin alpha 1-subunit: a receptor for laminin and collagen. J Cell Biol. 1990;111:709-720.
[213] Chu M, Weil D, De Wet W, Bernard M, Sippola M, Ramirez F. Isolation of cDNA and genomic clones encoding human pro-alpha 1 (III) collagen. Partial characterization of the 3'end region of the gene. J Biol Chem. 1985;260:4357-4363.
[214] Gerke V, Moss SE. Annexins: From structure to function. Physiol Rev. 2002;82:331-371.
[215] Pietak AM, Reid JW, Stott MJ, Sayer M. Silicon substitution in the calcium phosphate bioceramics. Biomaterials. 2007;28:4023-4032.
[216] Wiktor-Jedrzejczak W, Bartocci A, Ferrante AW, Jr., Ahmed-Ansari A, Sell KW, Pollard JW, *et al.* Total absence of colony-stimulating factor 1 in the macrophage-deficient osteopetrotic (op/op) mouse. Proc Natl Acad Sci U S A. 1990;87:4828-4832.
[217] Vermeer C. Gamma-carboxyglutamate-containing proteins and the vitamin K-dependent carboxylase. Biochem J. 1990;266:625-636.
[218] Itoh S, Itoh F, Goumans MJ, ten Dijke P. Signaling of transforming growth factor-β family members through Smad proteins. Eur J Biochem. 2000;267:6954-6967.
[219] Diamond S. A critical comparison of mercury porosimetry and capillary condensation pore size distributions of portland cement pastes. Cement and Concrete Research. 1971;1:531-545.
[220] Lin JM, Callon KE, Lin CQ, Bava U, Zheng MH, Reid IR, *et al.* Alteration of bone cell function by RANKL and OPG in different in vitro models. Eur J Clin Invest. 2007;37:407-415.

[221] Christodoulou I, Buttery LD, Saravanapavan P, Tai G, Hench LL, Polak JM. Dose- and time-dependent effect of bioactive gel-glass ionic-dissolution products on human fetal osteoblast-specific gene expression. J Biomed Mater Res B Appl Biomater. 2005;74:529-537.
[222] Myoung H, Park JY, Choung PH. Effects of a bisphosphonate on the expression of bone specific genes after autogenous free bone grafting in rats. J Periodontal Res. 2001;36:244-251.
[223] Keeting PE, Oursler MJ, Wiegand KE, Bonde SK, Spelsberg TC, Riggs BL. Zeolite A increases proliferation, differentiation, and transforming growth factor beta production in normal adult human osteoblast-like cells in vitro. J Bone Miner Res. 1992;7:1281-1289.
[224] Pacifici R. Estrogen, cytokines, and pathogenesis of postmenopausal osteoporosis. J Bone Miner Res. 1996;11:1043-1051.
[225] Canalis E, Mazziotti G, Giustina A, Bilezikian JP. Glucocorticoid-induced osteoporosis: pathophysiology and therapy. Osteoporosis International. 2007;18:1319-1328.
[226] Valimaki MJ, Tahtela R. Serum tartrate-resistant acid phosphatase 5b or amino-terminal propeptide of type I procollagen for monitoring bisphosphonate therapy in postmenopausal osteoporosis? Clin Chem. 2005;51:2382-2385.
[227] Peters A. Bone Circulation and Vascularization in Normal and Pathological Conditions. Bone turnover in osteoporosis (book):Springer;1993. p. 177-183.
[228] Leeming DJ, Alexandersen P, Karsdal MA, Qvist P, Schaller S, Tanko LB. An update on biomarkers of bone turnover and their utility in biomedical research and clinical practice. European Journal of Clinical Pharmacology. 2006;62:781-792.
[229] Hart SM, Eastell R. Biochemical markers of bone turnover. Curr Opin Nephrol Hypertens. 1999;8:421-427.
[230] Wichers M, Schmidt E, Bidlingmaier F, Klingmuller D. Diurnal rhythm of CrossLaps in human serum. Clin Chem. 1999;45:1858-1860.
[231] Delmas PD. Clinical Use of Biochemical Markers of Bone Remodeling in Osteoporosis. Bone. 1992;13:S17-S21.
[232] Eastell R, Simmons PS, Colwell A, Assiri AM, Burritt MF, Russell RG, *et al.* Nyctohemeral changes in bone turnover assessed by serum bone Gla-protein concentration and urinary deoxypyridinoline excretion: effects of growth and ageing. Clin Sci 1992;83:375-382.
[233] Garnero P, Shih WJ, Gineyts E, Karpf DB, Delmas PD. Comparison of new biochemical markers of bone turnover in late postmenopausal osteoporotic women in response to alendronate treatment. J Clin Endocrinol Metab. 1994;79:1693-1700.
[234] Garnero P, SornayRendu E, Chapuy MC, Delmas PD. Increased bone turnover in late postmenopausal women is a major determinant of osteoporosis. J Bone Miner Res. 1996;11:337-349.
[235] Pedrazzoni M, Alfano FS, Gatti C, Fantuzzi M, Girasole G, Campanini C, *et al.* Acute effects of bisphosphonates on new and traditional markers of bone resorption. Calcif Tissue Int. 1995;57:25-29.
[236] Seibel MJ, Woitge HW, Pecherstorfer M, Karmatschek M, Horn E, Ludwig H, *et al.* Serum immunoreactive bone sialoprotein as a new marker of bone turnover in metabolic and malignant bone disease. Journal of Clinical Endocrinology & Metabolism. 1996;81:3289-3294.
[237] Bobyn JD, Hacking SA, Krygier JJ, Harvey EJ, Little DG, Tanzer M. Zoledronic acid causes enhancement of bone growth into porous implants. Journal of Bone and Joint Surgery-British Volume. 2005;87B:416-420.

[238] Shimano RC, Macedo AP, Falcai MJ, Ervolino E, Shimano AC, Mardegan Issa JP. Biomechanical and microstructural benefits of physical exercise associated with risedronate in bones of ovariectomized rats. Microsc Res Tech. 2014;77:431-438.
[239] Cui X, Churchill GA. Statistical tests for differential expression in cDNA microarray experiments. Genome Biol. 2003;4:210.
[240] Tusher VG, Tibshirani R, Chu G. Significance analysis of microarrays applied to the ionizing radiation response. P Natl Acad Sci USA. 2001;98:5116-5121.
[241] Liu Z, Xu J, Colvin JS, Ornitz DM. Coordination of chondrogenesis and osteogenesis by fibroblast growth factor 18. Genes Dev. 2002;16:859-869.
[242] Ferrari D, Kosher RA. Dlx5 is a positive regulator of chondrocyte differentiation during endochondral ossification. Dev Biol 2002;252:257-270.
[243] Zhao Q, Eberspaecher H, Lefebvre V, De Crombrugghe B. Parallel expression of Sox9 and Col2a1 in cells undergoing chondrogenesis. Dev Dyn. 1997;209:377-386.
[244] Garnero P, Christgau S, Delmas PD. The bisphosphonate zoledronate decreases type II collagen breakdown in patients with Paget's disease of bone. Bone. 2001;28:461-464.
[245] Cheng Z, Yao W, Pham A, Balooch G, Busse C, Balooch M, *et al.* Bisphosphonates and raloxifene improve bone mineralization and strength through reduction in bone turnover and modulation of TGFbeta/Smad signaling pathways. J Bone Miner Res (conference) 2006. p. S442-S442.

APPENDICES

Appendix A List of equipment

Name	*Manufacturer and Model*	*Purpose*
Autoclave	SANYO MLS-3780 Autoclave	General Sterilization
Biological Safety Cabinets	Thermo Scientific MSC-Advantage™ Class II Biological Safety Cabinets	Cell Culture and MTT Assays
CO_2 Incubator	SANYO MCO-18AIC(UV) CO_2 Cell Culture Incubator	Cell Culture
CT Testing Station	GE Healthcare Discovery CT750 HD	CT Scans of Surgery
Disperser	IKA T25 Digital ULTRA-TURRAX®	RNA Extraction from Tissues and Bone Fragments
Dry Bath	BIOER Technology CHB-100 Dry Bath	RNA Separation from Cells
Electronic Balance	Mettler-Toledo AL204-1C	Chemical Weighing
Fourier Transform Infrared Spectrometer	PerkinElmer PE100 Series FTIR Spectrometer	FTIR Analysis
High Performance Liquid Chromatography	Agilent 1100 Series HPLC	Drug Release Detection
Ice Making	SANYO SIM-F140AY65 Laboratory	Ice Making for RNA and Protein

Name	*Manufacturer and Model*	*Purpose*
Machine	Shivering Ice Making Machine	Separation
Incubator	EYELA LTI-700 Low Temp Incubator	MTT and ELISA Assays, Drug Release and Cement Setting
Inverted Microscope	Olympus IX71 and CKX31 Inverted Microscope	Cell Culture and Histology
Low-Temperature Centrifuge	Beckman Coulter Allegra 64R Benchtop Centrifuge	RNA Extraction from Cells, Tissues and Bone Fragments
Low-Temperature Shaker	Thermo Scientific MaxQ™ 4000 Benchtop Orbital Shakers	Protein Separation from Cells
Magnetic Stirrer	Yuhua SZCL-4B Magnetic Heating Stirrer	Solution Preparation
Micro Centrifuge	eppendorf Micro Centrifuge 5430	RNA Extraction from Cells, Tissues and Bone Fragments
Micro-Computed Topography	SCANCO Medical AG MicroCT 100	μCT Analysis of Porosity
Microplate Strip Washer	BioTek ELx50 96-well Microplate Strip Washer	96-well Plates Washing
Multi-Mode Microplate Reader	BioTek Synergy HT Multi-Mode Microplate Reader	MTT Assay and ELISA Reading
PCR Amplifier	Bio-Rad Thermal Cycler S1000™	cDNA Reverse Transcription
Real-time PCR	Bio-Rad CFX96 Real-Time System	Gene Expression Analysis

Name	*Manufacturer and Model*	*Purpose*
Scanning Electron Microscope	Hitachi S-3000N Scanning Electron Microscope	SEM Micrographs
Testing System	Instron 3369 Test Machine	Compressive Strength Test
UV-Vis Spectrophotometer	Thermo Scientific Nanodrop 2000C	RNA Quality and Concentration Detection
Ventilating Dryer	JingHong DMG-9426A Constant Temperature Ventilating Dryer	Cement Setting and Sterilization
Water Bath	DongFang DianGong DFD-700	Chemical Dissolution
Water Purifier	Millipore Milli-Q® Integral Water Purification Systems	Cell Culture, RNA and Protein Separation, MTT Assays and ELISA
X-ray Diffractometer	Rigaku MultiFlex X-ray Diffractometer	X-ray Diffraction and Rietveld Refinement Analysis
X-ray Testing Station	Kodak DirectView DR7500	X-ray Observation of Surgery

Appendix B Experimental protocols

B.1 Protocol for total RNA isolation from cells

Total RNA was isolated by RNeasy® Mini kit (Qiagen, U.S.A.) according to the manufacture instructions. Protocols were modified to fit our experimental needs and listed below:

This kit includes the following reagents and consumables:

a) 70% ethanol
b) Buffer RLT
c) Buffer RW1
d) Buffer RPE
e) RNeasy spin column
f) RNase-free water

1. Harvest cells in a 6-well plate and maintain the cell number at 5×10^6 in each well;
2. Add 350 μL of lysis Buffer RLT in each well and mix by pipetting;
3. Add 350 μL 70% ethanol into lysate and mix by pipetting;
4. Aspirate 700 μL of lysate into a RNeasy spin column, which is placed in a 2 mL collection tube, close the lid on the RNeasy spin column, and centrifuge the column at 10,000 rpm for 15 sec at room temperature;
5. Discard the liquid flew though at the bottom of column;
6. Add 700 μL of Buffer RW1 into the RNeasy spin column, close the lid on the RNeasy spin column, and centrifuge the column at 10,000 rpm for 15 sec at room temperature;
7. Discard the liquid flew though at the bottom of column;
8. Add 500 μL of Buffer RPE into the RNeasy spin column, close the lid on the RNeasy spin column, and centrifuge the column at 10,000 rpm for 15 sec at room temperature;

9. Discard the liquid flew though at the bottom of column;
10. Add 500 μL of Buffer RPE into the RNeasy spin column, close the lid on the RNeasy spin column, and centrifuge the column at 10,000 rpm for 2 min at room temperature;
11. Place the RNeasy spin column in a new 2 mL collection tube and centrifuge the column at 14,000 rpm for 1 min at room temperature;
12. Place the RNeasy spin column in a new 1.5 mL collection tube, add 40 mL of RNase-free water into the column, centrifuge the column at 10,000 rpm for 1 min at room temperature;
13. Measure the quantity and quality of RNA on the UV-Vis spectrophotometer;
14. Keep RNA solutions in the -80 °C fridge for future use.

B.2 Protocol for extracted RNA stabilization

RNA in bone fragments must be stabilized immediately after these fragments were exercised from animal bodies. The stabilization reagent was RNAlater® (Qiagen, AMBION trademark, Texas, U.S.A.). The protocol is given below:

1. Prepare 15 mL RNAlater® reagent in a sterilized vial;
2. Excise a bone fragment of 50 mg approximately;
3. Remove tissues attached on the fragment;
4. Submerge the fragment into RNAlater® reagent;
5. Keep the tissue-containing RNAlater® reagent in the fridge under -80 °C.

B.3 Protocol for cDNA reverse transcription

cDNA is reversely transcribed with PrimeScript® RT reagent Kit (TaKaRa Biotechnology, Dalian, China) according to the manufacture instructions. Protocols were modified to fit our experimental needs and listed below:

This kit includes the following reagents:

a) 5x PrimeScript® Buffer
b) PrimeScript® RT Enzyme Mix I
c) Oligo dT Primer
d) Random 6 mers
e) RNase Free dH_2O

1. Prepare the mixture by mixing 2 μL 5x PrimeScript® Buffer, 0.5 μL PrimeScript® RT Enzyme Mix I, Oligo dT Primer and Random 6 mers, 2 μL RNA solution and add RNase Free dH2O up to 10 μL per vial;
2. Add 90 μL of PrimeScript® RT Enzyme Mix I to the mixture;
3. Prepare 10 vials of one RNA sample as mentioned above;
4. Reversely transcribe for 15 min at 40 °C;
5. Denature RT enzyme for 5 sec at 85 °C;
6. Remove cDNA vials from thermal cycler and cool them on ice to room temperature;
7. Keep cDNA in -80 °C fridge for future use.

B.4 Protocol for real-time PCR

RT-PCR is performed with RealMasterMix (SYBR Green, Tiangen Biotech, Tianjin, China) according to the manufacture instructions. Protocols were modified to fit our experimental needs and listed below:

This kit includes the following reagents:

a) RealMasterMix
b) 20× SYBR Solution
c) Specific Primers
d) cDNA templates
e) RNase-free water

1. Shake RealMasterMix vigorously at room temperature;
2. Add 125 μL of 20× SYBR Solution into 1 mL of RealMasterMix and shake well;
3. Aspirate 11.25 μL of the mixture , add 1 μL of forward primer, reverse primer and cDNA templates and dilute with RNase-free water to 25 μL;
4. Initialization of the sample for 2 min at 95 °C;
5. Denature the sample for 30 sec at 94 °C, anneal it for 30 sec at 55 °C and extend it for 30 sec at 68 °C; repeat this procedure for 40 cycles;
6. Export the data and calculate fold changes from the $2^{\Delta\Delta CT}$ equation.

B.5 Protocol for total RNA isolation from bone fragments

Total RNA was isolated by RNeasy® Mini Plus Kit (Qiagen, U.S.A.) according to the manufacture instructions. Protocols were modified to fit our experimental needs and listed below:

This kit includes the following reagents and consumables:

a) 70% ethanol
b) Qiazol
c) Chloroform

d) Buffer RW1
e) Buffer RPE
f) gDNA Eliminator spin column
g) RNeasy spin column
h) RNase-free water

1. Excise 5 mg of bone fragment from bone fragments stored in the RNAlater® reagent;
2. Grind the fragment into powders completely in the liquid nitrogen;
3. Add 2 mL of Qiazol into the fragment powder and lyze well;
4. Aspirate 1mL of lysate, add 200 μL of chloroform into lysate and shake vigorously; leave the mixture without any interruption for 15 min and centrifuge the mixture for 15 min at 4 ºC to allow phase separation;
5. Aspirate the top, clear layer carefully, transfer it to a gDNA Eliminator spin column and centrifuge the column at 10,000 rpm for 30 sec at room temperature;
6. Discard the column, aspirate 350 μL of the flow-through, add 350 μL of 70% ethanol and mix by pipetting;
7. Transfer 700 μL of the sample into a RNeasy spin column, which is placed in a 2 mL collection tube, close the lid on the RNeasy spin column, and centrifuge the column at 10,000 rpm for 15 sec at room temperature;
8. Discard the liquid flew though at the bottom of column;
9. Add 700 μL of Buffer RW1 into the RNeasy spin column, close the lid on the RNeasy spin column, and centrifuge the column at 10,000 rpm for 15 sec at room temperature;
10. Discard the liquid flew though at the bottom of column;

11. Add 700 μL of Buffer RW1 into the RNeasy spin column, close the lid on the RNeasy spin column, and centrifuge the column at 10,000 rpm for 15 sec at room temperature;
12. Discard the liquid flew though at the bottom of column;
13. Add 500 μL of Buffer RPE into the RNeasy spin column, close the lid on the RNeasy spin column, and centrifuge the column at 10,000 rpm for 15 sec at room temperature;
14. Discard the liquid flew though at the bottom of column;
15. Add 500 μL of Buffer RPE into the RNeasy spin column, close the lid on the RNeasy spin column, and centrifuge the column at 10,000 rpm for 2 min at room temperature;
16. Place the RNeasy spin column in a new 2 mL collection tube and centrifuge the column at 14,000 rpm for 1 min at room temperature;
17. Place the RNeasy spin column in a new 1.5 mL collection tube, add 40 mL of RNase-free water into the column, centrifuge the column at 10,000 rpm for 1 min at room temperature;
18. Measure the quantity and quality of RNA on the UV-Vis spectrophotometer;
19. Keep RNA solutions in the -80 °C fridge for future use.

B.6 Protocol for PCR array

PCR Arrays are performed with PCR Array (Osteogenesis PCR Array, catalogue #PANZ-026Z, Qiagen, U.S.A.) according to the manufacturer instructions. Protocols were modified to fit our experimental needs and listed below:

This kit includes the following reagents:

a) Buffer GE
b) 5x Buffer BC3
c) RE3 Reverse Transcriptase Mix
d) Control P2
e) RNase-free Water
f) 2x SYBR Green qPCR Mastermix
g) RNA solutions
h) Arrays

1. Thaw Buffer GE, 5x Buffer BC3, RE3 Reverse Transcriptase Mix and Control P2 at room temperature, centrifuge these reagents at 1,000 rpm for 15 sec;
2. Aspirate 3 µL of the RNA solution, add 2 µL of Buffer GE and dilute with RNase-free Water to 10 µL;
3. Incubate the mixture for 5 min at 42 °C and immediate place the mixture on ice for 5 min;
4. Mix 4 µL of 5x Buffer BC3, 1 µL of Control P2, 2 µL of RE3 Reverse Transcriptase Mix, and 3 µL of RNase-free Water and shake well;
5. Combine two mixtures, incubate this mixture for 15 min at 42 °C and then incubate for 5 min at 95 °C;
6. Add 91 µL of RNase-free Water , mix well by pipetting and place the mixture on ice;
7. Aspirate 102 µL of the mixture , add 1,350 µL of 2x SYBR Green qPCR Mastermix and 1,248 µL of RNase-free water and mix well;
8. Place the array on ice, aspirate 25 µL of the mixture and add it to each well;
9. Centrifuge the array for 1 min at room temperature to remove air bubbles at the bottom;

10. Activate the array for 10 min at 95 °C and repeat 40 cycles of fluorescent data collection by annealing and extending it for 15 sec at 95 °C and 1 min at 60 °C, respectively;
11. Export the data into an excel file, upload it to Qiagen web-based PCR array data analysis software and perform analysis.

Appendix C Long-term daily monitoring log

Animal #: Species:
Date of Surgery: Performed by:
Endpoint:

Date	Time	Body weight (g)	Urine/Feces	Incision	Pain assessment	Comments	Initials

Appendix D Post-surgery monitoring sheet

Animal # :
Date of Surgery:
Procedure:
Performed by:

Species :
Pre-operative weight:
Duration:

Post-Procedure	*~24 hours*	*24~48 hours*	*48~72 hours*
Monitoring Frequency			
Analgesia (Y/N)			
EXTERNAL OBSERVATIONS			
Activity level			
Piloerection (Y/N)			
Eye discharge (Y/N)			
Appetite			
Drinking			
Feces			
Urine			
PHYSICAL EXAMINATION			
Breathing			
Gait			
Diarrhea (Y/N)			
Signs of pain			
Dehydration			
Thin appearance (Y/N)			
Vocalization (Y/N)			
Body Weight (gm)			
Temperature			
SUTURE			
Incision red &swollen			
Mucus			
Drainage (Y/N)			
chewing/scratching			
Observer's initials			

Appendix E Supplementary data

E.1 Supplementary radiographic images

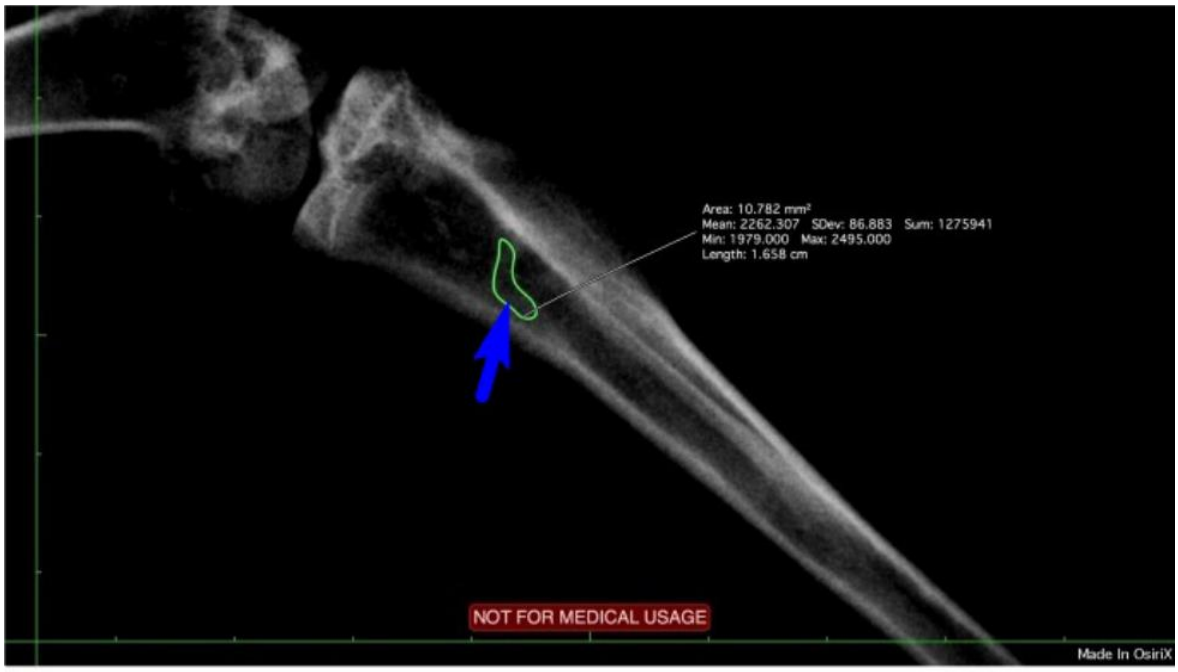

Appendix figure 1: Four selected X-ray radiographs of rabbit tibiae implanted with CPC for 2 months. One bar equals to 1 cm. Both remnant cement (red arrow) and newly formed trabecular bones (blue arrow) were identified.

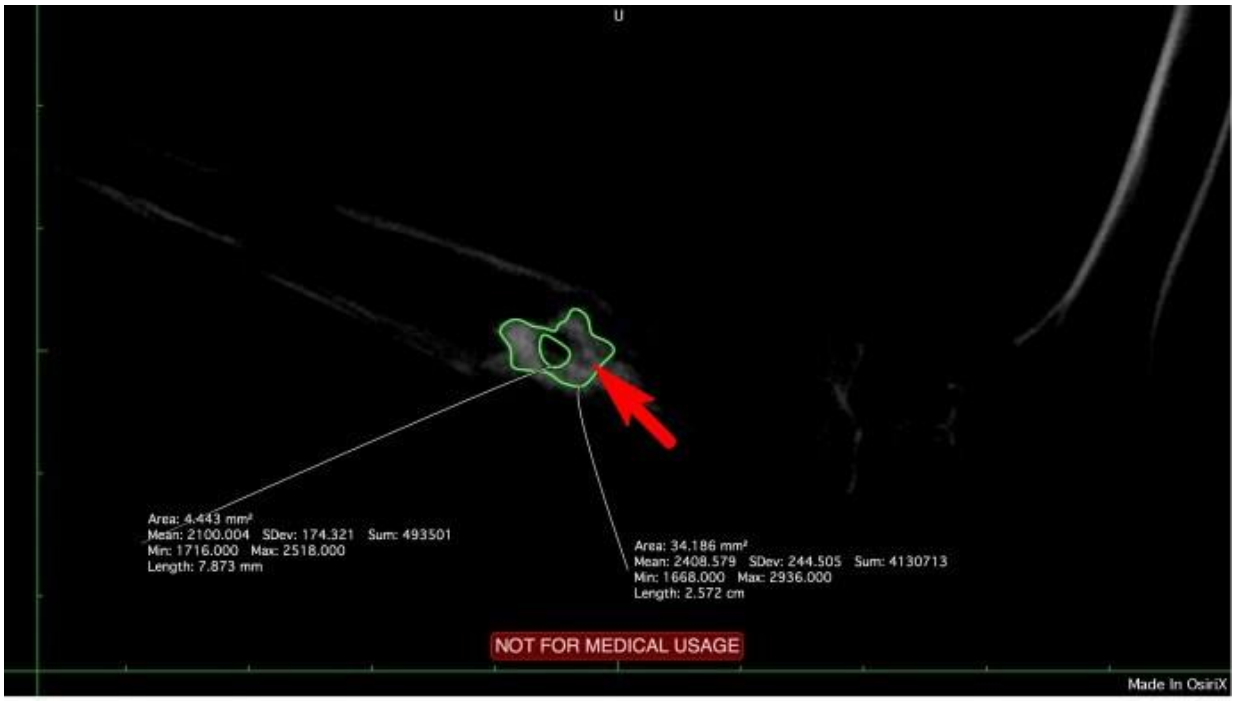
U
Area: 4.443 mm²
Mean: 2100.004 SDev: 174.321 Sum: 493501
Min: 1716.000 Max: 2518.000
Length: 7.873 mm
Area: 34.186 mm²
Mean: 2408.579 SDev: 244.505 Sum: 4130713
Min: 1668.000 Max: 2936.000
Length: 2.572 cm
NOT FOR MEDICAL USAGE
Made In OsiriX

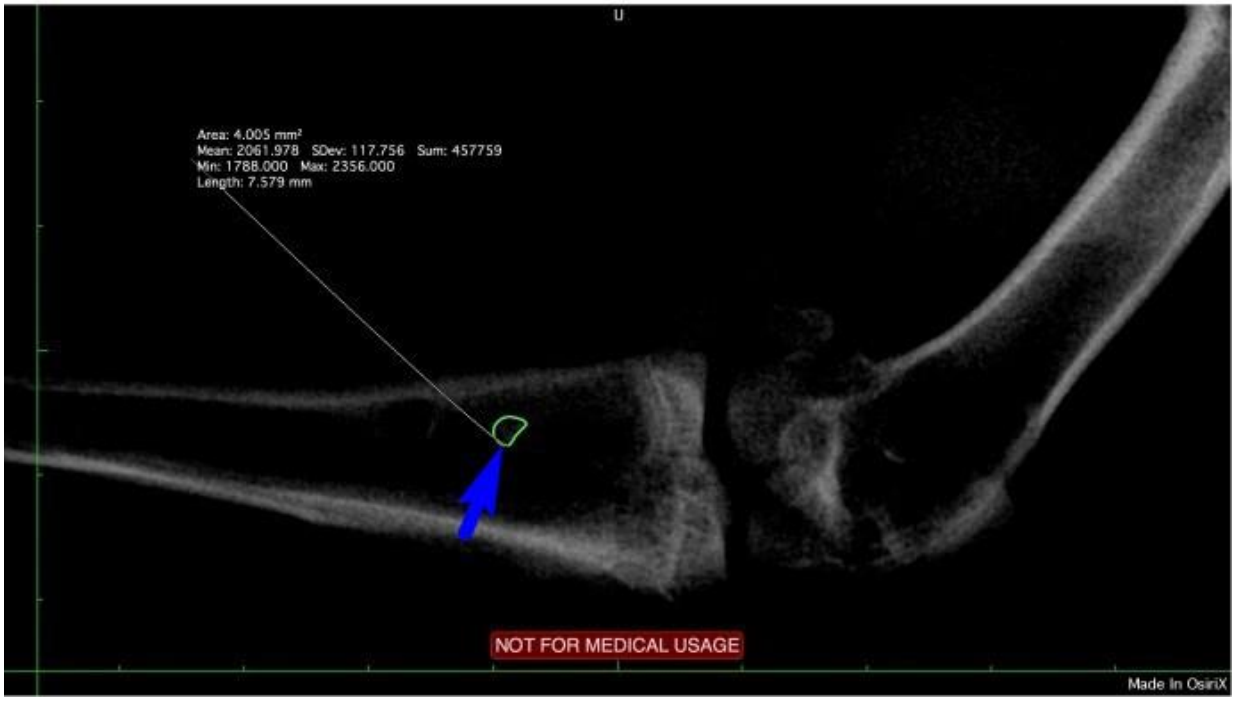
U
Area: 4.005 mm²
Mean: 2061.978 SDev: 117.756 Sum: 457759
Min: 1788.000 Max: 2356.000
Length: 7.579 mm
NOT FOR MEDICAL USAGE
Made In OsiriX

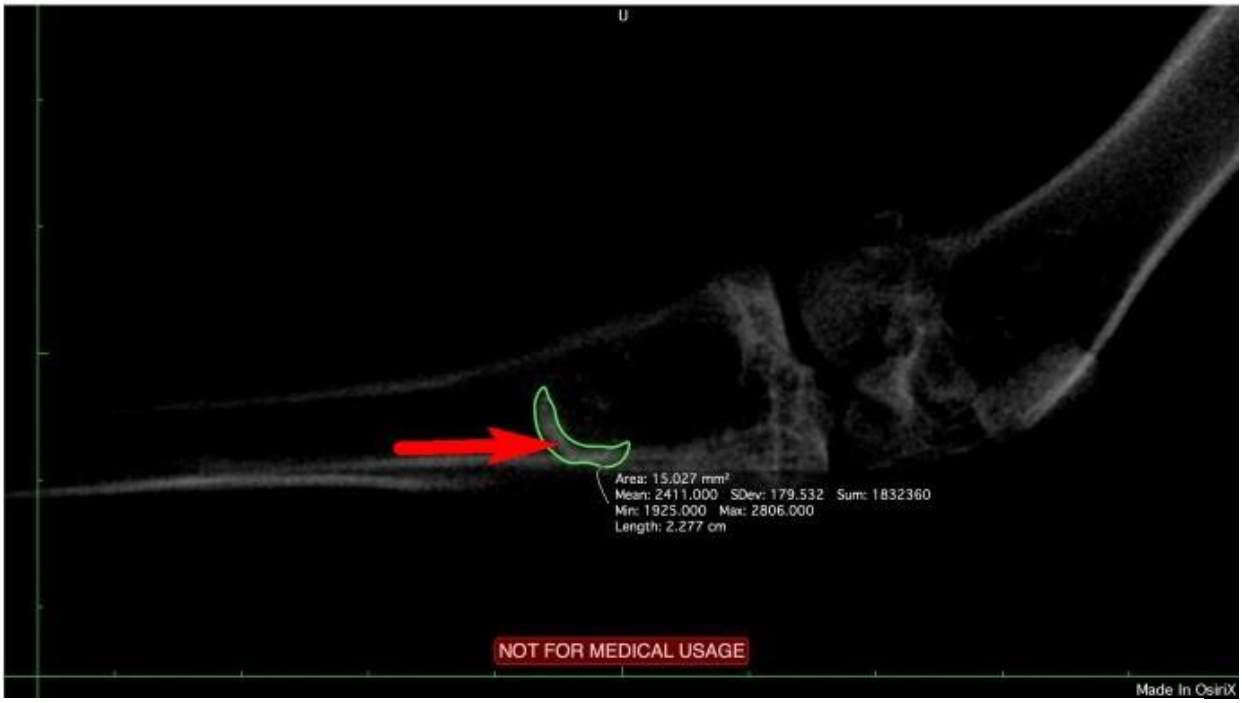

Appendix figure 2: Four selected X-ray radiographs of rabbit tibiae implanted with CPC for 3 months. One bar equals to 1 cm. Both remnant cement (red arrow) and newly formed trabecular bones (blue arrow) were identified.

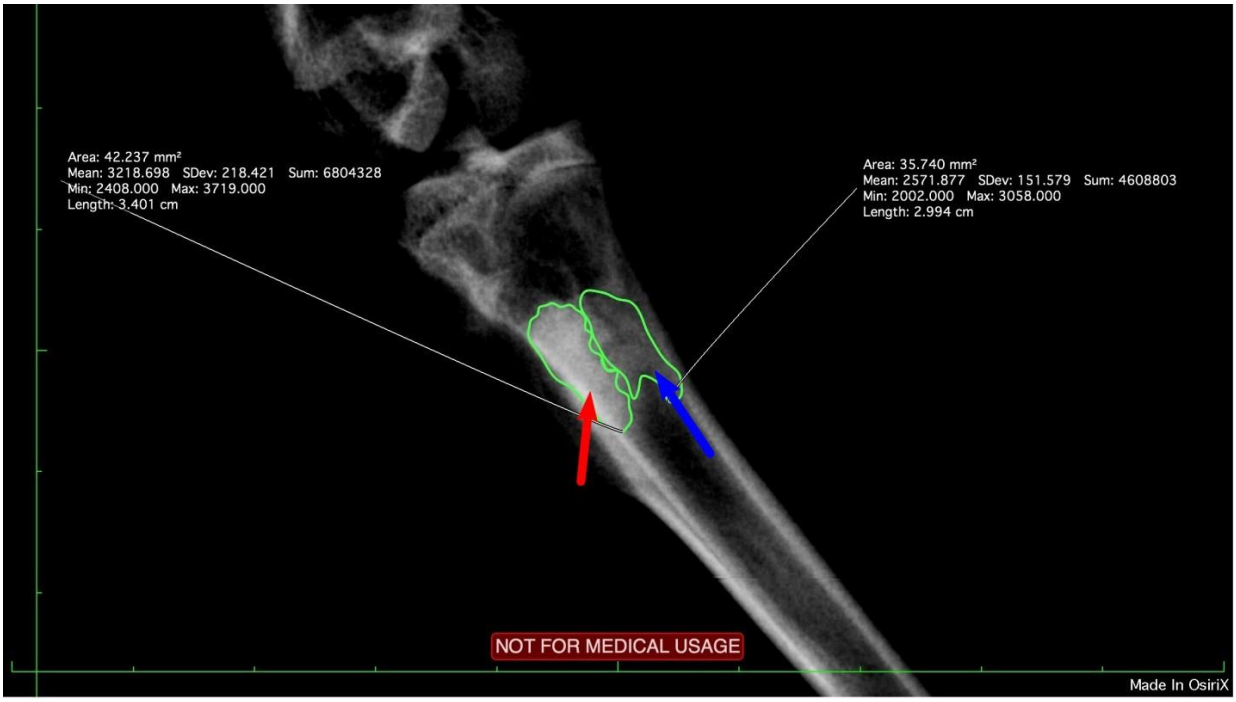
Area: 42.237 mm²
Mean: 3218.698 SDev: 218.421 Sum: 6804328
Min: 2408.000 Max: 3719.000
Length: 3.401 cm
Area: 35.740 mm²
Mean: 2571.877 SDev: 151.579 Sum: 4608803
Min: 2002.000 Max: 3058.000
Length: 2.994 cm
NOT FOR MEDICAL USAGE
Made In OsiriX

Area: 35.939 mm²
Mean: 3218.551 SDev: 156.377 Sum: 5780518
Min: 2616.000 Max: 3548.000
Length: 3.135 cm
Area: 23.859 mm²
Mean: 3083.557 SDev: 138.274 Sum: 3832861
Min: 2687.000 Max: 3466.000
Length: 1.965 cm
NOT FOR MEDICAL USAGE
Made In OsiriX

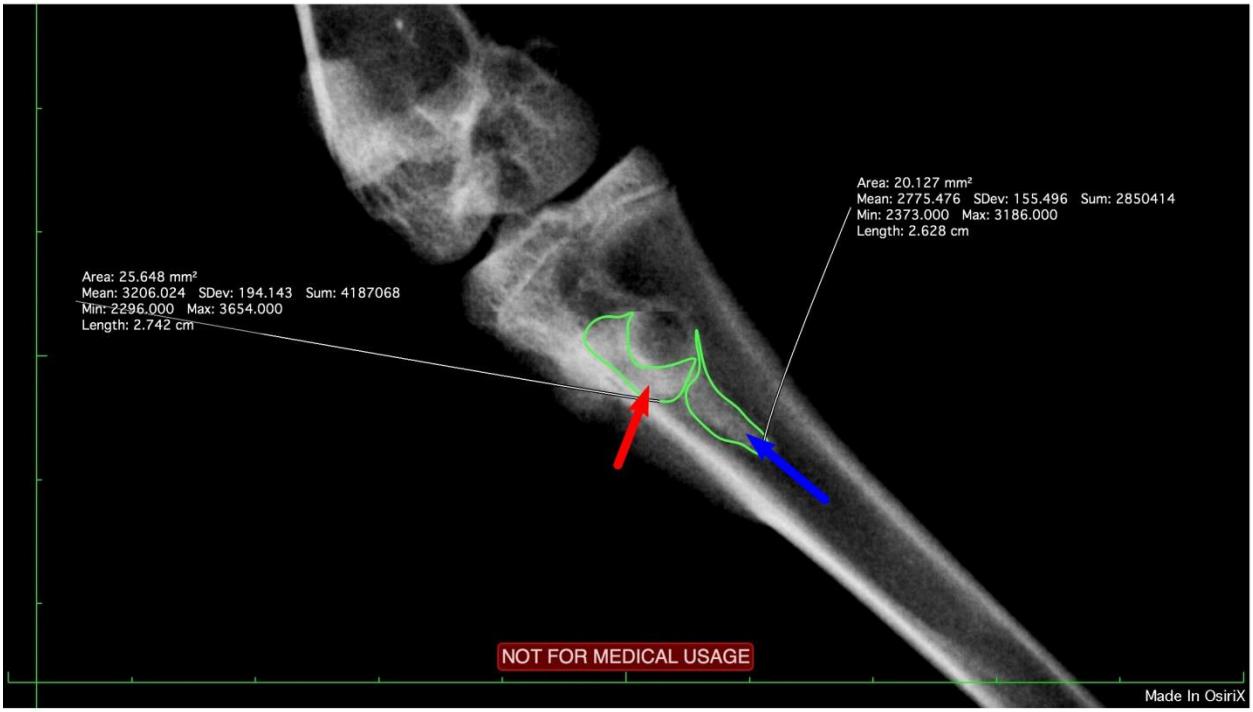

Appendix figure 3:Four selected X-ray radiographs of rabbit tibiae implanted with CPSC5 for 2 months. One bar equals to 1 cm. Both remnant cement (red arrow) and newly formed trabecular bones (blue arrow) were identified.

U
Area: 27.651 mm²
Mean: 2134.205 SDev: 116.757 Sum: 3011363
Min: 1696.000 Max: 2592.000
Length: 2.276 cm
NOT FOR MEDICAL USAGE
Made In OsiriX

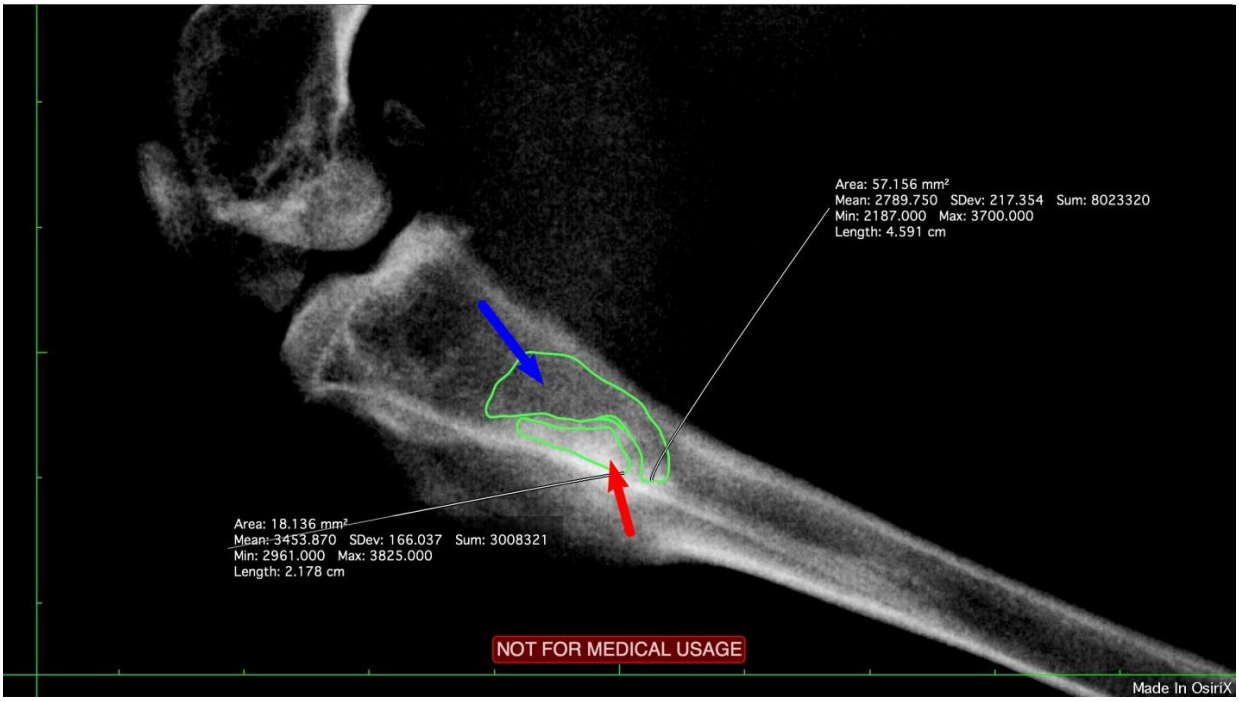
Area: 57.156 mm²
Mean: 2789.750 SDev: 217.354 Sum: 8023320
Min: 2187.000 Max: 3700.000
Length: 4.591 cm
Area: 18.136 mm²
Mean: 3453.870 SDev: 166.037 Sum: 3008321
Min: 2961.000 Max: 3825.000
Length: 2.178 cm
NOT FOR MEDICAL USAGE
Made In OsiriX

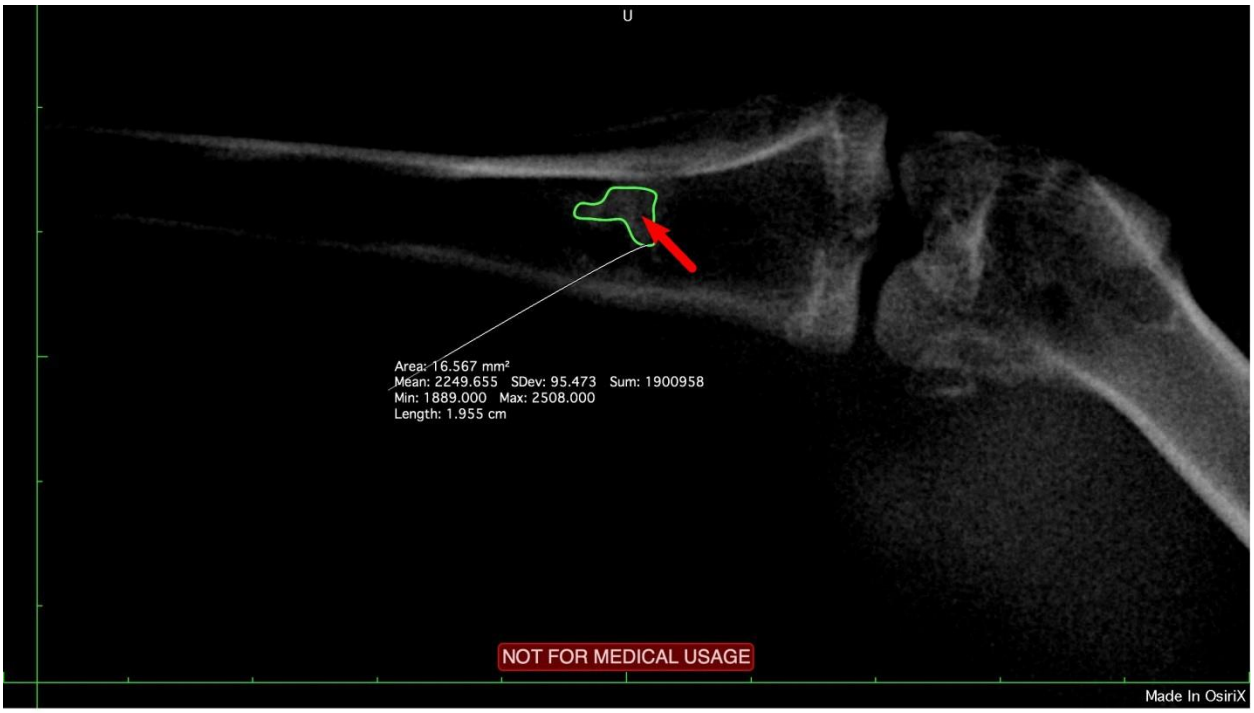

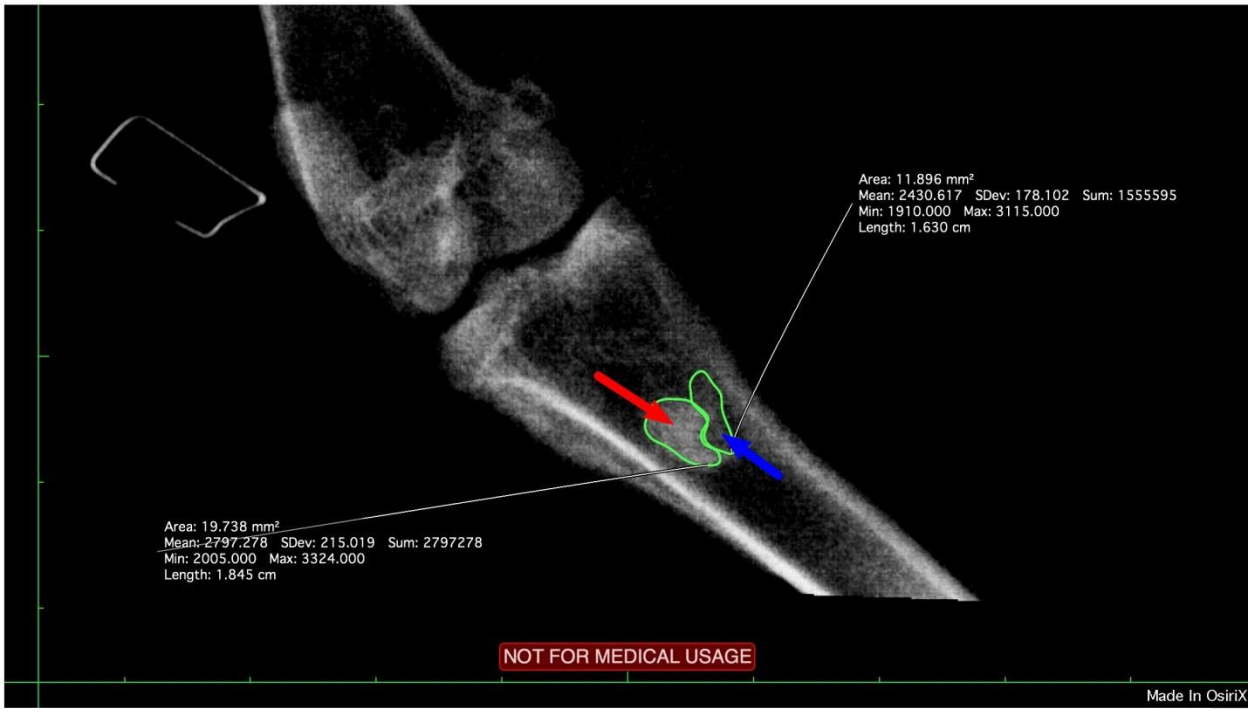

Appendix figure 4: Four selected X-ray radiographs of rabbit tibiae implanted with CPSC5 for 3 months. Both remnant cement (red arrow) and newly formed trabecular bones (blue arrow) were identified.

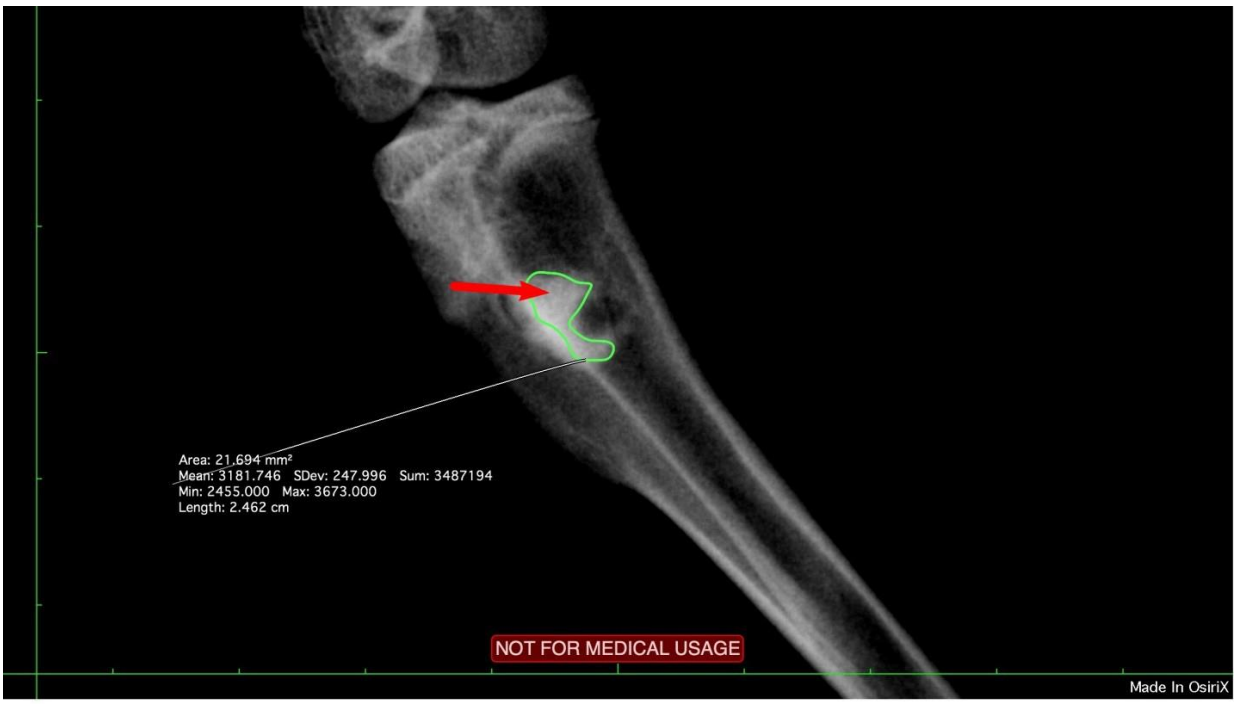
Area: 21.694 mm²
Mean: 3181.746 SDev: 247.996 Sum: 3487194
Min: 2455.000 Max: 3673.000
Length: 2.462 cm
NOT FOR MEDICAL USAGE
Made In OsiriX

Area: 34.160 mm²
Mean: 3383.394 SDev: 188.662 Sum: 5870188
Min: 2893.000 Max: 3753.000
Length: 2.200 cm
NOT FOR MEDICAL USAGE
Made In OsiriX

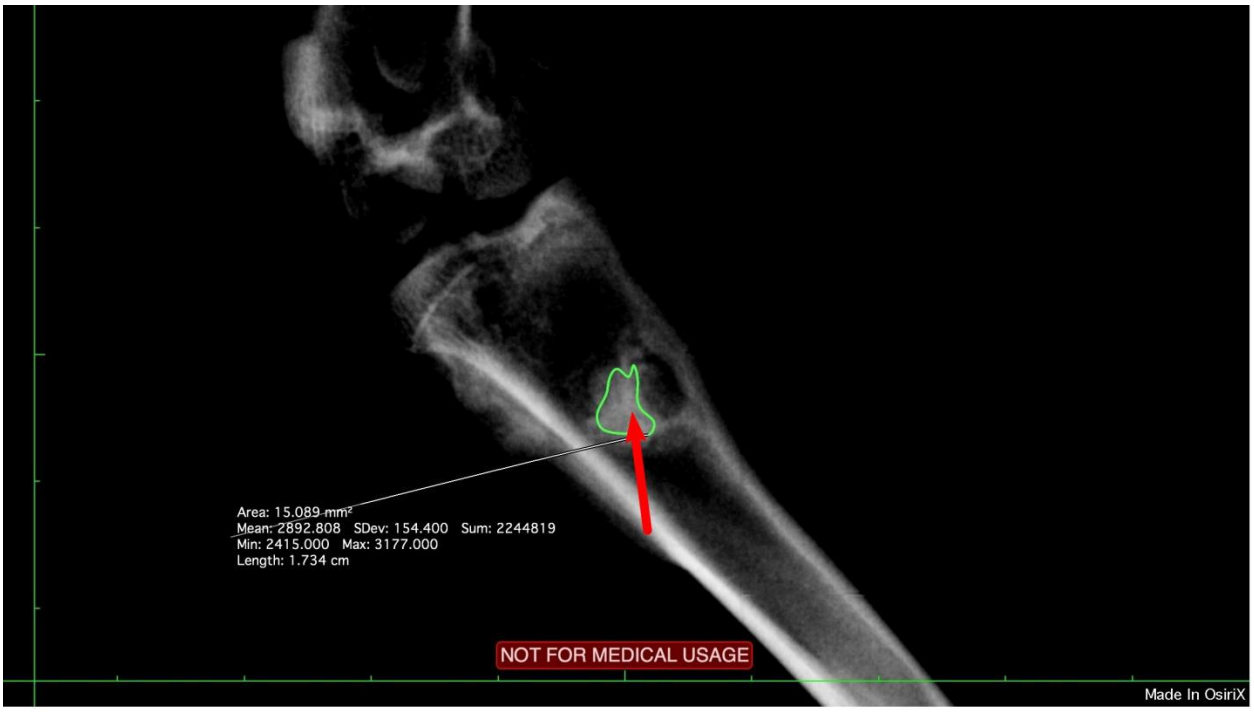

Appendix figure 5: Four selected X-ray radiographs of rabbit tibiae implanted with CPSC10 for 2 months. One bar equals to 1 cm. Both remnant cement (red arrow) and newly formed trabecular bones (blue arrow) were identified.

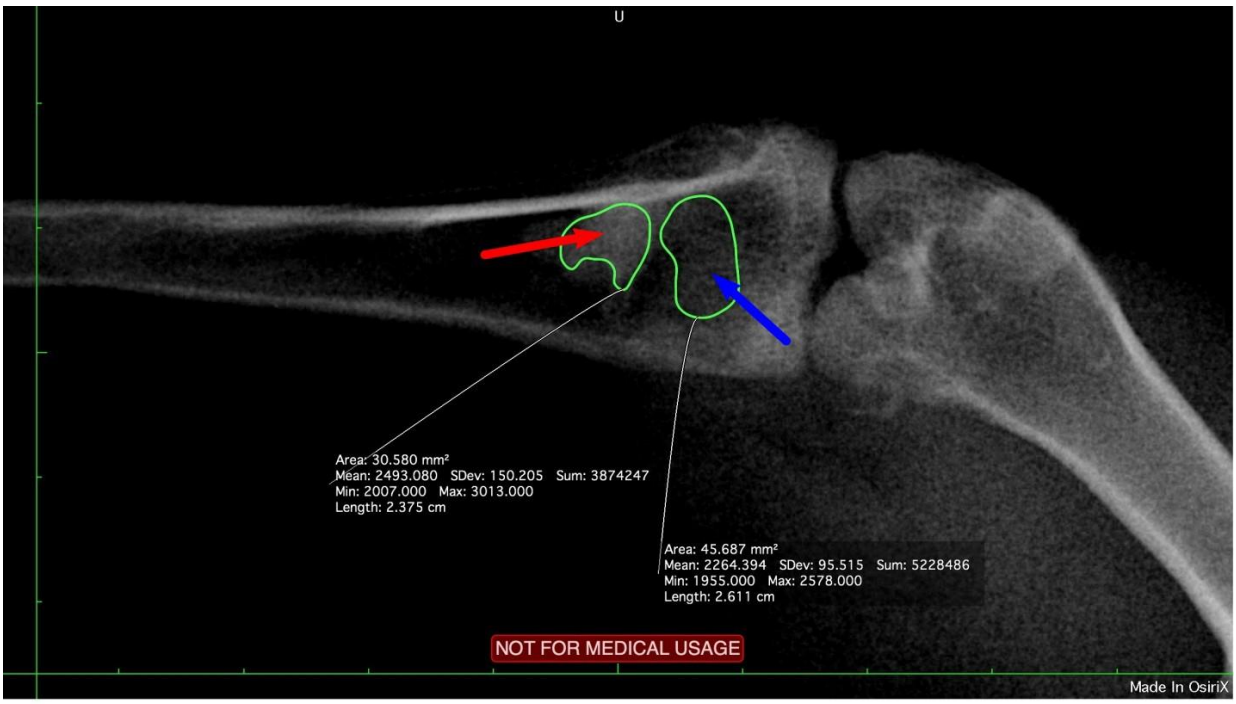
U
Area: 30.580 mm²
Mean: 2493.080 SDev: 150.205 Sum: 3874247
Min: 2007.000 Max: 3013.000
Length: 2.375 cm
Area: 45.687 mm²
Mean: 2264.394 SDev: 95.515 Sum: 5228486
Min: 1955.000 Max: 2578.000
Length: 2.611 cm
NOT FOR MEDICAL USAGE
Made In OsiriX

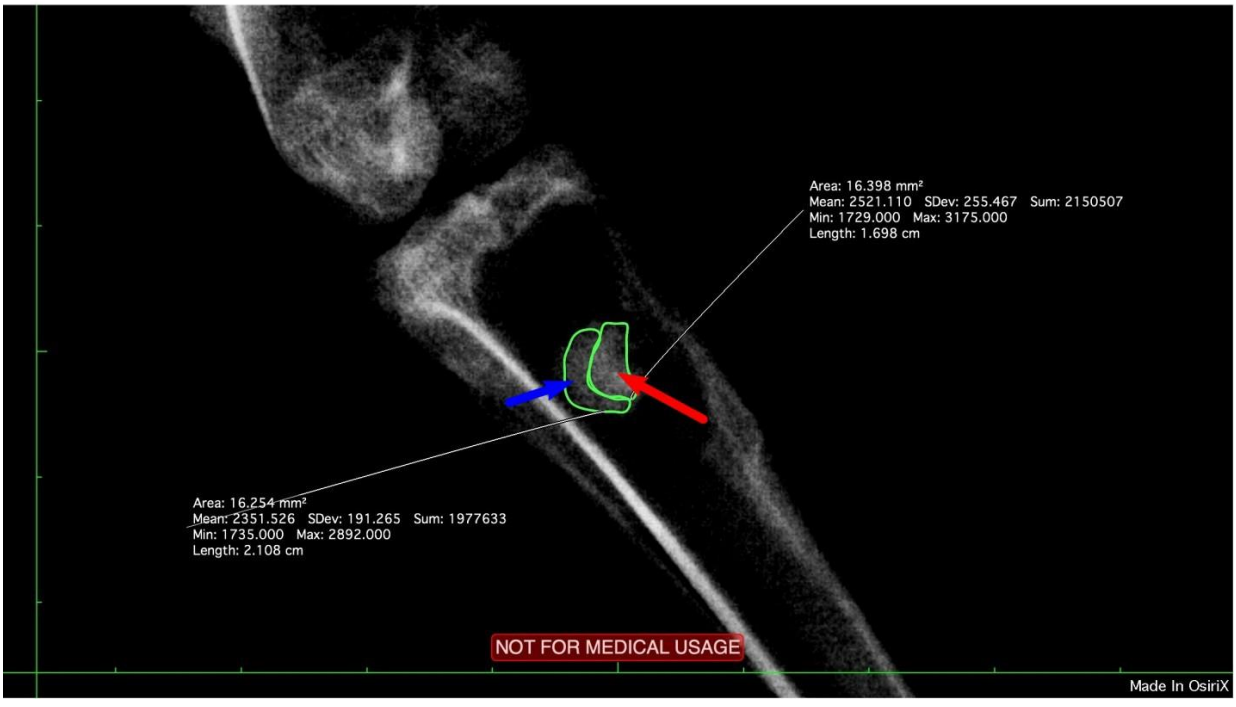
Area: 16.398 mm²
Mean: 2521.110 SDev: 255.467 Sum: 2150507
Min: 1729.000 Max: 3175.000
Length: 1.698 cm
Area: 16.254 mm²
Mean: 2351.526 SDev: 191.265 Sum: 1977633
Min: 1735.000 Max: 2892.000
Length: 2.108 cm
NOT FOR MEDICAL USAGE
Made In OsiriX

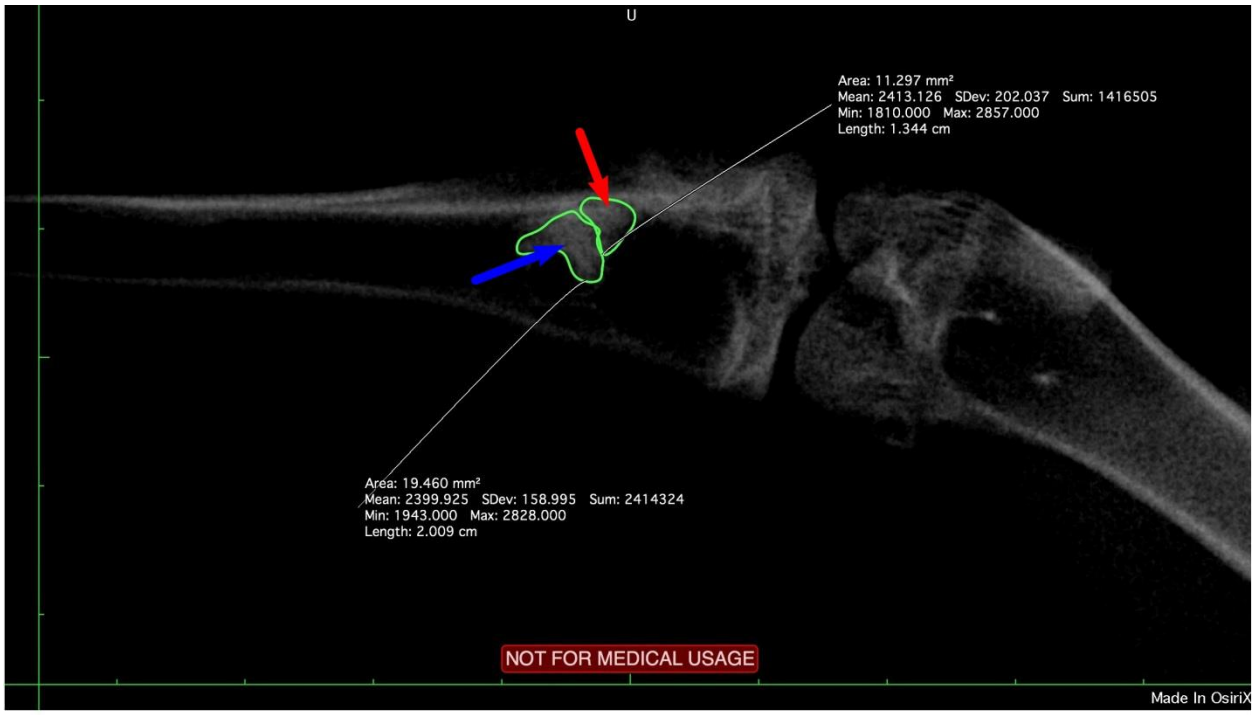

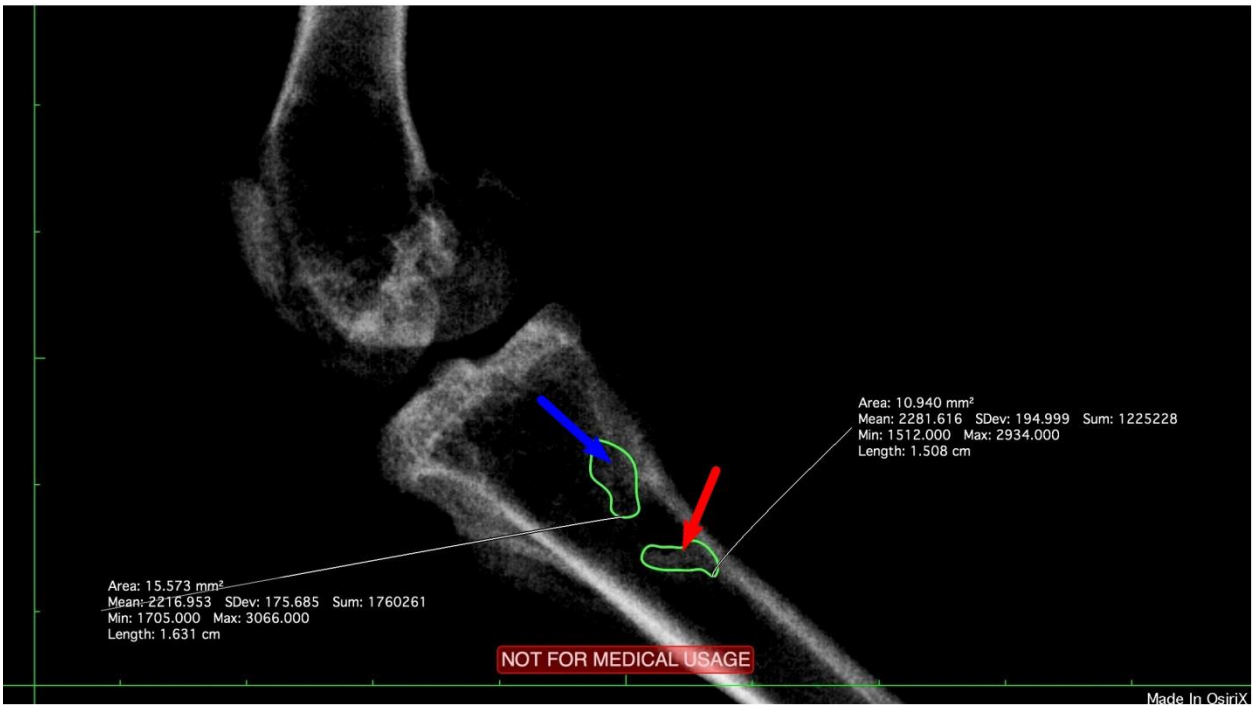

Appendix figure 6: Four selected X-ray radiographs of rabbit tibiae implanted with CPSC10 for 3 months. One bar equals to 1 cm. Both remnant cement (red arrow) and newly formed trabecular bones (blue arrow) were identified.

Area: 53.086 mm²
Mean: 3524.847 SDev: 191.428 Sum: 9390192
Min: 2818.000 Max: 3869.000
Length: 3.932 cm
NOT FOR MEDICAL USAGE
Made In OsiriX

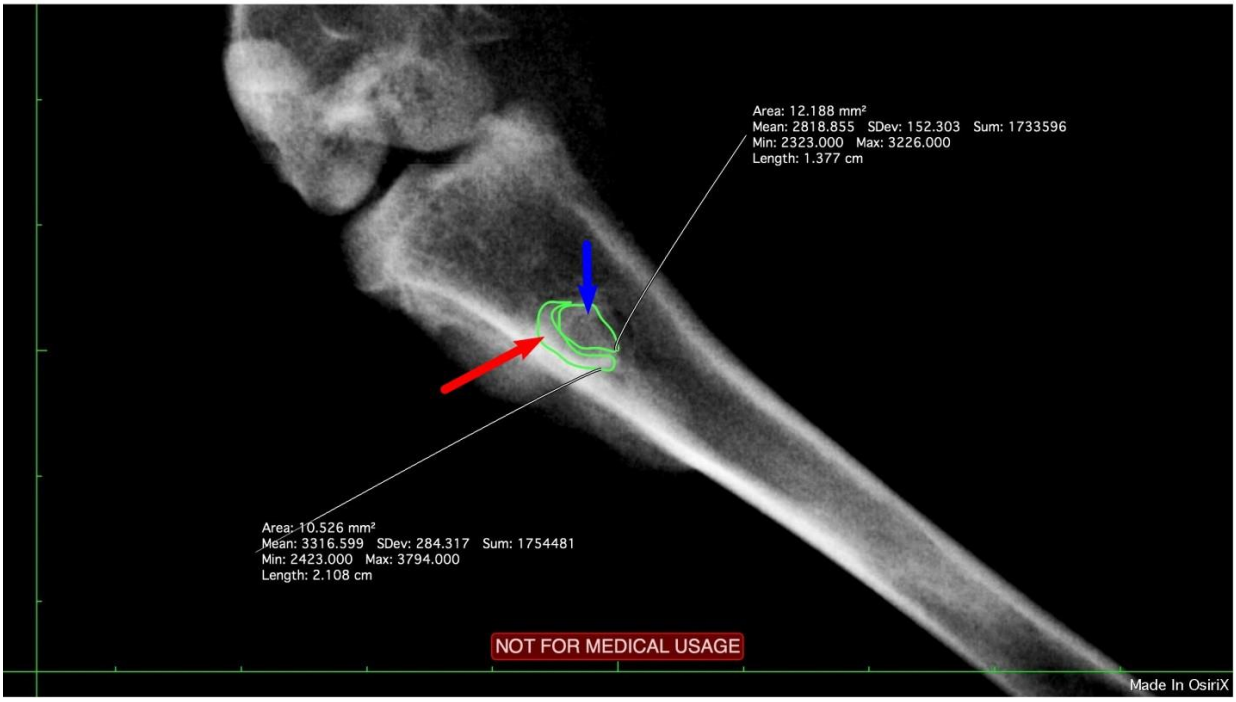
Area: 12.188 mm²
Mean: 2818.855 SDev: 152.303 Sum: 1733596
Min: 2323.000 Max: 3226.000
Length: 1.377 cm
Area: 10.526 mm²
Mean: 3316.599 SDev: 284.317 Sum: 1754481
Min: 2423.000 Max: 3794.000
Length: 2.108 cm
NOT FOR MEDICAL USAGE
Made In OsiriX

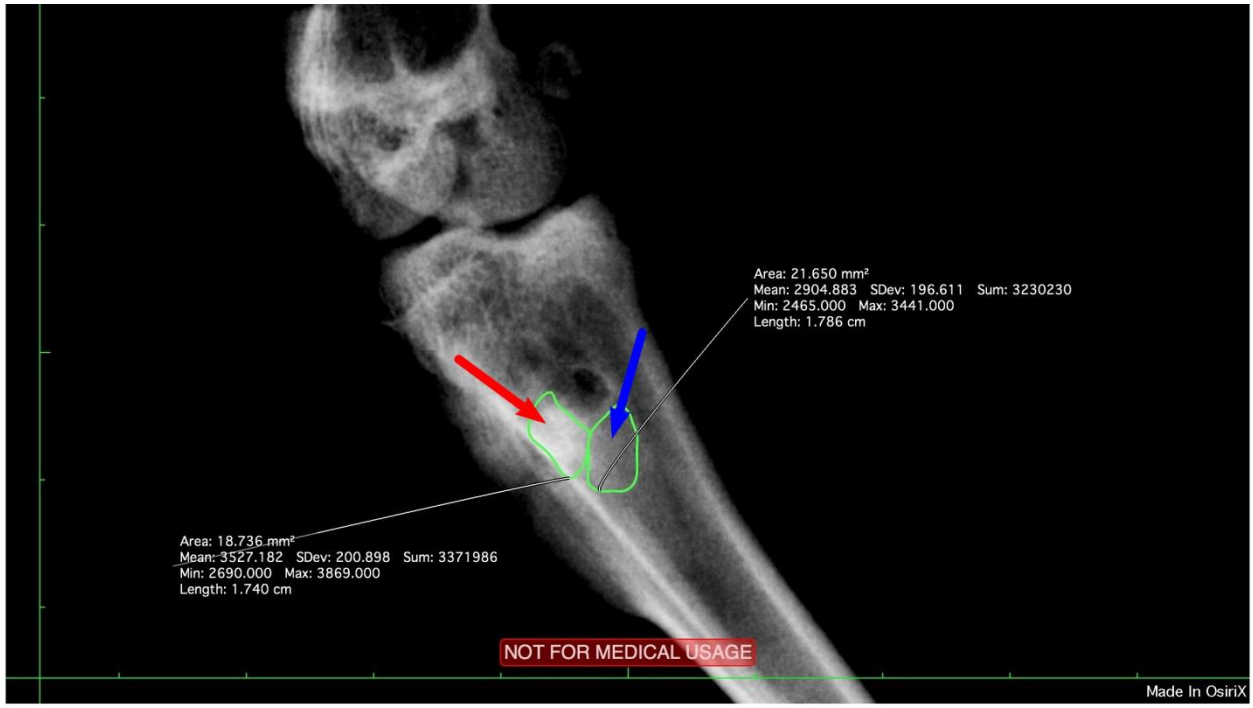

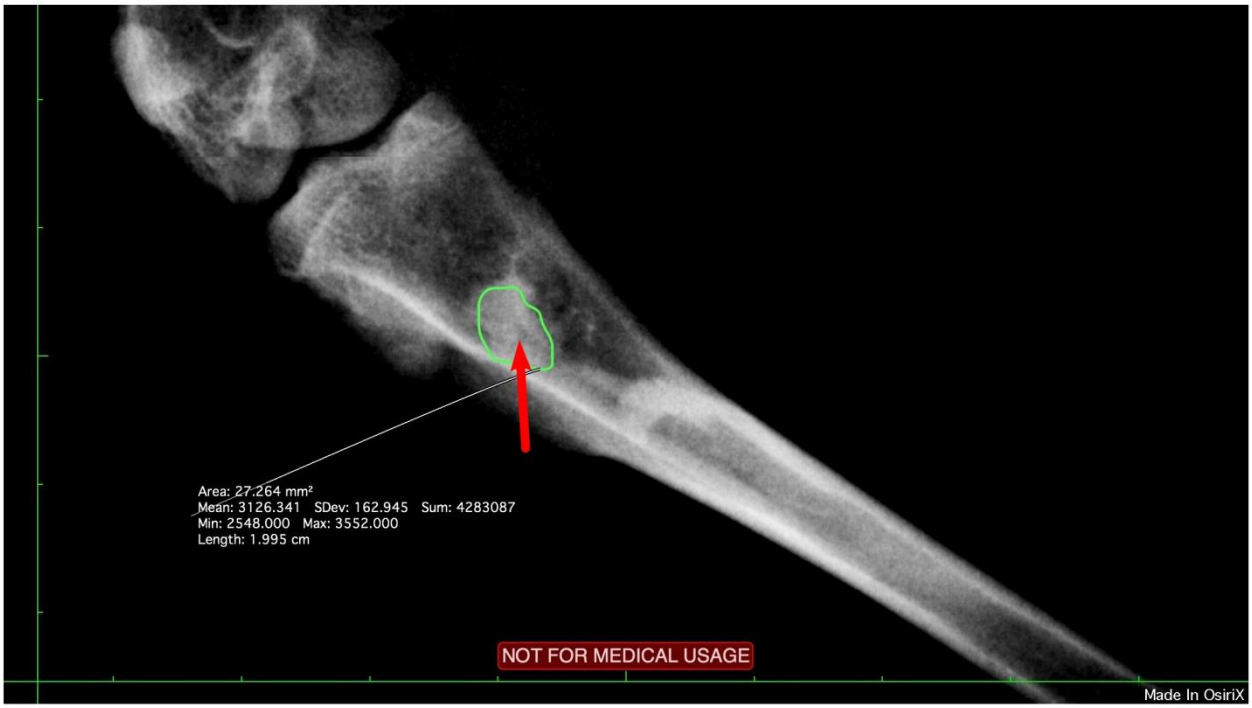

Appendix figure 7: Four selected X-ray radiographs of rabbit tibiae implanted CPSC15 for 2 months. One bar equals to 1 cm. Both remnant cement (red arrow) and newly formed trabecular bones (blue arrow) were identified.

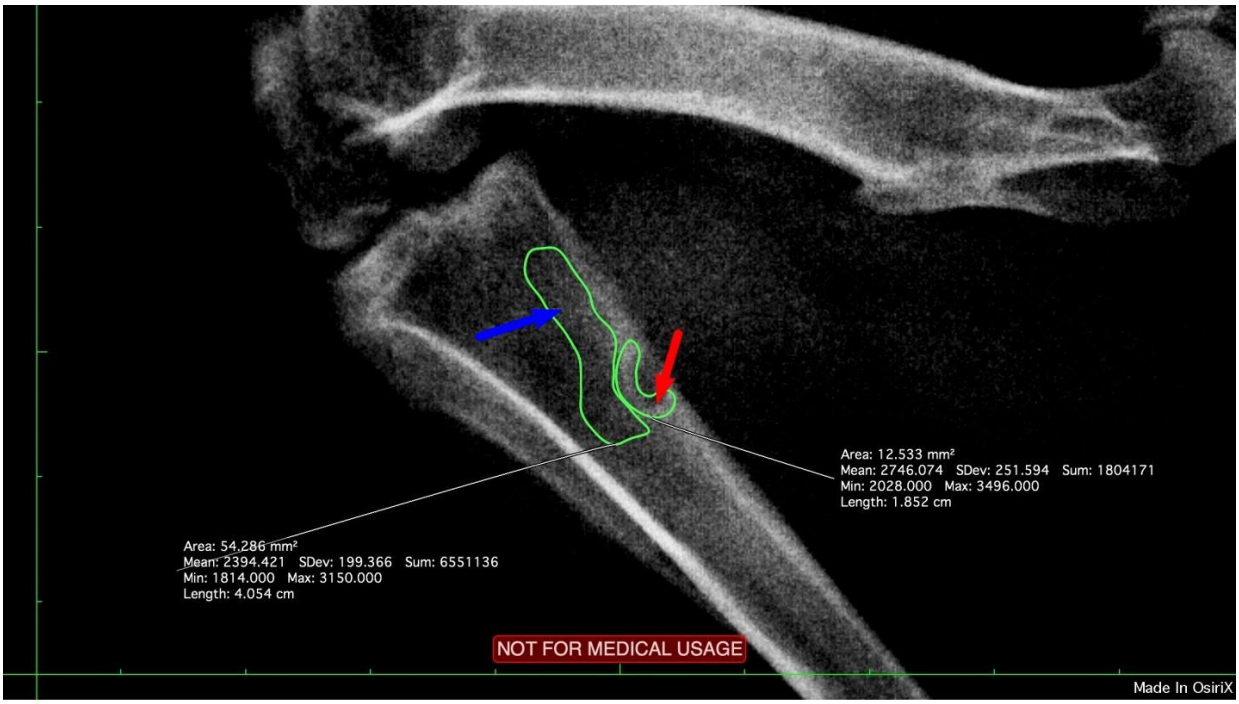
Area: 12.533 mm²
Mean: 2746.074 SDev: 251.594 Sum: 1804171
Min: 2028.000 Max: 3496.000
Length: 1.852 cm
Area: 54.286 mm²
Mean: 2394.421 SDev: 199.366 Sum: 6551136
Min: 1814.000 Max: 3150.000
Length: 4.054 cm
NOT FOR MEDICAL USAGE
Made In OsiriX

U
Area: 32.441 mm²
Mean: 2463.452 SDev: 168.978 Sum: 4008037
Min: 1966.000 Max: 3083.000
Length: 2.619 cm
NOT FOR MEDICAL USAGE
Made In OsiriX

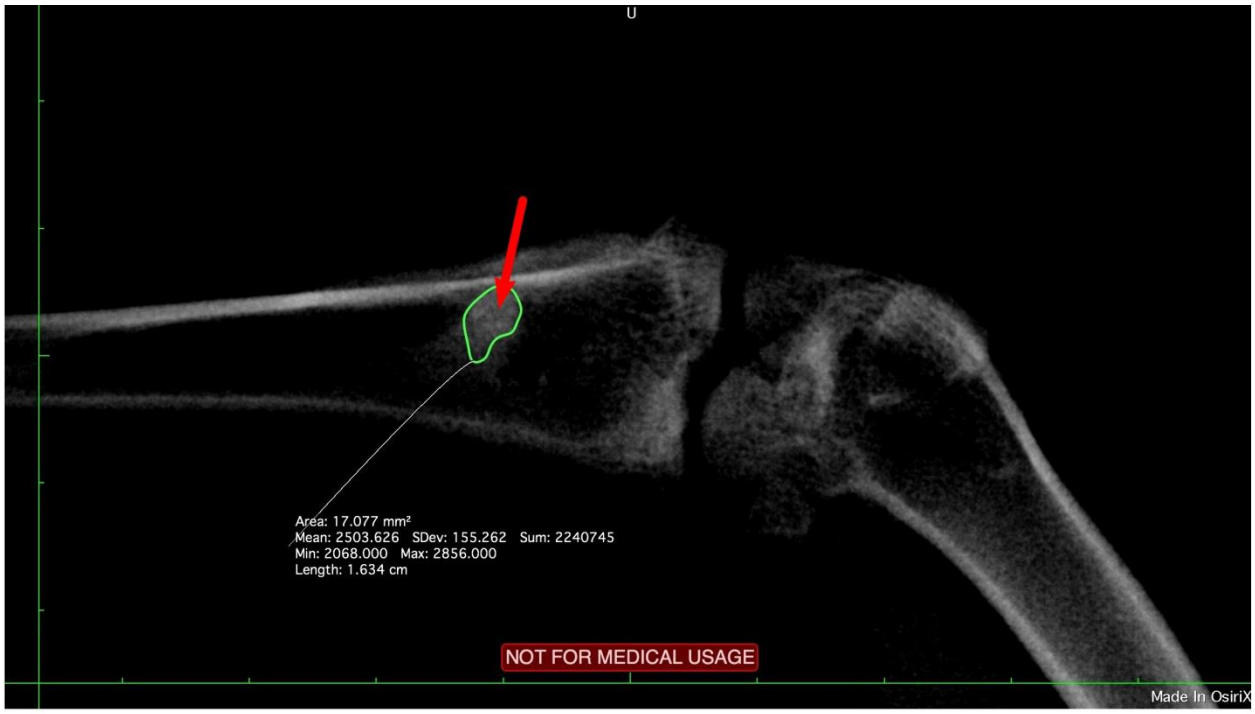

Appendix figure 8: Four selected X-ray radiographs of rabbit tibiae implanted with CPSC15 for 3 months. One bar equals to 1 cm. Both remnant cement (red arrow) and newly formed trabecular bones (blue arrow) were identified.

NOT FOR MEDICAL USAGE
Made In OsiriX

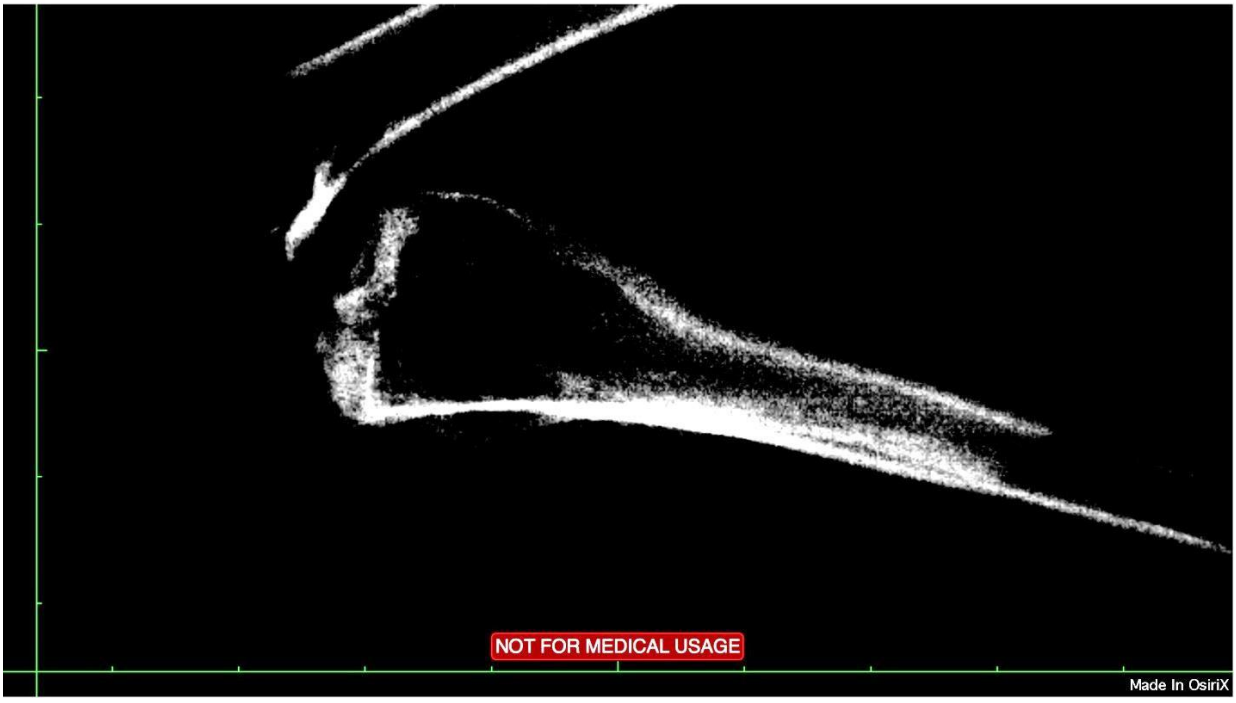
NOT FOR MEDICAL USAGE
Made In OsiriX

Appendix figure 9: Four selected X-ray radiographs of the sham control group after 8 weeks. One bar equals to 1 cm.

NOT FOR MEDICAL USAGE
Made In OsiriX

NOT FOR MEDICAL USAGE
Made In OsiriX

Appendix figure 10: Four selected X-ray radiographs of the sham control group after 10 weeks. One bar equals to 1 cm.

Area: 83.424 mm²
Mean: 2517.635 SDev: 280.629 Sum: 10697429
Min: 1673.000 Max: 3568.000
Length: 6.536 cm
NOT FOR MEDICAL USAGE
Made In OsiriX

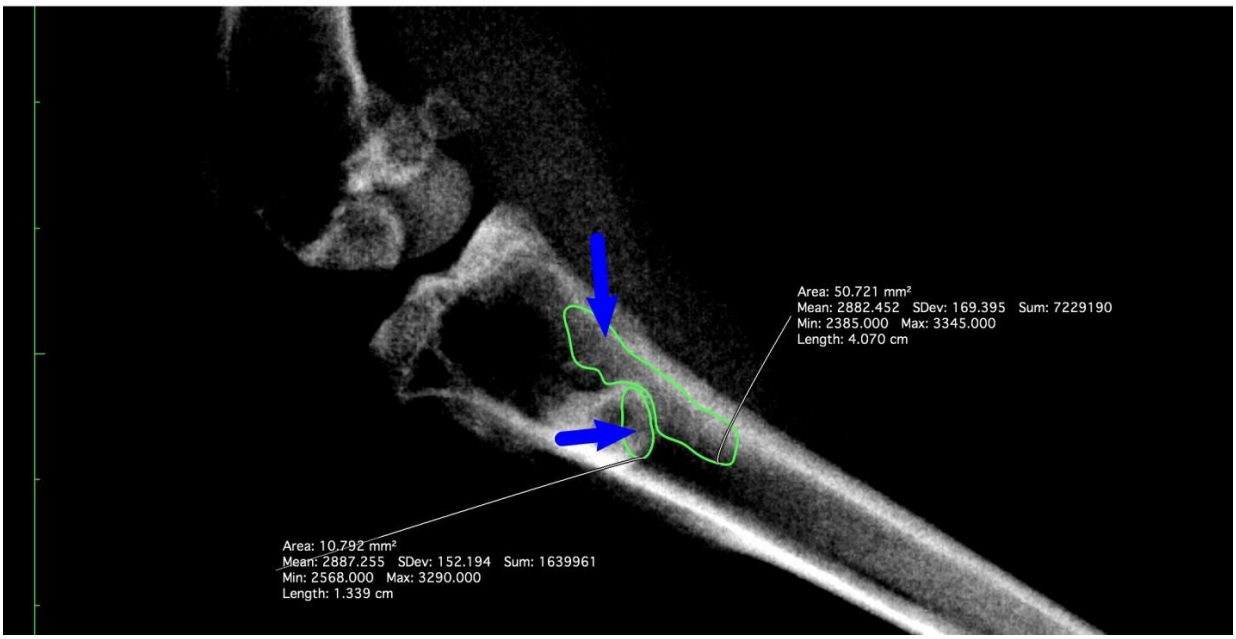
Area: 50.721 mm²
Mean: 2882.452 SDev: 169.395 Sum: 7229190
Min: 2385.000 Max: 3345.000
Length: 4.070 cm
Area: 10.792 mm²
Mean: 2887.255 SDev: 152.194 Sum: 1639961
Min: 2568.000 Max: 3290.000
Length: 1.339 cm

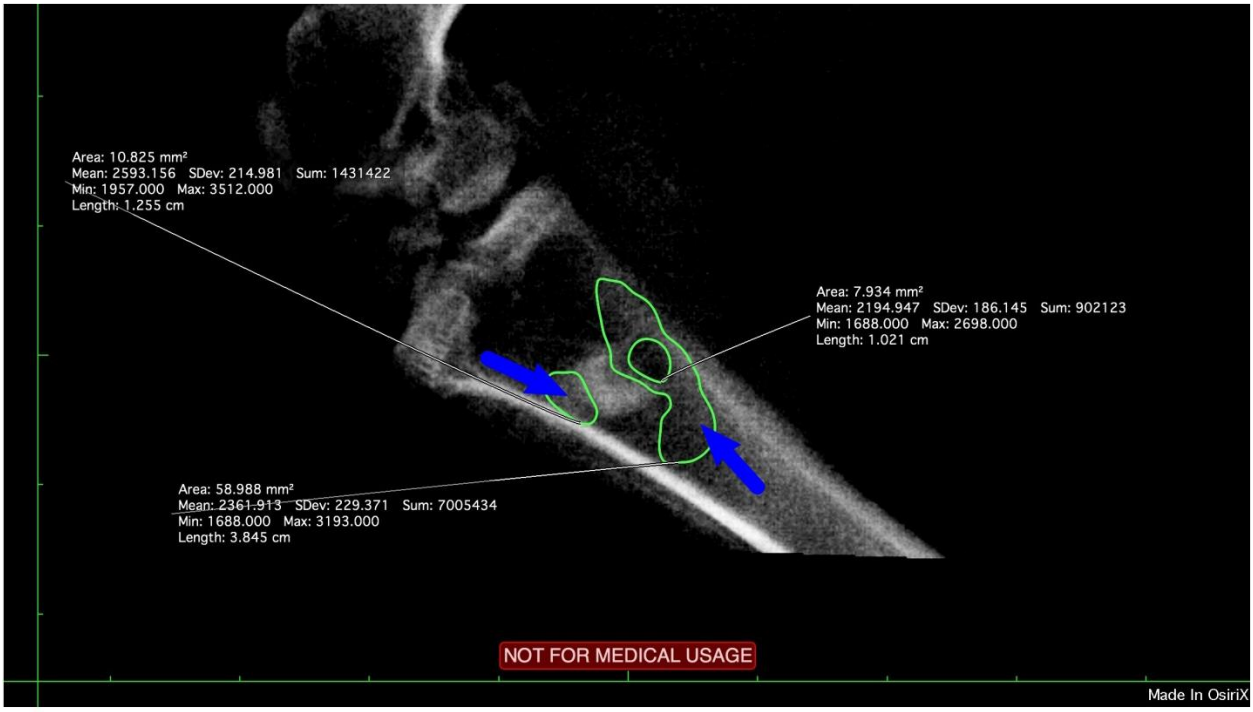

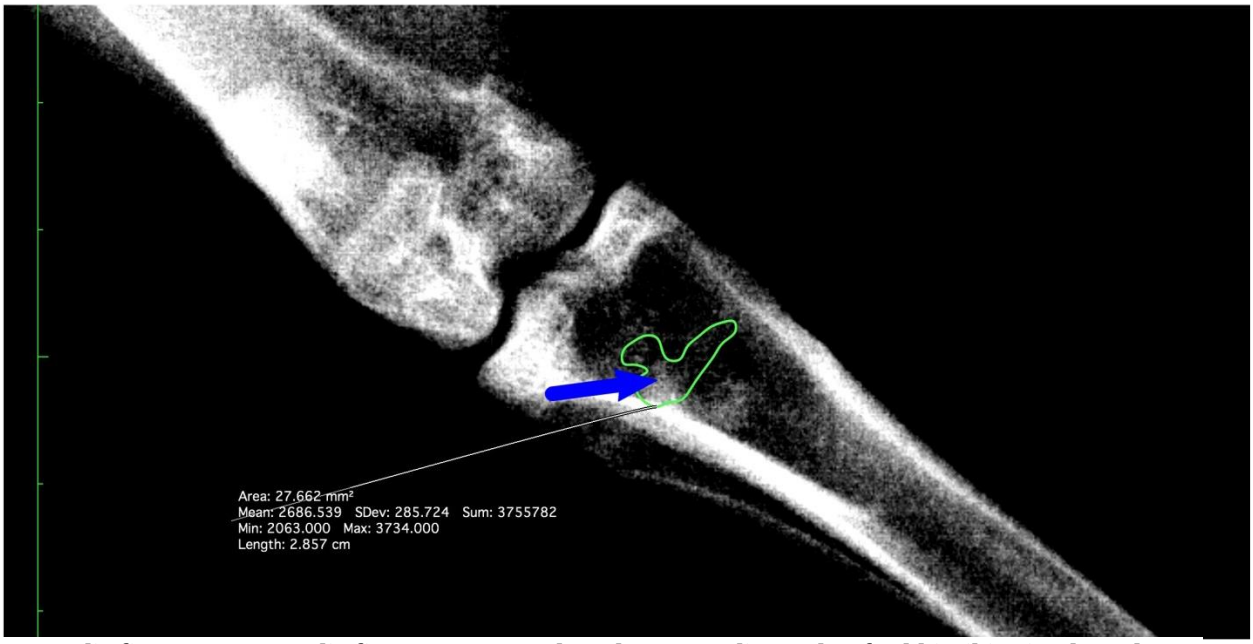

Appendix figure 11: Appendix figure 11: Four selected X-ray radiographs of rabbit tibiae implanted CPSC10 for 8 weeks. All analytical readings on images were used for semi-quantitative analyzes. One bar equals to 1 cm. Newly formed trabecular bones (blue arrow) were identified.

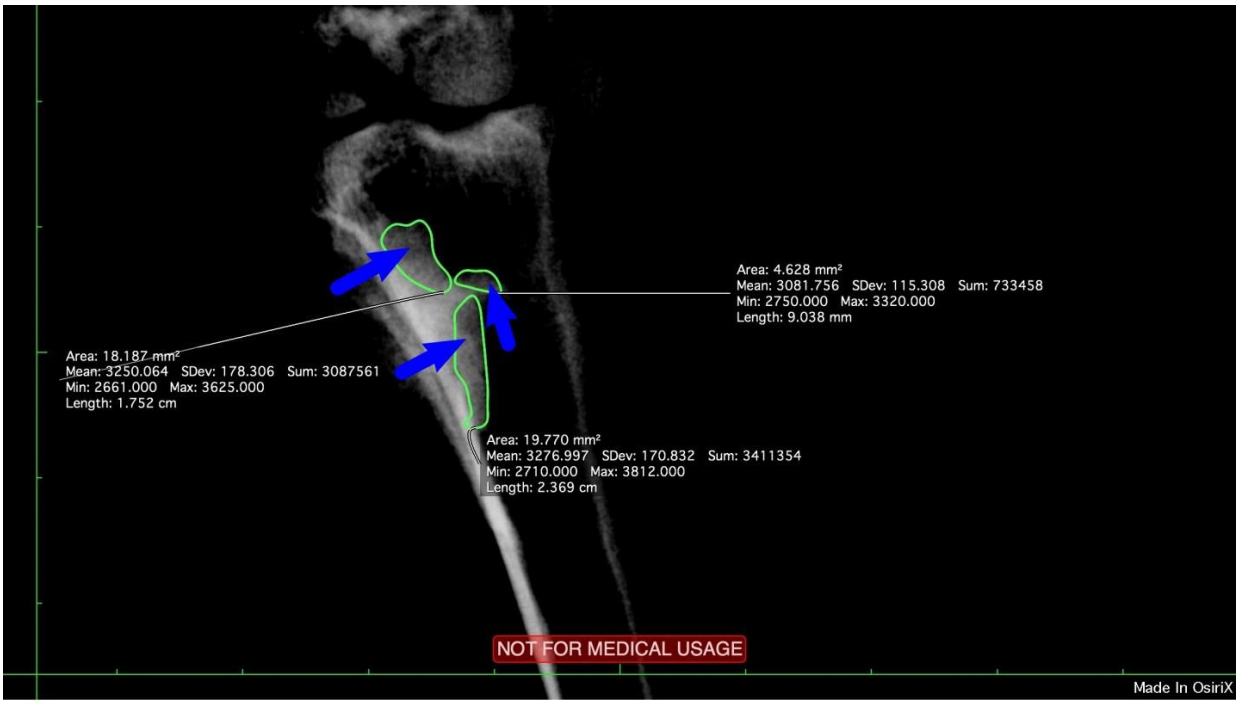
Area: 4.628 mm²
Mean: 3081.756 SDev: 115.308 Sum: 733458
Min: 2750.000 Max: 3320.000
Length: 9.038 mm
Area: 18.187 mm²
Mean: 3250.064 SDev: 178.306 Sum: 3087561
Min: 2661.000 Max: 3625.000
Length: 1.752 cm
Area: 19.770 mm²
Mean: 3276.997 SDev: 170.832 Sum: 3411354
Min: 2710.000 Max: 3812.000
Length: 2.369 cm
NOT FOR MEDICAL USAGE
Made In OsiriX

Area: 17.768 mm²
Mean: 2753.277 SDev: 139.516 Sum: 2645899
Min: 2390.000 Max: 3136.000
Length: 2.852 cm
Area: 16.592 mm²
Mean: 2823.808 SDev: 142.892 Sum: 2436946
Min: 2340.000 Max: 3261.000
Length: 2.558 cm
NOT FOR MEDICAL USAGE
Made In OsiriX

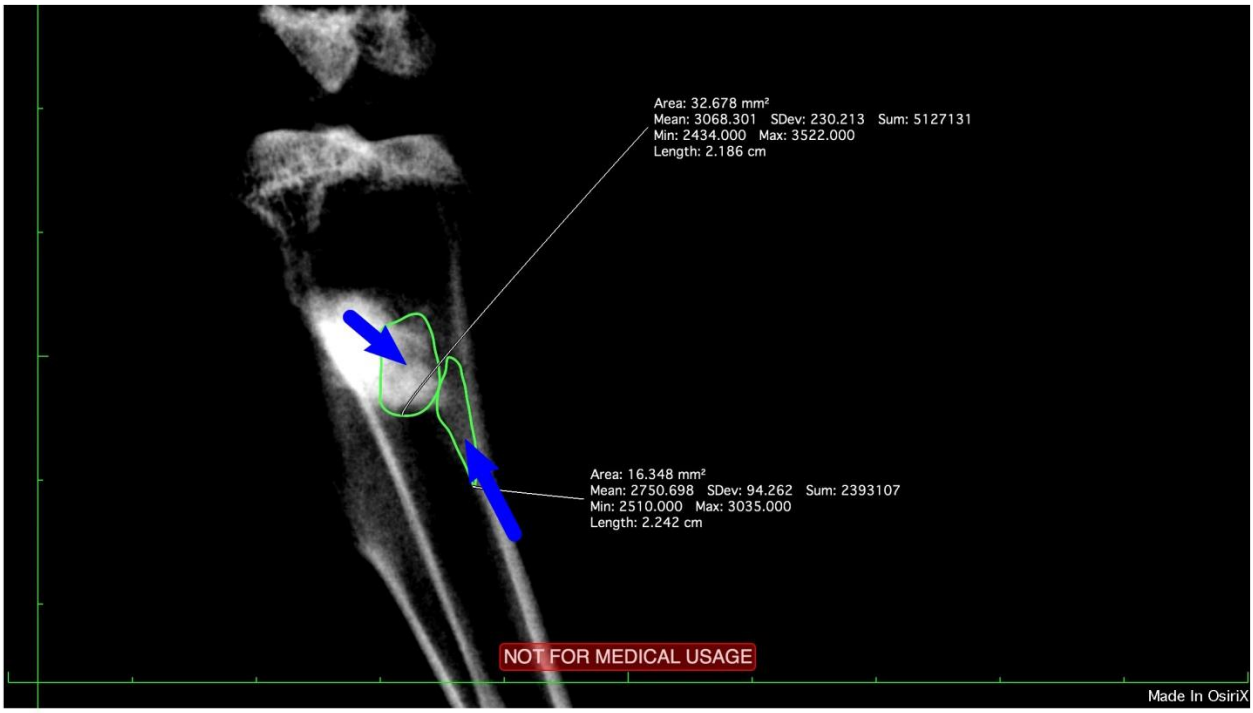

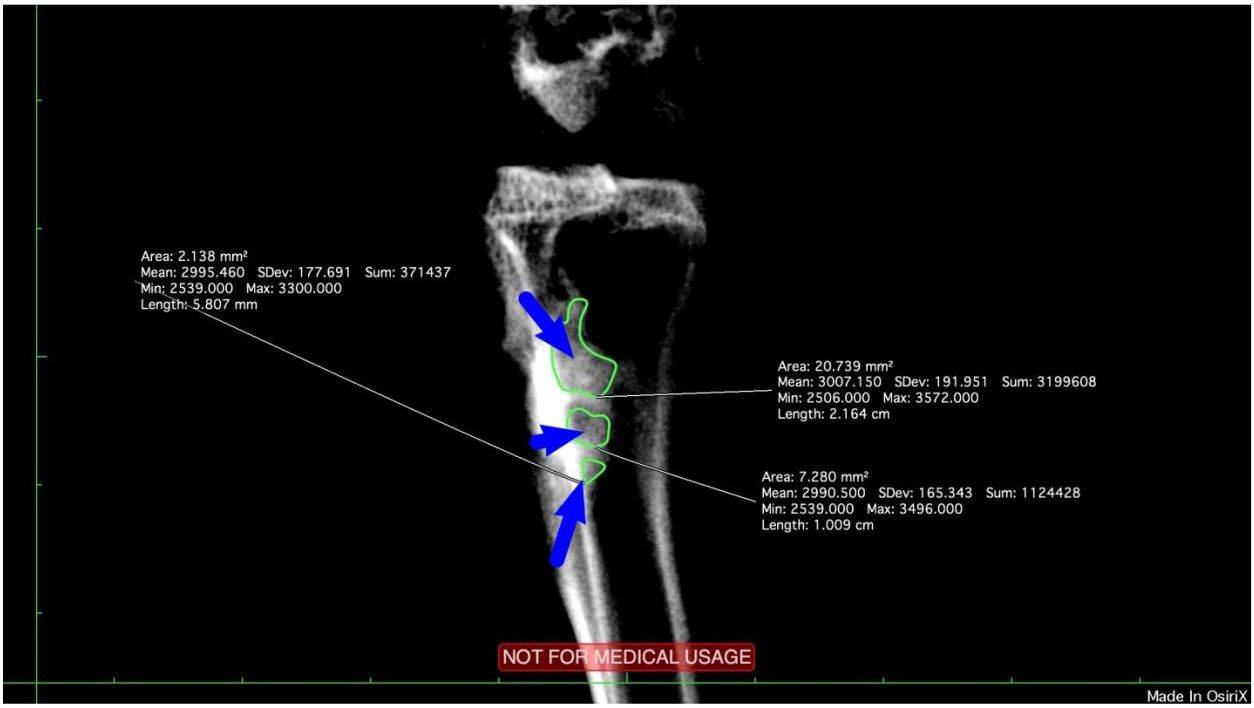

Appendix figure 12: Four selected X-ray radiographs of rabbit tibiae implanted CPSC10 for 10 weeks. All analytical readings on images were used for semi-quantitative analyzes. One bar equals to 1 cm. Newly formed trabecular bones (blue arrow) were identified.

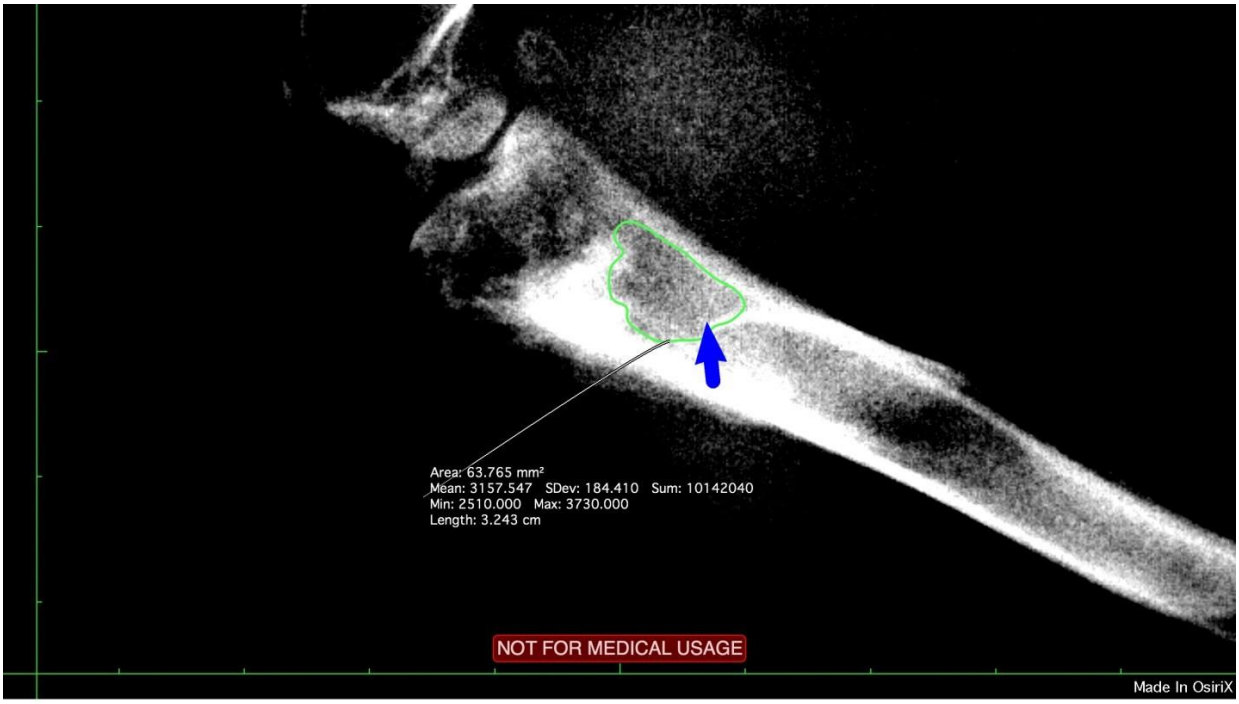
Area: 63.765 mm²
Mean: 3157.547 SDev: 184.410 Sum: 10142040
Min: 2510.000 Max: 3730.000
Length: 3.243 cm
NOT FOR MEDICAL USAGE
Made In OsiriX

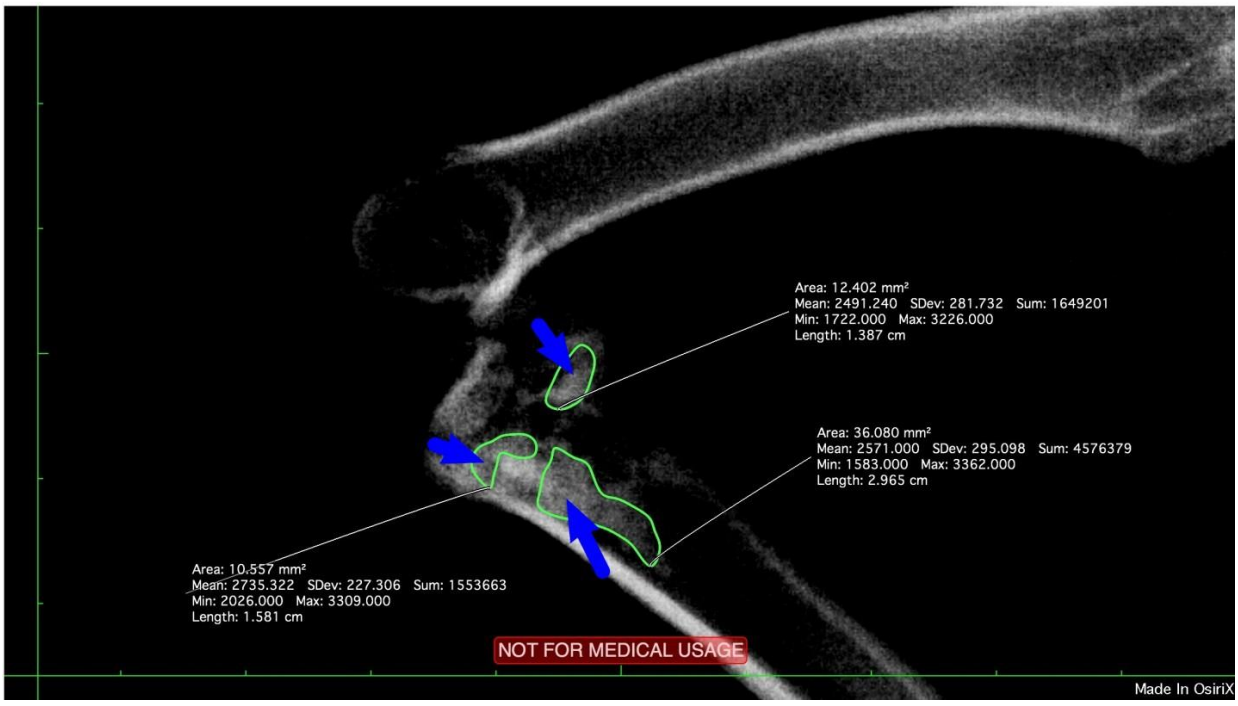
Area: 12.402 mm²
Mean: 2491.240 SDev: 281.732 Sum: 1649201
Min: 1722.000 Max: 3226.000
Length: 1.387 cm
Area: 36.080 mm²
Mean: 2571.000 SDev: 295.098 Sum: 4576379
Min: 1583.000 Max: 3362.000
Length: 2.965 cm
Area: 10.557 mm²
Mean: 2735.322 SDev: 227.306 Sum: 1553663
Min: 2026.000 Max: 3309.000
Length: 1.581 cm
NOT FOR MEDICAL USAGE
Made In OsiriX

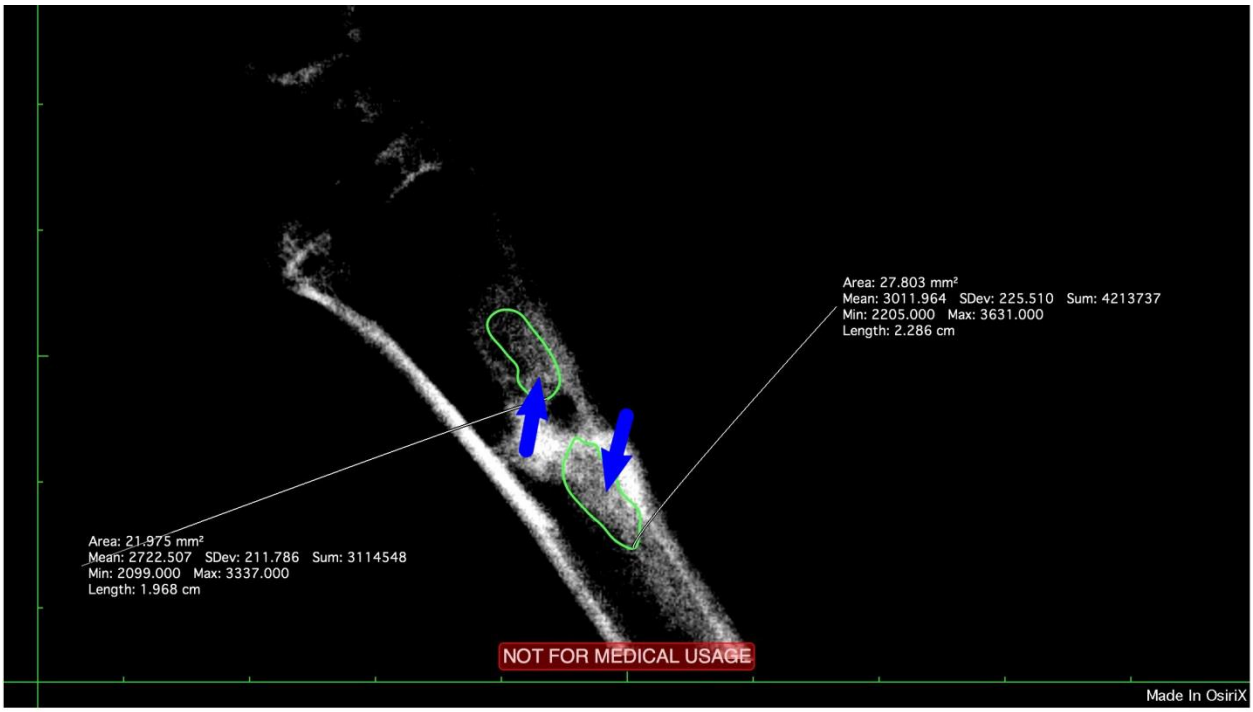

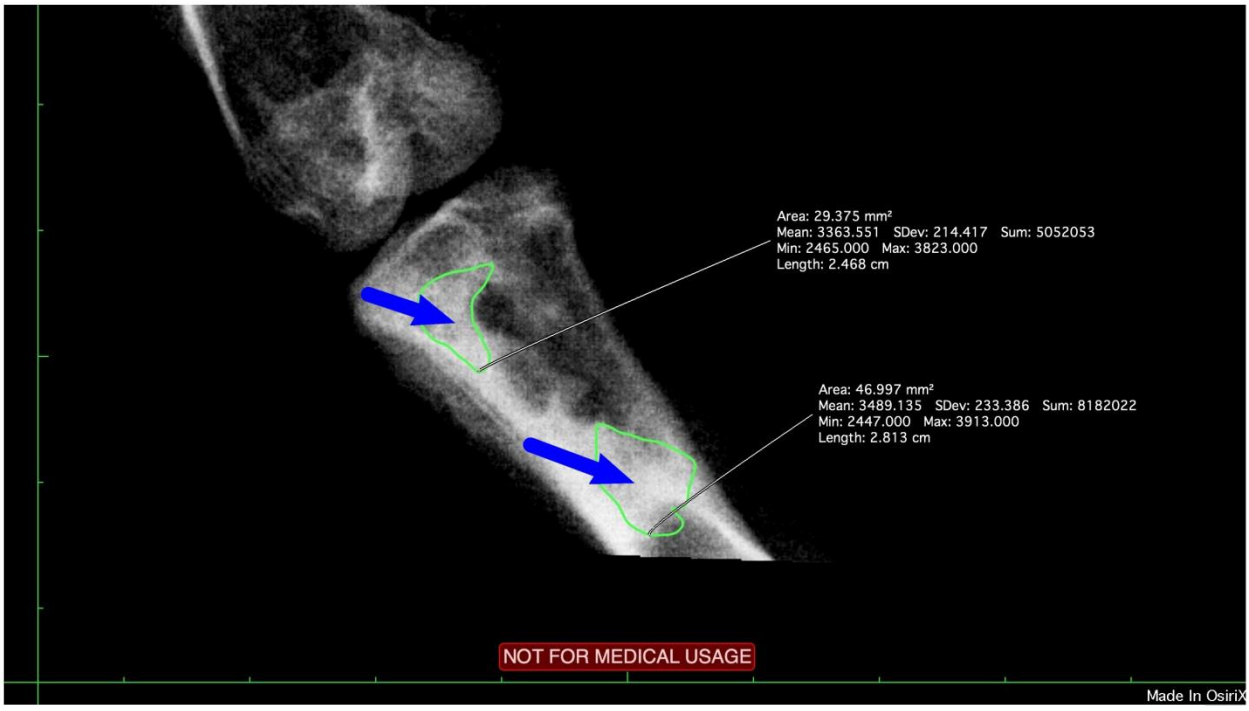

Appendix figure 13: Four selected X-ray radiographs of rabbit tibiae implanted CPSC10-05R for 8 weeks. All analytical readings on images were used for semi-quantitative analyzes. One bar equals to 1 cm. Newly formed trabecular bones (blue arrow) were identified.

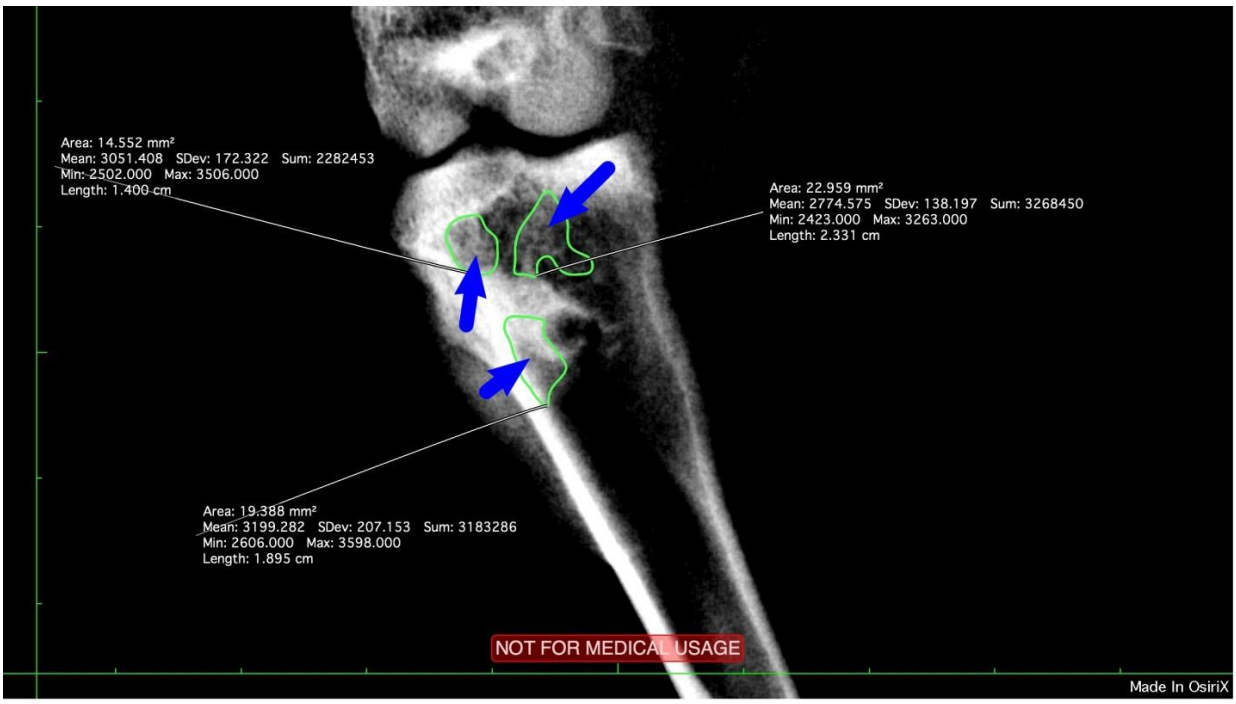
Area: 14.552 mm²
Mean: 3051.408 SDev: 172.322 Sum: 2282453
Min: 2502.000 Max: 3506.000
Length: 1.400 cm
Area: 22.959 mm²
Mean: 2774.575 SDev: 138.197 Sum: 3268450
Min: 2423.000 Max: 3263.000
Length: 2.331 cm
Area: 19.388 mm²
Mean: 3199.282 SDev: 207.153 Sum: 3183286
Min: 2606.000 Max: 3598.000
Length: 1.895 cm
NOT FOR MEDICAL USAGE
Made In OsiriX

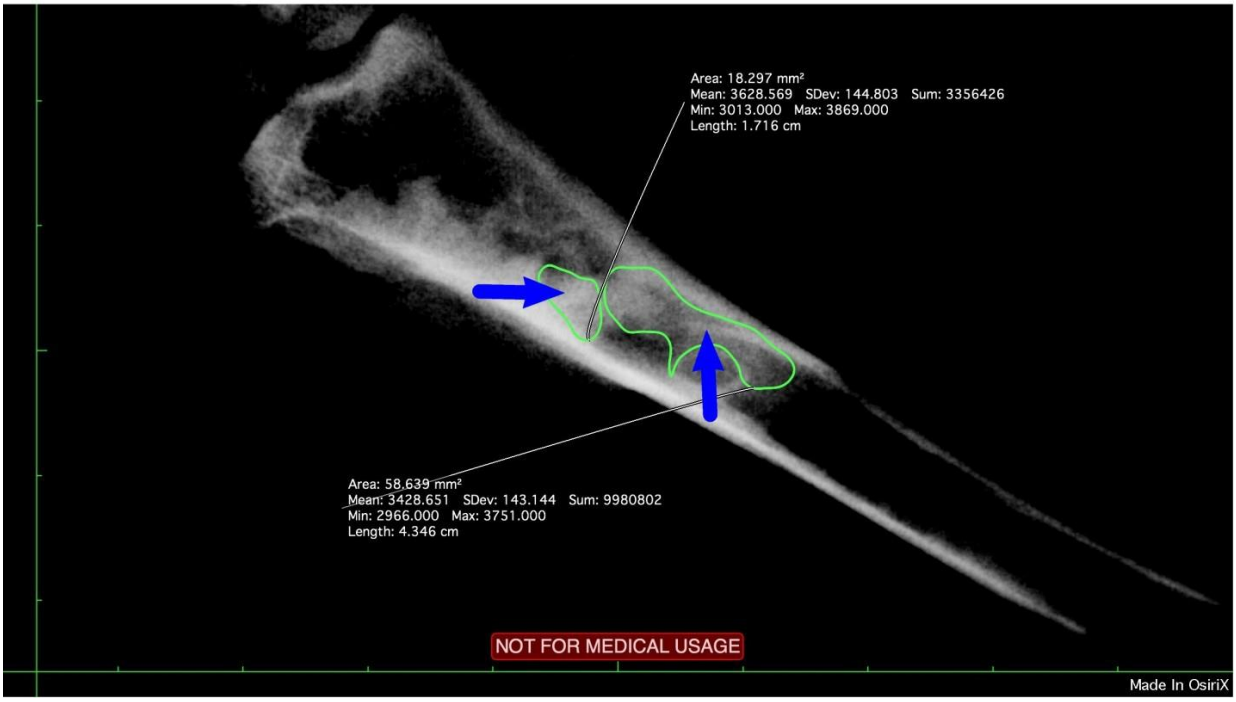
Area: 18.297 mm²
Mean: 3628.569 SDev: 144.803 Sum: 3356426
Min: 3013.000 Max: 3869.000
Length: 1.716 cm
Area: 58.639 mm²
Mean: 3428.651 SDev: 143.144 Sum: 9980802
Min: 2966.000 Max: 3751.000
Length: 4.346 cm
NOT FOR MEDICAL USAGE
Made In OsiriX

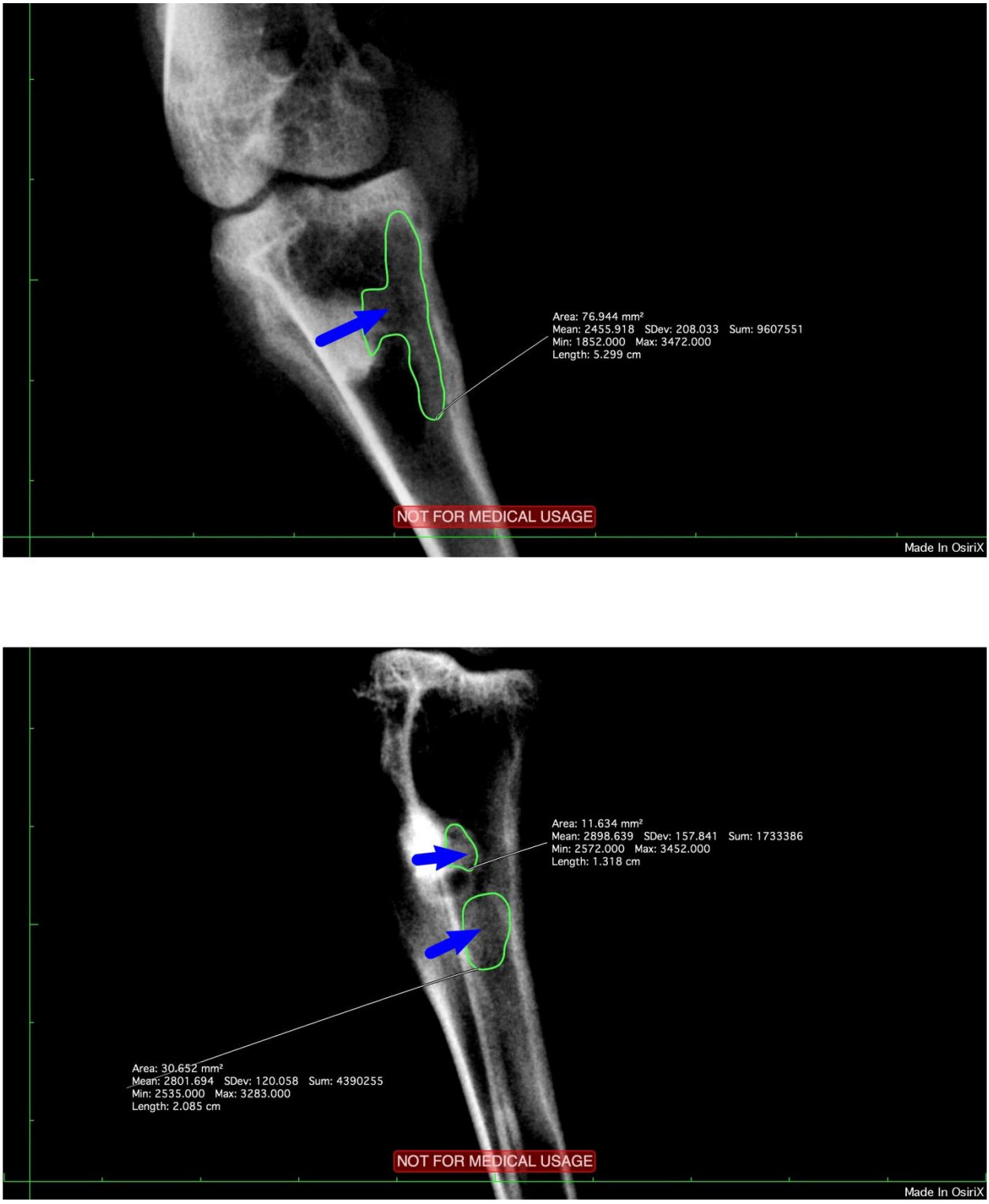

Appendix figure 14: Four selected X-ray radiographs of rabbit tibiae implanted CPSC10-05R for 10 weeks. All analytical readings on images were used for semi-quantitative analyzes. One bar equals to 1 cm. Newly formed trabecular bones (blue arrow) were identified.

E.2 Supplementary histological images

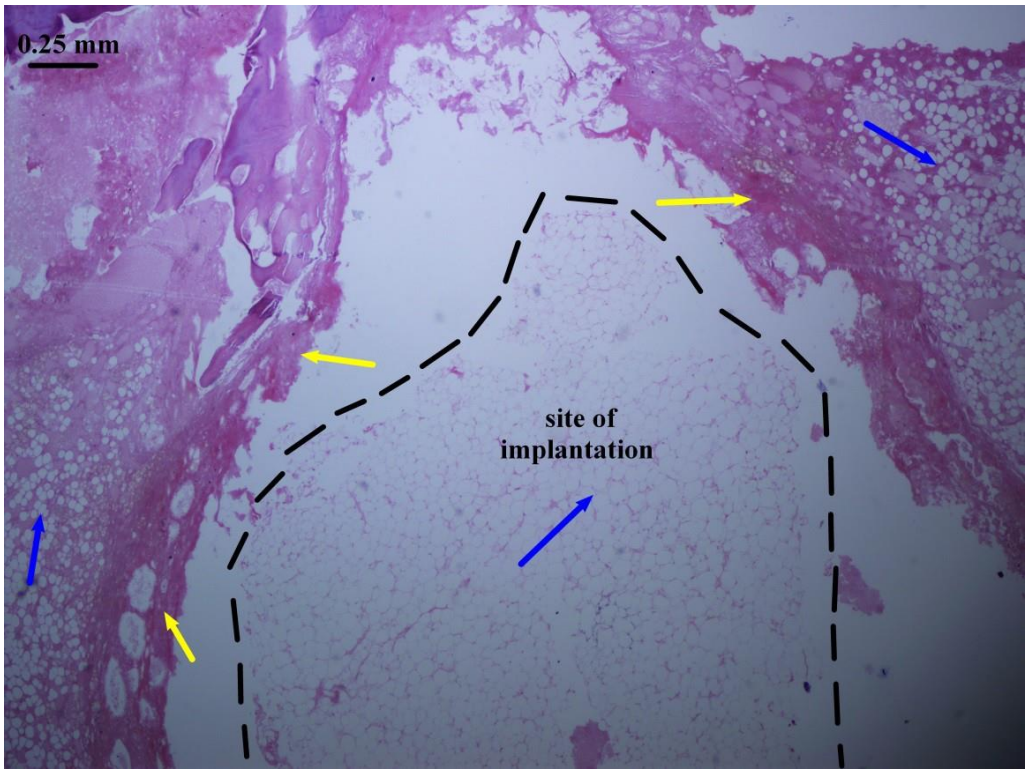

Appendix figure 15: Histological image of CPC implantation sites after the 2-month implantation (40X magnification). Proliferative fibrous tissue encapsulation (yellow arrows) and proliferated adipose tissue and fibrous tissue (blue arrows) are observed. Broken lines indicate the site of implantation. One bar equals to 0.25 mm.

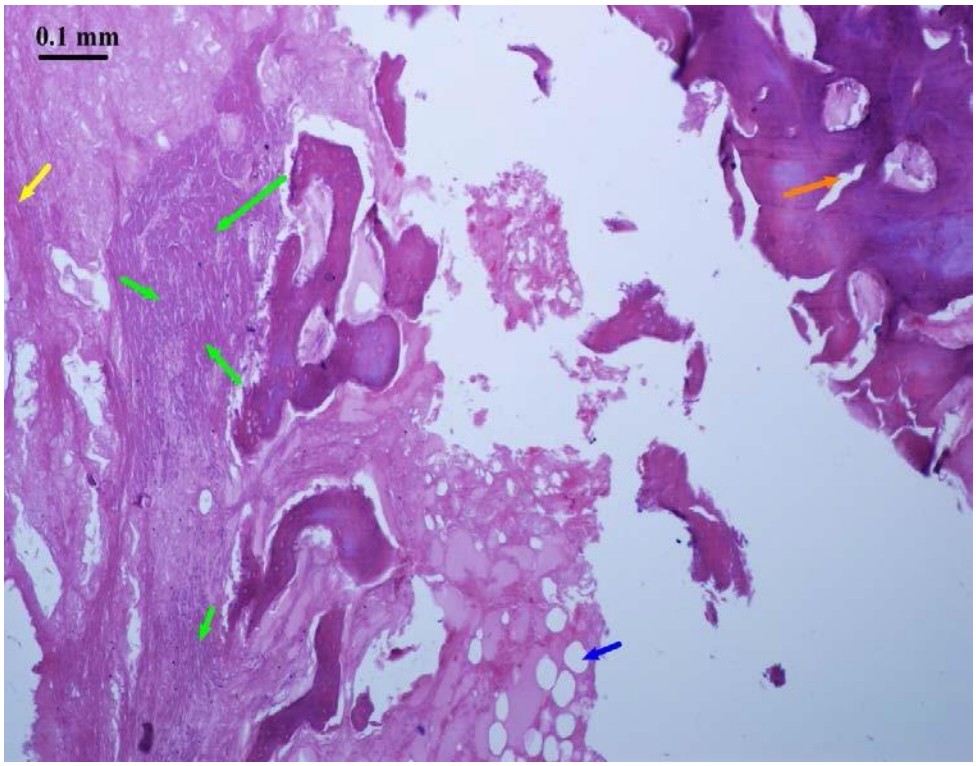

Appendix figure 16: Histological image of CPC implantation sites after the 2-month implantation (100X magnification). Proliferative fibrous tissue encapsulation (yellow arrows), proliferated adipose tissue and fibrous tissue (blue arrows), bone lacunae (orange arrows) and new bone formation (green arrows) are observed. One bar equals to 0.1 mm.

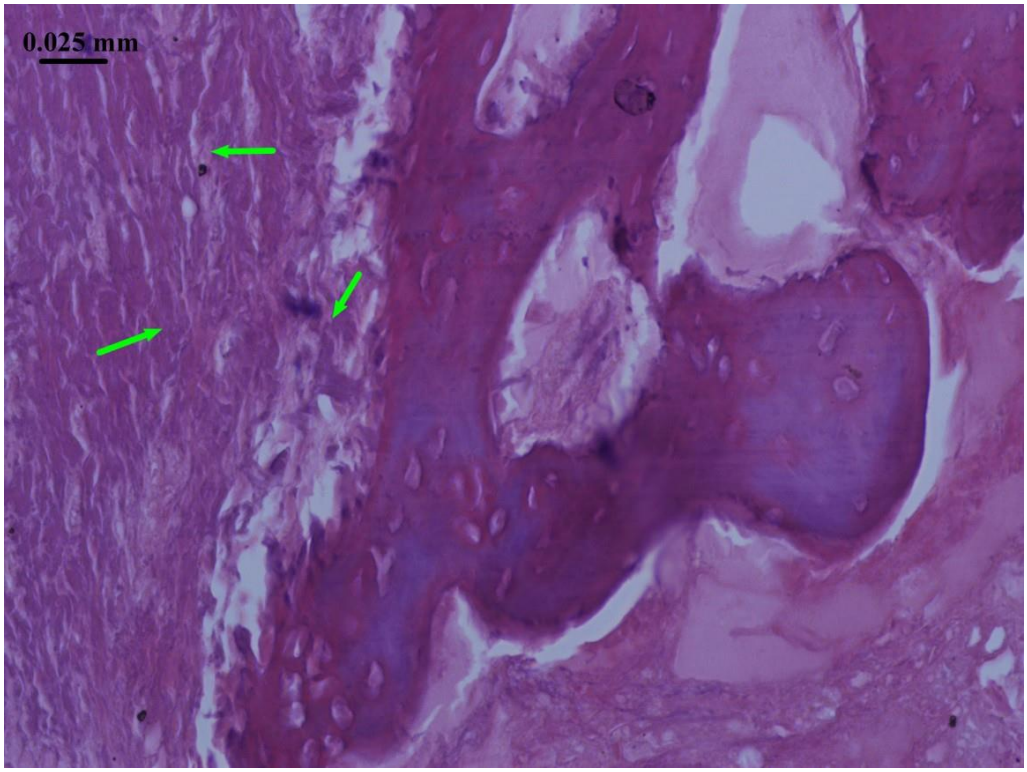

Appendix figure 17: Histological image of CPC implantation sites after the 2-month implantation (400X magnification). New bone formation (green arrows) is observed. One bar equals to 0.025 mm.

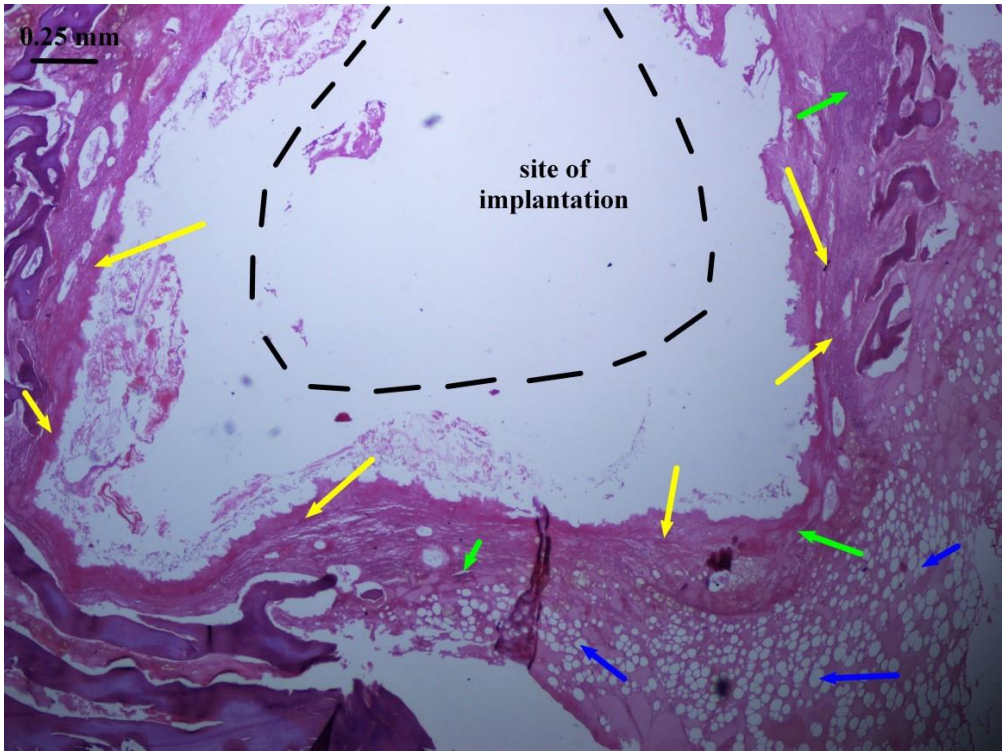

Appendix figure 18: Histological image of CPC implantation sites after the 3-month implantation (40X magnification). Proliferative fibrous tissue encapsulation (yellow arrows), proliferated adipose tissue and fibrous tissue (blue arrows) and new bone formation (green arrows) are observed. Broken lines indicate the site of implantation. One bar equals to 0.25 mm.

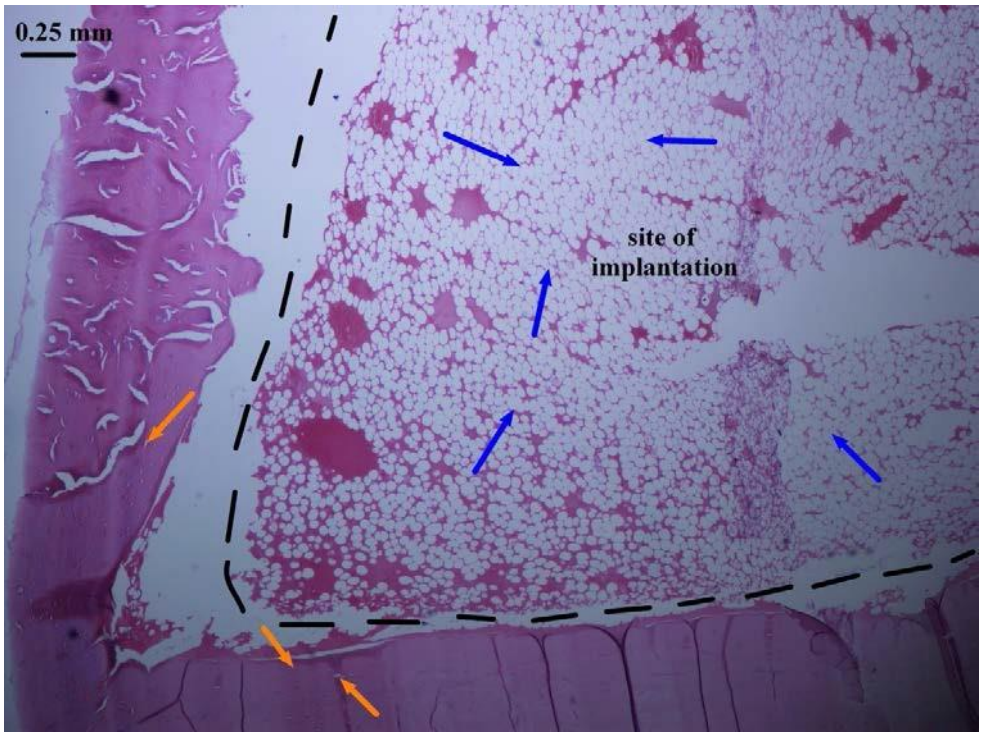

Appendix figure 19: Histological image of the sham control perforation site after the 2-month implantation (40X magnification). Bone lacunae (orange arrows), proliferated adipose tissue and fibrous tissue (blue arrows) are observed. Broken lines indicate the site of implantation. One bar equals to 0.25 mm.

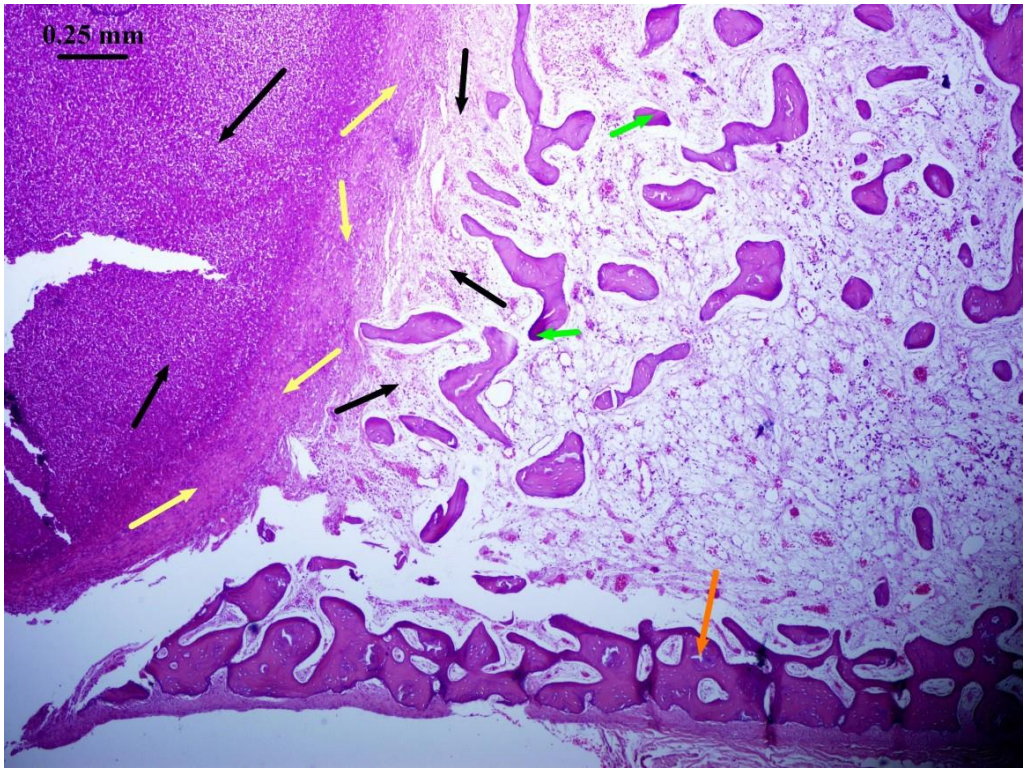

Appendix figure 20: Histological image of the sham control perforation site after the 3-month implantation (40X magnification). Inflammation by neutrophils infiltration (black arrows), proliferative fibrous tissue encapsulation (yellow arrows), bone lacunae (orange arrows) and new bone formation (green arrows) are observed. One bar equals to 0.25 mm.

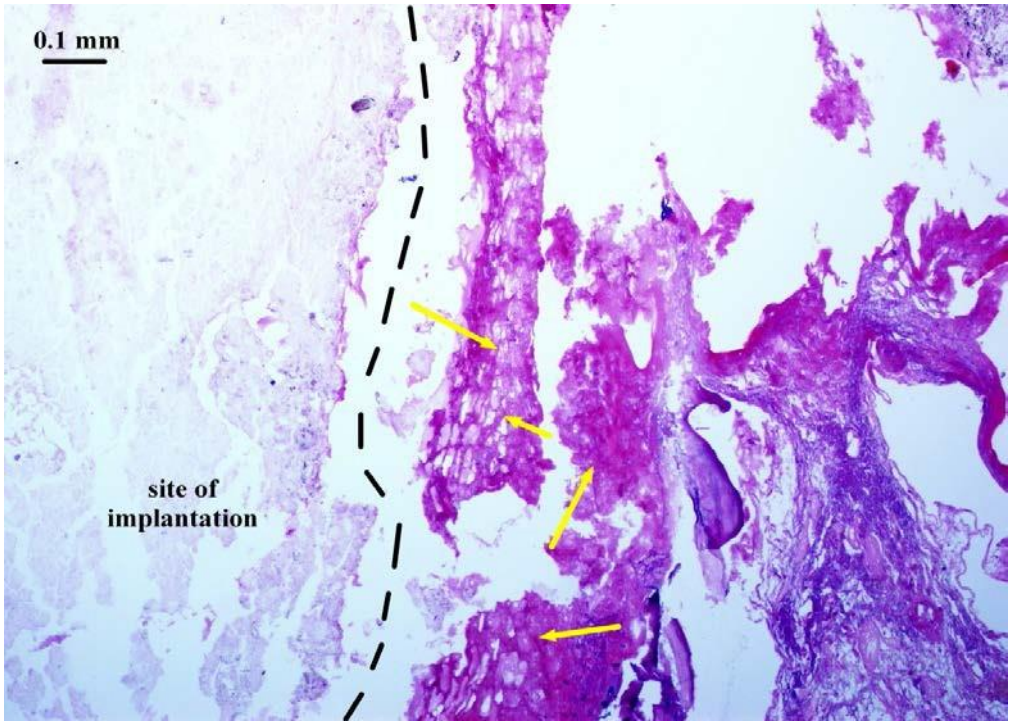

Appendix figure 21: Histological image of CPSC5 implantation sites after the 2-month implantation (100X magnification). Proliferative fibrous tissue encapsulation (yellow arrows) is observed. Broken lines indicate the site of implantation. One bar equals to 0.1 mm.

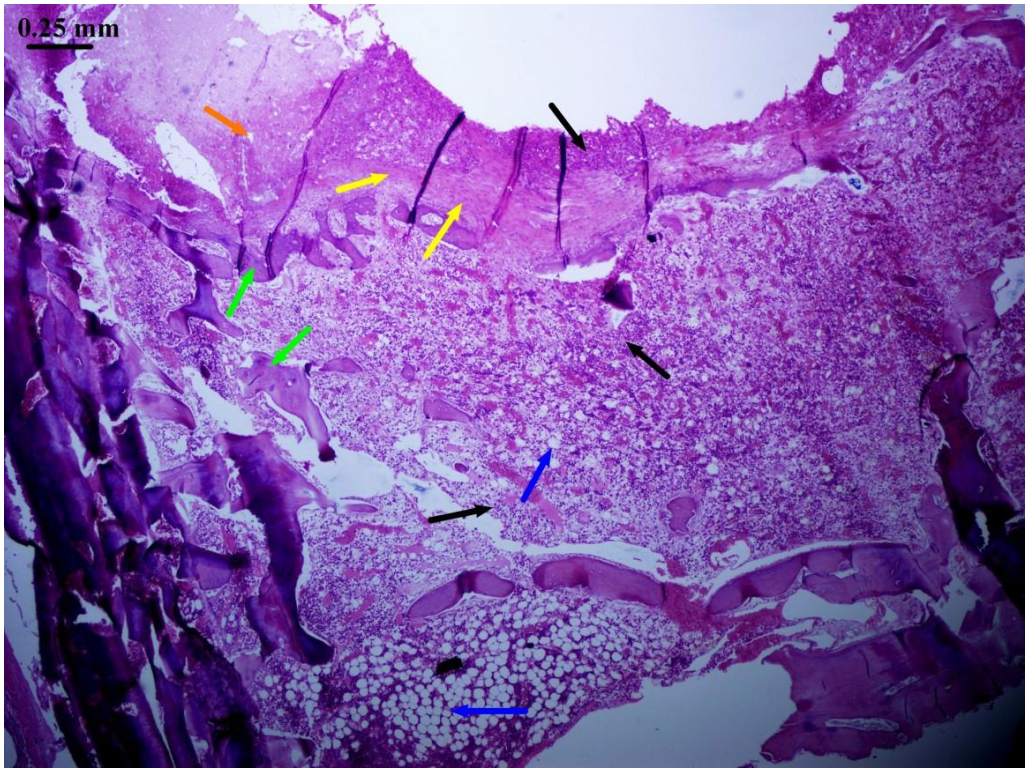

Appendix figure 22: Histological image of CPSC5 implantation sites after the 3-month implantation (40X magnification). Inflammation by neutrophils infiltration (black arrows), proliferative fibrous tissue encapsulation (yellow arrows), proliferated adipose tissue and fibrous tissue (blue arrows), bone lacunae (orange arrows) and new bone formation (green arrows) are observed. One bar equals to 0.25 mm.

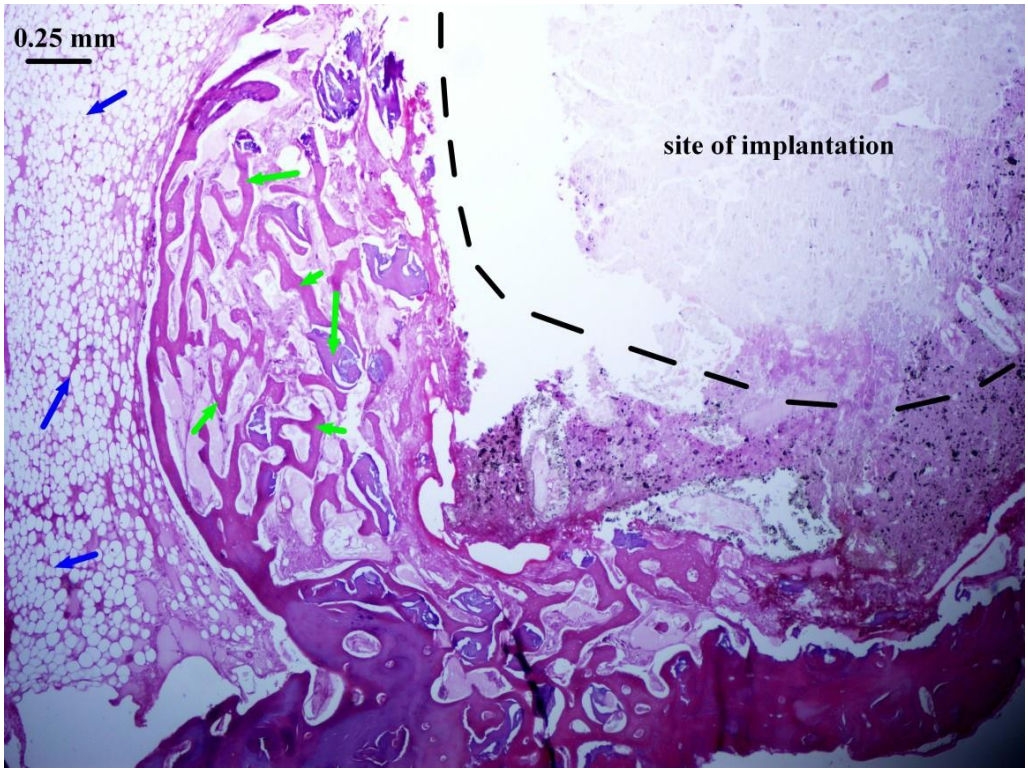

Appendix figure 23: Histological image of CPSC10 implantation sites after the 3-month implantation (40X magnification). New bone formation (green arrows) is observed. Broken lines indicate the site of implantation. One bar equals to 0.25 mm.

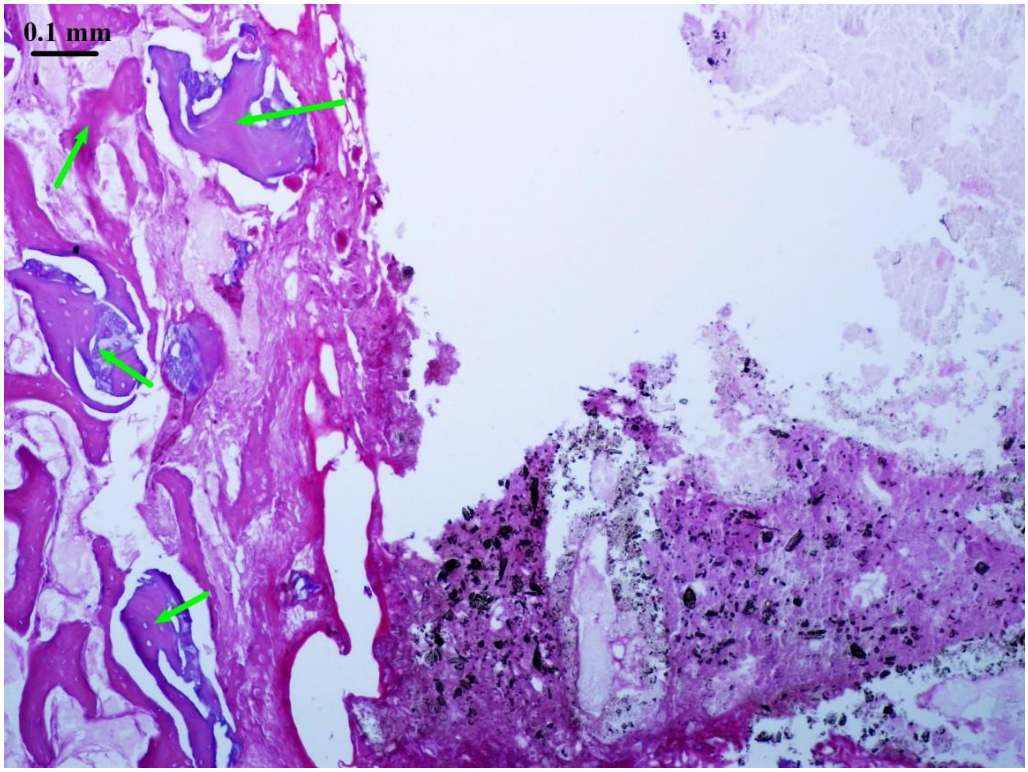

Appendix figure 24: Histological image of CPSC10 implantation sites after the 3-month implantation (100X magnification). Proliferated adipose tissue and fibrous tissue (blue arrows) and new bone formation (green arrows) are observed. One bar equals to 0.1 mm.

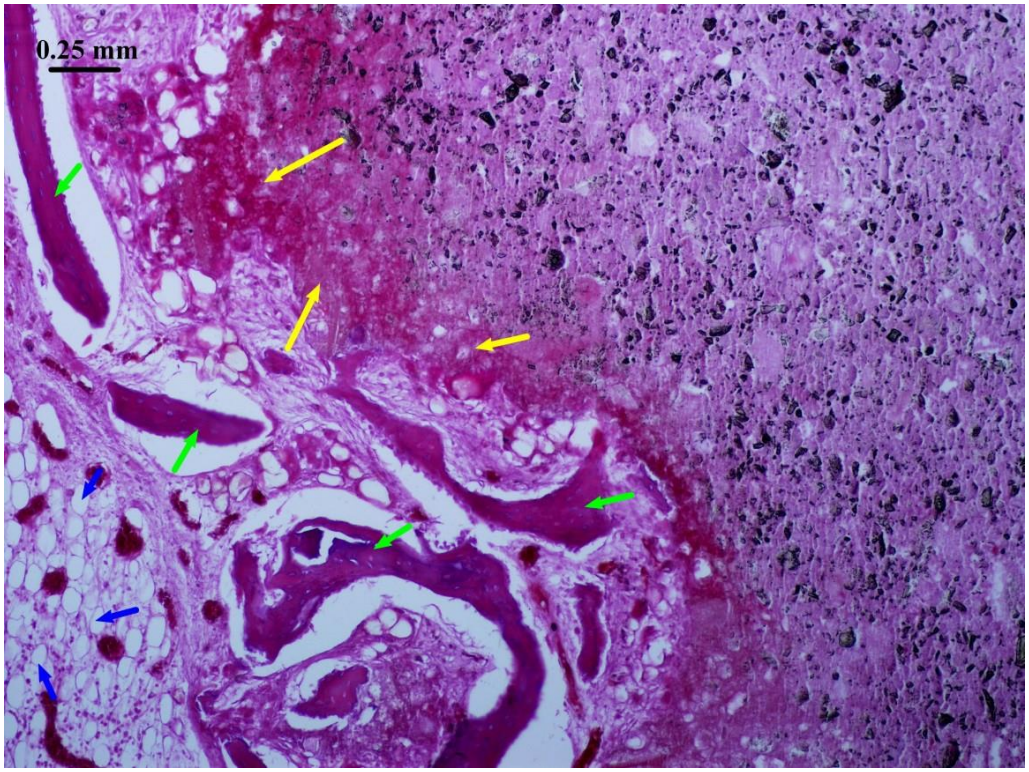

Appendix figure 25: Histological image of CPSC15 implantation sites after the 2-month implantation (40X magnification). Proliferative fibrous tissue encapsulation (yellow arrows), proliferated adipose tissue and fibrous tissue (blue arrows) and new bone formation (green arrows) are observed. One bar equals to 0.25 mm.

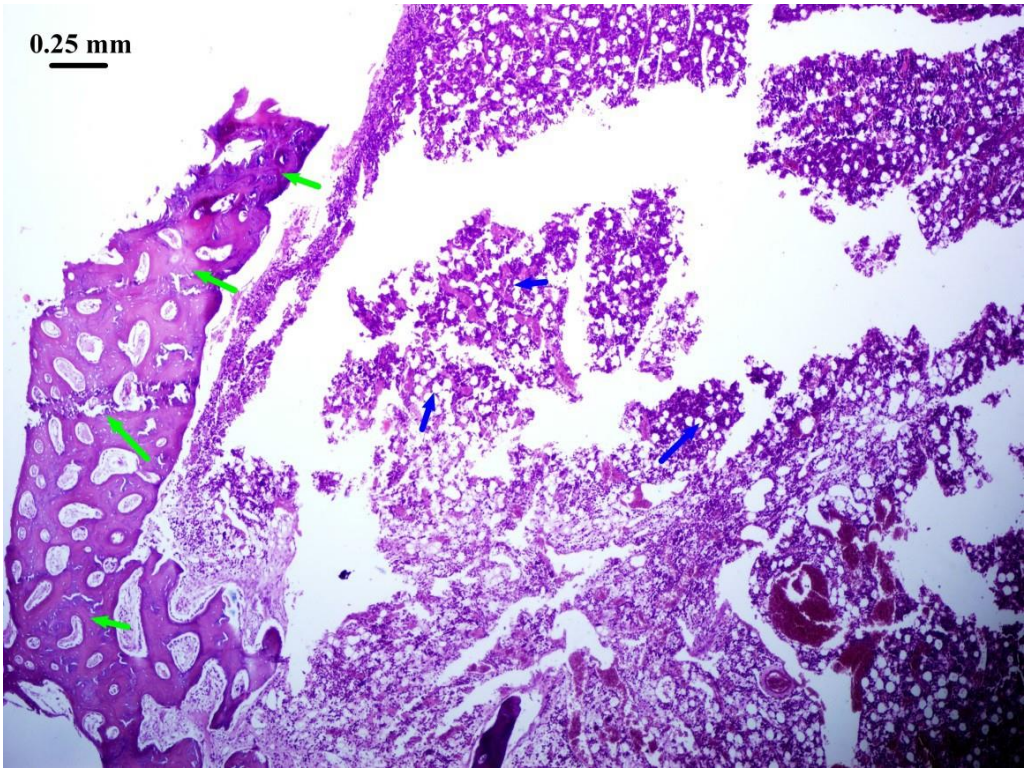

Appendix figure 26: Histological image of CPSC15 implantation sites after the 3-month implantation (40X magnification). Proliferated adipose tissue and fibrous tissue (blue arrows) and new bone formation (green arrows) are observed. One bar equals to 0.25 mm.

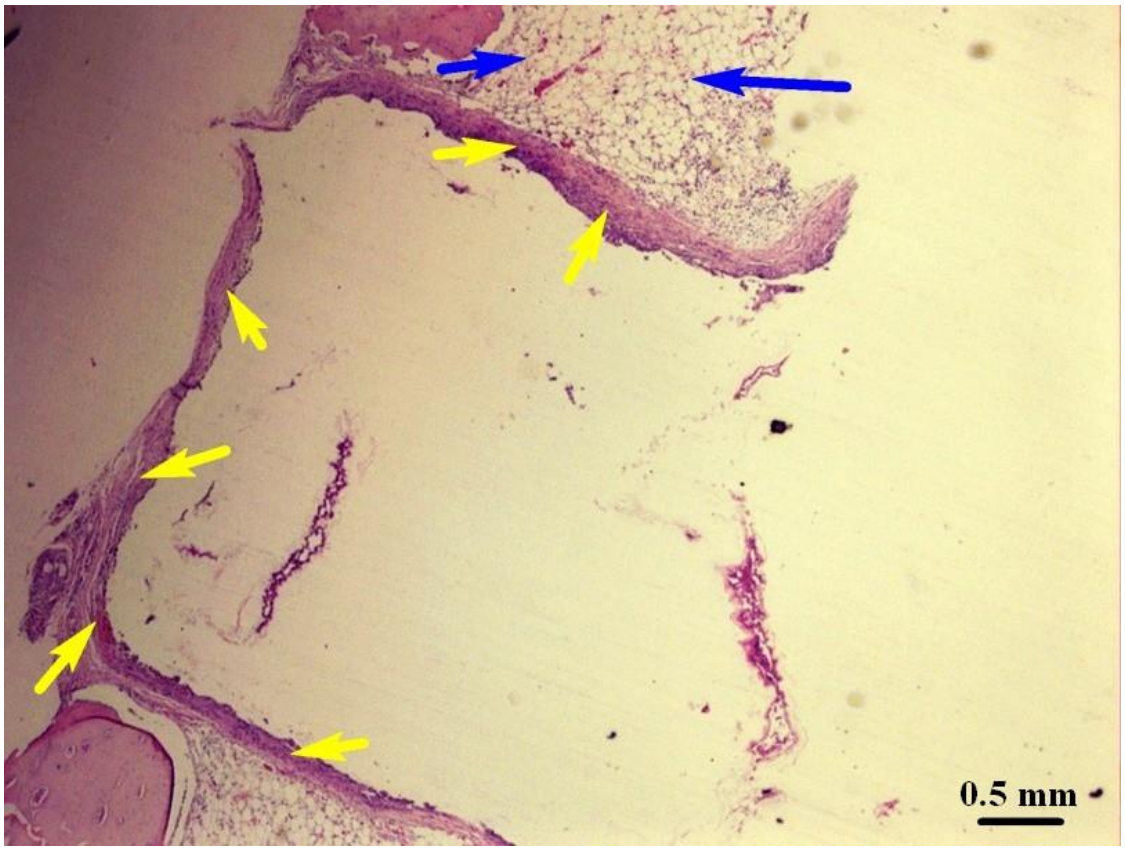

Appendix figure 27: Histological observations of the perforation in the sham control group after 10 weeks (20X magnification). Proliferative fibrous tissue encapsulation (yellow arrows) and proliferated adipose tissue and fibrous tissue (blue arrows) are observed. One bar equals to 0.5 mm. (Osteoporotic condition)

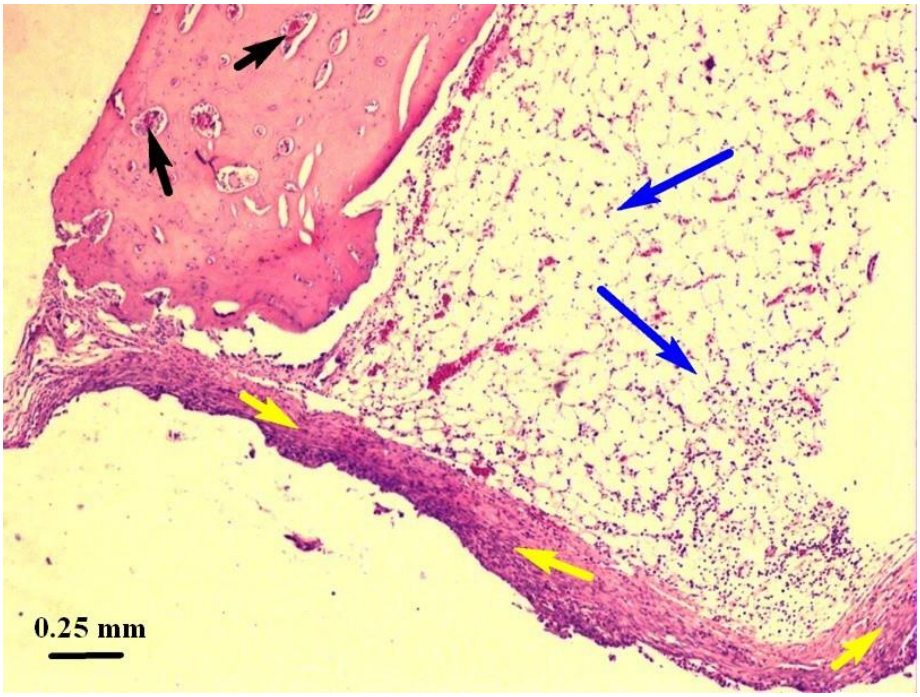

Appendix figure 28: Histological observations of the perforation in the sham control group after 10 weeks (40X magnification). Inflammation by neutrophils infiltration (black arrows), proliferative fibrous tissue encapsulation (yellow arrows) and proliferated adipose tissue and fibrous tissue (blue arrows) are observed. One bar equals to 0.25 mm. (Osteoporotic condition)

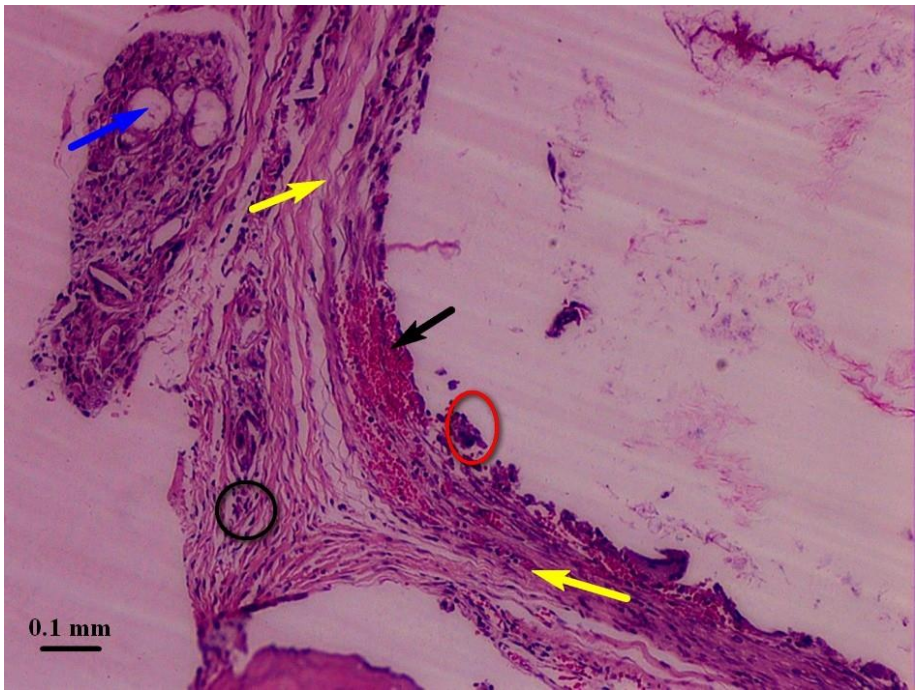

Appendix figure 29: Histological observations of the perforation in the sham control group after 10 weeks (100X magnification). Inflammation by neutrophils infiltration (black arrows), proliferative fibrous tissue encapsulation (yellow arrows), proliferated adipose tissue and fibrous tissue (blue arrows), osteoclast cells (red circle) and osteoblast cells (black circle) are observed. One bar equals to 0.1 mm. (Osteoporotic condition)

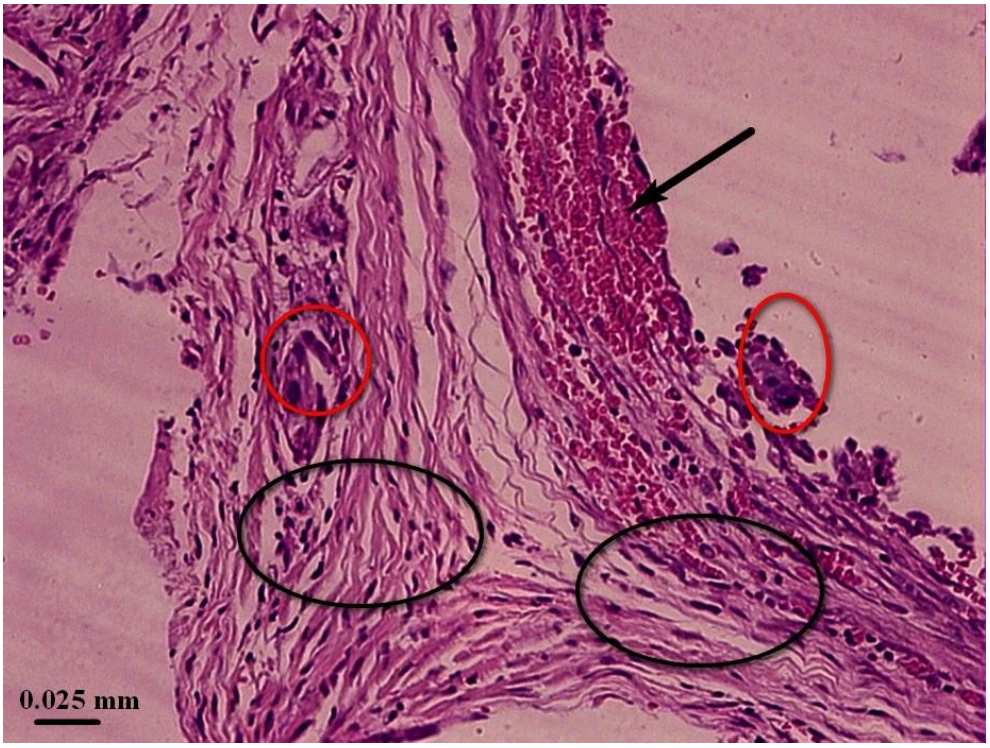

Appendix figure 30: Histological observations of the perforation in the sham control group after 10 weeks (400X magnification). Inflammation by neutrophils infiltration (black arrows), osteoclast cells (red circles) and osteoblast cells (black circles) are observed. One bar equals to 0.025 mm. (Osteoporotic condition)

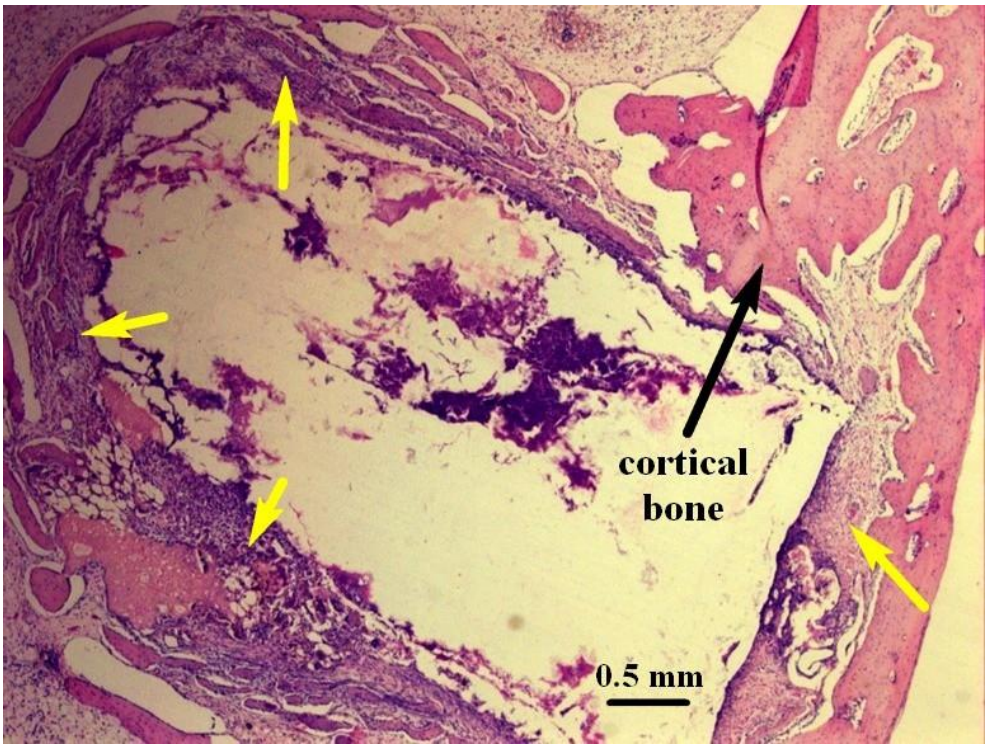

Appendix figure 31: Histological observations of the perforation in the CPSC10 group after 10 weeks (20X magnification). Proliferative fibrous tissue encapsulation (yellow arrows) is observed. One bar equals to 0.5 mm. (Osteoporotic condition)

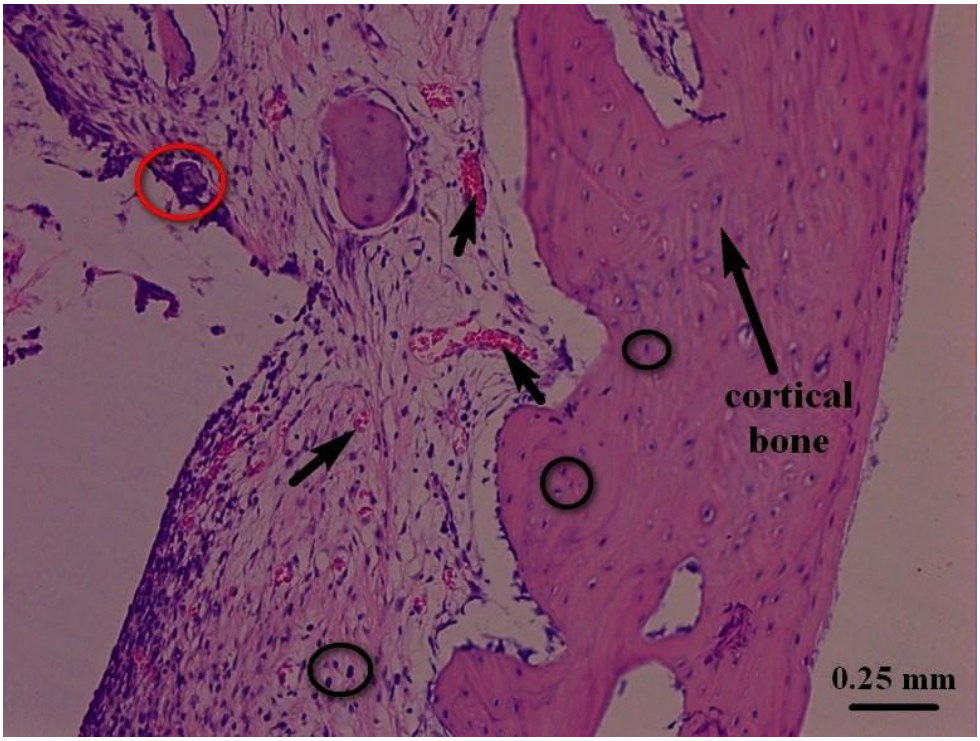

Appendix figure 32: Histological observations of the perforation in the CPSC10 group after 10 weeks (40X magnification). Inflammation by neutrophils infiltration (black arrows), osteoclast cells (red circles) and osteoblast cells (black circles) are observed. One bar equals to 0.25 mm. (Osteoporotic condition)

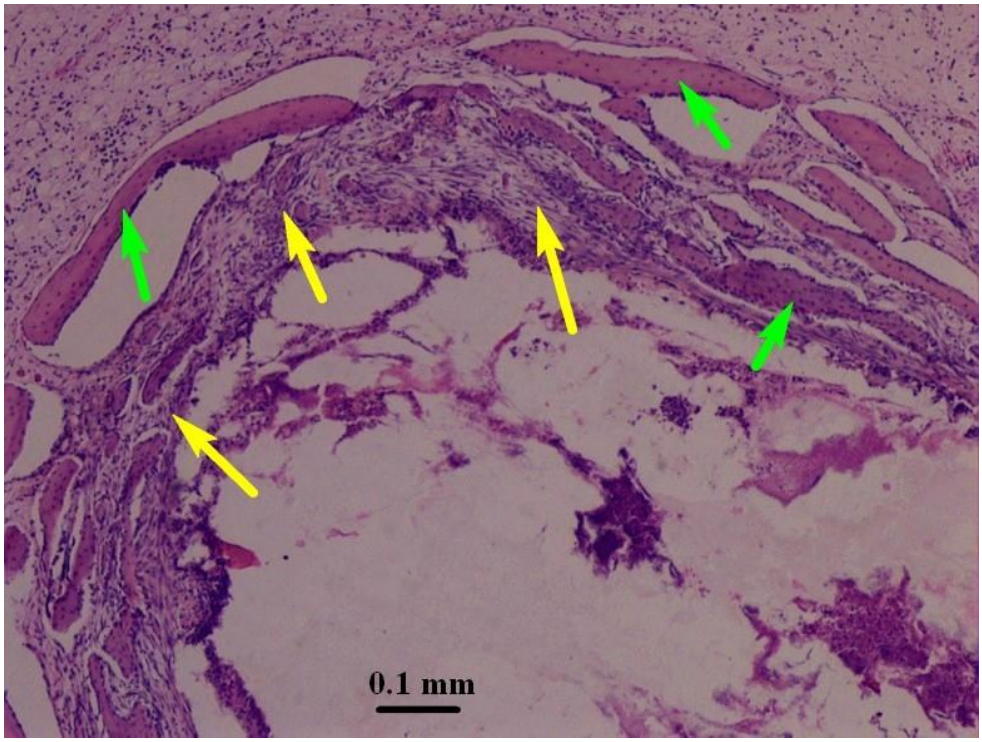

Appendix figure 33: Histological observations of the perforation in the CPSC10 group after 10 weeks (100X magnification). Proliferative fibrous tissue encapsulation (yellow arrows) and new bone formation (green arrows) are observed. One bar equals to 0.1 mm. (Osteoporotic condition)

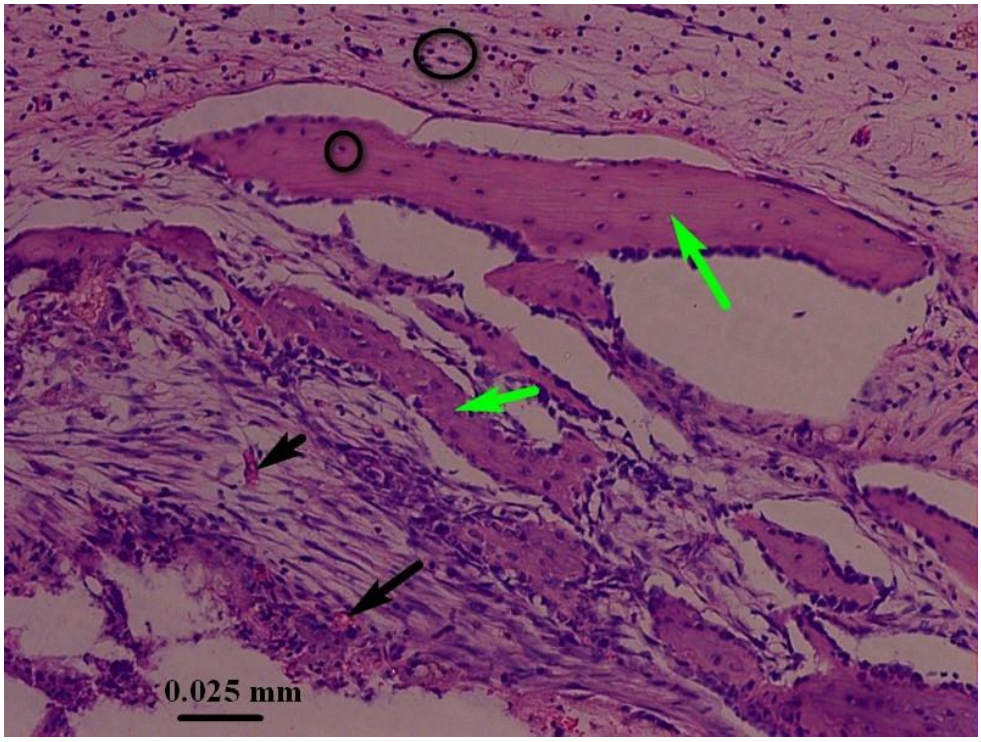

Appendix figure 34: Histological observations of the perforation in the CPSC10 group after 10 weeks (400X magnification). Inflammation by neutrophils infiltration (black arrows), new bone formation (green arrows) and osteoblast cells (black circles) are observed. One bar equals to 0.025 mm. (Osteoporotic condition)

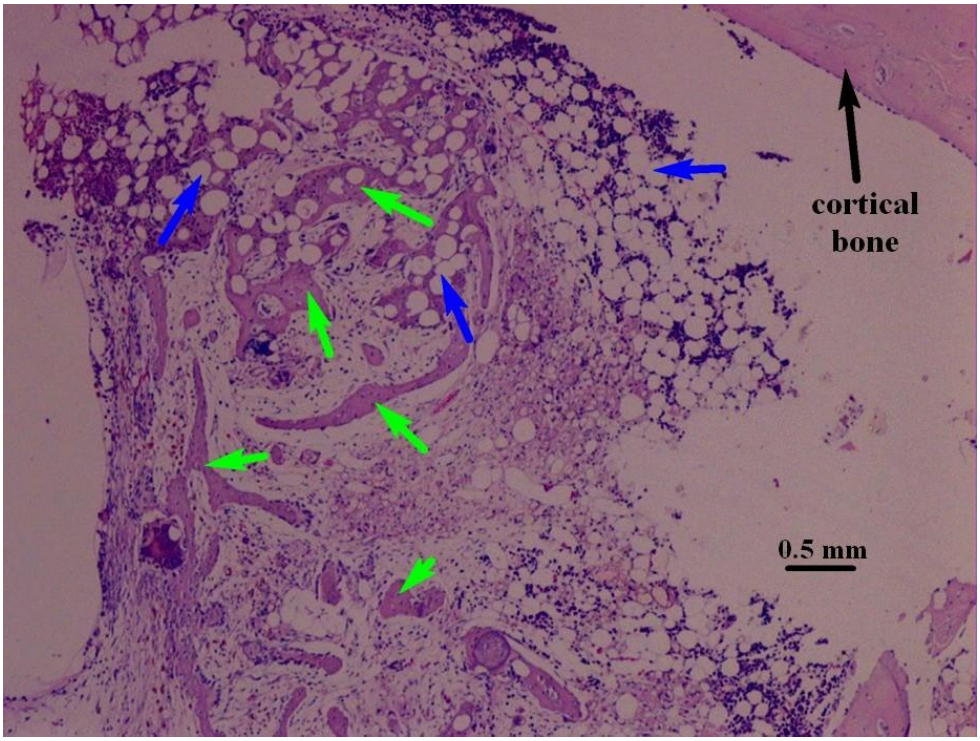

Appendix figure 35: Histological observations of the perforation in the CPSC10-05R group after 10 weeks (20X magnification). Proliferated adipose tissue and fibrous tissue (blue arrows) and new bone formation (green arrows) are observed. One bar equals to 0.5 mm. (Osteoporotic condition)

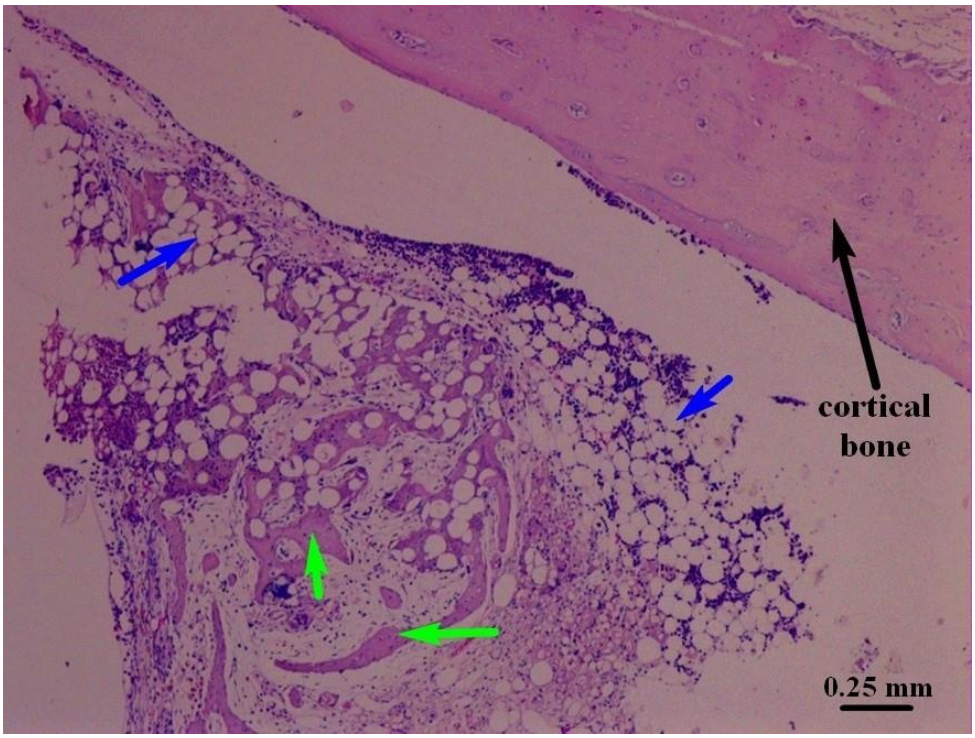

Appendix figure 36: Histological observations of the perforation in the CPSC10-05R group after 10 weeks (40X magnification). Proliferated adipose tissue and fibrous tissue (blue arrows) and new bone formation (green arrows) are observed. One bar equals to 0.25 mm. (Osteoporotic condition)

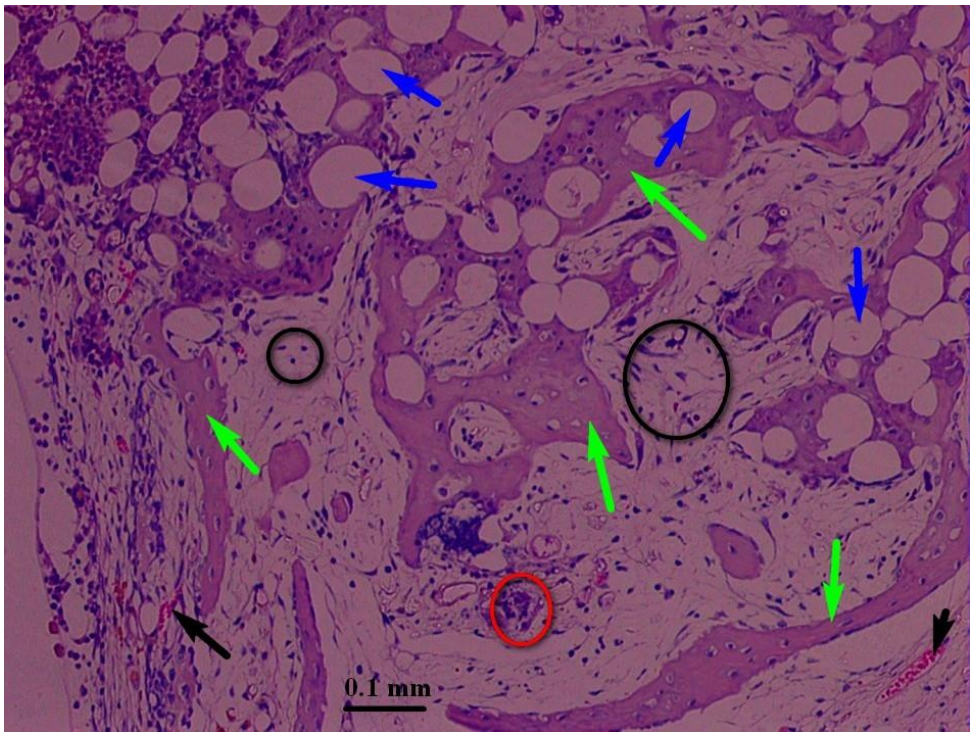

Appendix figure 37: Histological observations of the perforation in the CPSC10-05R group after 10 weeks (100X magnification). Inflammation by neutrophils infiltration (black arrows) proliferated adipose tissue and fibrous tissue (blue arrows), new bone formation (green arrows), osteoclast cells (red circles) and osteoblast cells (black circles) are observed. One bar equals to 0.1 mm. (Osteoporotic condition)

E.3 Supplementary PCR array results

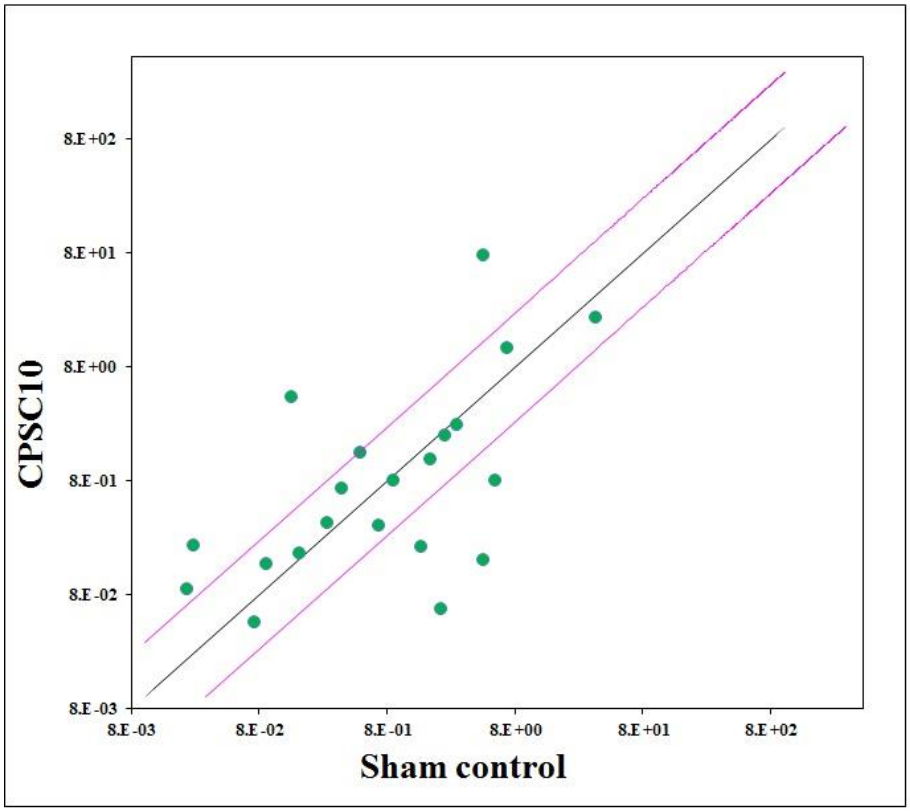

Appendix figure 38: Genes related to bone mineralization analyzed by PCR array in CPSC10 *vs.* the sham control. Pink lines represent threshold fold changes (= 3). The data are presented by fold changes of genes in CPSC10 (y-axis) versus fold changes of genes in the sham control (x-axis) in logarithm scale (base = 2). (*n* = 4)

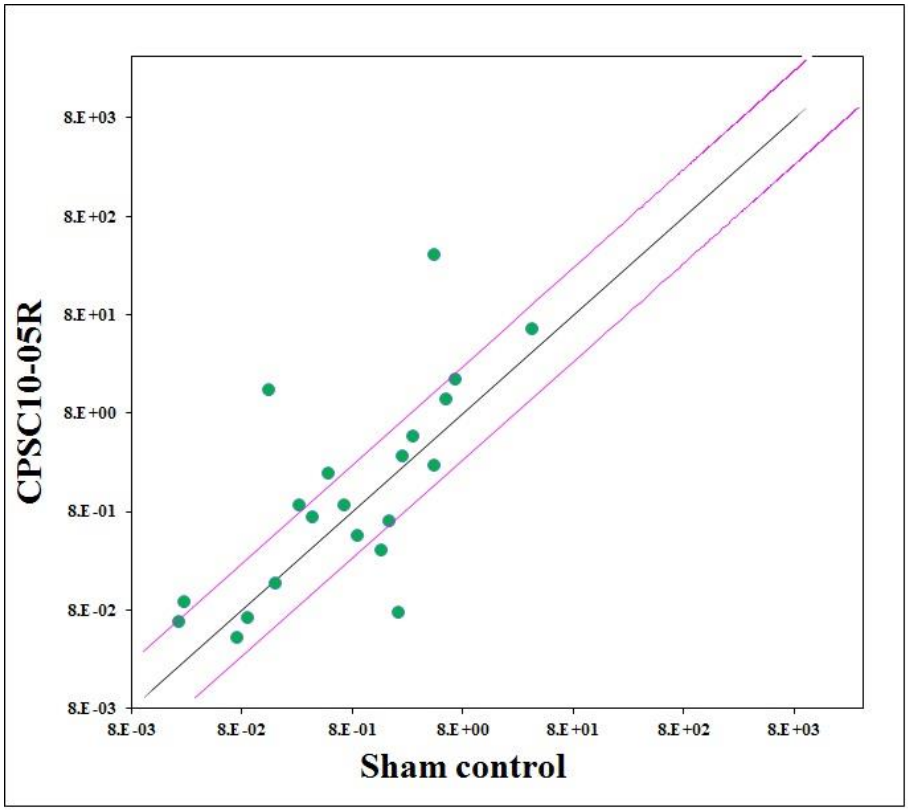

Appendix figure 39: Genes related to bone mineralization analyzed by PCR array in CPSC10-05R *vs.* the sham control. Pink lines represent threshold fold changes (= 3). The data are presented by fold changes of genes in CPSC10-05R (y-axis) versus fold changes of genes in the sham control (x-axis) in logarithm scale (base = 2). (*n* = 4)

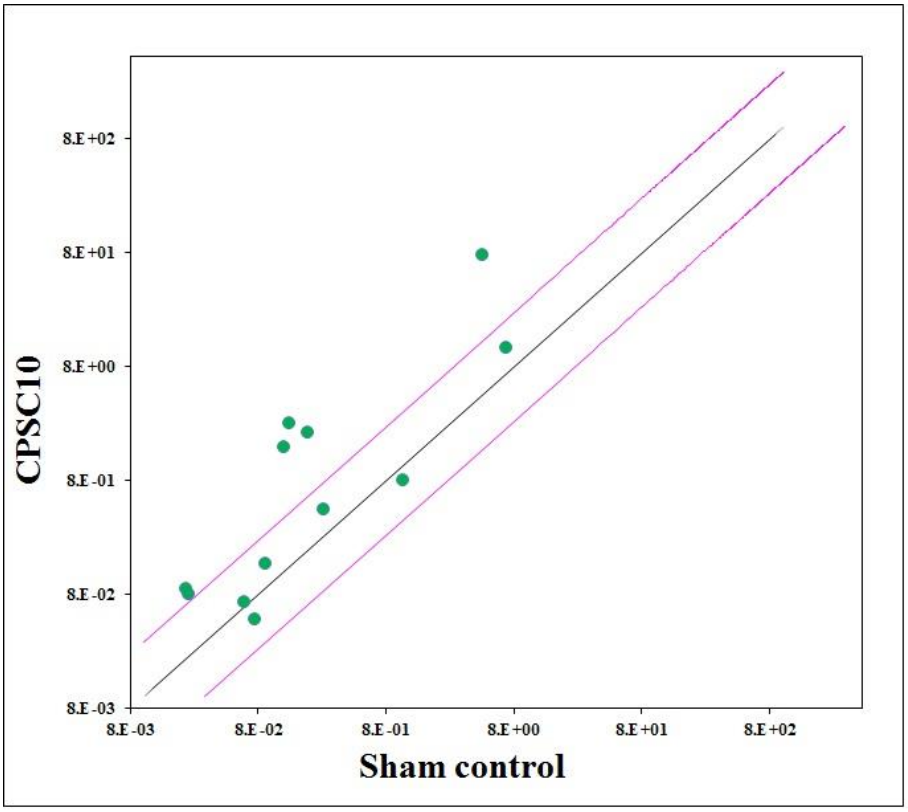

Appendix figure 40: Genes related to calcium ion binding and homeostasis analyzed by PCR array in CPSC10 *vs.* the sham control. Pink lines represent threshold fold changes (= 3). The data are presented by fold changes of genes in CPSC10 (y-axis) versus fold changes of genes in the sham control (x-axis) in logarithm scale (base = 2). (*n* = 4)

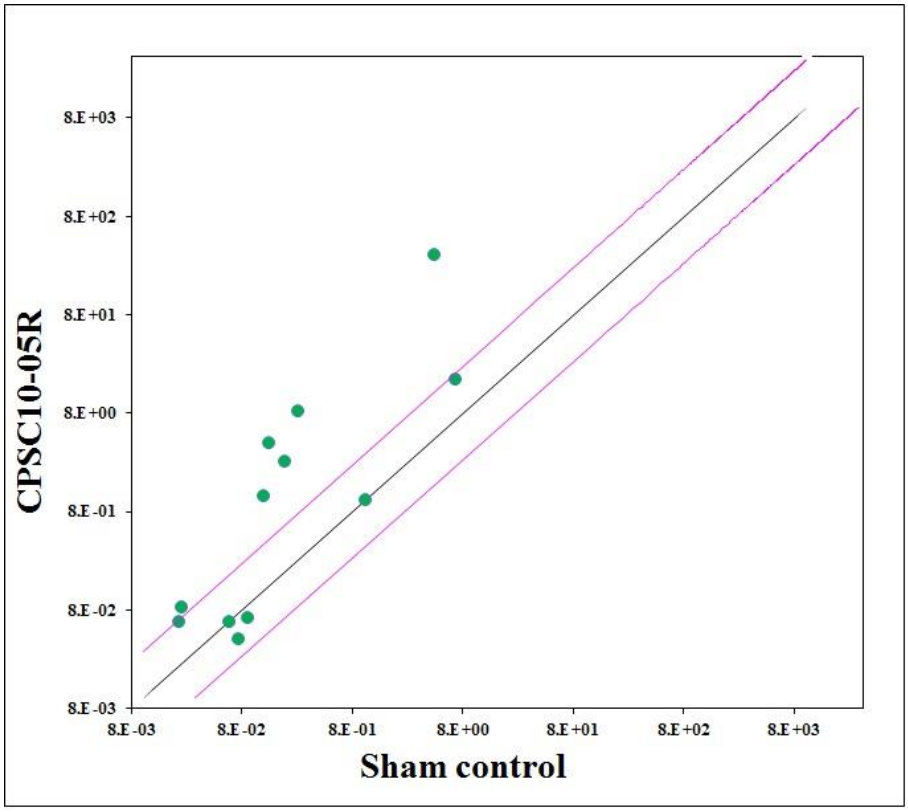

Appendix figure 41: Genes related to calcium ion binding and homeostasis analyzed by PCR array in CPSC10-05R *vs.* the sham control. Pink lines represent threshold fold changes (= 3). The data are presented by fold changes of genes in CPSC10-05R (y-axis) versus fold changes of genes in the sham control (x-axis) in logarithm scale (base = 2). (*n* = 4)

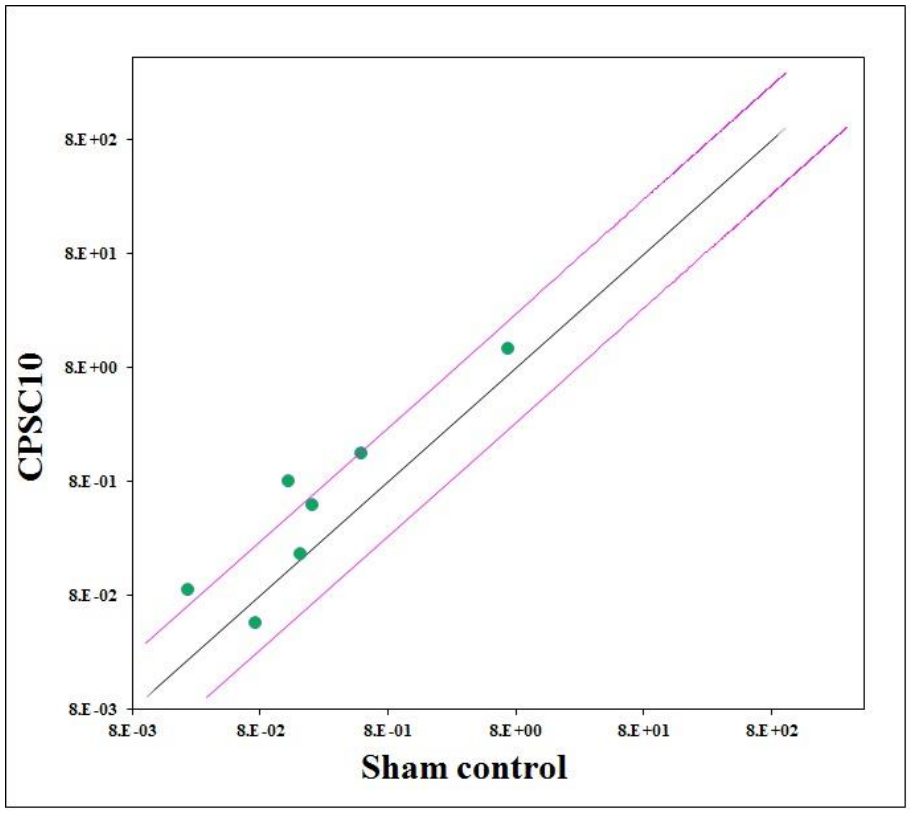

Appendix figure 42: Genes related to cartilage condensation analyzed by PCR array in CPSC10 *vs.* the sham control. Pink lines represent threshold fold changes (= 3). The data are presented by fold changes of genes in CPSC10 (y-axis) versus fold changes of genes in the sham control (x-axis) in logarithm scale (base = 2). (*n* = 4)

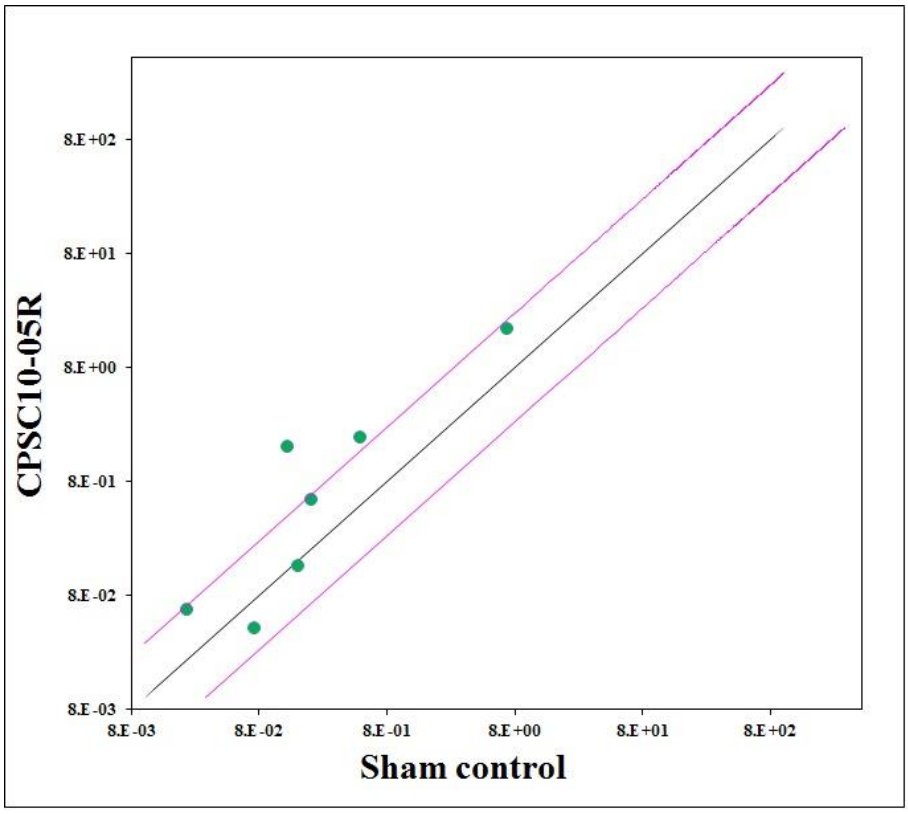

Appendix figure 43: Genes related to cartilage condensation analyzed by PCR array in CPSC10-05R *vs.* the sham control. Pink lines represent threshold fold changes (= 3). The data are presented by fold changes of genes in CPSC10-05R (y-axis) versus fold changes of genes in the sham control (x-axis) in logarithm scale (base = 2). (*n* = 4)

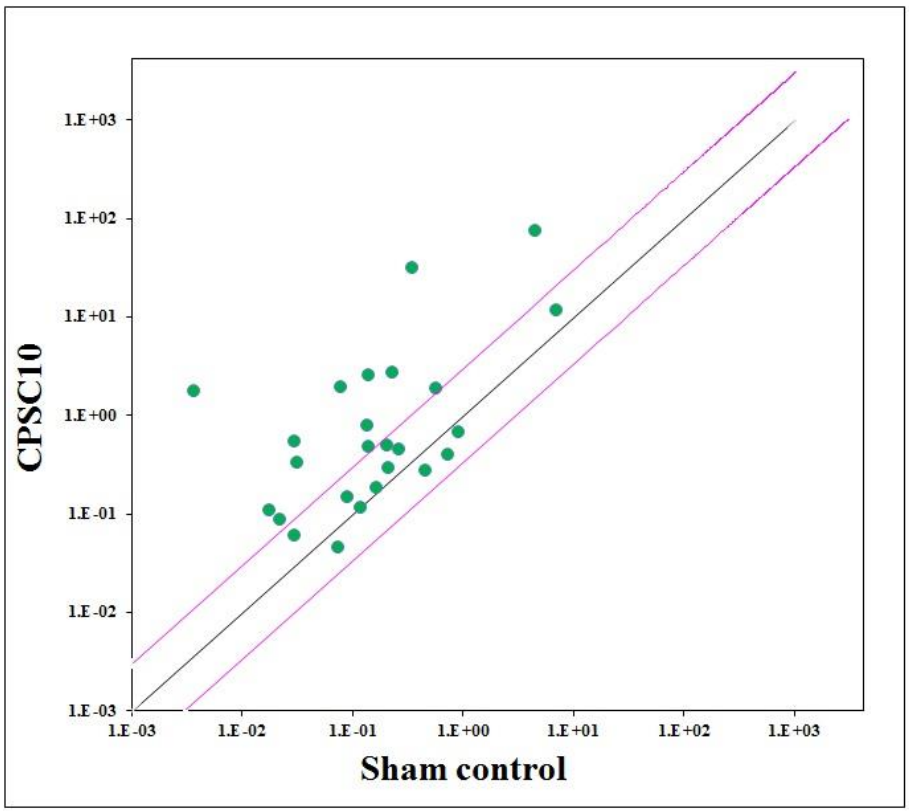

Appendix figure 44: Genes related to cell adhesion analyzed by PCR array in CPSC10 *vs.* the sham control. Pink lines represent threshold fold changes (= 3). The data are presented by fold changes of genes in CPSC10 (y-axis) versus fold changes of genes in the sham control (x-axis) in logarithm scale (base = 2). (*n* = 4)

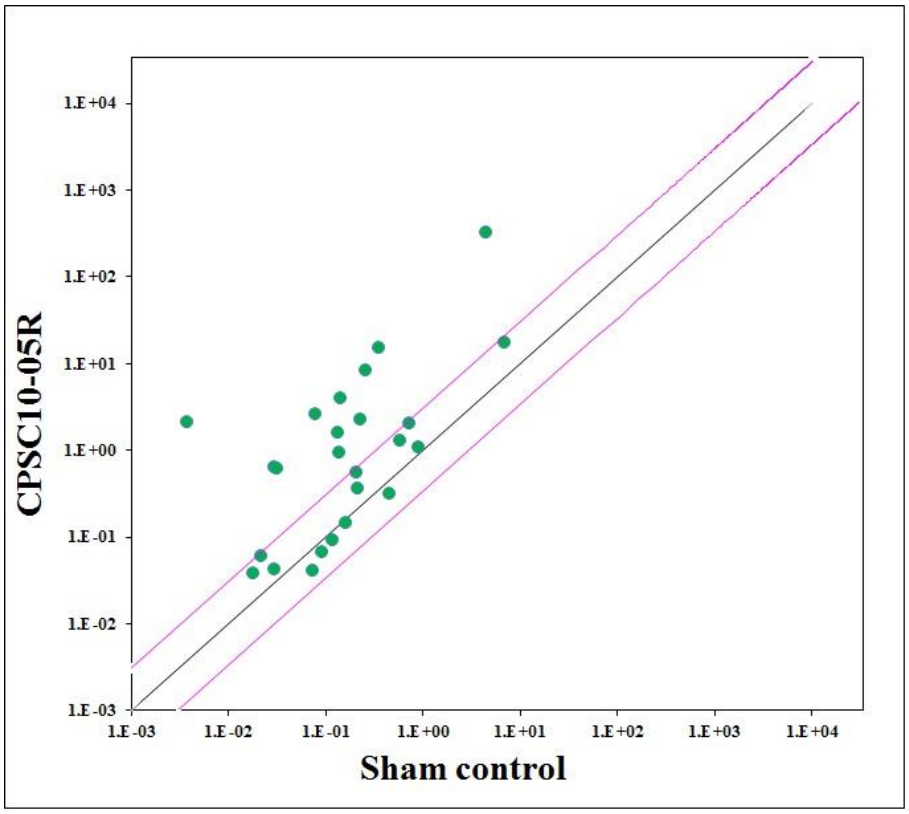

Appendix figure 45: Genes related to cell adhesion analyzed by PCR array in CPSC10-05R *vs.* the sham control. Pink lines represent threshold fold changes (= 3). The data are presented by fold changes of genes in CPSC10-05R (y-axis) versus fold changes of genes in the sham control (x-axis) in logarithm scale (base = 2). (*n* = 4)

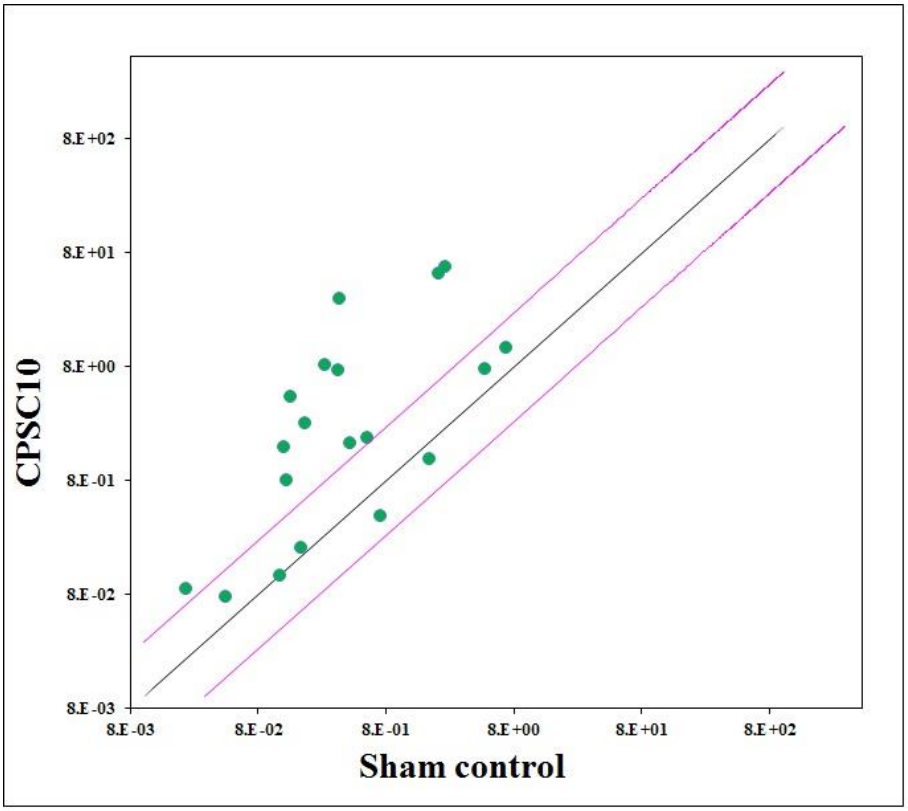

Appendix figure 46: Genes related to ECM analyzed by PCR array in CPSC10 *vs.* the sham control. Pink lines represent threshold fold changes (= 3). The data are presented by fold changes of genes in CPSC10 (y-axis) versus fold changes of genes in the sham control (x-axis) in logarithm scale (base = 2). (*n* = 4)

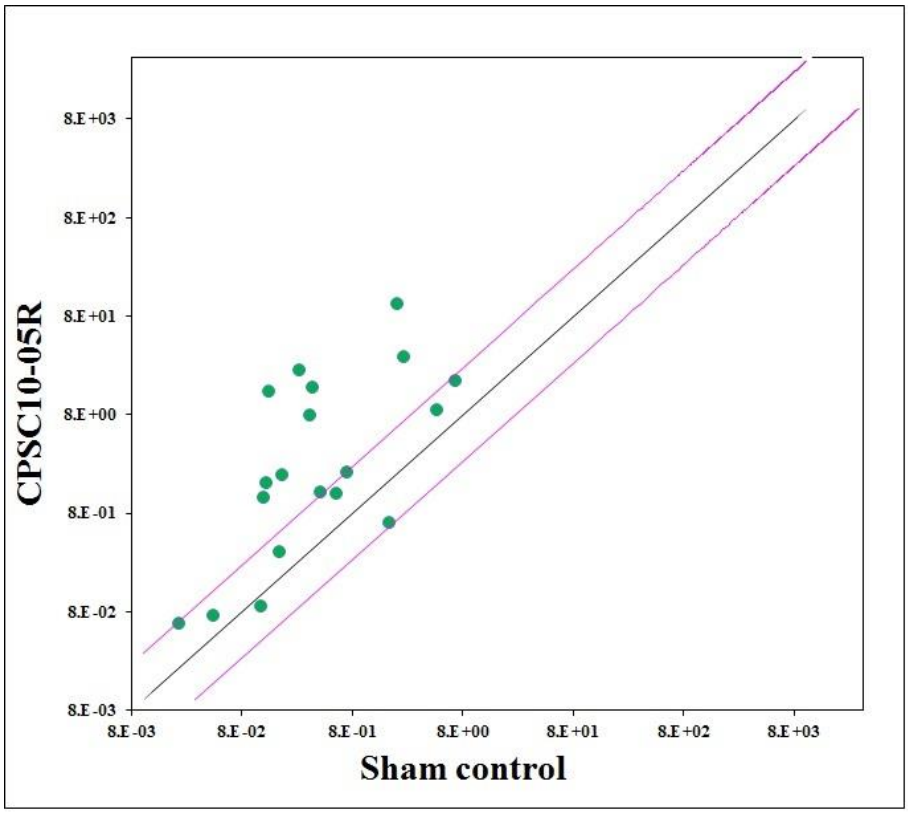

Appendix figure 47: Genes related to ECM analyzed by PCR array in CPSC10-05R *vs.* the sham control. Pink lines represent threshold fold changes (= 3). The data are presented by fold changes of genes in CPSC10-05R (y-axis) versus fold changes of genes in the sham control (x-axis) in logarithm scale (base = 2). (*n* = 4)

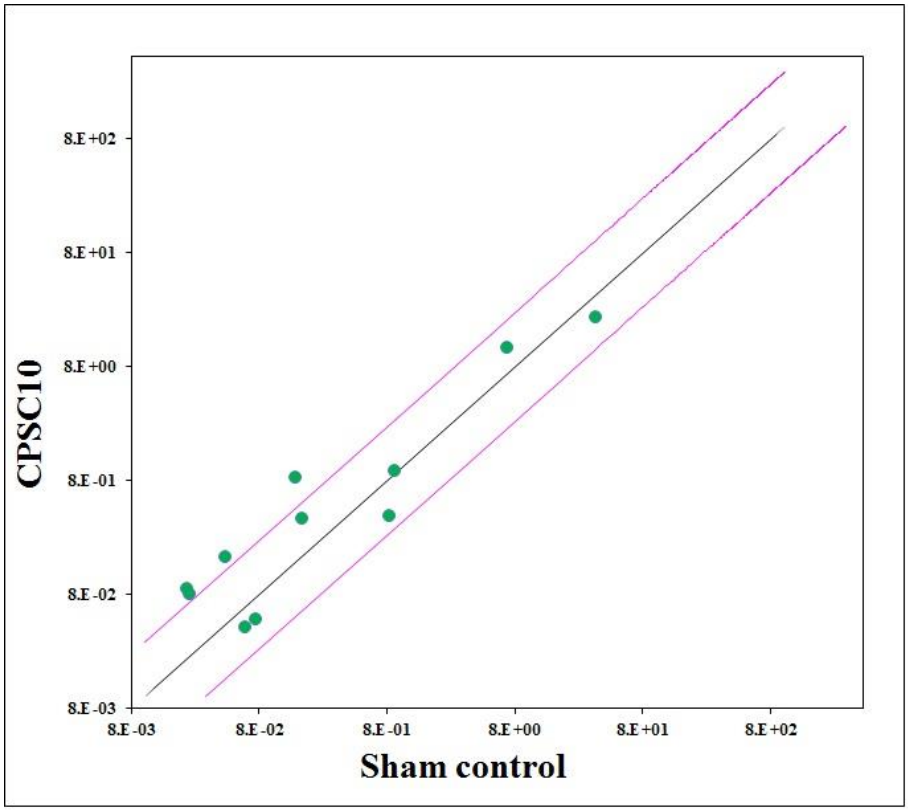

Appendix figure 48: Genes related to growth factors analyzed by PCR array in CPSC10 *vs.* the sham control. Pink lines represent threshold fold changes (= 3). The data are presented by fold changes of genes in CPSC10 (y-axis) versus fold changes of genes in the sham control (x-axis) in logarithm scale (base = 2). (*n* = 4)

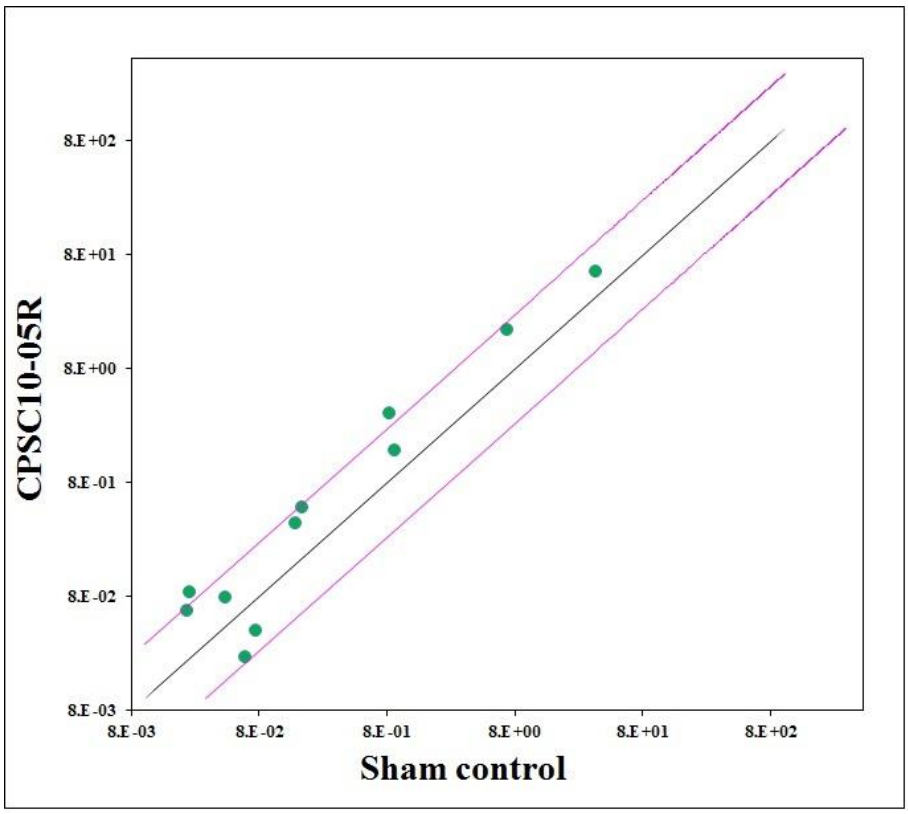

Appendix figure 49: Genes related to growth factors analyzed by PCR array in CPSC10-05R *vs.* the sham control. Pink lines represent threshold fold changes (= 3). The data are presented by fold changes of genes in CPSC10-05R (y-axis) versus fold changes of genes in the sham control (x-axis) in logarithm scale (base = 2). (*n* = 4)

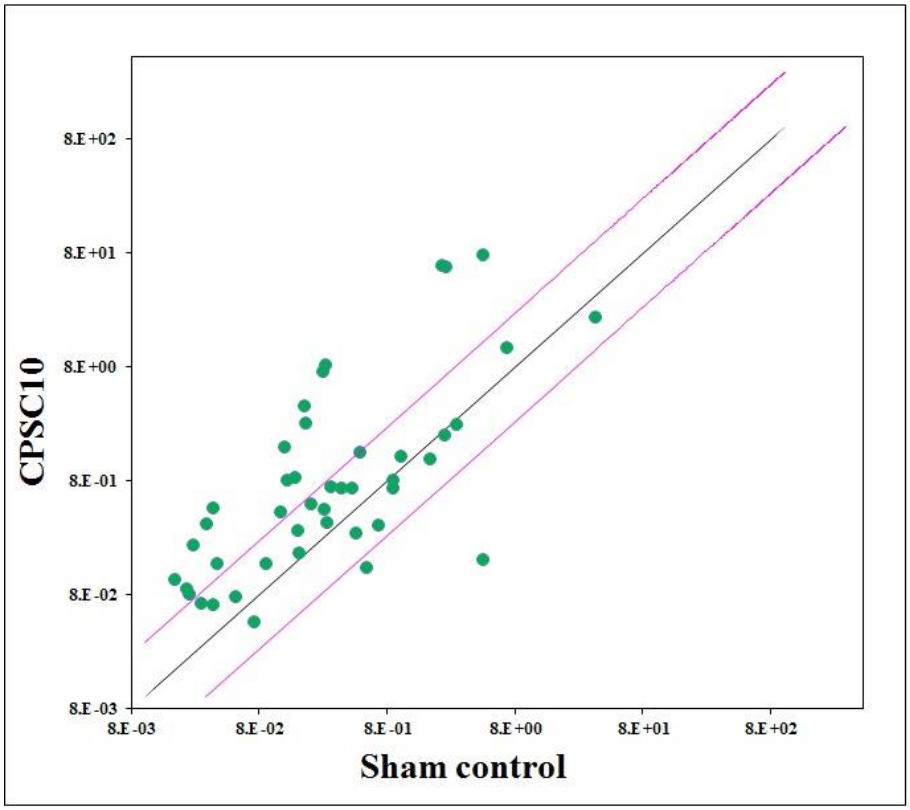

Appendix figure 50: Genes related to ossification analyzed by PCR array in CPSC10 *vs.* the sham control. Pink lines represent threshold fold changes (= 3). The data are presented by fold changes of genes in CPSC10 (y-axis) versus fold changes of genes in the sham control (x-axis) in logarithm scale (base = 2). (*n* = 4)

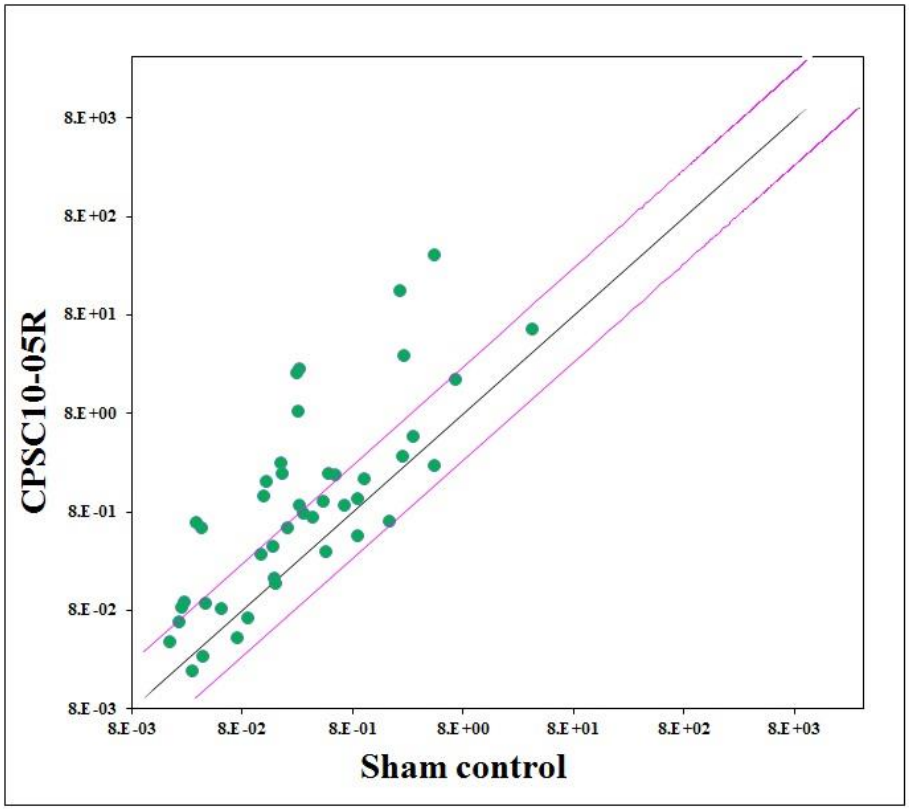

Appendix figure 51: Genes related to ossification analyzed by PCR array in CPSC10-05R *vs.* the sham control. Pink lines represent threshold fold changes (= 3). The data are presented by fold changes of genes in CPSC10-05R (y-axis) versus fold changes of genes in the sham control (x-axis) in logarithm scale (base = 2). (*n* = 4)

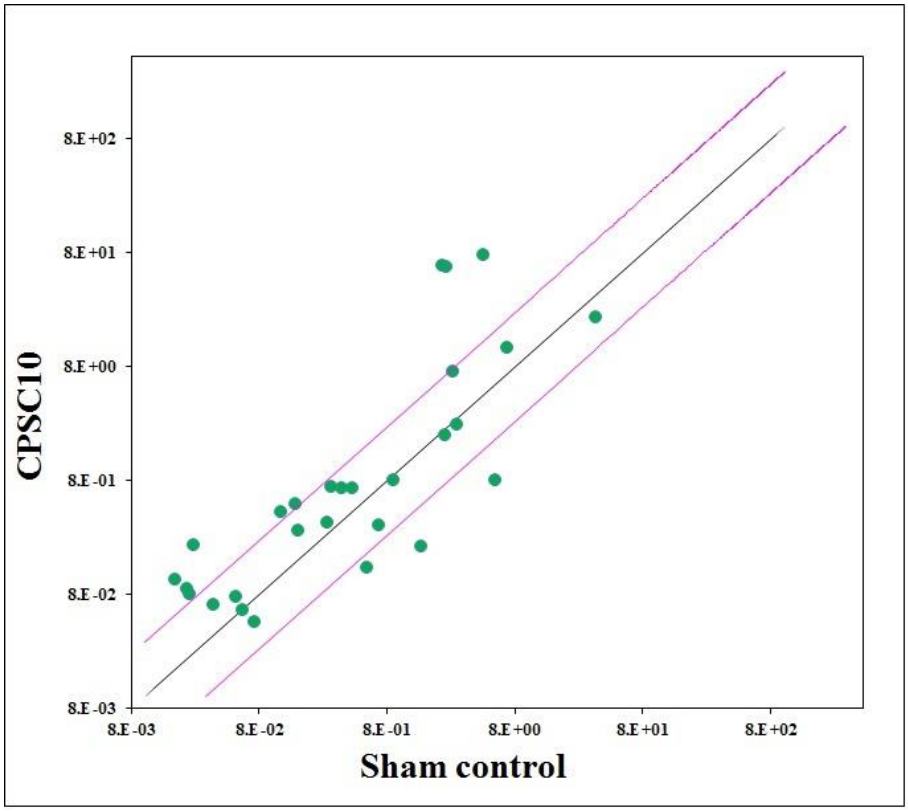

Appendix figure 52: Genes related to osteoblast differentiation analyzed by PCR array in CPSC10 *vs.* the sham control. Pink lines represent threshold fold changes (= 3). The data are presented by fold changes of genes in CPSC10 (y-axis) versus fold changes of genes in the sham control (x-axis) in logarithm scale (base = 2). (*n* = 4)

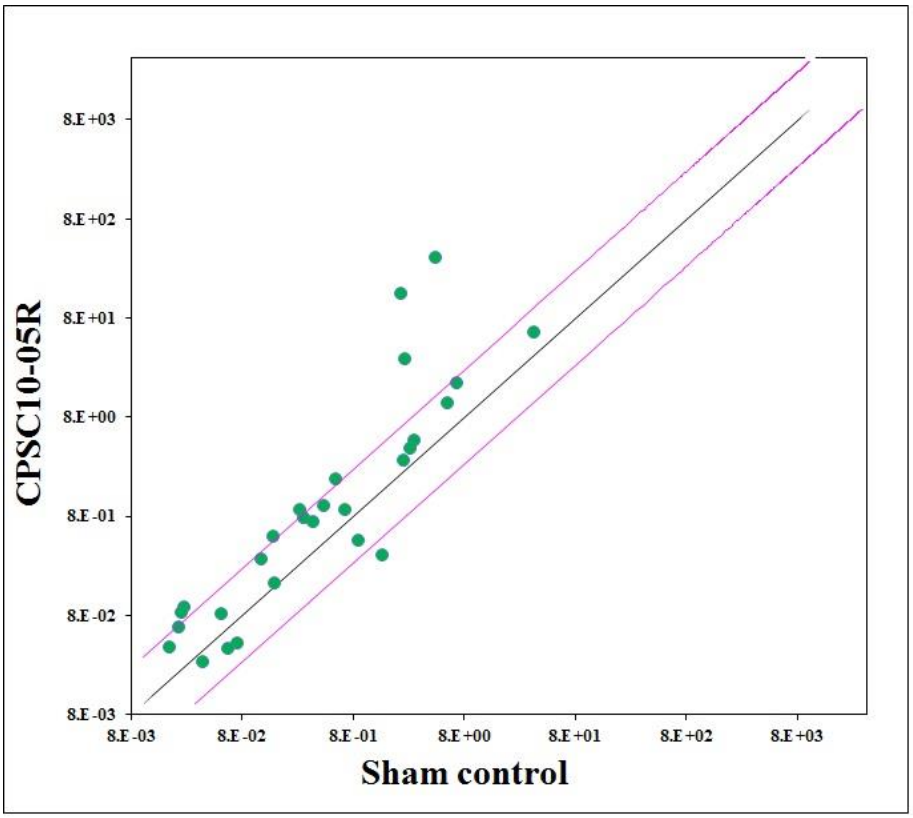

Appendix figure 53: Genes related to osteoblast differentiation analyzed by PCR array in CPSC10-05R *vs.* the sham control. Pink lines represent threshold fold changes (= 3). The data are presented by fold changes of genes in CPSC10-05R (y-axis) versus fold changes of genes in the sham control (x-axis) in logarithm scale (base = 2). (*n* = 4)

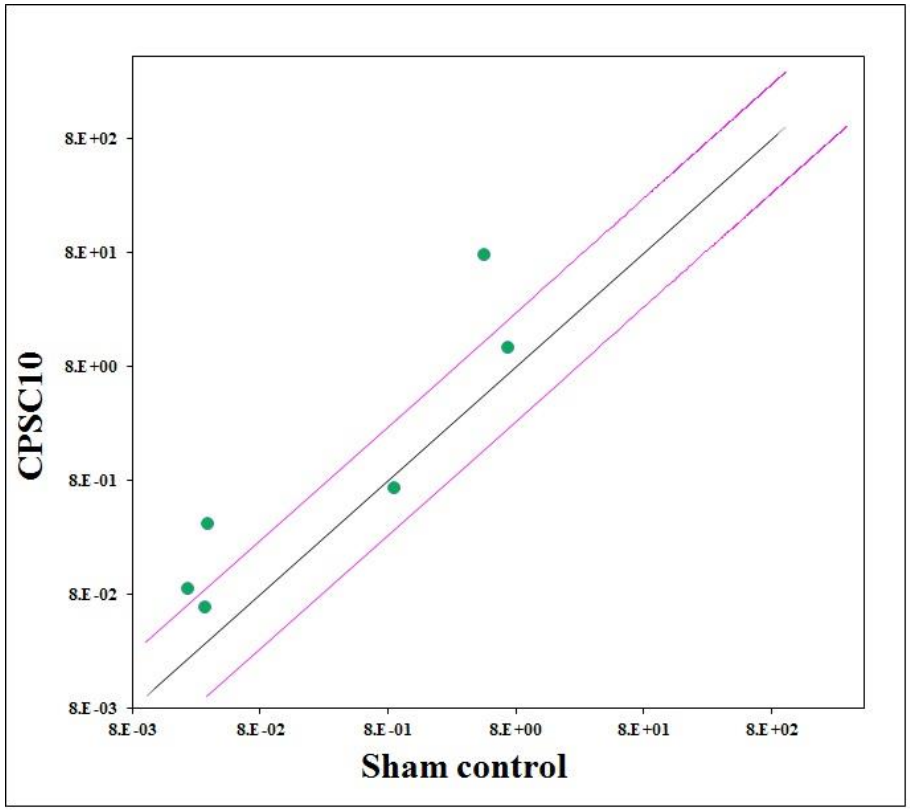

Appendix figure 54: Genes related to osteoclast differentiation analyzed by PCR array in CPSC10 *vs.* the sham control. Pink lines represent threshold fold changes (= 3). The data are presented by fold changes of genes in CPSC10 (y-axis) versus fold changes of genes in the sham control (x-axis) in logarithm scale (base = 2). (*n* = 4)

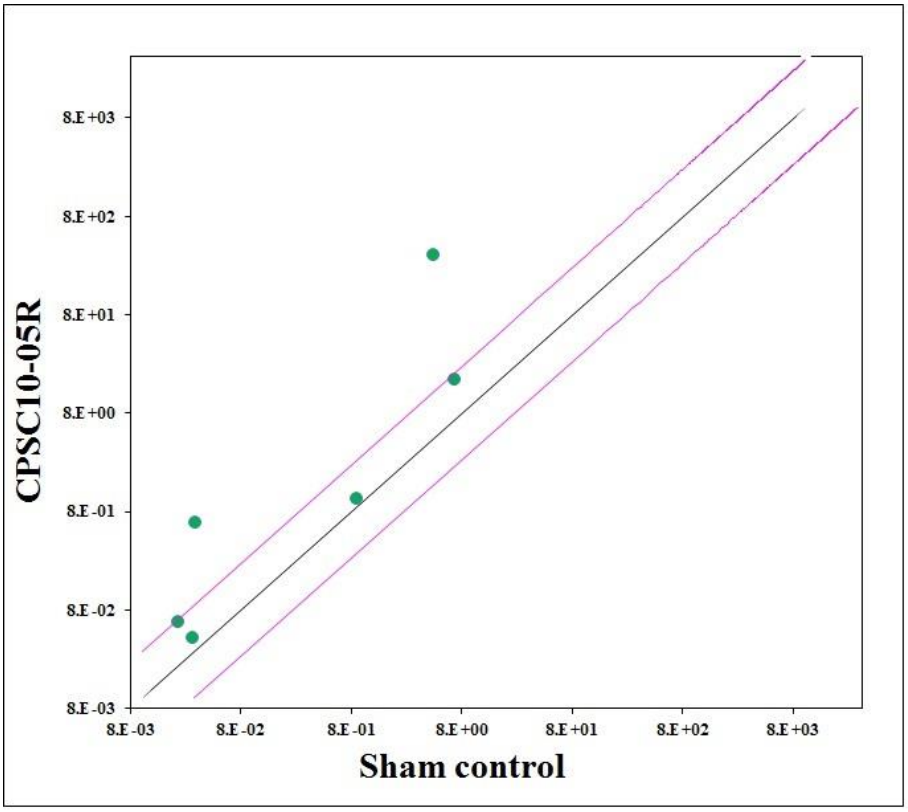

Appendix figure 55: Genes related to osteoclast differentiation analyzed by PCR array in CPSC10-05R *vs.* the sham control. Pink lines represent threshold fold changes (= 3). The data are presented by fold changes of genes in CPSC10-05R (y-axis) versus fold changes of genes in the sham control (x-axis) in logarithm scale (base = 2). (*n* = 4)

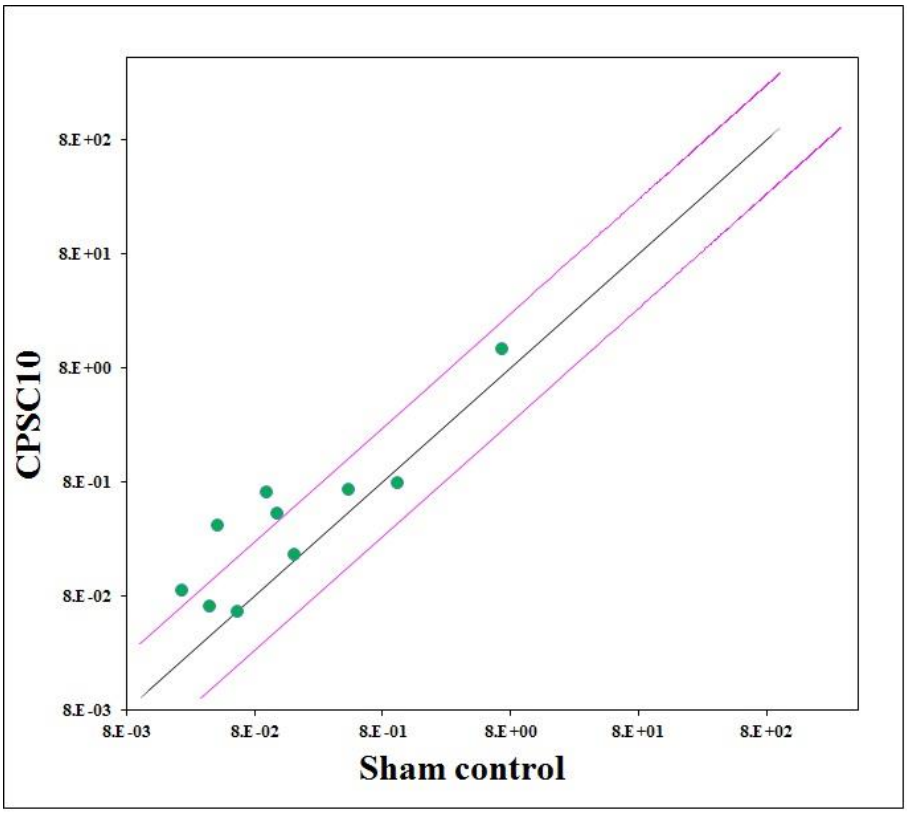

Appendix figure 56: Genes related to transcription factors analyzed by PCR array in CPSC10 *vs.* the sham control. Pink lines represent threshold fold changes (= 3). The data are presented by fold changes of genes in CPSC10 (y-axis) versus fold changes of genes in the sham control (x-axis) in logarithm scale (base = 2). (*n* = 4)

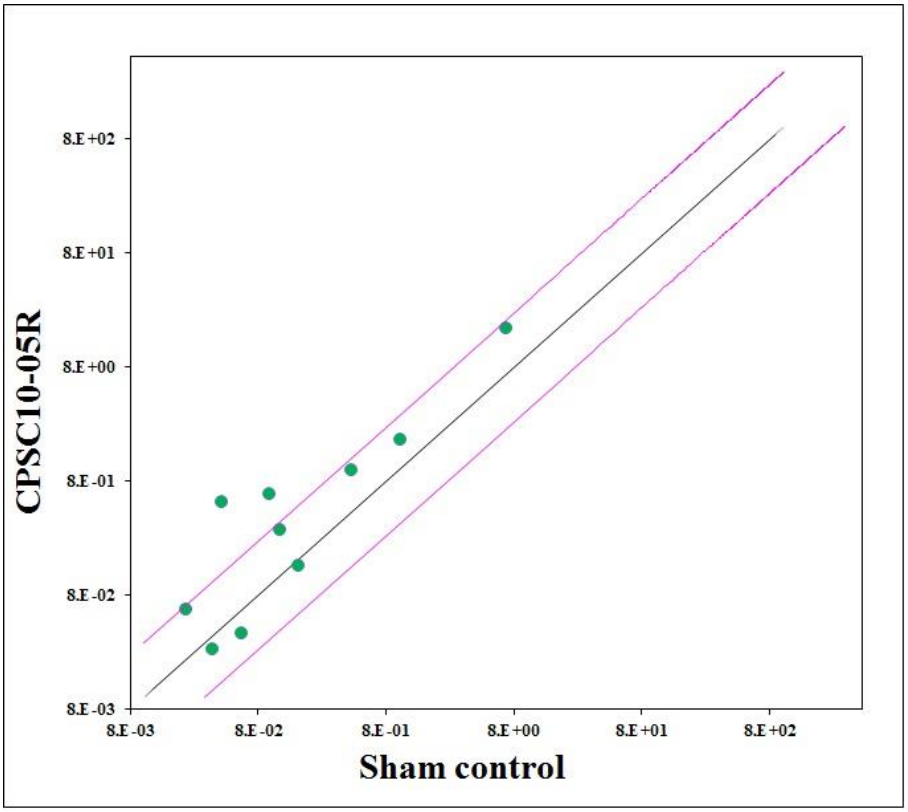

Appendix figure 57: Genes related to transcription factors analyzed by PCR array in CPSC10-05R *vs.* the sham control. Pink lines represent threshold fold changes (= 3). The data are presented by fold changes of genes in CPSC10-05R (y-axis) versus fold changes of genes in the sham control (x-axis) in logarithm scale (base = 2). (*n* = 4)